UNIVERSIDADE DE LISBOA

FACULDADE DE CIÊNCIAS

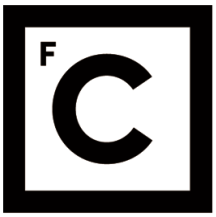

Ciências
ULisboa

HEADLAND SEDIMENT BYPASSING PROCESSES

Doutoramento em Geologia
Especialidade em Geodinâmica Externa

Mónica Sofia Afonso Ribeiro

Tese orientada por:
Professor Doutor Rui Pires de Matos Taborda
Doutora Aurora da Conceição Coutinho Rodrigues Bizarro

Documento especialmente elaborado para a obtenção do grau de doutor

2017

UNIVERSIDADE DE LISBOA

FACULDADE DE CIÊNCIAS

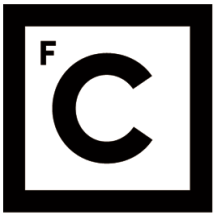

Ciências
ULisboa

HEADLAND SEDIMENT BYPASSING PROCESSES

Doutoramento em Geologia
Especialidade em Geodinâmica Externa

Mónica Sofia Afonso Ribeiro

Tese orientada por:
Professor Doutor Rui Pires de Matos Taborda
Doutora Aurora da Conceição Coutinho Rodrigues Bizarro

Júri:
Presidente:
- Doutora Maria da Conceição Pombo de Freitas

Vogais:
- Doutor António Henrique da Fontoura Klein
- Doutor Óscar Manuel Fernandes Cerveira Ferreira
- Doutora Anabela Tavares Campos Oliveira
- Doutor César Augusto Canelhas Freire de Andrade
- Doutor Rui Pires de Matos Taborda

Documento especialmente elaborado para a obtenção do grau de doutor

Fundação para a Ciência e Tecnologia, no âmbito da Bolsa de Doutoramento com a referência
SFRH/BD/79126/2011

2017

Em memória do meu irmão Luís

Acknowledgments | Agradecimentos

O doutoramento é um processo exigente, por vezes solitário, mas que só é possível com o apoio e a colaboração de outras pessoas e instituições. Portanto, resta-me agradecer a todos os que contribuíram para a conclusão deste trabalho.

Em primeiro lugar agradeço aos meus orientadores, Rui Taborda e Aurora Bizarro, que têm acompanhado o meu trabalho desde os meus primeiros passos na Geologia Marinha, já lá vão 10 anos! A eles agradeço o incentivo para iniciar este projeto, o apoio demonstrado em todas as fases do trabalho, a confiança e a amizade. Ao Rui agradeço, em particular, a partilha e discussão de ideias e os desafios constantes que me permitiram evoluir. À Aurora, o pragmatismo tão importante nos momentos cruciais e a possibilidade de terminar esta tarefa com o tempo e a tranquilidade necessários.

Durante estes cinco anos tive a oportunidade de trabalhar integrada em duas equipas, a do IH e a da FCUL, que foram fundamentais para levar este trabalho a bom porto. Agradeço a todos os que delas fazem parte, sem exceção, mas tenho de expressar a minha gratidão de forma particular a alguns deles:

- ao João Duarte, com quem partilhei toneladas de areia e algumas viagens de empilhador, agradeço a ajuda fundamental na concretização da experiência de traçadores e a orientação nas análises de suscetibilidade magnética.

- ao João Cascalho, a colaboração e o entusiamo no estudo dos minerais pesados, bem como a revisão crítica de parte do texto.

- à Anabela Oliveira, as análises de RX, as fotografias da Foz do Lizandro e, não menos importante, a companhia na subida da Calçada do Combro com direito a gelado *Santini* em dias de calor.

- à minha colega e amiga Cristina Lira, a ajuda preciosa na implementação do RUSLE e na análise das imagens de satélite, entre muitas outras coisas (*keep calm, our day will come!*).

- à minha colega e amiga Ana Silva, a ajuda no processamento das imagens de vídeo, assim como a revisão cuidada de parte da tese e as visitas dos "piolhos" que, tantas vezes, me esqueceram o coração.

- à minha irmã na ciência Ivana Bosnic, o companheirismo e a amizade que nasceu com o *Beach Sand Code*, e a partilhar ideias e experiências durante este período, ainda que os nossos doutoramentos não se tenham cruzado tantas vezes como gostaríamos.

- à Ana Bastos, Mafalda Carapuço e Umberto Andriolo, por literalmente me terem conduzido até ao campo e pela boa companhia. À Ana Bastos quero ainda agradecer as banhocas e as várias tentativas de amostragem na plataforma interna, onde a Conceição Conde e o João Matos tiveram uma participação.

- à Ana Santos e à guarnição da Andrómeda, em particular, à Comandante Dóris Ribeiro Fonseca, pela oportunidade de amostrar sedimentos ao largo do Cabo da Roca; à Maria João Balsinha, pela boa vontade e prontidão com que atendeu a todos os meus pedidos de ajuda, além da partilha do Esporão da Estremadura; ao Frederico Ferreira, pela ajuda no processamento e interpretação dos dados de sonar lateral; à Cecília Luz e ao Joaquim Pombo, pelo tempo que "esbotanaram" no *Nautilus* para ter acesso aos resultados das análises laboratoriais.

- ao José Paulo Pinto e à Sara Almeida, pela disponibilidade e simpatia com que responderam às minhas solicitações; e ao José Aguiar, pela boa disposição e amabilidade com que, tantas vezes, fez "aquela pergunta".

- um agradecimento especial e saudoso aos que com boa disposição partilharam comigo o magnífico cheiro do diluente ao som das betoneiras, o belíssimo dia 8 de Setembro de 2014 e os intermináveis tabuleiros de areia no laboratório das Trinas: Aida Seabra, Ana Bastos, Ana Santos, Ana Silva (e Marta), Armando Marques, Aurora Bizarro, Cassandra Pólvora, César Jesus, Cesarina Pádua, Cristina Lira, Ernesto Mendes, Isaac Silva, Ivana Bosnic (e Lucas), João Cascalho, João Duarte, João Hermínio, Laura Reis, Milton Cabral, Nuno Lapa, Pedro Costa, Ruben Santos, Rui Taborda, Umberto Andriolo e Zenaida Diogo.

No plano institucional agradeço à Fundação para a Ciência e Tecnologia (FCT) pelo financiamento concedido (SFRH/BD/79126/2011); ao Instituto Hidrográfico, Instituto Dom Luiz e Departamento de Geologia da FCUL, pelo espaço e condições necessárias à realização das minhas atividades; e à Capitania do Porto de Cascais e Agência Portuguesa do Ambiente (APA), pela permissão para realizar a experiência de traçadores.

Ao projeto *Beach to Canyon* (PTDC/MAR/114674/2009), pelo suporte fundamental à realização da experiência de traçadores; e aos projetos MICORE (ID 202798, FP7-ENVIRONMENT) e

"Criação e implementação de um sistema de monitorização no litoral abrangido pela área de jurisdição da Administração da Região Hidrográfica do Tejo" da Fundação da FCUL e da APA, os dados disponibilizados.

Ao professor Fernando Marques da FCUL, a disponibilidade para esclarecer alguns aspetos sobre as arribas da área de estudo; ao professor Xavier Bertin da Universidade de *La Rochelle*, os dados de ondas; e ao doutor Fernando Magalhães da APA, a informação disponibilizada sobre as dragagens no Porto da Ericeira.

Ao meu primo Francisco Carneiro, a fotografia de última hora na praia da Baleia; ao meu amigo João Marques, aquele bocadinho de areia da praia Grande; e ao Manuel Coelho e à Zoa pela boa companhia naquela viagem entre Sta. Cruz e a Ericeira.

Um agradecimento muito especial às minhas colegas de doutoramento da 6.2.79, Ivana, Mafalda e Tanya, com quem partilhei os altos e baixos inevitáveis deste percurso e as inesquecíveis sessões do MIMT.

Às minhas colegas e amigas de tertúlia na *Casa da Índia*, Cata, Sandrinha e Xana, agradeço as risadas e as sessões de exorcismo fundamentais à saúde mental de qualquer doutorando.

À família das Olaias e à família do Cacém que, sem compreenderem muito bem porque é que um doutoramento consome tanto tempo e energia, estiveram sempre lá e tornaram tudo mais fácil.

Aos meus pais, aos meus sogros e ao meu 1berto, por partilharem comigo os dias de chuva e os dias de sol.

Muito obrigada!

Abstract

Headland sediment bypassing (HSB) processes play an important role in the definition of the littoral sediment budget, having particular relevance on headland-bay coasts. However, HSB has received little attention compared to other topics of headland-bay beach research, such as the beach planform rotation and stability. Thus, the main goal of this thesis was to increase the knowledge on HSB and recognize its role on the sediment budget of headland-bay beaches.

The study was carried out in a 100 km rocky coastal stretch located at the Portuguese western coast, between the Carvoeiro and Raso capes, where numerous headland-bay beaches develops in a wide range of different geomorphological settings.

To achieve the proposed goals, the work was supported by several complementary approaches that gave insights on the processes that constrain headland-bay beaches evolution at a wide range of spatial and temporal scales. These approaches included: (1) detailed morphological and sedimentological analysis of the beaches and inner continental shelf; (2) the study of the longshore drift based on a fluorescent tracer experiment (short-term approach) and empirical modelling (long-term approach); (3) the development and application of a new shoreline evolution model (SEM-PLAT) that simulate shoreline changes on beaches develop over a rocky shore platform; and (4) the analysis of the sediment sources and sinks along the studied coastal stretch and study of long-term evolution trends.

The results obtained allowed to classify dominant HSB processes in two main modes, which are in line with two of the existing conceptual models. The processes were classified according to the prevailing domain where sediment bypass the headlands as: (1) beach headland sediment bypassing (BSB) – a process that takes place at the subaerial section of the beach, and (2) inner shelf headland sediment bypassing (SSB) – a process that occurs on the submarine domain. BSB process is triggered by the persistence of incoming wave direction, inducing beach rotation that, especially in low-degree embayments, can result in a continuous inner sandbar along the headland coast, which migrates downdrift and welds to the downdrift beach. This process is dominated by the longshore drift, occurring mainly in the intertidal zone and, eventually, in very

shallow depths of the submarine domain. SSB process, on the other hand, is triggered by high-energy wave conditions. Under these conditions, the strong offshore currents can transport sediment outside the embayments. The sediment that is pushed offshore is distributed on the inner shelf and eventually transported alongshore, bypassing the headlands. When wave energy start to reduce, the sediment is slowly transported onshore and start to weld to the downdrift beaches. This process depends on both cross- and longshore transport components and can occur in both low- and high-indented beaches.

The results also showed that HSB is a selective process. Coarser particles such gravel and very coarse sand tend to be trapped inside the embayments, being their bypass very low or negligible. Coarse sand bypass occurs mainly in the subaerial beach, except during major storm events, when the wave energy triggers an extreme efficient selective process, transporting the lighter sediment particles offshore (including coarser sands), originating heavy mineral placer deposits. This selective process can generate large placer deposits (*e.g.* Grande beach) due to a long-term enrichment in heavy mineral particles. In the case of medium sand particles, headland bypass can occur either subaerial beach or inner shelf domain, depend on the wave energy; while fine sand bypass occur mainly at the inner shelf.

This work also allowed to have a better understanding of the coastal dynamics of the target coastal stretch. The sediment transport patterns suggest that the studied coast is segmented in four sediment sub-cells: (1) Carvoeiro-Consolação; (2) Consolação-Lamporeira; (3) Lamporeira-Roca; and (4) Roca-Raso. The first sub-cell have particular characteristics due to the shelter promoted by the Peniche peninsula to the NW dominant waves and corresponds to a small closed system. The sub-cells (2) to (4) are macro scale embayments that are connected and have a similar sedimentary dynamics. The northern sectors of these embayments have a NW-SE or N- S general orientation and net longshore drift is southward for both winter and summer wave conditions. Thus, within these sectors, HSB occurs always southward, independently of the HSB process. The southern sectors, on the other hand, have a NE-SW general orientation and net longshore drift is southward, in the summer, and northward, in the winter. In these sectors, HSB occur mainly through the BSB, during summer, induced by the higher persistence of NW waves. While in winter, occur preferable through the SSB due to the increase of wave energy and considering that, BSB northward is unlikely due to the larger distances between the shoreline (beach berm) and the tip of the headlands and the lower persistence of W and SW waves. The balance between the longshore transport components within the southern sectors of the macro scale embayments, results in a sediment recirculation, which explains the sandier nature of inner shelf in these sectors compared to the northern ones. This also suggest that sediment can have

a relatively long residence time inside these sub-cells. However, once sediment cross the sub-cell boundaries cannot return, because at the downdrift side the net longshore drift is permanently southward (gated boundaries). The frequency of the sediment linkage between these sub-cells depends on the seasonal and interannual wave climate variability; while the magnitude depends on the balance between the sediment sources and sinks of each sub-cell and was estimated in the order of 10^4 $m^3.yr^{-1}$.

The sediment budget and beach long-term evolution study, indicate that the studied littoral is in equilibrium with present-day conditions. However, SEM-PLAT model results showed that seasonal (and interannual) changes in the incident wave climate can significantly affect the beach configuration or even its development, putting in evidence the delicate dynamic equilibrium of these beaches. This delicate equilibrium and the linkage of the beaches through the HSB processes, suggests that climate changes can have strong impacts on their evolution.

Keywords: Headland sediment bypassing; Headland-bay beaches; Longshore sediment transport; Coastal dynamics; Portuguese western coast.

Resumo

O conhecimento dos processos de transposição sedimentar de promontórios (TSP) é fundamental para definir o balanço sedimentar das células litorais, sendo particularmente relevante nos sistemas de praia em enseadas, típicos de costas rochosas. No entanto, o estudo das praias em enseada têm sido essencialmente focado na investigação da rotação e da configuração de equilíbrio da sua forma planar, uma vez que, estas praias são habitualmente consideradas como sistemas relativamente fechados. Comparativamente, pouco se tem investido na compreensão dos processos de TSP. Assim, o principal objetivo desta tese foi contribuir para o conhecimento dos processos de TSP e perceber a sua influência no balanço sedimentar das praias em enseada.

O estudo foi desenvolvido num troço litoral com cerca de 100 km de extensão, localizado na costa ocidental portuguesa, entre o cabo Carvoeiro e o cabo Raso. Este troço é particularmente rochoso, inclui promontórios de várias dimensões e acomoda um conjunto de praias com diferente comprimento, orientação, grau de encaixe e exposição à agitação marítima dominante de noroeste.

Para alcançar os objetivos propostos, o trabalho foi suportado por várias abordagens complementares que permitiram estudar os processos que condicionam a evolução das praias em enseada, a diferentes escalas espaciais e temporais. As aproximações utilizadas foram: (1) a análise morfológica e sedimentológica das praias e da plataforma continental interna; (2) o estudo da deriva litoral através de uma aproximação de curto prazo, baseada numa experiência de traçadores fluorescentes, e uma aproximação de longo prazo, baseada em taxas de transporte sedimentar potencial estimadas a partir de formulações empíricas; (3) o desenvolvimento e aplicação de um modelo de evolução de linha de costa – o modelo SEM- PLAT, que simula a evolução da linha de costa em praias que se desenvolvem sobre plataformas rochosas; e por último, (4) a análise das fontes e sumidouros sedimentares ao longo da costa em estudo e, das tendências de evolução a longo prazo das praias.

Os resultados obtidos sugerem a existência de dois processos de TSP dominantes que estão em linha com dois dos modelos conceptuais existentes. Estes processos foram classificados de acordo com o domínio onde a transposição ocorre em: (1) transposição sedimentar de promontórios na praia - um processo que ocorre essencialmente na praia subaérea, e transposição sedimentar de promontórios na plataforma continental interna - um processo que ocorre no domínio submarino. O processo de transposição na praia é desencadeado pela persistência da direção de onda incidente, induzindo a rotação das praias que, em enseadas com baixa indentação, pode resultar numa barra arenosa interna, contínua, que atravessa a costa do promontório, migrando e soldando-se com a praia a sotamar. Este processo é dominado pela deriva litoral, ocorrendo principalmente na zona intertidal e, eventualmente, nas zonas menos profundas da praia submarina. A transposição na plataforma interna, por outro lado, é desencadeada por condições de agitação marítima de elevada energia. Nessas condições, as intensas correntes em direção ao largo, podem transportar sedimentos para fora das enseadas. Esse sedimento é distribuído na plataforma interna e, eventualmente, transportado longilitoralmente, transpondo os promontórios. Quando a energia das ondas começa a diminuir, o sedimento é transportado lentamente em direção à costa, alimentado as praias a sotamar. Este processo depende de ambas as componentes de transporte (transversal e longilitoral) e pode ocorrer em praias com baixo ou elevado grau de encaixe.

Os resultados também mostraram que a transposição é um processo seletivo. As partículas mais grosseiras, como o cascalho e a areia muito grosseira, tendem a ficar retidas nas enseadas, sendo a transposição destas partículas negligível ou de baixa magnitude. No caso das areias grosseiras, a transposição ocorre essencialmente na praia subaérea, exceto durante tempestades extremas, quando a energia das ondas desencadeia um processo extremamente seletivo, que transporta a partículas mais leve para o largo (incluindo as areias mais grosseiras), originando depósitos de *placer*. Em algumas praias (*e.g.* praia Grande) estes depósitos de *placer* podem apresentar uma dimensão considerável devido a um processo cumulativo de longo prazo de partículas de minerais pesados. A transposição de areias médias pode ocorrer em ambos os domínios, isto é, na praia subaérea e na plataforma interna, dependo da energia das ondas; enquanto a transposição de areias finas ocorre essencialmente em domínio de plataforma interna.

Os resultados obtidos no âmbito deste trabalho permitiram também uma melhor compreensão da dinâmica sedimentar do troço costeiro em estudo. Os padrões de deriva litoral ao longo da costa sugerem que esta se encontra segmentada em quatro sub-células sedimentares: (1) Carvoeiro-Consolação; (2) Consolação-Lamporeira; (3) Lamporeira-Roca; E (4) Roca-Raso. A primeira sub-célula corresponde a uma pequena enseada com características particulares

devido ao abrigo gerado pela península de Peniche às ondas dominantes de noroeste e, corresponde a um pequeno sistema fechado. As sub-células (2) a (4) constituem três enseadas de macro escala que se encontram conectadas e apresentam uma dinâmica sedimentar semelhante. Os setores norte destas sub-células têm uma orientação geral NO-SE ou N-S e uma deriva litoral residual dirigida para sul, quer para as condições de agitação marítima de verão, quer de inverno. Assim, nestes setores, a transposição é unidirecional (para sul), independentemente do processo de transposição. Nos setores sul, a orientação geral da costa é NE-SO e a deriva litoral residual é dirigida para sul, no verão, e para norte, no inverno. No verão a transposição ocorre através do processo de transposição na praia subaérea, devido à maior persistência de ondas vindas de noroeste; enquanto no inverno, deverá ocorrer essencialmente através do processo de transposição na plataforma interna, devido ao aumento de energia do clima de agitação marítima. No inverno, o processo de transposição na praia dirigido para norte, é pouco provável tendo em conta as maiores distâncias entre a linha de costa (neste caso, a crista da berma) e a ponta dos promontórios e, também, porque as condições de agitação marítima de oeste e sudoeste são menos persistentes. O equilíbrio entre as componentes norte e sul do transporte longilitoral, nos sectores sul destas sub-células, origina uma recirculação de sedimentos que explica a natureza arenosa da plataforma interna nesses setores, em oposição aos sectores norte mais rochosos. Este facto sugere que o sedimento pode ter um tempo de permanência relativamente longo dentro das sub-células. No entanto, quando o sedimento transpõem as fronteiras das sub-células, não pode reverter o seu movimento porque no lado sotamar a deriva litoral residual é permanentemente dirigida para sul. A frequência da ligação sedimentar entre as sub-células, depende da variabilidade sazonal e interanual do clima de agitação marítima. A magnitude, por outro lado, depende do balanço entre as fontes e sumidouros sedimentares de cada sub-célula e foi estimada na ordem de 10^4 $m^3.ano^{-1}$.

O balanço sedimentar e o estudo da evolução de longo prazo das praias, indicam que o litoral estudado está em equilíbrio com as condições atuais. No entanto, os resultados do modelo SEM- PLAT mostraram que variações sazonais (e interanuais) no clima de agitação marítima podem afetar significativamente a sua configuração, colocando em evidência o equilíbrio dinâmico delicado destas praias. Este equilíbrio delicado e a ligação das praias através do processos de transposição sedimentar, sugerem que alterações climáticas podem ter impactos significativos na sua evolução.

Palavras-chave: Transposição sedimentar de promontórios; Praias de enseada; Transporte longilitoral de sedimentos; Dinâmica costeira; Costa ocidental portuguesa.

Contents

Chapter 1

General Introduction

1.1 THESIS MOTIVATION

Headland sediment bypassing (HSB) plays an important role in the definition of coastal sediment budget, having particular relevance in headland-bay coasts. However, headland-bay beaches research is usually focused on beach planform rotation and stability (*e.g*. Yasso, 1965; Silvester and Ho, 1972; Hsu *et al*., 1989; Moreno and Kraus 1999; Klein *et al*., 2002; Bowman *et al*., 2009; Iglesias *et al*., 2009; Silveira *et al*., 2010; Thomas *et al*., 2010; Oliveira and Barreiro, 2010; Harley *et al*., 2011; Short *et al*., 2014; Daly *et al*., 2015), since these beaches are generally regarded as fairly closed systems. On the other hand, sediment bypassing have been extensively studied in the context of tidal inlets and harbours, due to navigation safety issues and to solve downdrift erosion problems induced by the channels dredging and jetties implementation. Examples of these studies are Fitzgerald (1982), Sexton and Hayes (1982), Bruun and Willekes (1992), Fitzgerald *et al*. (2000), Kraus (2000), Walton (2005), Mariani *et al*., 2010, Acworth and Lawson (2011), but many others can be found in the compilation report provided by Boswood and Murray (2001). Furthermore, despite the several references to the natural HSB found in literature, as will be seen below, few are those that focus on a detail description and conceptualization of the these processes. For these reasons and taking into account that 51 % of the world's coast consists of mountainous or hilly coastline (Inman and Nordstrom, 1971), where embayed beaches tend to occur, the study of HSB processes continues to be a challenge.

1.2 RESEARCH OBJECTIVES

This thesis aimed to improve the current understanding of HSB through the identification and the description of controlling processes. To achieve this goal a rocky coastal stretch that hosts several headland-bay beaches, located at the Portuguese western coast, was chosen as case study. Depth, direction, frequency, magnitude and sediment characteristics of the HSB were investigated, as well as their relationship. Moreover, this work also intended to define the sediment budget and to understand the implications of the HSB in the sedimentary dynamics of the studied coastal stretch. The results obtained were synthetized through conceptual models of both HSB processes and sedimentary dynamics of the study site.

1.3 THESIS OUTLINE

In order to achieve the proposed objectives this study covered a wide range of topics, including morphological, sedimentological and oceanographic data analyses, a tracer experiment and processes modelling, and was structured in eight chapters:

Chapter 1 provides a general introduction that includes the thesis motivation, objectives and outline, as well as an overview about HSB processes and the general settings of the study site.

Chapter 2 presents a geomorphological and sedimentological characterization of the inner continental shelf based on bathymetric LiDAR and side-scan sonar surveys, satellite images, orthophotomaps, sediment samples and on the sedimentological map of Portuguese continental shelf.

Chapter 3 characterizes the beach morphology and its relation with the incident wave conditions. Beach morphodynamics is characterized through a beach planform analysis, based on orthophotomaps and satellite images, and a cross-shore morphological analysis, based on topographic data.

Chapter 4 includes the sedimentological characterization of the studied beaches based on sediment grain-size and compositional analyses.

Chapter 5 analysis longshore sediment transport patterns using a short-term approach, based on a fluorescent tracer experiment, and a long-term approach, based on the potential longshore transport estimated with empirical formulas and a wave time-series.

Chapter 6 includes the description and application of a new shoreline evolution model – SEM- PLAT, developed to simulate shoreline changes on coastal stretches where beaches develop over a rocky shore platform.

Chapter 7 defines the sediment budget of the study site, based on the: (i) literature review about sediment sources and sinks; (ii) new estimates of sediment supply and sediment retention related with the sea-level rise; (iii) beach evolution trends observed through recent and historical ground-photographs; and (iv) information obtained from the previous chapters.

Chapter 8 presents a synthesis of the results obtained in the scope of this thesis and put forward conceptual models for HSB processes and their implications in the sedimentary dynamics of the study site; it also presents the general conclusions and give guidelines for further research.

1.4 OVERVIEW OF HEADLAND SEDIMENT BYPASSING

Headlands can be described as a piece of land with steep cliff face, jutting out from the coast into a large body of water (Neuendorf *et al*., 2005). These landforms can act as obstacles to the longshore sediment transport dividing the coast into littoral cells, which are compartments where sediment transport is relatively self-contain. However, depending on the headland size and morphology (George *et al*., 2015), on sediment availability and on sediment transport mechanisms, HSB can occurred at different depths, with variable magnitude and frequency.

HSB is a process in which sediment is transported by wind or waves from the upstream side of a headland to the downstream side. Notwithstanding the importance of headland bypass dune fields in the sediment budget of some coasts (*e.g.* McLachlan *et al*., 1994; Boeyinga *et al*., 2010), the present study focuses on the HSB induce by waves.

The HSB induced by waves has been study by some authors, such as Short and Masselink (1999) that presented a conceptual model based on their observations on several relatively long beaches (> 5 km), separated by headlands at the Australian eastern coast. The model assumes that longshore sand transport, perhaps assisted by beach rotation, causes a sand accumulation on the updrift side of the headland (**Figure 1.1A**). Then an apparent sub-aqueous movement of this sand around the headland occur; the sand manifests itself as a sub-aqueous sand wave on the tip and immediately downdrift of the headland (**Figure 1.1B**). The sand wave may then moves along the downdrift side of the headland as an offshore bar, a shallow attached bar or as an elongate spit which may impound a backing swash lagoon (**Figure 1.1C**). When the sand bar/spit is attached to the beach it usually initiates a topographically controlled rip that migrates in its advance, often causing severe localized beach erosion (**Figure 1.1D**). Finally, the sand wave merges with the downdrift beach causing a slight accretion (**Figure 1.1E**).

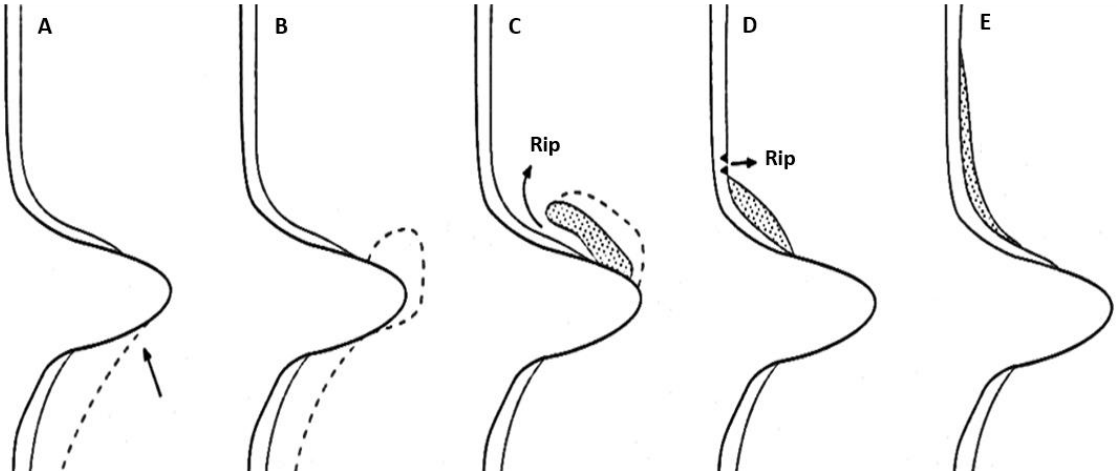

Figure 1.1. Schematic illustration of headland-attached sand bar/spit bypassing. (A) Updrift accumulation; (B) headland sub-aqueous sand wave; (C) downdrift attached sand bar/spit; (D) advancing of sand wave and erosion rip; (E) merges with downdrift beach (extracted from Short and Masselink, 1999).

Smith (2001) also presented a HSB conceptual model based on his observations at Australian eastern coast. According to this model, HSB manifests itself as an almost straight strand of sand that is initiated at the headland and ends upon the downdrift beach at, or very close to, the null point of the wave refraction orthogonal (**Figure 1.2**). The bypass strand converts the zone shoreward of the strand into a closed rotating cell opposite to the strand until the transport reaches the headland tip again. This closed transport cell contributes to the strand flow again and a rotary quasi-stability is attained. If this cell is sufficiently shallow, a lagoon can be observed in the centre cell during the very low tides. The author also notes that pure headland bypassing strands will only occur when the shoaling seabed is sediment rich. When the downdrift beach is highly curved in plan, such as many pocket beaches, without a straight beach section, it may be impossible the bypass strand occurrence. A similar model was earlier presented by Evans (1944), referring that depending on the available sediment and strength of waves and currents, the sediment bypass deposit (strand) can be brought above the water and extended to downdrift side of the headland as a broad or narrow spit.

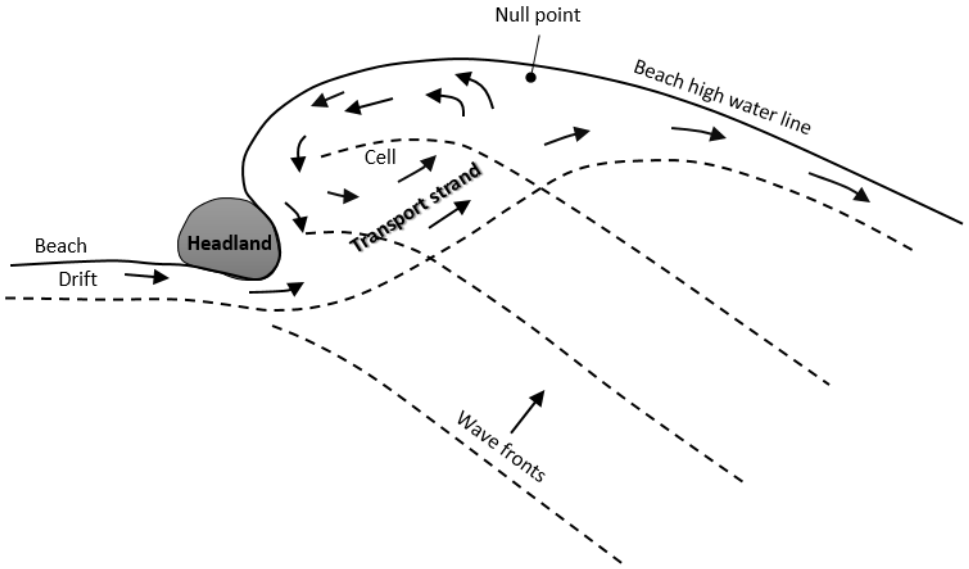

Figure 1.2. Schematic illustration of headland strand bypassing (adapted from Smith, 2001).

Storlazzi and Field (2000) studied the sediment paths on a rocky embayed stretch at the U.S.A. western coast, where small pocket beaches typically occur on stream mouths (**Figure 1.3A**). This study showed that at active-margin coasts, headlands can extend offshore as barriers to the longshore drift, and under these conditions, HSB can only occur during high-energy events. According to these authors, during storms, subaerial beach sediment can be eroded and carried offshore by either, seaward near-bed flows driven by wave- and wind-induced setup or intense rip currents, dispersing part of the sediment across shoreface and transporting the other part further offshore to the mid shelf (**Figure 1.3B**). After storm, smaller short-period waves obliquely approaching the coast can initiate alongshore currents, which can sweep the sediment deposited in the subaqueous bedrock ridges front of headlands, feeding the downdrift beaches and their adjacent subaqueous depressions (paleo-stream channels). The reconstruction of the pre-storm shoreface profile would then be aided by long period, low-energy swells carrying sediment onshore from greater depths (**Figure 1.3C**). A similar HSB process had been already hypothesized by Scholar and Griggs (1997).

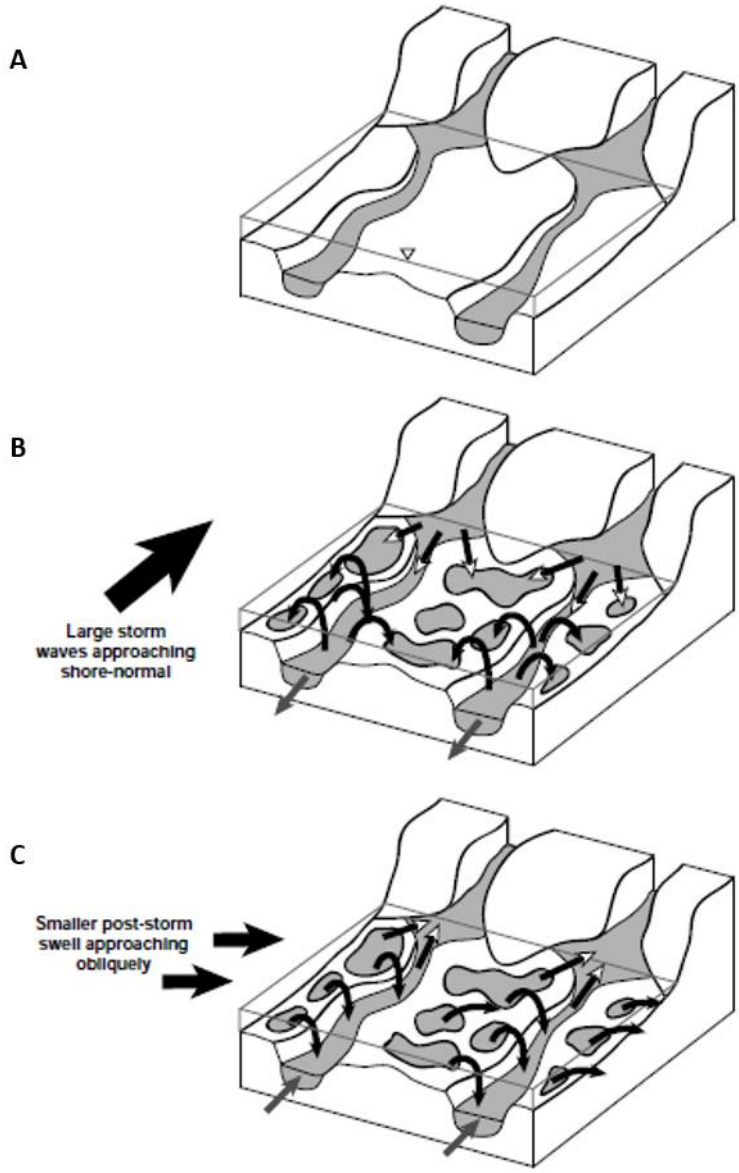

Figure 1.3. Schematic illustration headland sediment bypassing model hypothesized by Storlazzi and Field (2000) for a headland-bay coast where the beaches typically occur on stream mouths: (A) pre-storm situation; (B) during storm; and (C) after storm.

Barriolo *et al.* (2012) and Ferrari *et al.* (2014) also reported a significant transport of gravelly sediment around the Punta del Maiolo headland (NW Mediterranean Sea, Italy), induced by a rip current. In fact, severe erosion on headland-bay beaches has been associated with the occurrence of large-scale topographically controlled rip currents during storm events. The velocities of rip currents under these conditions are higher and can carry large quantities of sediment to great distances from the shore and to great depths (*e.g.* Short, 1985; Short and Masselink, 1999; Smith *et al*., 2010; Loureiro *et al*., 2012). This sediment may be lost from the beach system to offshore, being deposited beyond the closure depth (Smith *et al*., 2010) or

transported alongshore to the downdrift side of the headland as explained by Storlazzi and Field (2000).

Evidences of HSB have been reported in other works, Lord and Van Kerkvoort (1981), for example, observed a significant sediment bypassing at Diggers Headland (Australia) through a tracer experiment, carried out under moderate wave conditions (3-4 m).

Hume *et al.* (2000) analysed sand paths around a preeminent headland (Cape Rodney, New Zealand) that protrudes 3-4 km into deep water, based on observational data and numerical modelling. The study suggest that HSB in deep water is dependent of both tide and wave generated currents, and that this occurs episodically during storm events. The sediment bypass is small and intermittent occurring as thin, discontinuous and patchy sand bodies.

Patterson (2011) and Acworth and Lawson (2011) studied Fingal Head (Australia) sand bypass, based on topo-bathymetric surveys. The authors describe HSB as episodic "slugs" of sand (relatively large) moving around the headland, generally associated with periods of high-energy waves, aided by accelerated longshore currents.

Goodwin *et al*. (2013) investigated the sand bypass of a preeminent headland (Cape Bayron, Australia) based on the historical shoreface bathymetric changes and multi-decadal wave climate variability. Two bypassing mechanisms were interpreted: (1) a predominantly cross-embayment transport connecting a headland-attached sand wave and the outer bar of downdrift beach – like strand bypass of Smith (2001), during unimodal wave direction climate; and (2) a split transport between the nearshore path along the inner bar and cross-embayment path, during a bimodal wave direction climate. The authors conclude that the switching between HSB mechanisms on interannual to decadal timescales determines the geometry of the bypass strand with the downdrift littoral zone.

Cascalho *et al*. (2014), Duarte *et al*. (2014), Lira and Taborda (2014) found evidences of sediment bypass at Nazaré headland (Portuguese western coast), based on sediment textural analysis, a fluorescent tracer experiment and satellite images analysis, respectively. According to these works, an ephemeral beach appears at the downdrift side of the headland as an attached-sand wave, when the updrift beach reaches its full capacity and the wave regime is low enough to preserve sand accumulation on that location.

Ab Razak (2015) used numerical modelling to explore the mechanisms and processes of HSB. The author concluded that increasing the wave angle, wave height and sediment grain-size leads to the increment of sand bypassing volume; nevertheless, in all cases the process remain unchanged. The increasing of the wave height had limited the development of surf zone currents

in the middle of embayment by creating a large seaward flowing rip current, which enhances the sand transport outside the surf zone. The author also noticed that the presence of the headland rips currents in the model is favoured by the large wave directional spreading.

Silva *et al*. (2016) studied HSB at Santa Catarina Island (Brazil), using both *in situ* measurements and numerical modelling. This study demonstrated that in higher energy beaches, sand bypassing is entirely subaqueous, while in lower energy beaches the sand bypassing manifest by periodic subaerial spit development and migration. The authors reinforce the idea that HSB, including links to inner shelf transport, should be considered in any study of headland-bay beaches.

1.5 REGIONAL SETTINGS OF THE STUDY SITE

The study site is located at Portuguese west coast and encompasses the coastal stretch from Carvoeiro cape to Raso cape (**Figure 1.4**).

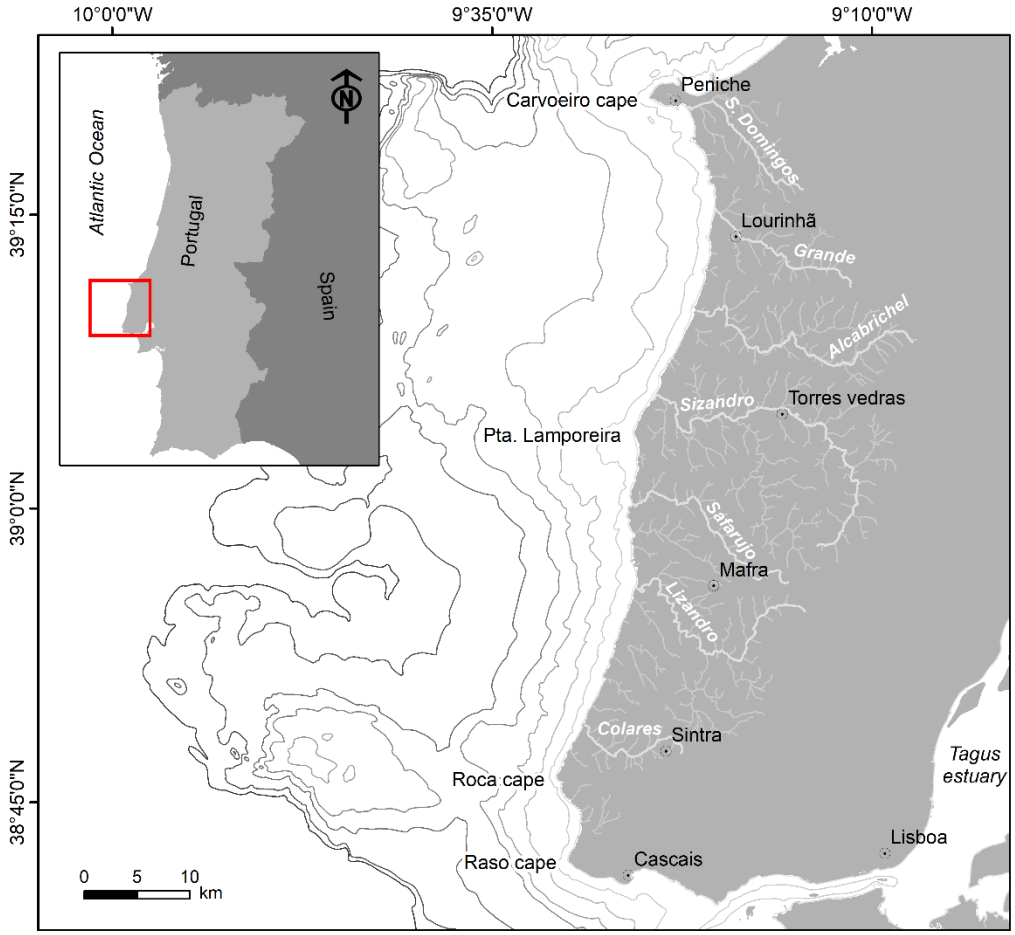

Figure 1.4. Location the study area; toponymy of main headlands; continental shelf bathymetrics spaced 20 m, between 0 and 140 m depths (Vanney and Mougenot, 1981); and fluvial network provided by *Agência Portuguesa do Ambiente* - APA (available online at: http://sniamb.apambiente.pt, accessed Apr. 2017).

1.5.1 Geology and geomorphology

The studied coastal stretch extends for approximately 100 km, with orientation ranging from NW-SE to NE-SW, depending on the sector. The continental shelf in this sector constitutes a huge submarine promontory, known as Esporão da Estremadura (Vanney and Mougenot, 1981). The most preeminent headlands are Carvoeiro cape, Ponta da Lamporeira, Roca cape and Raso cape, as can be noticed by the shape of the coastline and bathymetric contours presented in **Figure 1.4**.

The geomorphological classification presented by Marques *et al.* (2013), shows that about 40 % of this coast are beaches, most of which are hinged with cliffs (30 %) and a lesser extent backed by dunes (6 %) and artificial structures (4 %). The other 60 % of the coast are cliffs that plunge directly into the sea (11 %) or are hinged on a rocky shore platform (40 %) and, artificial structures in contact with the sea or a rocky shore platform (9 %) (**Figure 1.5**).

The studied beaches are predominantly sandy and exhibit different geometries, some present a high degree of embayment, while others correspond to a narrow and elongated thin sand strip that covers a rocky shore platform. Several beaches developed in the dependence of small fluvial streams, some of them with an intermittent outflow regime (**Figure 1.5**). These beaches result from the sedimentary infill that occurred on the Portuguese coast after mid Holocene (ca. 5000 BP), in association with the stabilization of the sea-level, and was later increased by the anthropic activities such deforestation and agriculture (Dias *et al*., 2000; Freitas *et al*., 2002). Currently, the littoral sediment supply from fluvial streams have a modest magnitude in the order of 10^4 $m^3.yr^{-1}$ (Lira *et al.*, 2013).

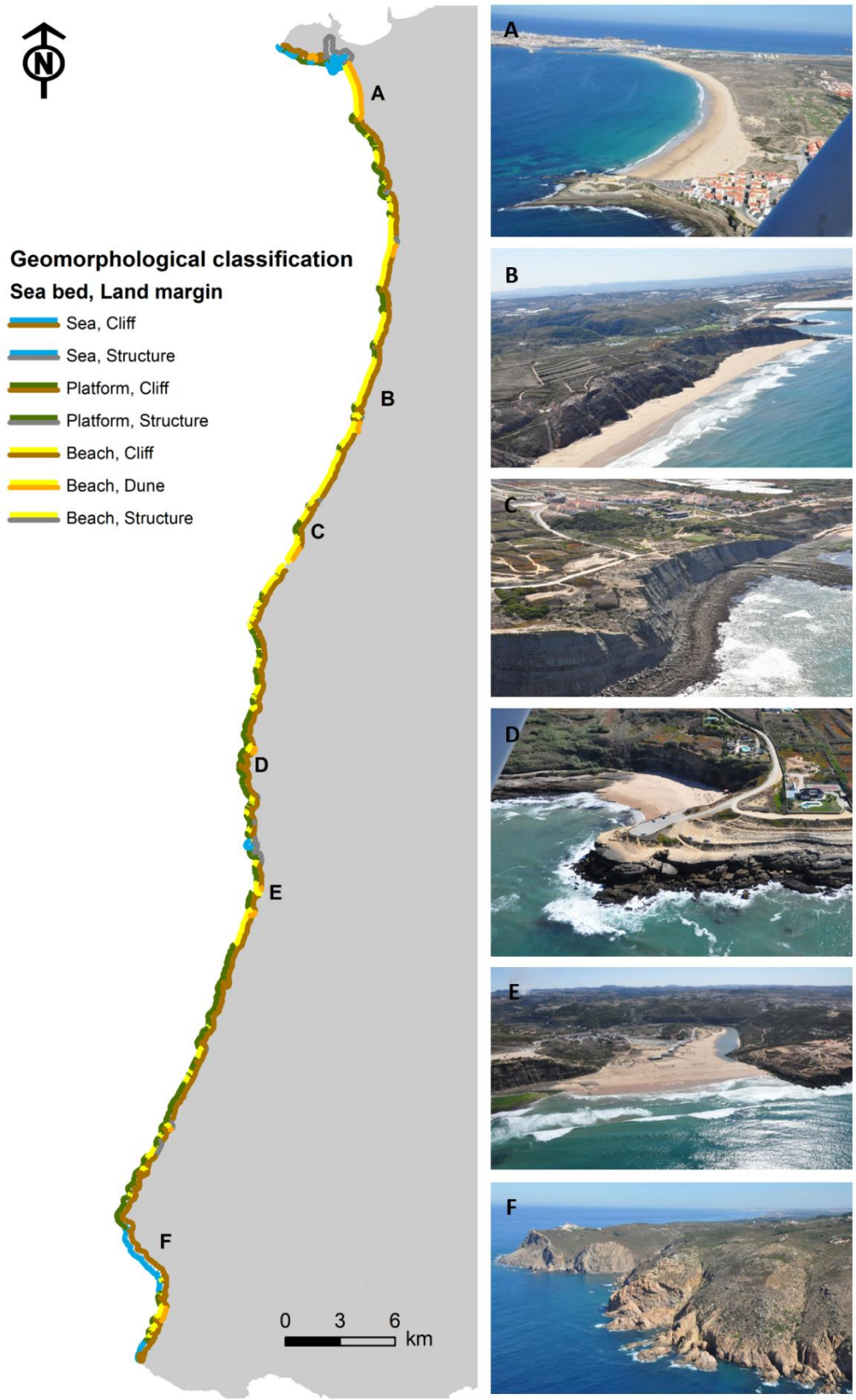

Figure 1.5. Geomorphological classification of the littoral (Marques *et al.*, 2013) and oblique aerial photographs taken in 2009, provided by *Sistema de Administração do Recurso Litoral* - SIARL (available online at: http://www.siarl.igeo.pt, accessed Sep. 2015): (A) the large bay of Consolação beach backed by a dune field (Peniche); (B) the narrow and elongated beach of Valmitão (Lourinhã), (C) the rocky shore platform north of Azul beach (Torres Vedras), (D) the high-degree embayment of Coxos beach (Mafra); (E) Foz do Lizandro beach in the dependence of Lizandro river (Mafra); and (F) the plunging cliffs of Roca cape (Sintra-Cascais).

The drainage network has a dendritic pattern (**Figure 1.4**) and develops on a Meso-cenozoic sedimentary sequence, except in southern sector, where the Mesozoic formations are cut by the Sintra Igneous Complex and the Lisbon Volcanic Complex (**Figure 1.6**). According to the explanatory notes of the Geologic Map of Portugal at 1:50 000 scale (Zbyszewski *et al*., 1955; França *et al*., 1960; França *et al*., 1961; Zbyszewski and Assunção, 1965; Zbyszewski *et al*., 1966; Ramalho *et al*., 1993; Ramalho *et al*., 2001):

- Meso-cenozoic sequence includes Jurassic and Cretaceous formations composed of alternating limestones, marls, sandstones, conglomerates and mudstones; Eocene-Oligocene conglomerates, sands and clays with some intercalations of marls and limestones; Miocene lacustrine limestones (without cartographic expression in the **Figure 1.6**); Pliocene sands and clays; Pleistocene sandy and gravelly beaches and fluvial terrace deposits and, small outcrops of consolidate dunes; Holocene alluvial deposits, dunes and beach sands.
- Sintra Igneous Complex (82-95 Ma) is an intrusive mass body, mainly formed by syenites and granites, although it is possible to find gabbro-diorite and igneous breccia. Lisbon Volcanic Complex (70-72 Ma) is mainly composed by basalt, occurring in the form of vents, lavas, dikes and sills. Other igneous rocks associated with the earlier rifting phases of the North Atlantic Ocean, outcrop as veins of dolerite and teschenit among others. Associated with the intrusion of igneous rocks, some contact metamorphic rocks also occur.

The geology of the shallower continental shelf is an extension the emerged geologic formations and structures. The inner shelf sector (up to 30-40 m depth) is composed by Jurassic and Cretaceous sedimentary formations, except in front of the Roca Cape, in relation to the underwater extension of the Sintra Igneous Complex (**Figure 1.6**). This bedrock is partially covered by unconsolidated deposits, mainly composed by gravelly, coarse, medium and fine sand (IH, 2010).

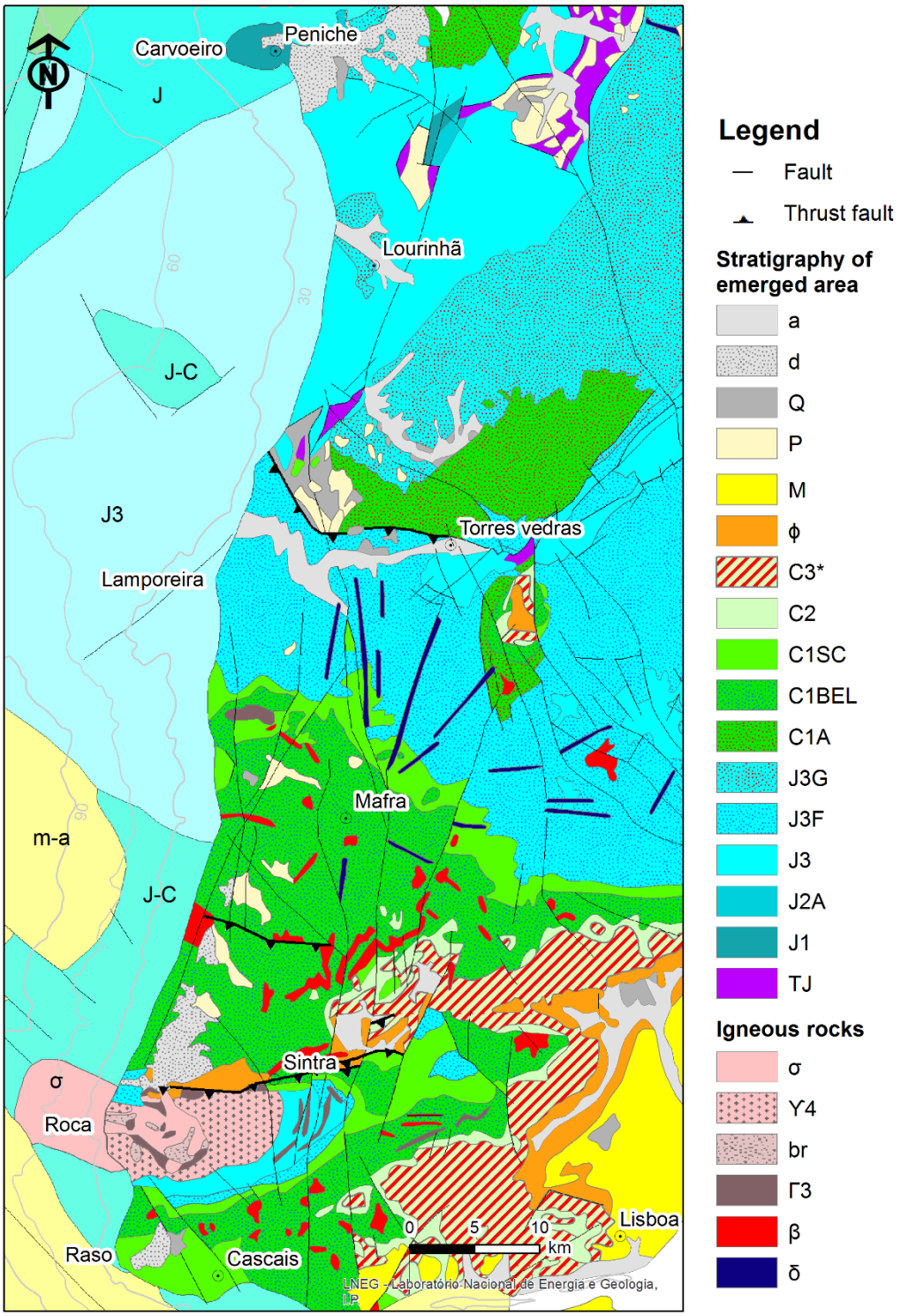

Figure 1.6. Geology of the study area based on Geological Map of Portugal 1:500 000 scale published by *Serviços Geológicos de Portugal* in 1992 (provided online by *Laboratório Nacional de Energia e Geologia* – LNEG, at: http://geoportal.lneg.pt/ArcGIS/rest/services/CGP500K/MapServer, accessed Sep. 2015). Inland: sedimentary formations of Holocene (a, d); Pleistocene (Q), Pliocene (P), Miocene (M), Oligocene-Eocene (ϕ), Cretaceous (C1A, C1BEL, C1SC), Jurassic (J1; J2A, J3, J3F, J3G) and Triassic and Jurassic undifferentiated (TJ); Lisbon Volcanic Complex (C3*); syenites (σ), granites (ϒ4), volcanic breccia (br) and gabbro (Γ3) of Sintra Igneous Complex; volcanic vents and veins composed by basalts and other volcanic rocks (β); dolerite and other basic rocks (δ). Continental shelf: sedimentary formations of Neogene (m-a), Jurassic superior and Cretaceous undifferentiated (J-C), and Jurassic superior (J3); Sintra Igneous Complex (σ) – Cretaceous superior.

1.5.2 Climatic and oceanographic settings

The climatic characterization of the Portuguese mainland is synthetized in Miranda *et al.* (2002), ADAPT (2015) and IPMA (2015). According to the information provided by these works, the climate of the study area (*i.e.* between the coastline and the inland limit of the watersheds) is characterized by moderate temperatures with dry warm summer (Köppen-Geiger classification). The mean annual air temperature ranging between 13 and 18 °C; and the mean annual accumulated precipitation increases from the coast to inland and do not exceed the 1000 mm.

The study coast has a semidiurnal mesotidal regime, with a spring tidal range averaging 2.8- 2.9 m (Andrade *et al*., 2002), and is exposed to swells generated in the North Atlantic. According to the 56-years hindcast wave time-series obtained by Dodet *et al.* (2010), using a spectral wave model forced with reanalysis wind field and validated with buoy data, the dominant wave regime for the Portuguese west coast comes from NW. The W and SW waves have lower frequencies and are typical of winter and autumn seasons (**Figure 1.7**). The average offshore wave conditions are characterized by a significant wave height of 2 m, a peak period of 11 s and a direction of 308°.

The summer directional spreading is particularly small compared to the other seasons, as result of the persistence of the NW waves (**Figure 1.7**). Summer/spring (April to September) wave climate is characterized by a mean significant height of 1.5 m, a mean peak period of 9 s and a mean wave peak direction of 311°. In the winter/autumn (October to March), wave climate is quite energetic, being characterized by a mean significant height of 2.5 m, a mean peak period of 12 s and a mean wave peak direction of 306°; although maximum wave heights of 13 m and peak periods of 23 s, can be reached (**Figure 1.8**). According to the buoy data analysis performed by Costa and Esteves (2009), the most frequent storm conditions at the Portuguese western coast, come from WNW and NW with maximum significant wave heights between 4 and 6 m and a duration usually less than two days. However, extreme cases can exceed 8 m and extend for longer times.

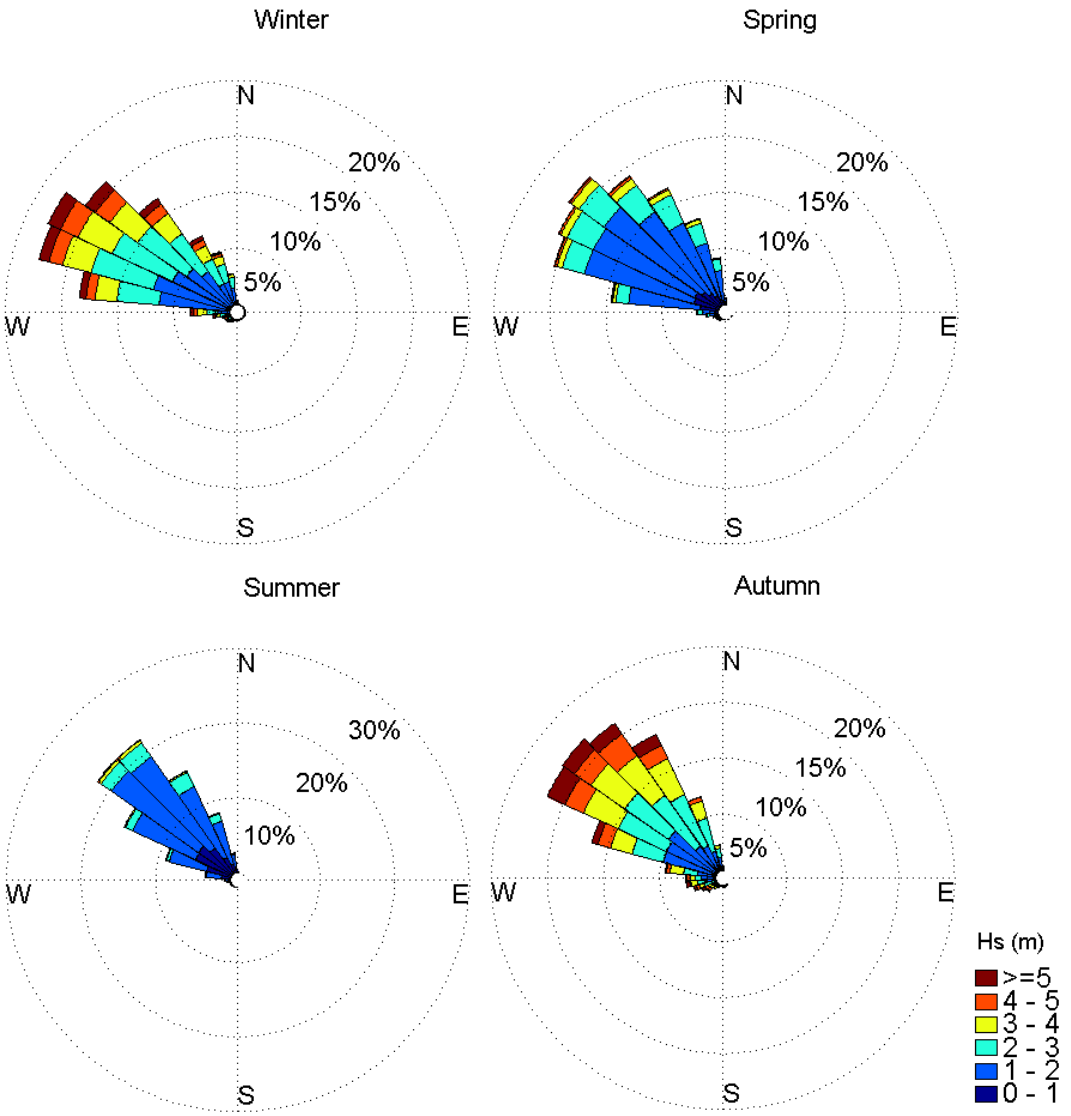

Figure 1.7. Relation between significant wave height (Hs) and peak wave direction for each season: winter (Jan-Mar); spring (Abr-Jun); summer (Jul-Sep); autumn (Oct-Dez). Based on a 56-years (1953-2008) hindcast wave time-series (Dodet *et al.,* 2010). Data provided by the European project MICORE - Morphological Impacts and COastal Risks induced by Extreme storm events.

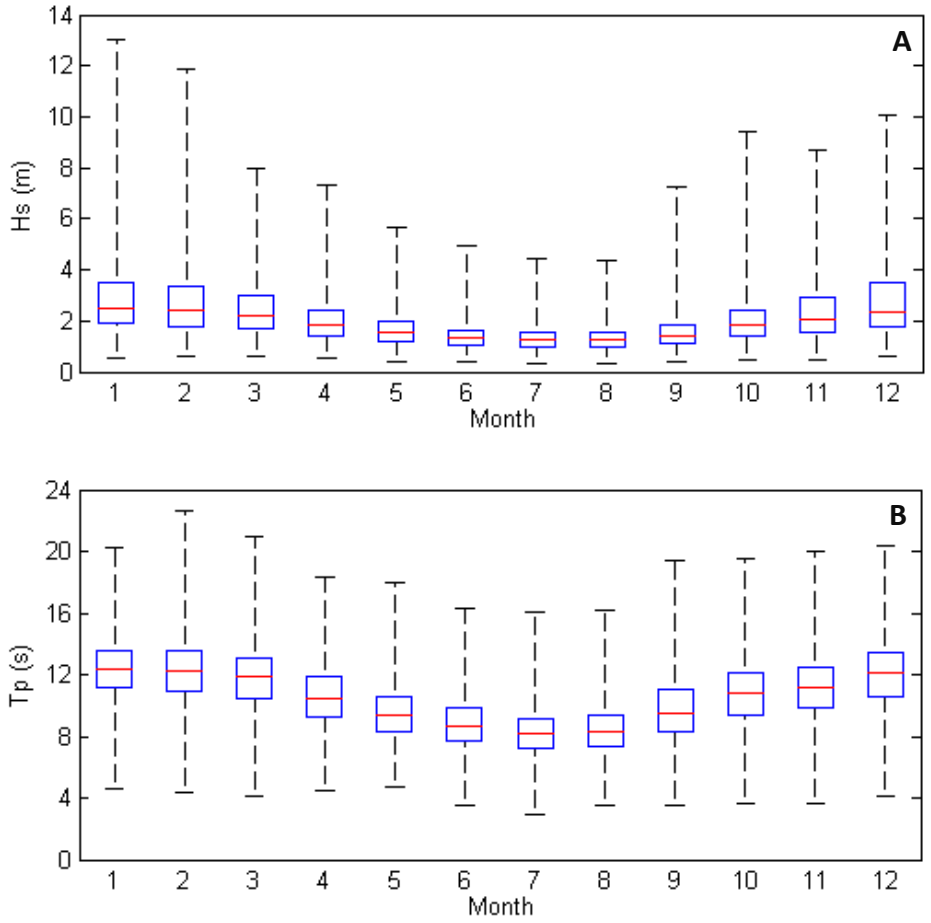

Figure 1.8. Monthly statistics of the: (A) significant wave height (Hs) and (B) peak wave period (Tp) based on a 56-years (1953-2008) hindcast wave time-series (Dodet *et al*., 2010). Data provided by the European project MICORE - Morphological Impacts and COastal Risks induced by Extreme storm events. Boxes limits are the 25th and 75th percentiles, respectively; the mid-range is the median value; and whiskers extremes are the maximum and minimum values.

Chapter 2

Inner Continental Shelf Geomorphology and Sedimentology

2.1 INTRODUCTION

Previous works have shown that headland sediment bypassing (HSB) can occur in association with submarine sediment transport, along a transition region between littoral and continental shelf environments (*e.g.* Hume *et al*., 2000; Silva *et al*., 2016). However, terminology and limits of this region are not a consensual matter. Wright (1987) and Wright (1993), for example, define inner shelf or shoreface as the region immediately seaward the surf zone where waves agitate the seabed. Smith (1995) also consider inner shelf and shoreface terms as being synonymous, but define it as the region extending from the seaward edge of the surf zone to the closure depth[1]. Notwithstanding, Niedoroda and Swift (1981) and Niedoroda *et al. (*1985), had previously used the shoreface term to define the region between the surf zone and the inner shelf, considering that shoreface blends into inner shelf when the slope of the seabed reach values on the order of 1:2000. Cowell *et al.* (1999), on the other hand, define shoreface as the

[1] Closure depth is defined, for a given or characteristic time interval, as "the most landward depth seaward of which there is no significant change in bottom elevation and no significant net sediment transport between the nearshore and the offshore" (Kraus *et al*., 1998).

wave-dominated region, *i.e.* the region that extends from the limit of wave run-up on the beach face, seaward to the limit of effective influence by gravity waves in shaping seabed morphology.

In the present work, inner shelf term was adopted to define the subtidal zone where waves can affect seabed. Thus, the landward limit of the inner shelf was defined based on lowest water level (LWL), *i.e.* the hydrographic zero[2] (ZH). Definition of the seaward limit, however, is more complex and may be based on oceanographic, morphological and sedimentological criteria, *i.e* the depth corresponding to a wave base[3], a slope break on the seafloor or to the offshore limit of the recent littoral sand deposits. Nevertheless, considering the main goal of the present work, the use of the sedimentological criteria seems the most appropriate, as it reflects the sediment transport conditions.

Despite the poor sediment cover and irregularity of the sediment deposits of the continental shelf in the studied sector, the sedimentological map (IH, 2010), shows that the offshore limit of the littoral sands deposits, occur in general, close to 40 m depth; the only observed exception is in stretch between Ericeira and Roca cape, where littoral sand extends up to 90/100 m depth, probably due to a local structure or phenomena. The limit of the littoral sand deposits are in agreement with the slope breaks identified by Badagola (2008), in his morphological analysis of the continental shelf in this sector. Despite the local variations, the limit identified at 30/40 m depth seems consistent, considering other studies carried out in this and other sectors of the Portuguese western continental shelf (*e.g.* Dias, 1987; Taborda, 1999; Balsinha, 2008).

Taking into account the previous considerations, it was assumed that inner shelf under analysis is located between LWL (2 m depth relative to the mean sea-level - MSL) and the depth that usually represent the offshore limit of recent littoral deposits (40 m depth relative to the MSL). The inner shelf was divided into two domains, the upper domain that extends from LWL to the closure depth, and the lower domain lying between the closure depth and 40 m depth (**Figure 2.1**). Since there are no data or previous works regarding the accurate closure depth for the study site, the value estimated by Lapa *et al.* (2012), for the littoral north of Carvoeiro cape, were considered valid for this work. According to these authors, closure depth range between 11 m and 16 m depth (MSL), with a mean value of 14 m (MSL).

[2] Is a nautical chart datum defined based on the Lowest Astronomical Tide Level that for the Portuguese main land is located 2 m below the mean sea level (according to information provided by *Instituto Hidrográfico*, available online at: http://www.hidrografico.pt/, accessed Oct. 2015).

[3] Is the depth beyond which "wave action ceases to stir the sediments" (Baker *et al*., 1966), corresponding about half the wavelength in deep water.

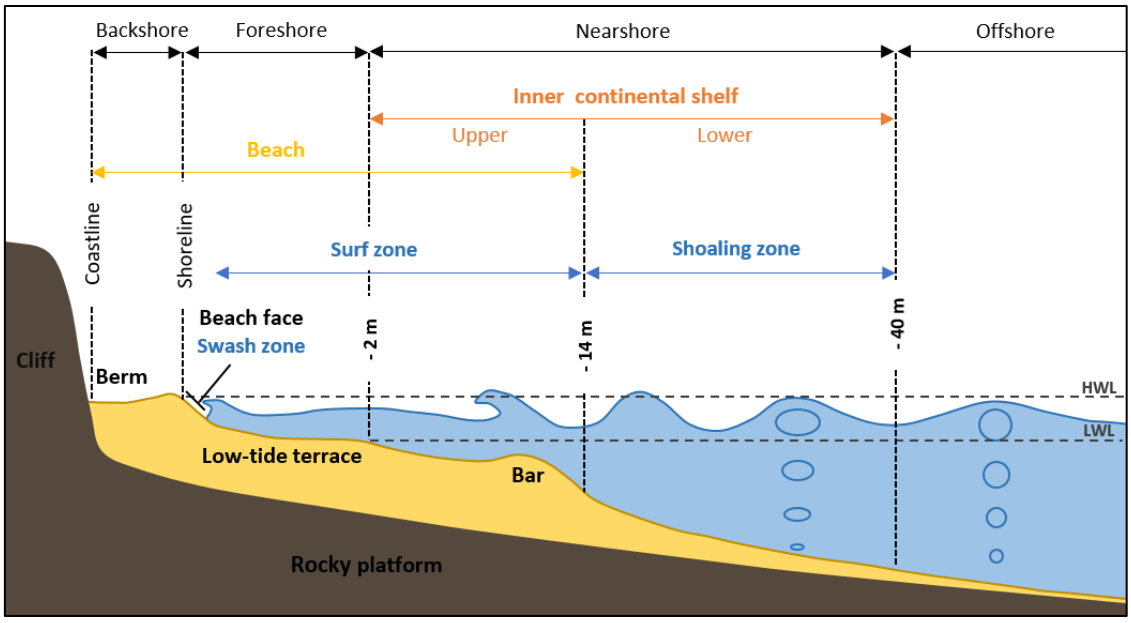

Figure 2.1. Beach and inner shelf limits adopted in this work. Depths are relative to the mean sea-level; HWL is the high water level and LWL is the low water level, in relation with the tide.

The main goal of this chapter was to investigate the possible sediment pathways and geomorphological constrains to sediment transport on the inner continental shelf. To achieve this goal a geomorphological and sedimentological analysis of the inner shelf was performed based on bathymetric LiDAR, sedimentological data (mapping and samples), side-scan sonar survey, satellite images and orthophotomaps.

2.2 METHODS

2.2.1 LiDAR data analysis

Bathymetric LiDAR data were acquired between June 22nd and August 19th 2011, with a spatial resolution of 2 m (Silva *et al.*, 2012b). These data were validated by *Instituto Hidrográfico* (Moura *et al*., 2014) and provided by *Direção-Geral do Território* - DGT.

The depth range surveyed by LiDAR is not uniform, hence the morphological analysis was performed using a depth range well represented along the studied littoral, *i.e.* between -2 m and -10 m (MSL), covering a large part of the upper inner shelf. From the digital terrain model obtained, 71 profiles orthogonal to the depth contour lines were extracted, with a spacing of about 1 km (along N-S direction). The small stretches front of Carvoeiro and north of Magoito, were not characterized through this analysis, because LiDAR survey did not cover the area deeper than the -10 m contour line.

Width, mean slope and roughness of each profile were computed. The roughness was estimated using the root mean square relative to a smoothed profile (computed through a moving average window of 10 m) according to the expression:

$$R_{RMS} = \sqrt{\frac{\sum_{i=1}^{n}(z_i - \overline{z_i})^2}{n}} \quad (\mathbf{2.1})$$

where z_i is the observed elevation, $\overline{z_i}$ is the moving average elevation and n is the number of observations.

Additionally, a detail morphological description of the inner shelf fronting most prominent headlands (Carvoeiro, Lamporeira, Roca and Raso) was also held, based on total depth range obtained from LiDAR survey.

2.2.2 Sedimentological data analysis

Sedimentological analysis was based on sedimentological map of the Portuguese continental shelf IH (2010). In addition, an attempt to collect sediment samples on the upper inner shelf contiguous to the Roca Cape was made, during the oceanographic campaign carried out by *Instituto Hidrográfico* on May 28th 2015. However, wave conditions only allowed sediment sampling at the lower inner shelf. Four sediment samples were collected, with a Smith-McIntyre grab, between 30 and 40 m depth.

Sediment grain-size analysis was taken by sieving method for the particles larger than 1 ϕ and by laser diffraction for particles smaller than 1 ϕ. Both methods were performed according to the internal protocols of *Instituto Hidrográfico*, which are based on the standards NP EN 933-1 and ISO 13320-1. The size grade scale adopted was the Wentworth scale modified by Krumbein (1934) and the statistic parameters of the grain-size distributions were computed through the method of moments described in Boggs (1995).

2.2.3 Side-scan sonar data analysis

Side-scan sonar data were acquired by *Instituto Hidrográfico*, on February 9th and 11th 2015, using a dynamically-focused multi-beam side-scan sonar KLEIN 5000, with a longitudinal resolution of 0.20 m and a pulse duration of 100 μs chirp to obtain a lateral range of 100 m. The survey cover an area of about 15 km^2, approximately between 10 and 40 m depth, offshore the Sintra coast. Data processing was performed using DELPH SONAR INTERPRETATION software of IXBLUE; time varying gain, speed and lateral range were corrected and the water column was removed from the signal.

Considering that the acoustic backscatter intensity depends on seafloor properties, this was characterized based on the different acoustic patterns identified, assuming that hard bottoms, such as rocky outcrops and coarse sediment result in a strong acoustic backscatter, while the softer bottoms (fine sand and mud) generate a weaker acoustic return signal (*e.g.* Davis *et al*., 1996; Collier and Brown, 2005; Hamouda *et al.*, 2016). Moreover, height and wavelength of the bedforms identified, were also measured based on the acoustic shadows of these "objects", using the slant range to the target object (time that the signal takes to return) and the height of the side-scan above the seafloor.

2.2.4 Satellite images and orthophotomaps analysis

Landsat 8 satellite images and orthophotomaps were used to get insights on the seabed characteristics. The satellite images were provided by National Aeronautics and Space Administration - NASA and United States Geological Survey – USGS (available online at: http://earthexplorer.usgs.gov/, accessed between Dec. 2013 and Dec. 2015), while the orthophotomaps can be consulted online (available online at: http://mapas.dgterritorio.pt/, accessed Oct. 2015).

The image analysis was qualitative, consisting on a visual inspection to identify rocky and sandy bottoms and morphological features such sandbars. The latter can be directly observed or inferred from the breakers lines. The high frequency of Landsat 8 images allowed to characterize the surf zone, during low- and high-energy wave conditions, and make considerations about how this determines HSB processes. The orthophotomaps were used to confirm some aspects that cannot be clearly observed on the satellite images due to their lower resolution (30 m).

2.3 RESULTS

2.3.1 Inner shelf morphology

The inner shelf up to 10 m depth has an average width of 380 m, with a standard deviation of 127 m. The narrower stretches are located front of Ribamar and immediately south of Carvoeiro and Roca capes, where the width decrease down to 155 m, 84 m and 16 m, respectively. Mean slopes are, in general, gentle and less than 2° (92% of the observations). Steeper zones coincide with the narrower stretches mentioned above, reaching a maximum of 25° at Roca cape. The roughness varies between 0.03 and 0.18 m and its spatial distribution indicate that stretches north of the headlands tend to be lesser rough than southern ones. This is particularly evident front of prominent headlands, such as Lamporeira, Roca and Raso, although the same

morphological trend is observed at smaller headlands, such as Consolação and Peralta. Exceptions to this trend are Carvoeiro cape, with a high-rough shelf at both sides, and Magoito headland, where roughness is higher at the northern sector compared to the southern one (**Figure 2.2**).

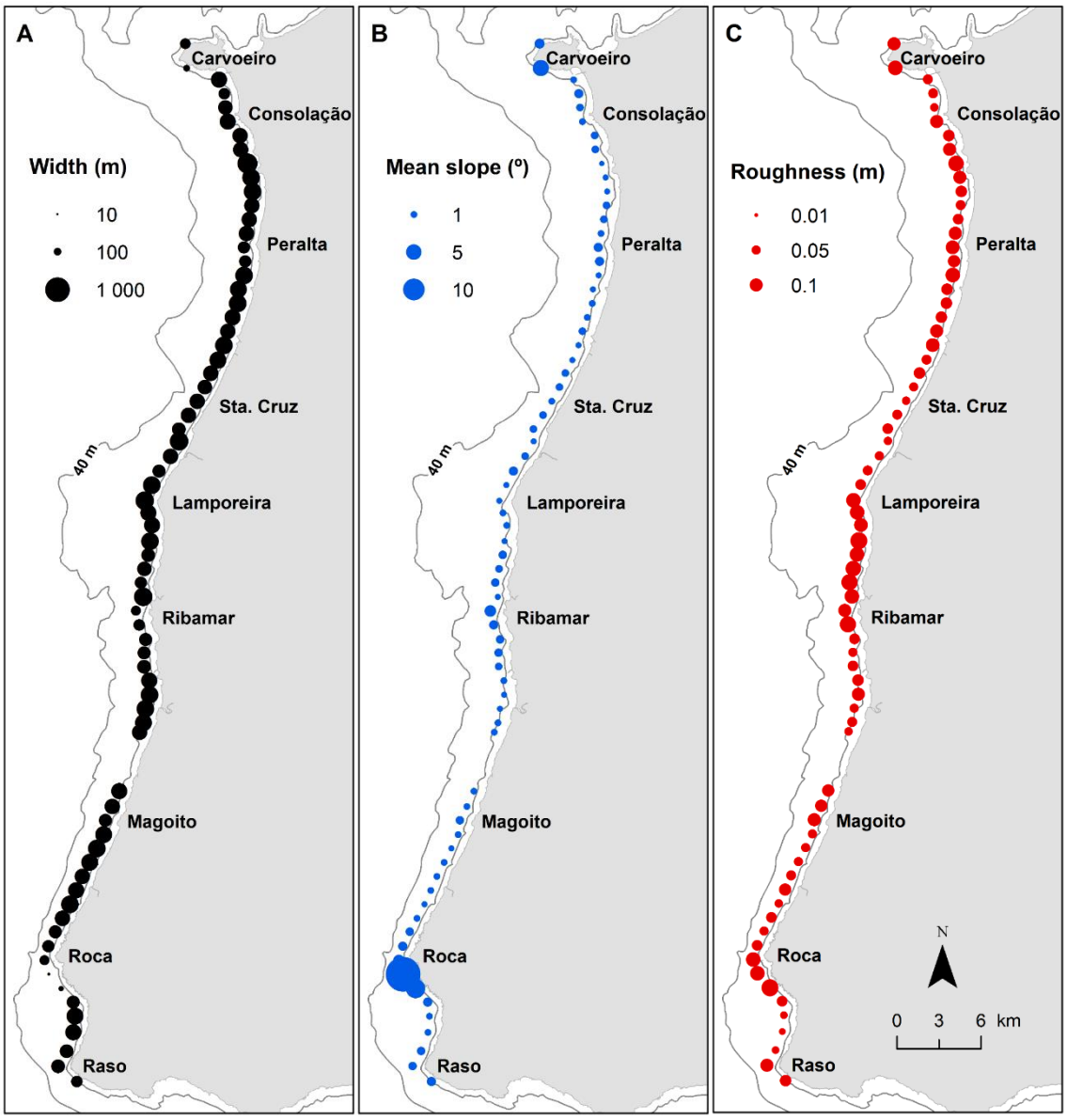

Figure 2.2. Morphological parameters of the inner shelf up to 10 m depth: (A) width, (B) mean slope and (C) roughness (40 m contour depth extracted from Vanney and Mougenot, 1981).

Digital terrain models of the inner shelf in the vicinity of the most prominent headlands and respective cross-shore bathymetric profiles show rough surfaces (**Figure 2.3** and **Figure 2.4**). In the case of Carvoeiro cape, the inner shelf plunges abruptly up to 5 m depth with a mean slope of 11°, and then extends as a large and rough submarine plateau with a mean slope of 0.4°; north and south sides of this headland have a narrow and steeper upper inner shelf, reaching

15 m depth at 300/400 m from the coastline. At the Lamporeira headland region the inner shelf is shallower, comparatively to the other headlands, plunging gently up to 6 m depth with a mean slope of 0.6°. On the contrary, the inner shelf offshore Roca cape is deeper, plunging up to 13 m depth with a mean slope of 4.8°; between 13 and 16 m depth, it becomes less steep with a mean slope of 1.4°; and then presents a shape almost horizontal. The inner shelf close to Raso cape, presents a horizontal platform around 3 m depth, becoming rougher and plunging up to 10 m depth with a slope of 1.3°; from 10 to 17 m depth, mean slope increases to 6.9°, and then presents a surface approximately horizontal.

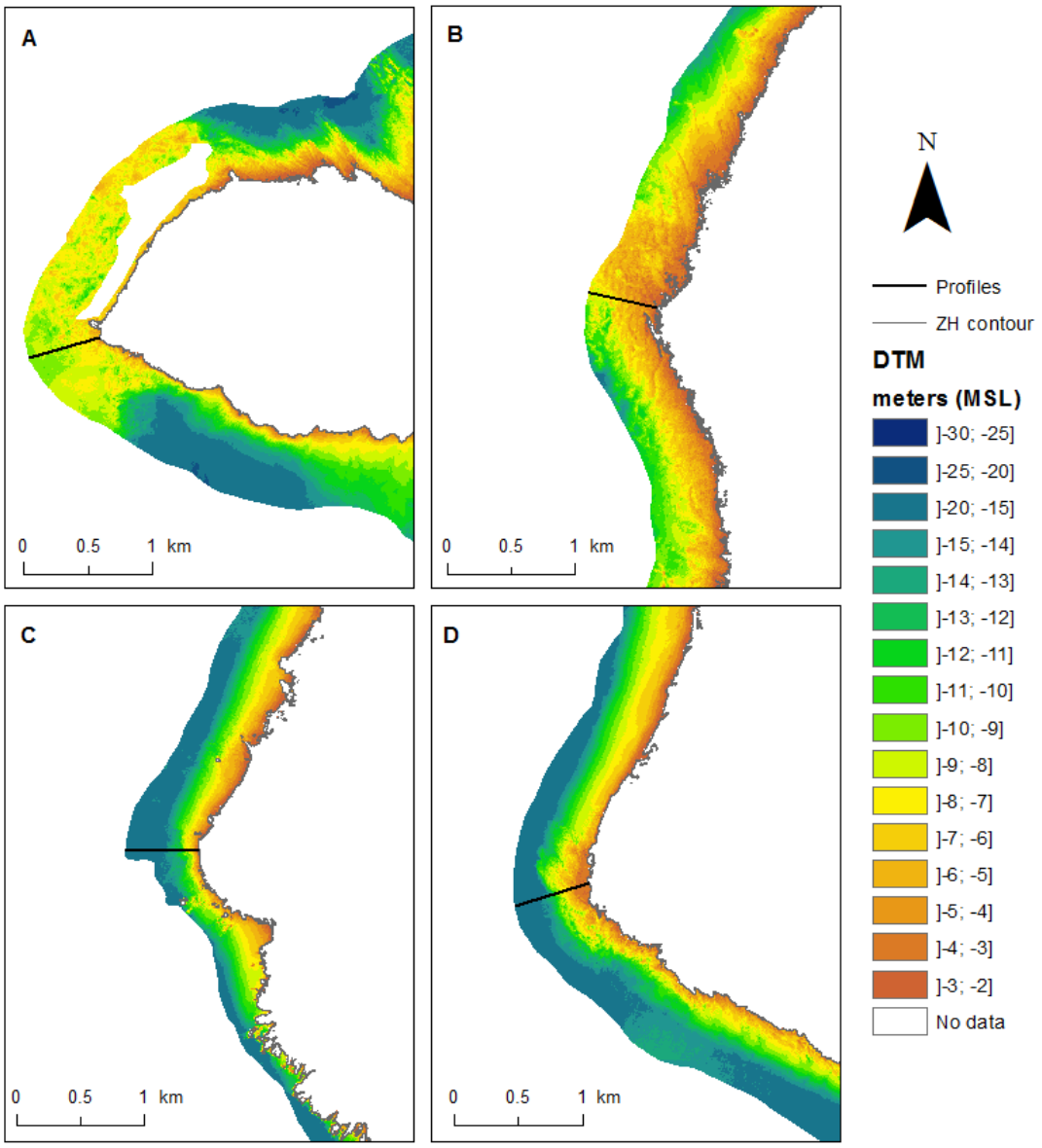

Figure 2.3. Digital terrain models of the inner shelf offshore main headlands: (A) Carvoeiro cape; (B) Ponta da Lamporeira; (C) Roca cape; (D) Raso cape.

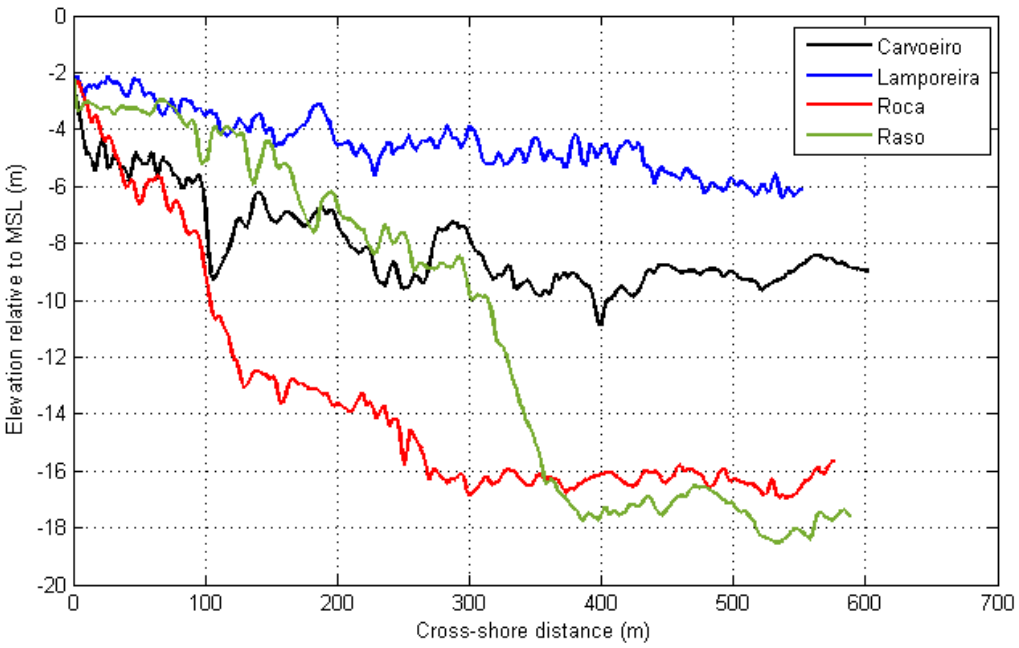

Figure 2.4. Bathymetric profiles crossing the inner shelf offshore main headlands: Carvoeiro cape, Ponta da Lamporeira, Roca cape and Raso cape (see profiles location and orientation in **Figure 2.3**).

2.3.2 Inner shelf sedimentology

The sedimentary deposits covering the inner continental shelf are presented in **Figure 2.5**. Only 52 % of the studied inner shelf is covered by unconsolidated sedimentary deposits, the other 48 % are rocky outcrops, which are preferably located offshore of prominent headlands. Between Carvoeiro and Peralta headlands, the sedimentary cover is mainly composed by coarse sediments, such as gravels, gravelly sands and coarse sands; and some of these coarse deposits have an important biogenic component. South of Peralta the sedimentary deposits are mainly medium and fine sands, despite the existence of small stains of coarse and muddy sands. Medium sand deposits usually occur at depths shallower than 20 m, for greater depths fine sand became dominant. The stretch between Sta. Cruz and Ericeira is particularly rocky, while the stretch between Ericeira and Roca cape is the sandiest.

The four sediment samples collected in the framework of this study, at the lower inner shelf near Roca cape, are mainly composed by fine sand (**Figure 2.6**), except sample S3 that corresponds to rock and coral fragments. The sediment collected northern of Roca cape (S1 and S2) have mean grain-sizes of 2.46 and 2.34 ϕ, and a standard deviation of 0.54 and 0.58 ϕ; while the sediment from southern side (S4) is slightly finer and less sorted, with a mean grain-size of 2.84 ϕ and a standard deviation of 0.85 ϕ. The main differences observed between the sediment samples and the sedimentological map, were found at sample S3 (**Figure 2.5**). Still, this

difference are acceptable, considering that map results from data interpolation and the time interval between samplings.

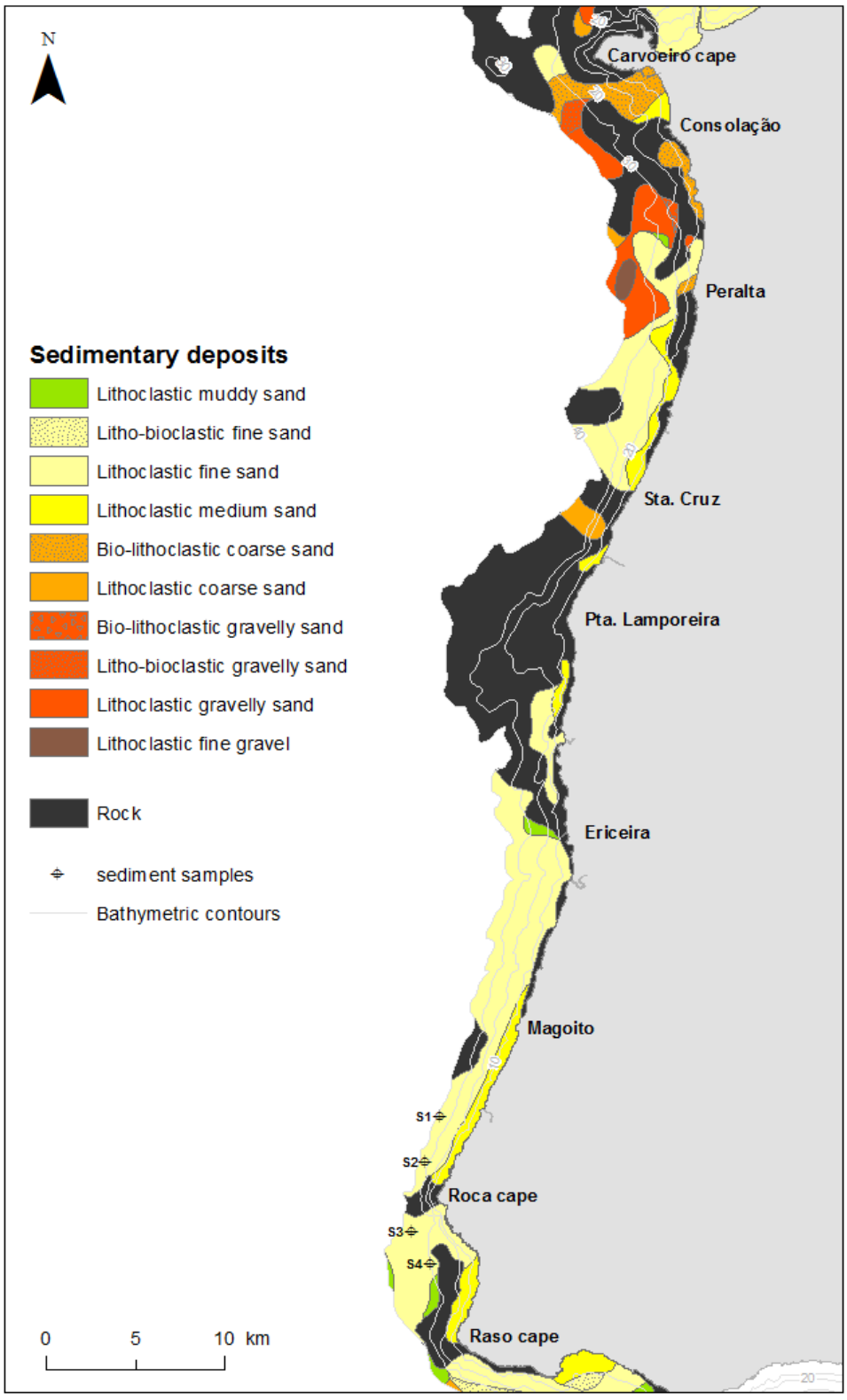

Figure 2.5. Sedimentary deposits of inner continental shelf vectorized from the sedimentological map provided by IH (2010) and location of the sediment samples collected in the scope of this work. The offshore limit of the inner shelf area was defined using the 40 m bathymetric contour of Vanney and Mougenot (1981).

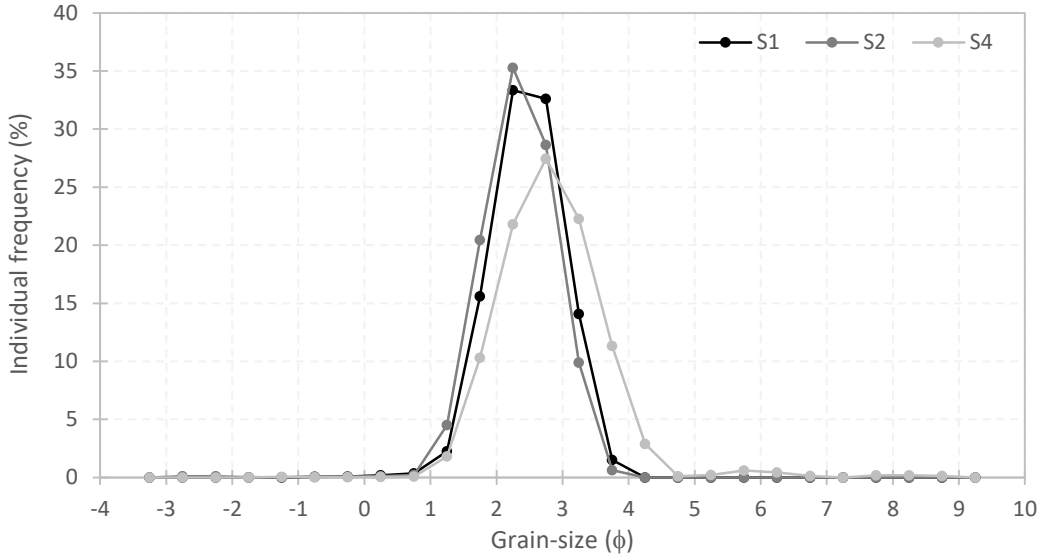

Figure 2.6. Grain-size distribution of inner shelf sediment samples. The depths measure by the vessel's probe during sediment sampling (without any correction) were 33, 35, 34 m for samples S1, S2 and S4, respectively.

2.3.3 Inner shelf seafloor texture and bedforms

Side-scan sonar imagery presented in **Figure 2.7**, covers essentially the lower inner shelf offshore the coastal stretch between Magoito and Adraga. The light greys tones correspond to high backscatter intensity and dark greys tones to low backscatter intensity.

Three main patterns were identified, the first one correspond to the areas with low backscatter intensity and smooth surfaces, typical of seafloors cover by fine sediment (**Figure 2.7B**). This pattern occupies the larger part of the surveyed area and, considering the sediment distribution from **Figure 2.5**, it corresponds to fine sand.

The second pattern encompasses the areas with high backscatter intensity and large shadows indicating the high roughness of the seafloor (**Figure 2.7B** and **Figure 2.7C**). In these areas it is possible to observe linear features that should correspond to the stratification of a rocky substrate, probably from Jurassic formations (see **Figure 1.6**). The larger outcrop is located offshore Azenhas do Mar, but small outcrops can be found in the northern sector of the surveyed area.

The third pattern corresponds to small patches that also present high backscatter intensity, morphologically smoother and presenting symmetric rhythmic forms oriented NE-SW (**Figure 2.7C** and **Figure 2.7D**). These features indicate that this pattern corresponds to sediment deposits, while its high reflectivity suggest that this sediment should be coarse. The rhythmic bedforms of the sediment located in the cavities of the larger rocky outcrop have a mean wavelength of 2 m and a mean height of 0.25 m. On the other hand, the bedforms observed at

depths between 15 and 20 m have a mean wavelength of 0.80 m and a mean height of 0.12 m. For shallower depths, bedforms become more common but decrease in size, which makes measurement quite difficult.

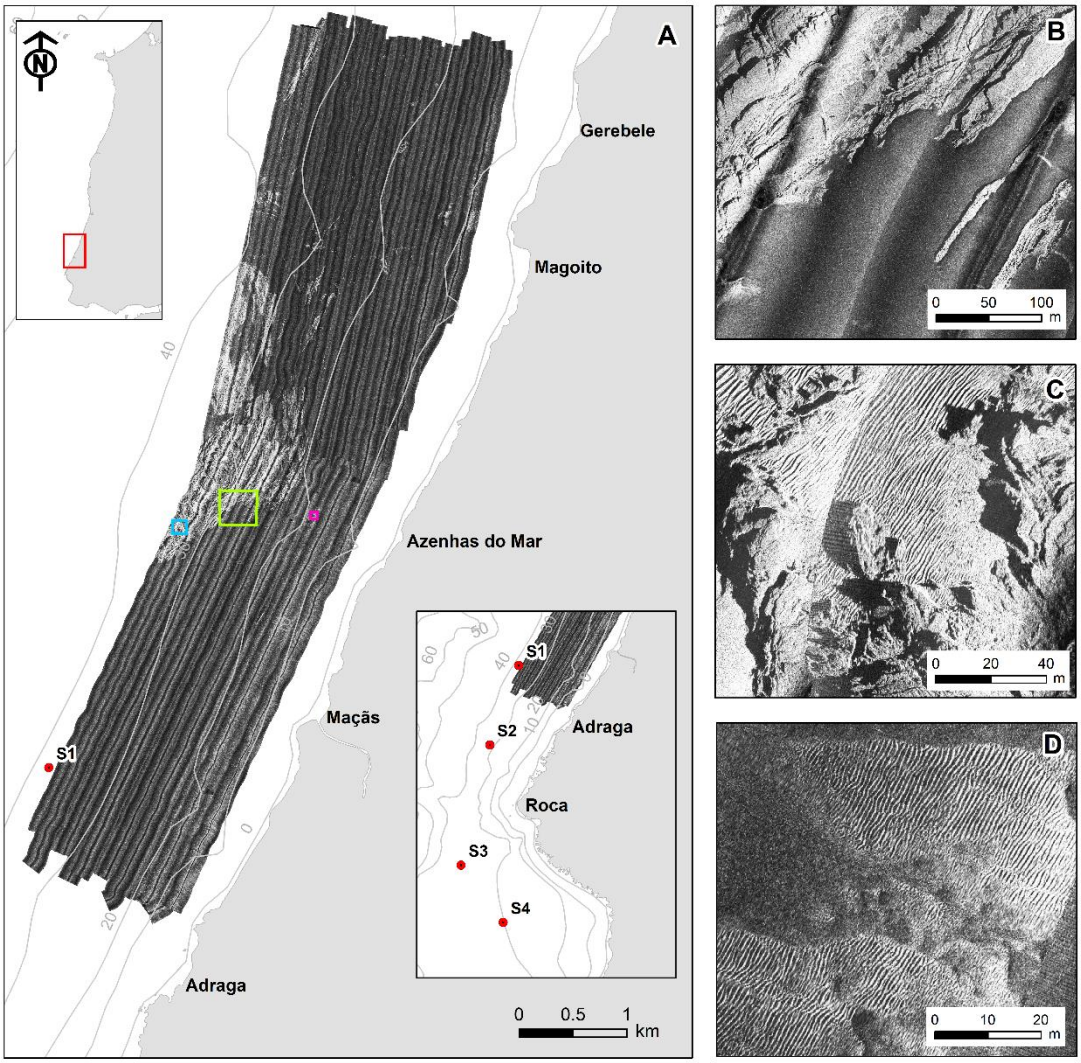

Figure 2.7. (A) Mosaic of side-scan sonnar imagery, where light greys correspond to high backscatter intensity and dark greys to low backscatter intensity, and sediment sampling sites (red dots); (B) contrast between rock and sediment (green rectangle); (C) coarse sediment pockets with bedforms (blue rectangle); and (D) light patches of coarse sediment with bedforms contrasting with dark finer sediment (mangenta rectangle).

2.3.4 Sandbars and surf zone width

Satellite images show well-developed sandbars along the stretches with NE-SW general orientation, located north of the most prominent headlands, except in the case of Carvoeiro cape (**Figure 2.8**). The projection of the bathymetric contour obtained from LiDAR data on the images suggest that sandbars are located mainly between 7 and 10 m depth (MSL). It can be

noticed that the development of these sandbars is not constrained to the sectors front of the beaches, extending in front of the rocky sectors, where usually get closer to the coastline.

In the case of stretches with a N-S to NW-SE general orientation, sandbar are absent and sometimes it is possible to observe rocky outcrops with patchy sand bodies, such as is the case of the inner shelf south of Consolação headland, where the stratification of the Jurassic formations can be noticed (**Figure 2.8A**). These structures, as well as the rocky seafloor offshore Ribarmar (Ericeira) and downdrift Raso cape, were clearly observed in the orthophotomaps.

The analysis of the surf zone width, under different wave energy conditions, was performed in two coastal stretches with 9 km long. The first stretch, has a NE-SW general orientation and is located between Magoito and Adraga (**Figure 2.9**). The second stretch, is more crenulated, have a N-S general orientation and is located northward Ericeira, between Baleia and Calada beaches. As expected, under low-energy wave conditions the surf zone is narrow for both cases, being almost imperceptive inside the deeper embayments (**Figure 2.9A** and **Figure 2.10A**).

The increase of the wave energy, increases the surf zone width. However, between Magoito and Adraga, the surf zone easier reach the tip of the headlands, extending continuously alongshore under both moderated and high-energy wave conditions (**Figure 2.9B** and **Figure 2.9C**); while between Baleia and Calada beaches, the surf zone only extend outside the embayments, during high-energy events (**Figure 2.10B** and **Figure 2.10C**).

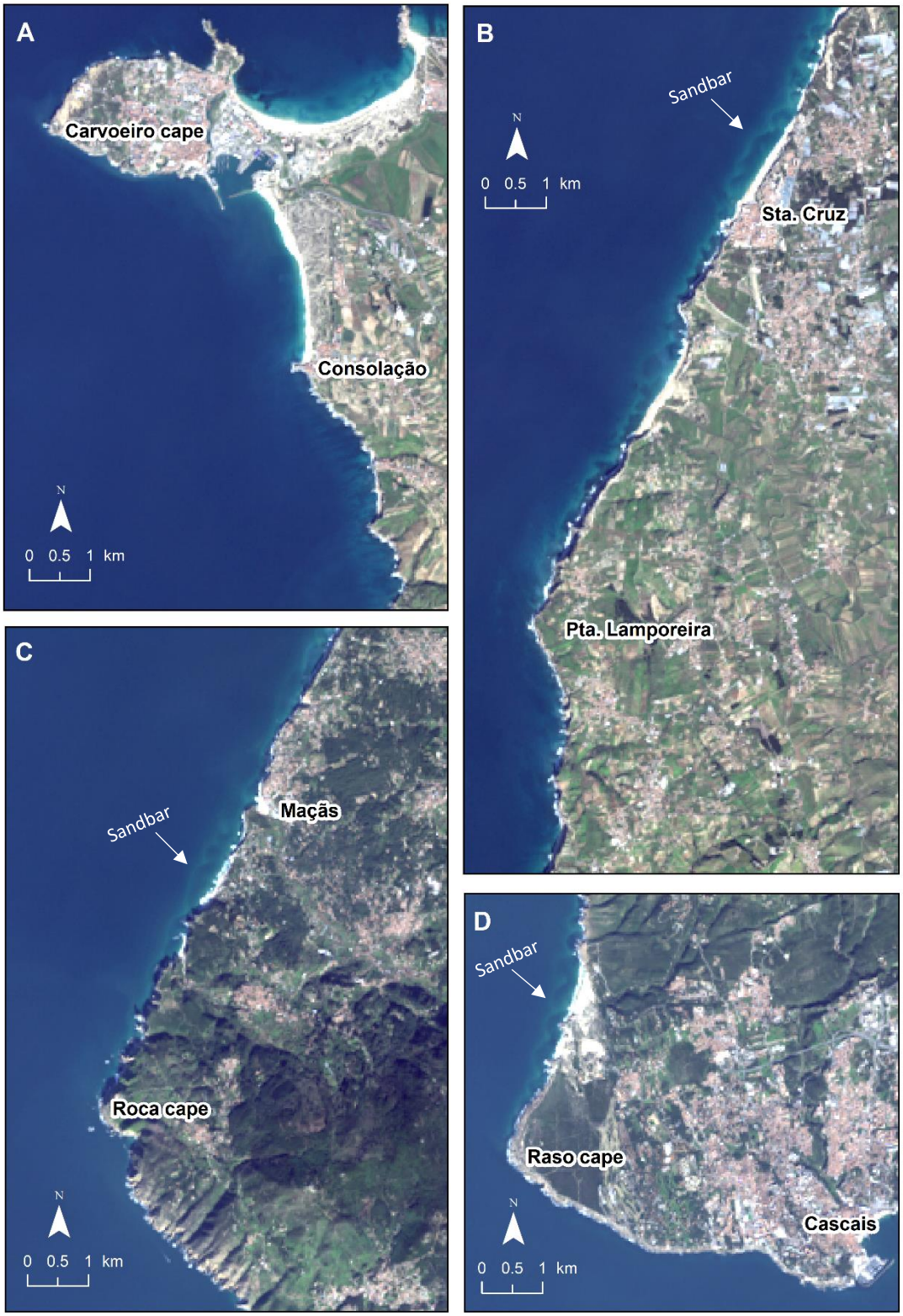

Figure 2.8. Presence and absence of the sandbar along the stretches in the vicinity of: (A) Carvoeiro cape and Consolação headland; (B) Ponta da Lamporeira headland; (C) Roca cape; and (D) Raso cape, on January 1st 2015 (Landsat 8 image provided by NASA and USGS). The tide level at the time of the image acquisition is 1.06 m (MSL) and was computed based on Cascais tide gauge data using the UTIDE model (Codiga, 2011); the mean wave conditions are Hs = 1.2 m, Tp = 10 s and Dir = 265°, and were obtained from the wave time-series numerically modeled and provided by Professor Xavier Bertin, University of *La Rochelle*.

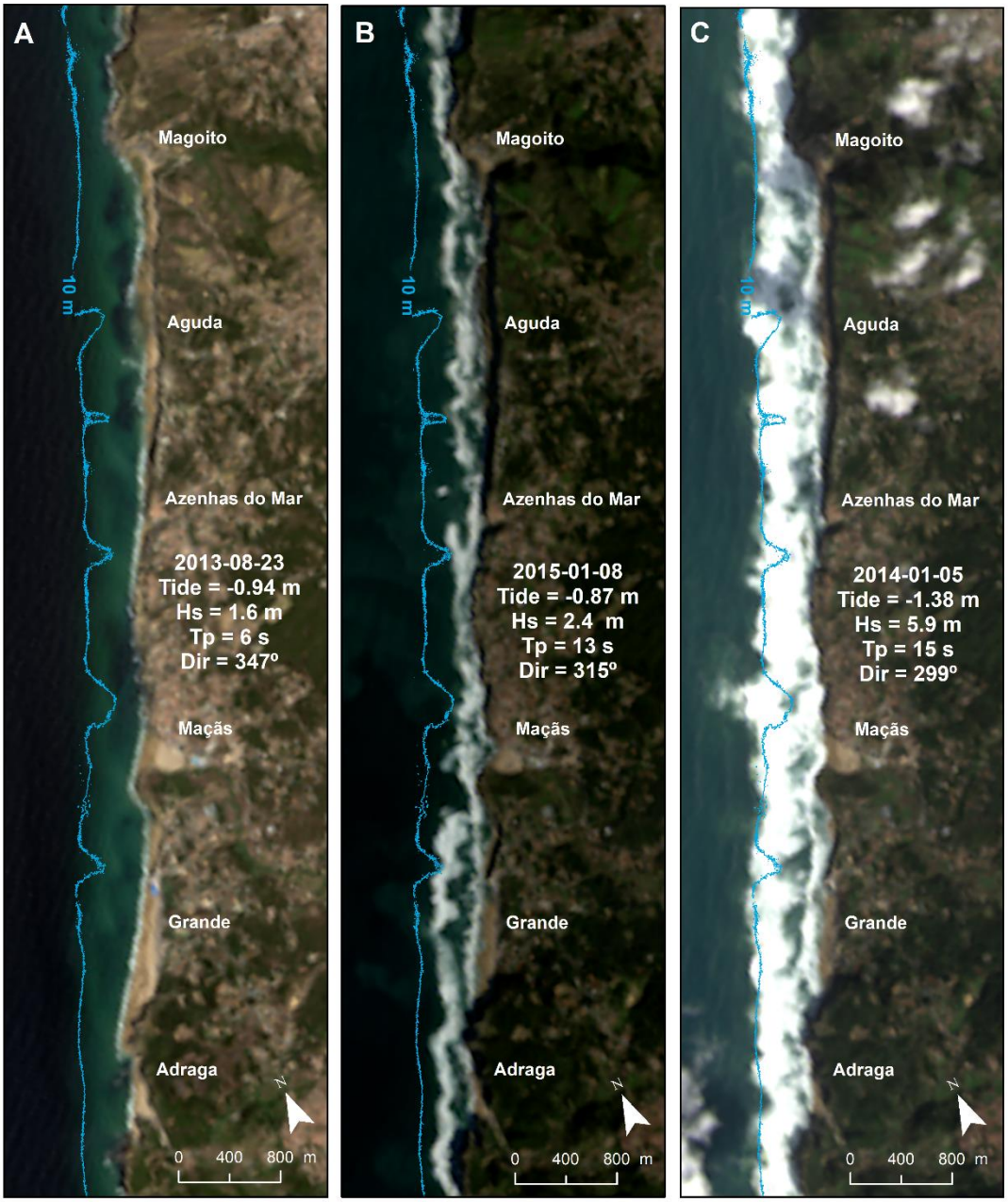

Figure 2.9. Surf zone width at the stretch between Magoito and Adraga (Sintra coast) during: (A) low; (B) moderate and (C) high-energy wave conditions (Landsat 8 images provided by NASA and USGS). The blue line is the 10 m depth contour extract from LiDAR survey. The tide level (T) is relative to the MSL and was estimated based on Cascais tide gauge data using the UTIDE model (Codiga, 2011); the mean wave conditions (Hs, Tp and Dir) were obtained from the wave time-series numerically modeled and provided by Professor Xavier Bertin, University of *La Rochelle*.

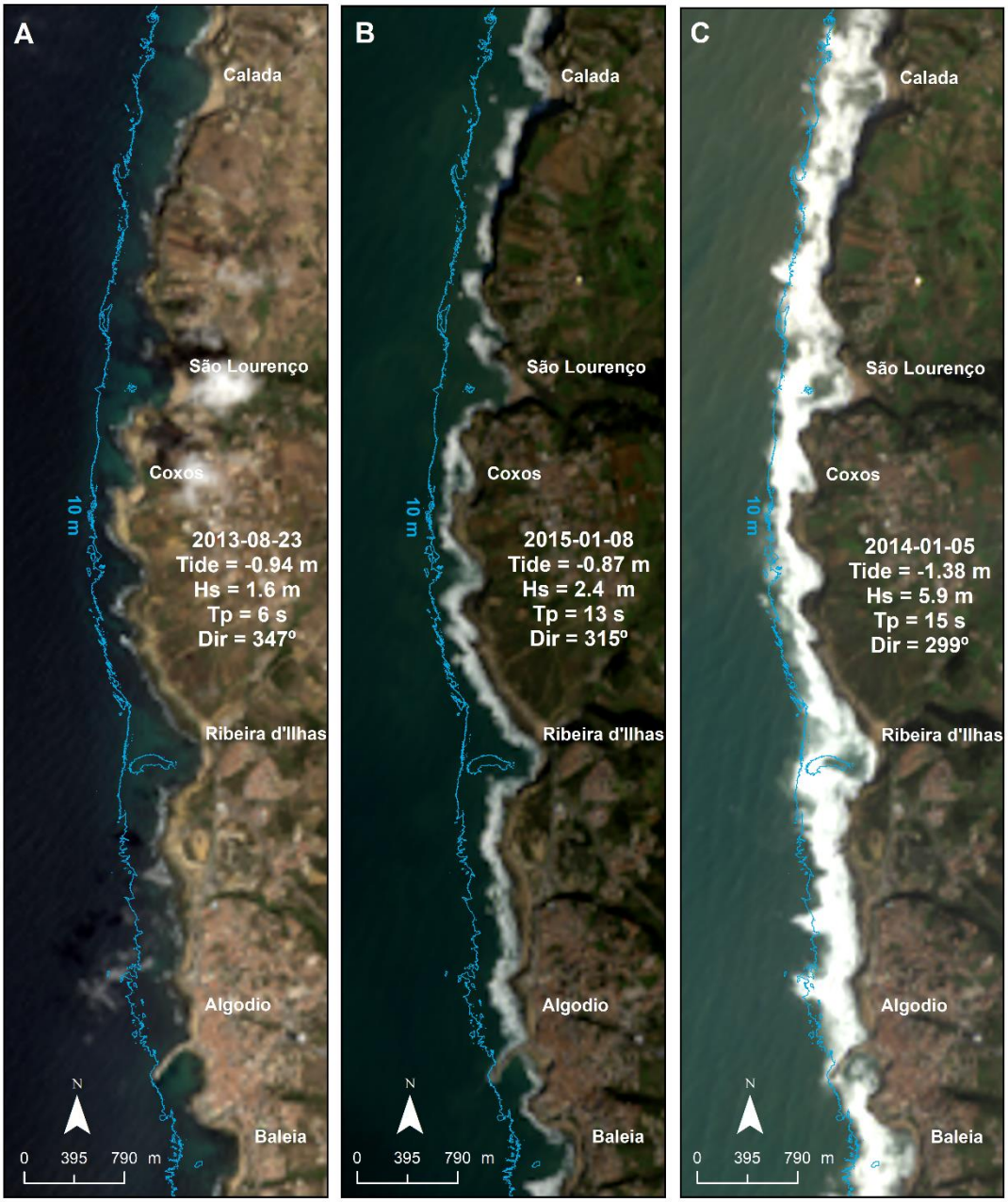

Figure 2.10. Surf zone width at the stretch between Calada and Baleia (Ericeira) during: (A) low; (B) moderate and (C) high-energy wave conditions (Landsat 8 images provided by NASA and USGS). The blue line is the 10 m depth contour extract from LiDAR survey. The tide level (T) is relative to the MSL and was computed based on Cascais tide gauge data using the UTIDE model (Codiga, 2011); the mean wave conditions (Hs, Tp and Dir) were obtained from the wave time-series numerically modeled and provided by Professor Xavier Bertin, University of *La Rochelle*.

2.4 DISCUSSION AND CONCLUSIONS

The inner continental shelf present variations in the width along the studied site, being particularly larger front of Carvoeiro and Lamporeira (≈7 km) and narrower in the stretch between Magoito and Roca cape (< 4 km), as can be seen by the location of 40 m depth bathymetric in the **Figure 2.2**. However, the morphological analysis shows that this is relatively

uniform with respect to the width and slope up to 10 m depth. Exceptions are downdrift sides of some headlands, where inner shelf is narrower and steeper, being Roca cape the most notorious case.

Sectors updrift the headlands typically have NE-SW orientations and lower roughness, indicating that these should be sandier than downdrift sectors that generally have N-S and NW-SE orientations and higher roughness. This is particularly evident at the most prominent headlands, such as Lamporeira, Roca and Raso (**Figure 2.2**). These results put in evidence the role of the aforementioned headlands in the sediment retention and are supported by the presence of well-developed outer sandbars, as well as by the sedimentological map and side-scan data that show sandier seafloors updrift these headlands.

Bathymetric profiles offshore most prominent headlands show that from the morphological point of view, there are conditions for inner shelf bypassing. However, bypass occurrence is also conditioned by sedimentary constrains.

Sediment bypass of Carvoeiro cape seems difficult considering: (1) the rocky nature of the inner shelf around the headland; (2) its location at the tip of Peniche Peninsula that protrudes into the water 2.5 km from the adjacent sandy coastline; (3) the inexistence of sand accumulation on the western jetty of Peniche harbour; and (4) the differences of the inner shelf sediment grain-size and composition north and south of the headland. The sedimentary cover of northern inner shelf is mainly composed by lithoclastic fine sands, while the southern one is composed by bio-lithoclastic coarse sands (**Figure 2.5**). Furthermore, longshore sediment pathway from updrift sector occurred in the past through what is today the Peniche isthmus (Calado, 1994).

In the case of Lamporeira, the inner shelf is shallow and have a low slope (**Figure 2.4**), favouring sediment bypass. Offshore Roca cape, inner shelf is very steep down to 13 m depth, with slope decreasing seaward slope, becoming almost horizontal at 16 m depth (**Figure 2.4**). Under these conditions, the most likely is that sediment bypass occur either near the coastline or at depths greater than 13 m. This hypothesis is acceptable considering that the closure depth ranges from 11 to 16 m (Lapa *et al.*, 2012), and the bedforms present in the inner shelf updrift of Roca cape at these depths. These bedforms have a symmetrical rhythmic patterns, typical of oscillatory flows, and a NE-SW orientation, orthogonal to the NW dominant wave conditions. Considering the seafloor sediment cover near this headland, sediment bypassed at these depths should be medium to fine sand (**Figure 2.5**).

Raso cape has two distinct sectors with gentle mean slopes, a first one at 3 m depth and, a second one that extends from 17 m depth to deeper waters. Considering the closure depth

mentioned before, the first pathway is the most plausible for the sediment bypassing. However, the shallower sector of the inner shelf downdrift this headland, is extremely rocky (**Figure 2.5**). Orthophotomaps show that in this sector cliffs are hinged with a rocky submarine platform that presents a sediment cover very incipient close to the coastline. This sediment scarcity is observed along 7 km between the Raso cape and the Cascais bay (**Figure 2.8D**), where the coastline has a crenulated shape changing its orientation several times, favourable conditions for sediment deposition. However, no significant littoral sediment accumulation is observed, including at the Cascais marina structure built in the later 90's. Under these conditions sediment bypassing of Raso cape should be negligible.

The outer sandbars observed along the NE-SW oriented stretches, as well as the surf zone extension seaward the tip of the headlands, under moderate to high-energy wave conditions, indicate a sediment linkage of the submarine beach along these stretches. In the rockier stretches, located at NW-SE sectors, the coast present a more crenulated shape and the sediment linkage between deeper bays only seems possible during high-energy wave conditions.

Chapter 3

Beach Morphology

3.1 INTRODUCTION

Headland-bay beaches exhibit a wide range of sizes (from several tens metres to few kilometres), shapes and indentations. Morphological features of these beaches are distinct from sandy-coast beaches, because sediment transport is generally confined to the embayment. The three-dimensional morphology of headland-bay beaches is the result of a closely relation between the cross-shore morphology (profile) and alongshore morphology (planform). A common feature of these beaches is the asymmetric shape of the planform, which is characterised by a curved zone, a gentle transition and/or a relatively straight tangential segment on the downdrift end. Sometimes, the curved zone may not exist or the straight tangential section does not appear. The planform may even become symmetric between two headlands in identical layout (Hsu *et al*., 2010). The long-term equilibrium state of the beach planform has been extensively studied (*e.g.* Yasso, 1965; Silvester and Ho, 1972; Hsu *et al*., 1989; Moreno and Kraus, 1999; Klein *et al*., 2010; Daly *et al*., 2015), as well as the short- to medium-term beach clockwise/counter-clockwise rotation (*e.g.* Klein *et al*., 2002; Short and Trembanis, 2004; Ranasinghe *et al*., 2004; Pinto *et al*., 2009; Thomas *et al*., 2010; Turki *et al*., 2013; Harley *et al*., 2015). However, little attention has been given to the relationship between beach morphology and headland sediment bypassing (HSB). Thus, the main goal of this chapter was the description of the beach morphology along and across-shore to get insights on HSB

processes. To achieve this goal, a characterization of the beach planform geometry along the entire study coast was performed based on beach length, orientation, embayment degree and exposure to the dominant wave regime. The planform rotation and cross-shore morphology were also analysed for a subset of the studied beaches and related with incident wave conditions.

3.2 METHODS

3.2.1 Wave data analysis

For a better interpretation of the results a hindcast wave time-series was used to characterize the offshore wave climate between 2009 and 2015, which covers the time-interval of the morphological data. The wave series (kindly provided by Professor Xavier Bertin, University of *La Rochelle*) was obtained following the modelling strategy presented by Dodet *et al.* (2010). Wave significant height (Hs), peak period (Tp) and peak direction (Dir), obtained for a time interval of 6 hours, were used to characterise the seasonal and interannual wave conditions.

3.2.2 Beach planform analysis

3.2.2.1 Planform geometry

Beach planform geometry analysis was performed for all the sandy stretches observed on the orthophotomaps acquired on June 2012 and provided *Direcção-Geral do Território* – DGT. The planform geometry can be described by a set of planform parameters (see for example Bowman *et al*., 2009). In this work the following parameters were used (**Figure 3.1**):

- Length and azimuth of the straight line between headland's tips (Ro);
- Length and azimuth of the beach between headlands (S), which was assumed as the wet-dry line that matches the wave swash limit and typically represents berm crest position;
- maximum distance between the Ro and S lines that corresponds the bay indentation (a);
- distance between the Ro and S lines close to the headlands that limit the beach system ($d1$ and $d2$).

Ro and S lines were manually vectorized on orthophotomaps at a fixed scale (1:5000), using the ArcGIS v10.3 software. The a, $d1$ and $d2$ distances were obtained through the orthogonal

distances between Ro and S lines, measured alongshore for a distance interval of 10 m, using the Digital Shoreline Analysis v4.3 software (Thieler *et al.*, 2009).

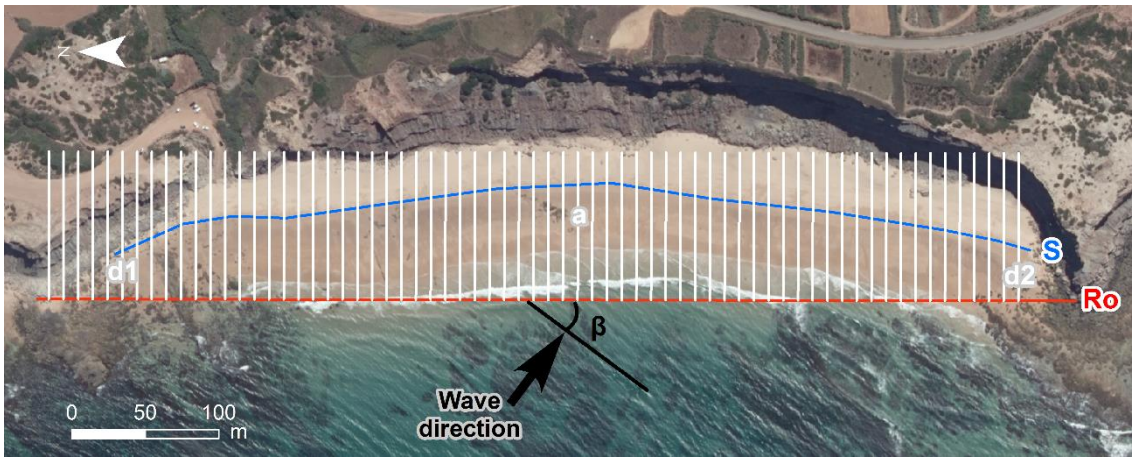

Figure 3.1. Parameters used to describe the beach planform geometry (example of Caniçal beach at Lourinhã). S is the beach stretch between headlands; Ro is the straight line between headland's tips; a is the maximum distance between the Ro and S lines; and β is the wave crest obliquity to Ro line.

Following previous works (*e.g.* Klein and Menezes, 2001; Bowman *et al.*, 2009) beach embayment index was obtained from the relation:

$$Embayment\ index = \frac{a}{Ro\ length} \quad (\mathbf{3.1})$$

Exposure to the dominant wave conditions was obtained based on the wave crest obliquity to Ro line (β), as illustrated in **Figure 3.1**. Maximum and minimum beach exposure occurs when β is 0 and ±90°, respectively. Thus, exposure index was computed according to the expression:

$$Exposure\ index = 1 - \left(\frac{|\beta|}{90}\right) \quad (\mathbf{3.2})$$

β values were computed assuming the mean wave peak direction (307°) obtained from the 56-years hindcast wave time-series provided by Dodet *et al.* (2010).

3.2.2.2 Planform rotation

The analysis of beach planform evolution was performed using Landsat 8 images acquired between April 2013 and December 2015, with a 16 days revisit cycle. These images were provided by National Aeronautics and Space Administration - NASA and United States Geological Survey – USGS Landsat program (available online at: http://earthexplorer.usgs.gov/, accessed between Dec. 2013 and Dec. 2015).

The beach stretches orientation was obtained based on the wet-dry line extracted from the satellite images according to the flowchart presented in **Figure 3.2**. The images were pre-

processed with the Semi-Automatic Classification Plugin of QGIS software that convert Landsat Digital Numbers (DNs) to Top of Atmosphere (TOA) Reflectance using the rescaling factors and parameters given in the Landsat metadata file. This image pre-processing consist in a radiometric correction and also included an atmospheric correction through the DOS1 method (Dark Object Subtraction 1). DOS is a simple atmospheric correction method that remove the effects of atmospheric scattering from an image by subtracting a pixel value that represents a background signature from each band (see details in Congedo, 2016).

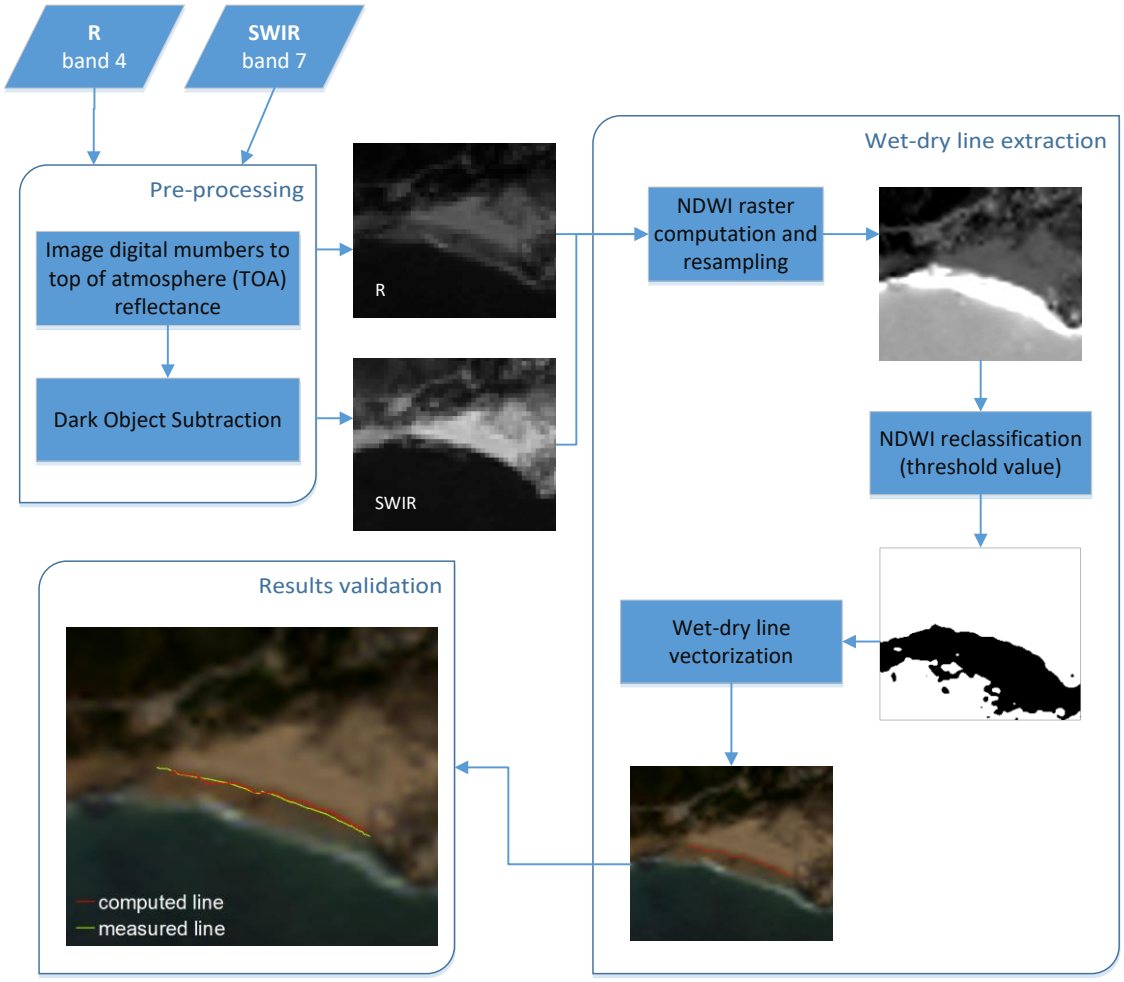

Figure 3.2. Flowchart of the Landsat image analisys for wet-dry line extration and results validation.

The wet-dry line was extract automatically from the pre-processed images, using a toolbox created in the ArcGIS v10.3 software for this propose. This toolbox uses a Normalized Differences Water Index ($NDWI$) to identify wet and dry areas, assuming that wet sand appears darker, *i.e.* less reflective than dry sand (Nolet *et al.*, 2014). $NDWI$ is an arithmetic operation that enhances the spectral signals by contrasting the reflectance between different wavelengths

(*e.g.* Gao, 1996; McFeeters, 1996). In the present study $NDWI$ was computed based on the Red (R) and Short Wave Infra-Red ($SWIR$) bands through the equation:

$$NSWI = \frac{R - SWIR}{R + SWIR} \quad (\mathbf{3.3})$$

The $NSWI$ obtained was resampled for a pixel with 5 m using the cubic method that calculates the value of each pixel by fitting a smooth curve based on the surrounding 16 pixels. The resampled image was then reclassified based on a threshold value of 0.075 to separate wet and dry areas. Finally, the wet-dry limit was automatically vectorised.

The results of image analysis were validated with field data acquired at Guincho beach on 9th and on 16th July of 2014, at the same time of satellite image acquisition (**Figure 3.2**). In the first case, during high-tide (3.08 m - MSL), and in the second case, during low-tide (0.73 m - MSL). The comparison between the lines extract by image analysis and the measured ones have a root mean square error of 6.25 m, in the first case, and 9.75 m, in the second case, which are quite good considering the 30 m image pixel resolution of the Landsat 8 images. However, many of the studied beaches are narrow and the dry zone width is often close or within the pixel resolution. In this conditions the lines obtained usually correspond to the cliff's foot, producing unreliable results. Thus, the beach rotation analysis was performed only for beaches that usually present larger dry areas. Considering this constraint, 13 beaches with different features and located at different coastal stretches, were chosen (**Figure 3.3**). Image analysis results for each beach were excluded when the wet-dry limit coincides the cliff foot and when clouds cover the area under analysis. **Figure 3.4** show the image time-series used for each beach.

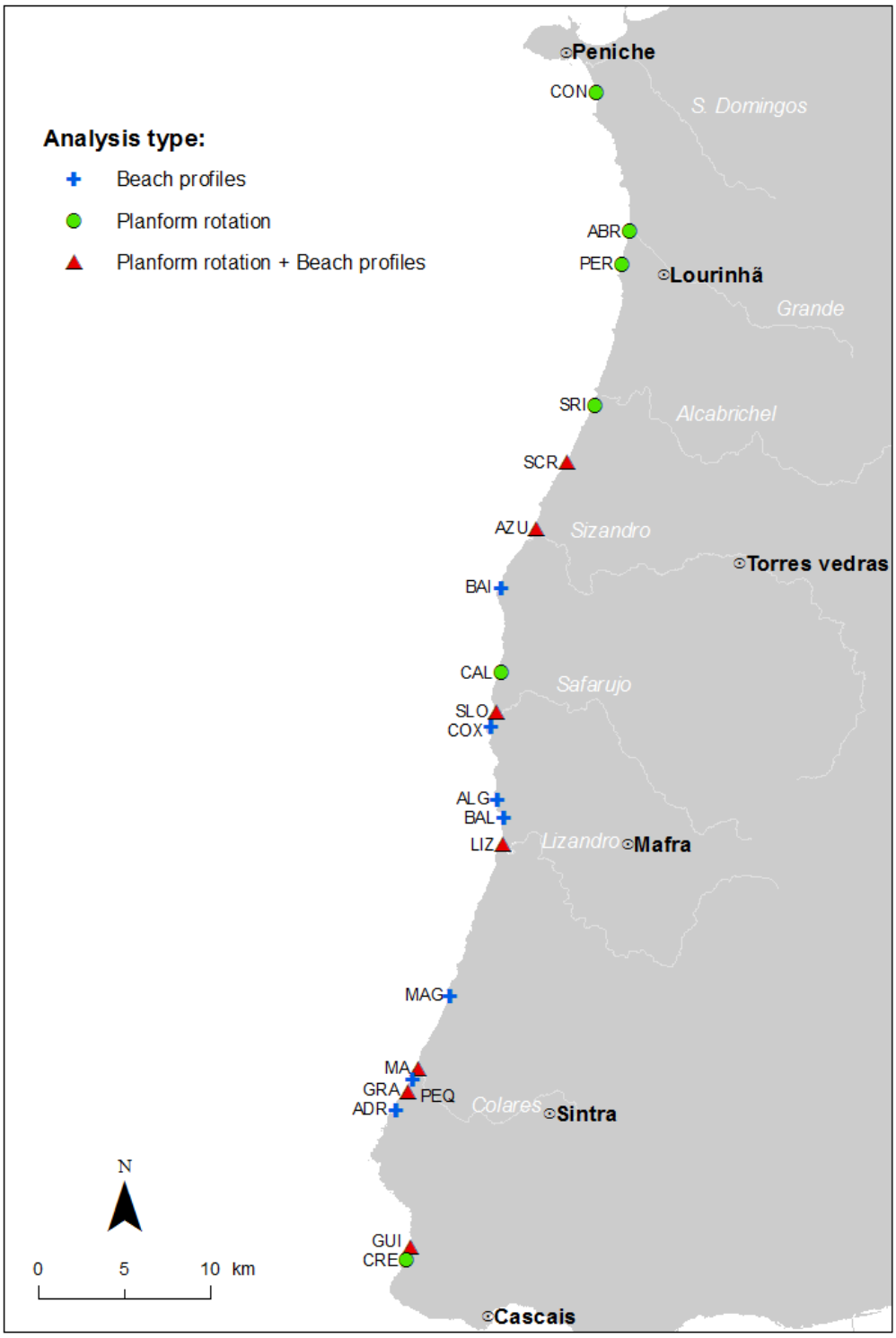

Figure 3.3. Location of the beaches for which planform rotation and cross-shore morphological analysis were performed: Consolação (CON); Areia Branca (ABR); PER (Peralta); Sta. Rita (SRI); Sta.Cruz (SCR); Azul (AZU); Baío (BAI); Porto da Calada (CAL); São Lourenço (SLO); Coxos (COX); Algodio (ALG); Baleia (BAL); Foz do Lizandro (LIZ); Magoito (MAG); Maçãs (MA); Pequena (PEQ); Grande (GRA); Adraga (ADR); Guincho (GUI); Cresmina (CRE).

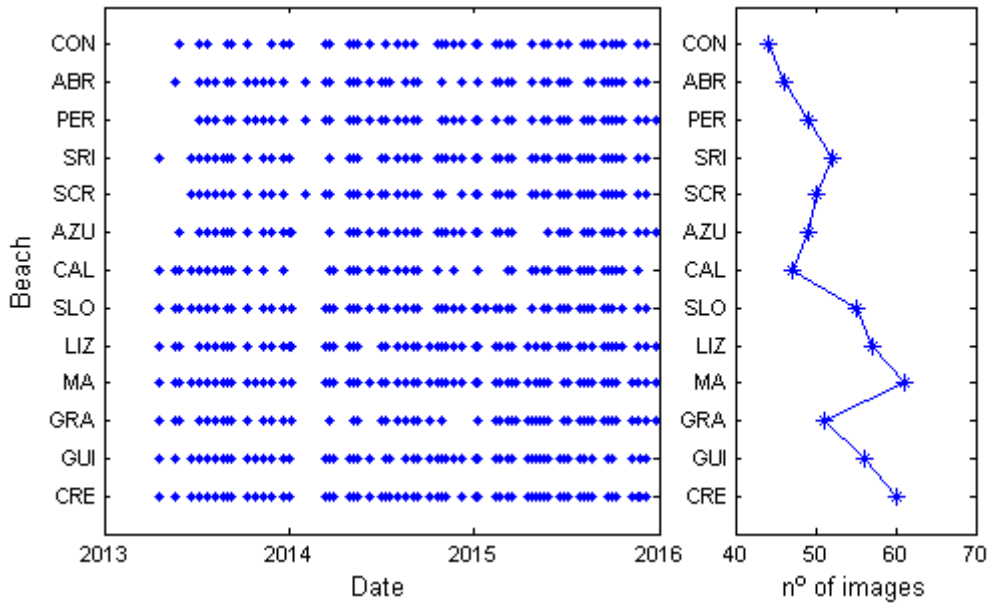

Figure 3.4. Images used in the planform rotation analysis of each beach.

3.2.3 Beach profile analysis

The analysis of cross-shore morphology was performed for a set of 14 beaches (see **Figure 3.3**), based on available topographic data and data acquired during this study (**Table 3.1**).

Table 3.1. Beach topographic data.

Monitoring period	Beach acronym *	Work/Project
December 2009	GUI	Field campaign in the framework of the GARGOT master program (FCUL)
March 2010 and October 2012	MA; GUI	Coastal Process group (FCUL)
March 2011 to March 2013	SCR; COX; BAL; MAG	"Criação e implementação de um sistema de monitorização no litoral abrangido pela área de jurisdição da Administração da Região Hidrográfica do Tejo. FFCUL/APA, I.P."
June 2013 to November 2015	SCR; AZU; BAI; SLO; COX; ALG; LIZ; MAG; MA; PEQ; GRA; ADR; GUI	In the scope of this work in collaboration with other works carried out by the Coastal Process group (GeoFCUL)

* Beaches names are presented in the legend of **Figure 3.3**.

Most of the topographic data were acquired with a GPS-RTK, although some data of Coxos beach were acquired with terrestrial LiDAR (Diogo *et al.*, 2014; Bastos *et al.*, 2015). Based on the available dataset it was possible to identify and compare beach morphological features, such as beach face slope and berm crest height. The beach slope was estimated based on the profile segment between 1 and 2 m of elevation (relative to the MSL). When a considerable number of

profile surveys are available, it was possible make some considerations about the beach morphological changes.

3.2.4 Beach photo-monitoring

During the field work carried out in the scope of this study, some beaches were also monitored using close range photography. Although the periodicity and tide level of the image acquisition were not systematic, this information is considered relevant to understand and illustrate some aspects related to the beach morphological changes. All photographs acquired were compiled online using the application Flickr and are available at: https://www.flickr.com/photos/114969613@N05/albums. The image subsets chosen to illustrate changes observed in the beaches can be seen in the web addresses listed in the Appendix A, through a visualization window similar to the one presented in **Figure 3.5**.

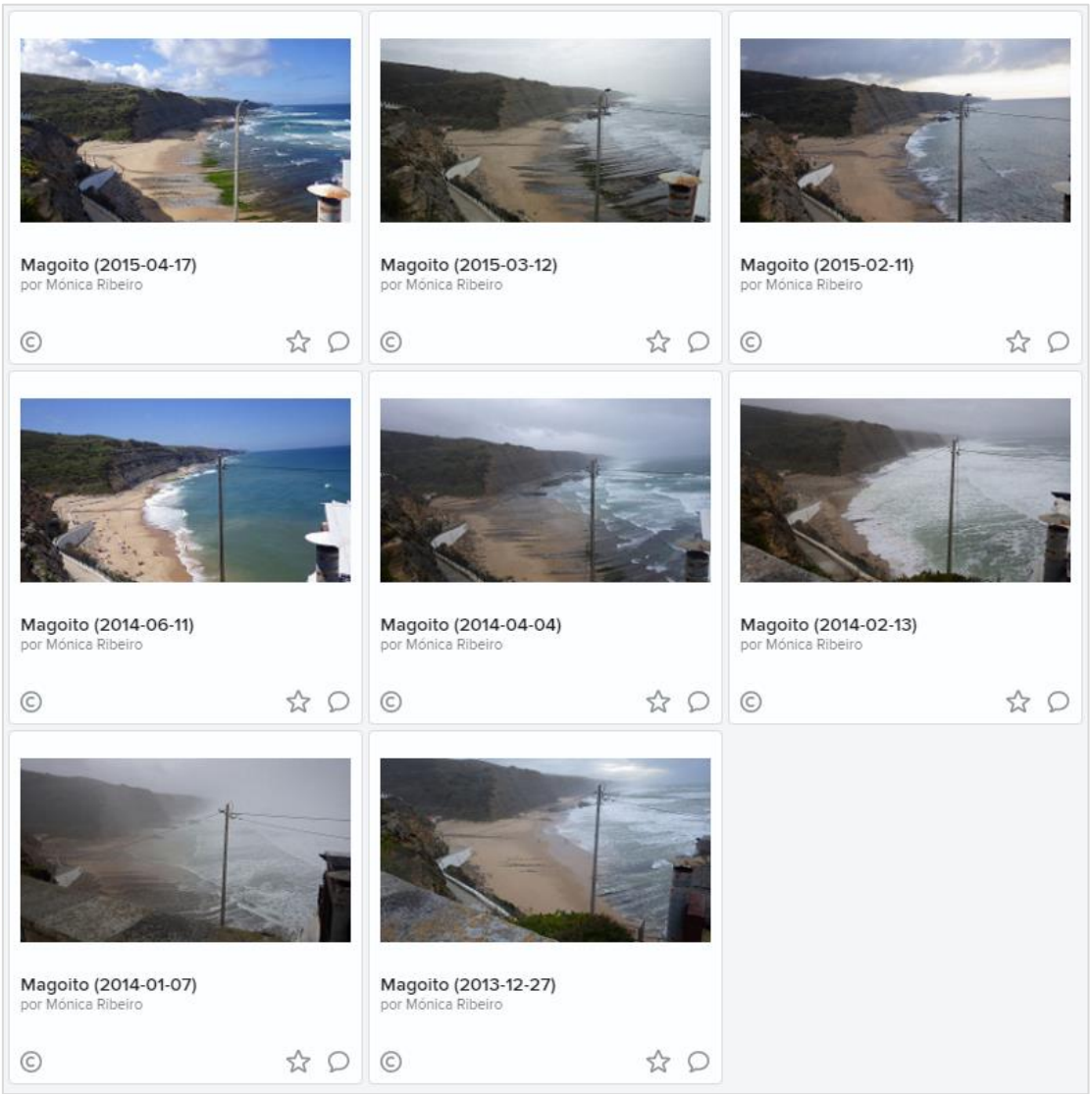

Figure 3.5. Photo-monitoring of Magoito beach between December 2013 and April 2015 (images compiled in Flickr application - see web addresses of this and the other beaches in Appendix A).

3.3 RESULTS

3.3.1 Offshore wave conditions

Seasonal wave climate for the period under analysis (2009-2015, in **Figure 3.6**), agree in general, with wave climate presented in Chapter 1 (1953-2008, in **Figure 1.7**). The NW waves are dominant, while W and SW waves are less frequent and typical of winter/autumn seasons. The main differences are the higher frequency of higher waves, typical of the winter/autumn season, and the greater directional spreading during summer/spring seasons, related with the higher frequency of waves coming from NNW direction. The mean winter/autumn wave conditions exhibit a Hs of 2.5 m, a Tp of 12 s and a Dir of 306°, while mean summer wave conditions are characterized by a Hs of 1.9 m, a Tp of 10 s and a Dir of 315°.

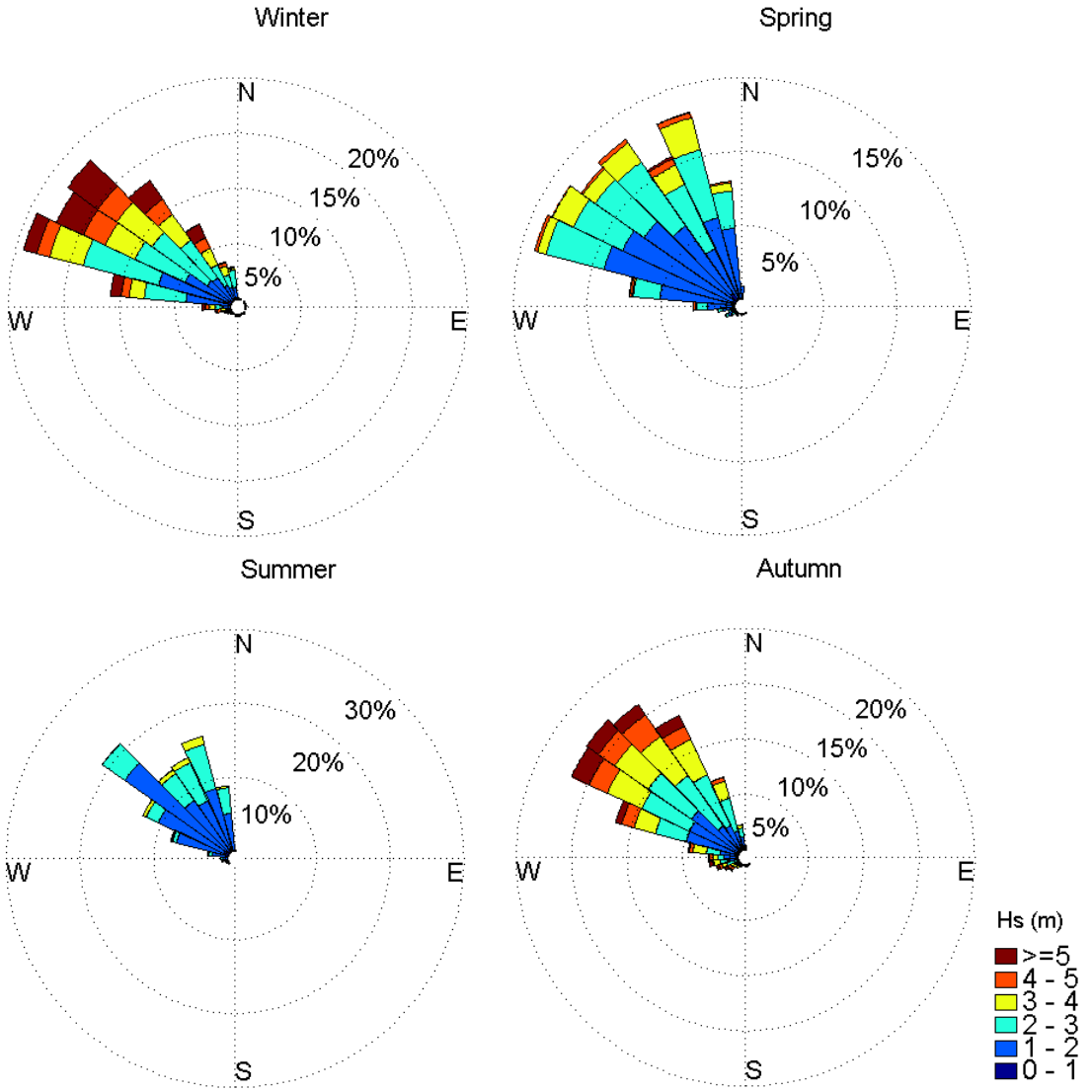

Figure 3.6. Wave significant height (Hs) and peak direction by season: winter (Jan-Mar); spring (Abr-Jun); summer (Jul-Sep); autumn (Oct-Dez). Data provided by professor Xavier Bertin (University of *La Rochelle*).

The annual distribution of significant wave height do not show significant differences, being the median value of each year, approximately, 2 m. The box-plot diagrams in the **Figure 3.7** indicate that the years of 2013 and 2014 had a slightly higher frequency of higher waves. On the other hand, the years of 2012 and 2015 were characterized by the lowest maximum heights. The annual median peak periods varied between 11 and 12 s, being the highest wave period (23 s) reached in 2010 and 2014.

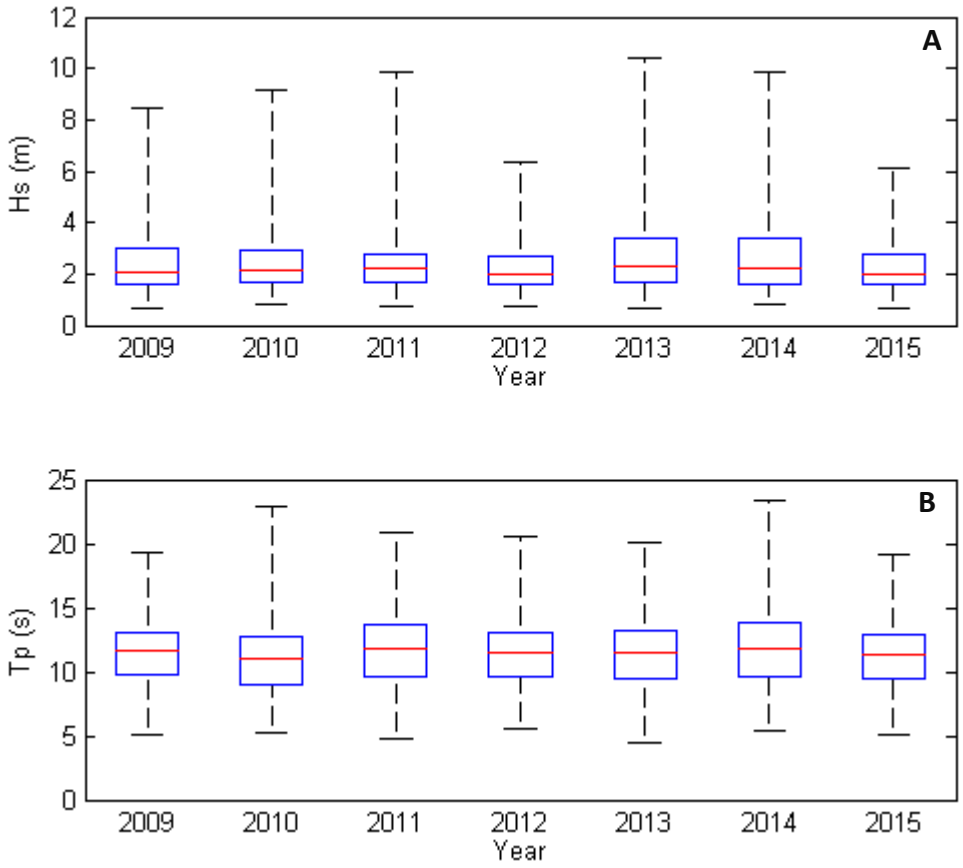

Figure 3.7. Annual conditions for (A) significant wave height (Hs) and (B) peak period (Tp). Boxes limits are the 25th and 75th percentiles, respectively; the mid-range is the median value; and whiskers extremes are the maximum and minimum values. Data provided by professor Xavier Bertin (University of *La Rochelle*).

Annual distribution of peak wave directional classes shows once again that waves coming from NW quadrant are dominant. The years of 2011 and 2013, were characterized by higher frequency of NNW waves; while the years of 2009, 2010 and 2012 had higher frequencies of WSW waves. The most significant percentages of SSW waves occurred in the years of 2010 and 2015 (**Figure 3.8**).

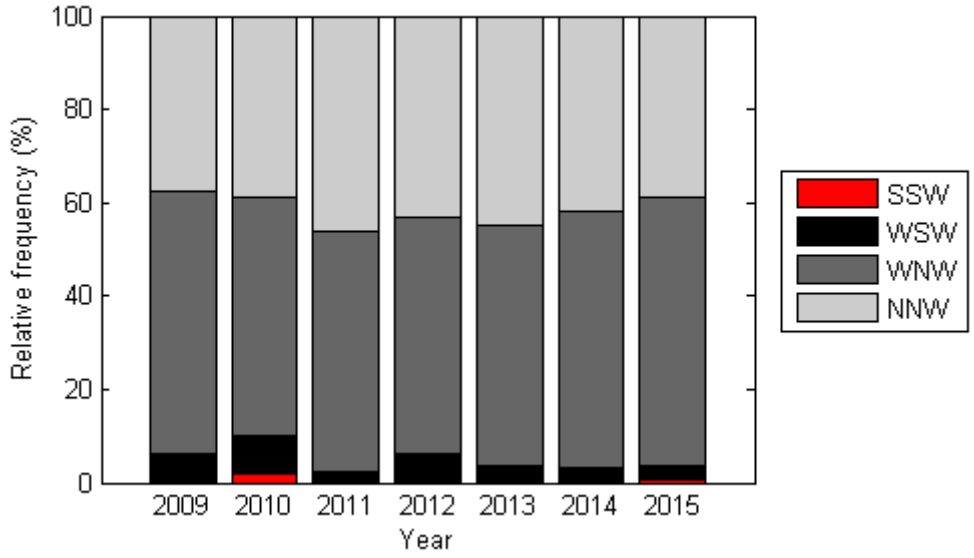

Figure 3.8. Relative frequency of peak wave directional classes: NNW (315-360°); WNW (270-315°); WSW (225-270°); SSW (180-225°).

3.3.2 Beach planform

3.3.2.1 Planform geometry

Results of planform geometry show that studied beach length varies between 25 m and 3 km. The longest beaches are located in the NE-SW oriented stretches, being Consolação beach, located at the north end of the study site, an exception. The results also show that the coastal stretch located between Paimôgo and Lamporeira is the sandier (**Figure 3.9A**).

Beach orientation varies between the 146° and 247° azimuths and coincides, in general, with the general orientation of the coastal stretch where the beaches are hosted. Exceptions are the cases of Samarra beach, and same beaches located between São Lourenço and Foz do Lizandro, where the most extreme case is the Coxos beach located immediately south of São Lourenço (**Figure 3.9B**).

The most exposed beaches (to the NW dominant wave direction) are located at the coastal stretches with a NE-SW orientation, while the most sheltered beaches are at the stretches with a NW-SE and NNW-SSE orientation (**Figure 3.9C**).

Beach embayment index shows a more irregular distribution along coast. However, it can be noticed that the most embayed beaches occurred preferably on the most crenulated stretches, *i.e.* nearby Roca cape and Paimôgo, and between São Lourenço and Foz do Lizandro. Also worth mentioning the isolated cases of Porto Novo and Samarra beaches (**Figure 3.10A**).

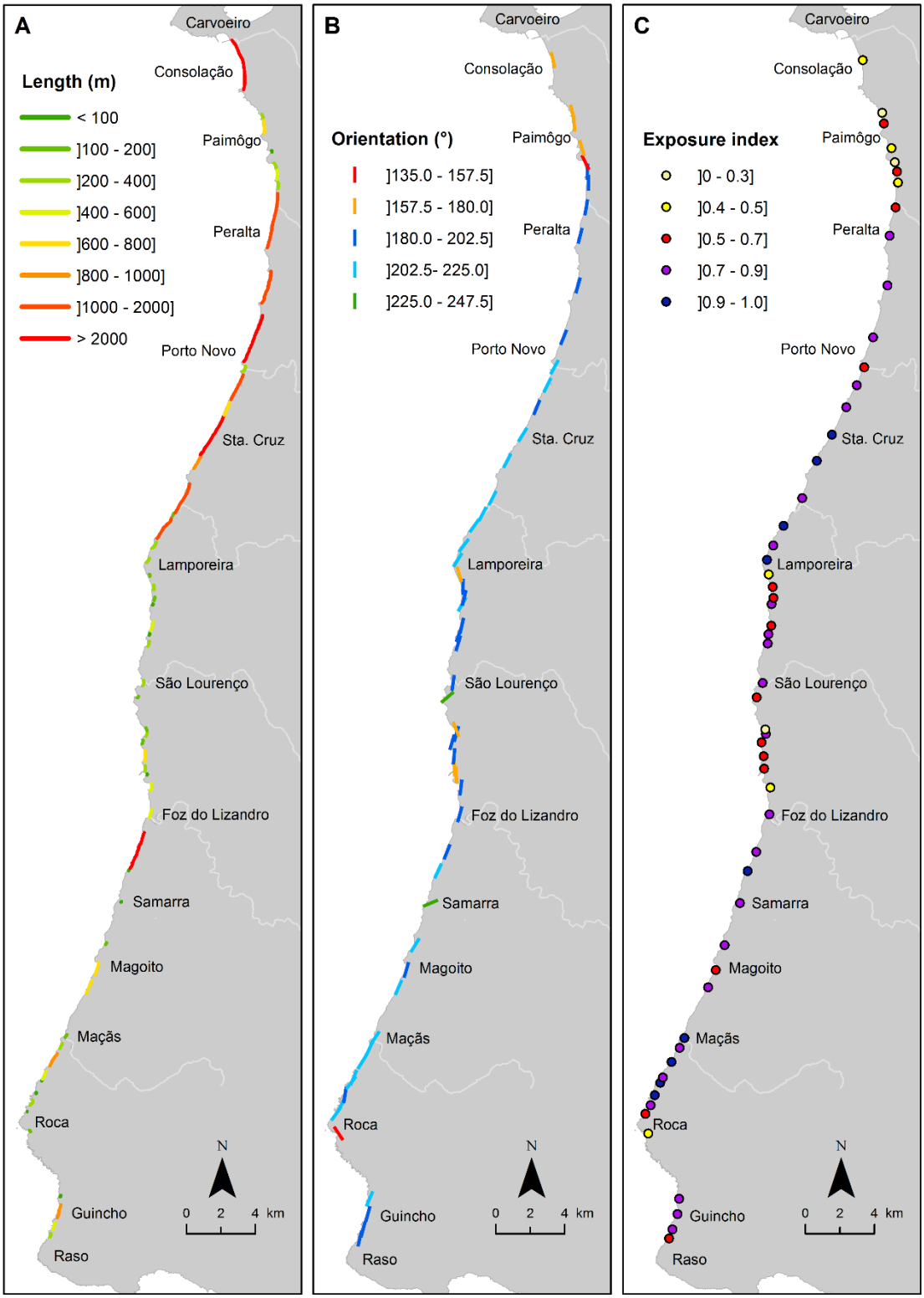

Figure 3.9. Beach length (A), orientation (B) and exposure to the NW dominant waves (C).

The distance between the berm crest and the tip of the headlands is, in general, shorter close to the southern limit. On the other hand, it can be also noticed that larger distances do not always match with higher embayments, see for example Consolação beach and Abano beach

(north of Guincho) that have a similar embayment degree, but significant differences in distance to the tip of the headlands (**Figure 3.10B**).

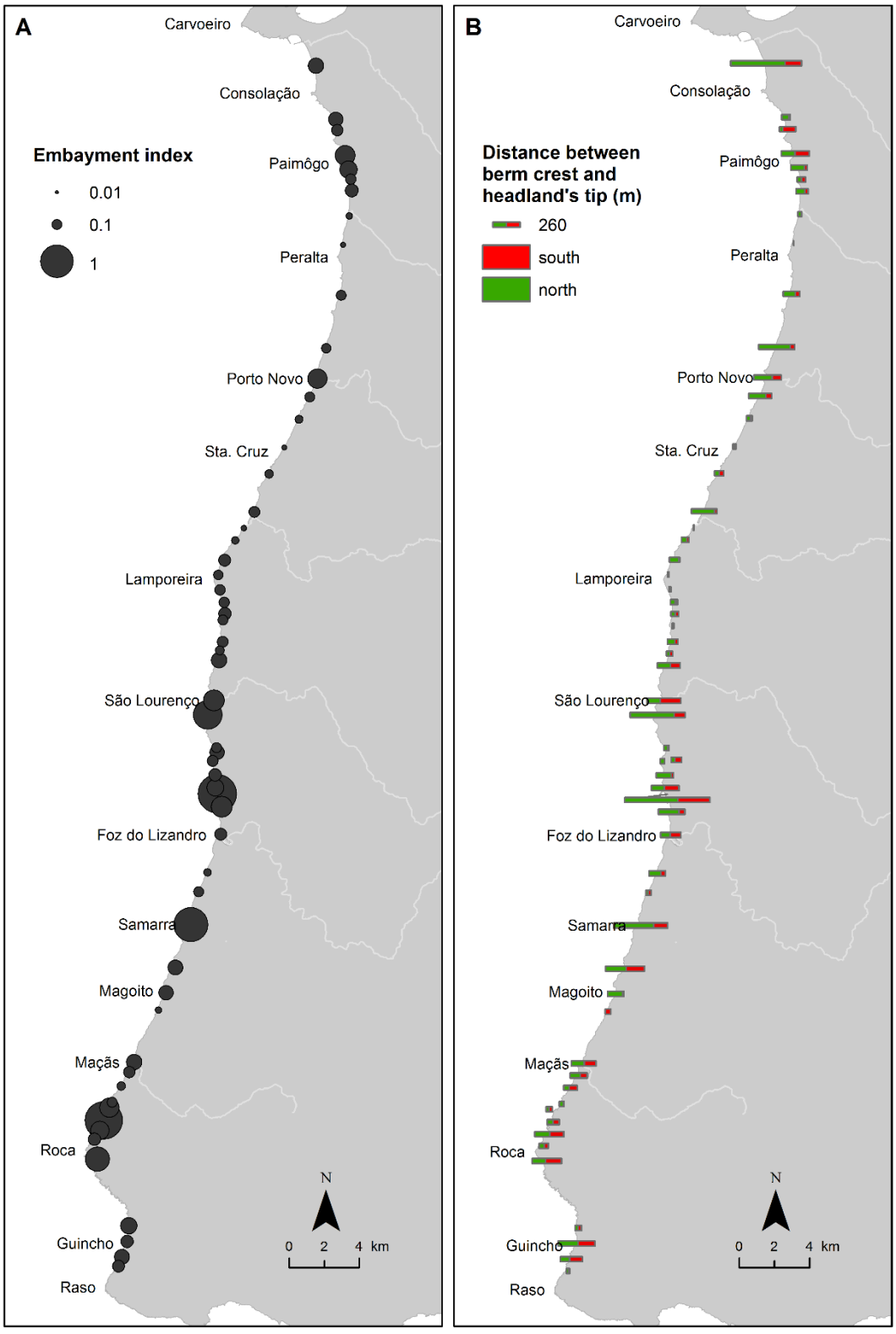

Figure 3.10. Beach embayment degree (A) and distance between the beach berm crest and the tip of the headlands that limit the beach (B).

Considering the beach embayment degree and exposure to the dominant waves, **Figure 3.11A** show that there is no direct relation between them. The beach exposure is related with the beach orientation that as stated before is conditioned by the general orientation of the coast. However, it can be noticed that the two beaches (Samarra and Coxos) presenting ENE-WSW orientations, have a high-degree of embayment (see **Figure 3.3** and **Figure 3.9**).

On the other hand, it can be also noticed that the longest beaches (> 1 km) have NE-SW and NNE-SSW orientations, a low-degree of embayment and a high exposure to the dominant waves (**Figure 3.11B and Figure 3.11C**). Except Consolação beach, located at the north end of the studied site, with a NNW-SSE orientation, a slightly higher embayment degree and a lower exposure. The shorter beaches have variable orientations, embayment degrees and exposures.

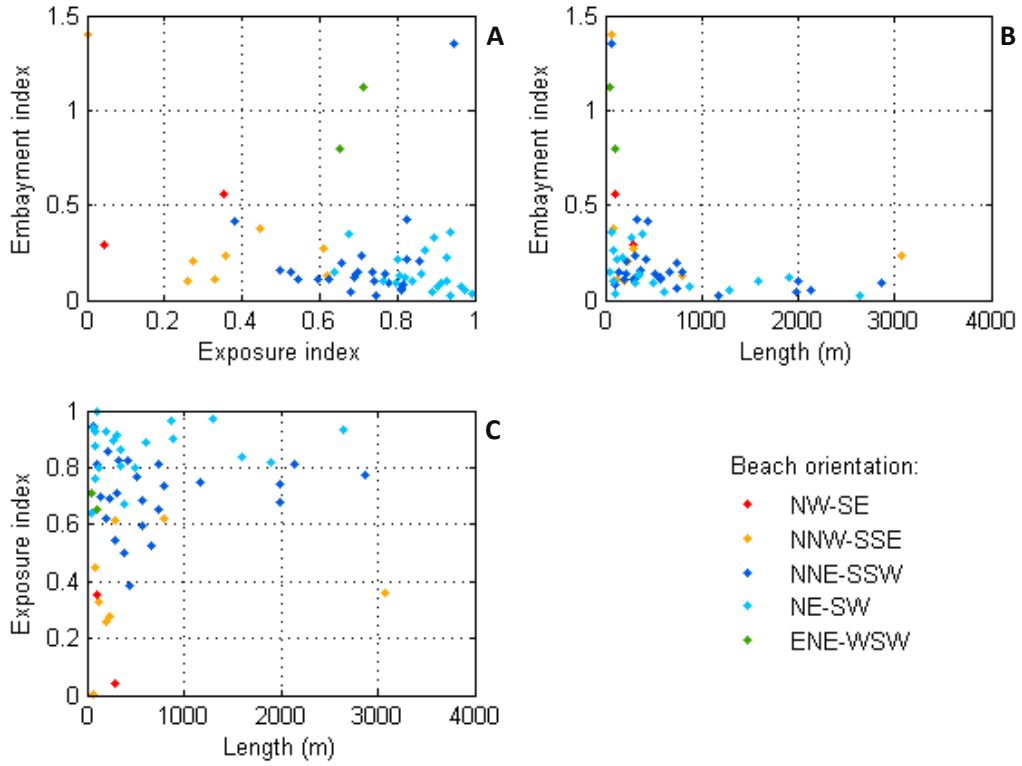

Figure 3.11. Relation between beach planform parameters: (A) embayment versus exposure; (B) embayment versus length; and (C) exposure vesrus length. Dots are projected with different colors representing beach orientation.

3.3.2.2 Planform rotation

The results of beach planform rotation show a coherent signal in time with a range that depends, once again, on the orientation of the stretch where each beach is included. The northern beaches (Consolação to Azul – see location in **Figure 3.3**) have minor variations, while the southern beaches present larger changes, mainly in the cases of Calada, São Lourenço, Foz do

Lizandro and Maçãs beaches (**Figure 3.12**). In general, beaches display a clockwise rotation during summer that is particularly evident in August month, and a counter-clockwise rotation in the winter. The asymmetry of box-plots, indicate that the clockwise rotations are more deviate from the median orientation than the counter-clockwise rotations (**Figure 3.13**).

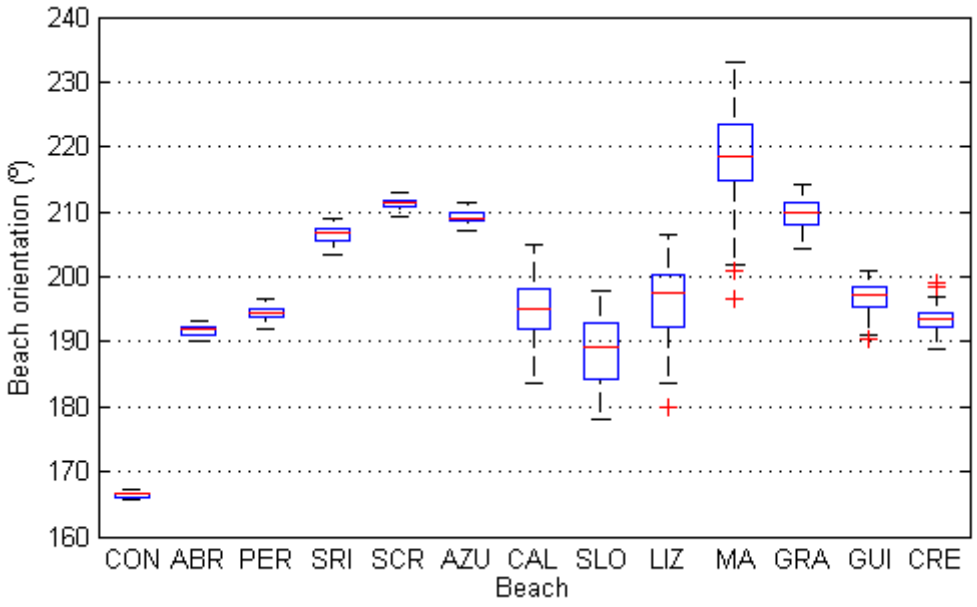

Figure 3.12. Planform rotation of each beach for the period under analysis (April 2013 to December 2015). Boxes limits are the 25th and 75th percentiles, respectively; the mid-range is the median value; and whiskers extremes are 1.5 times the interquartile range.

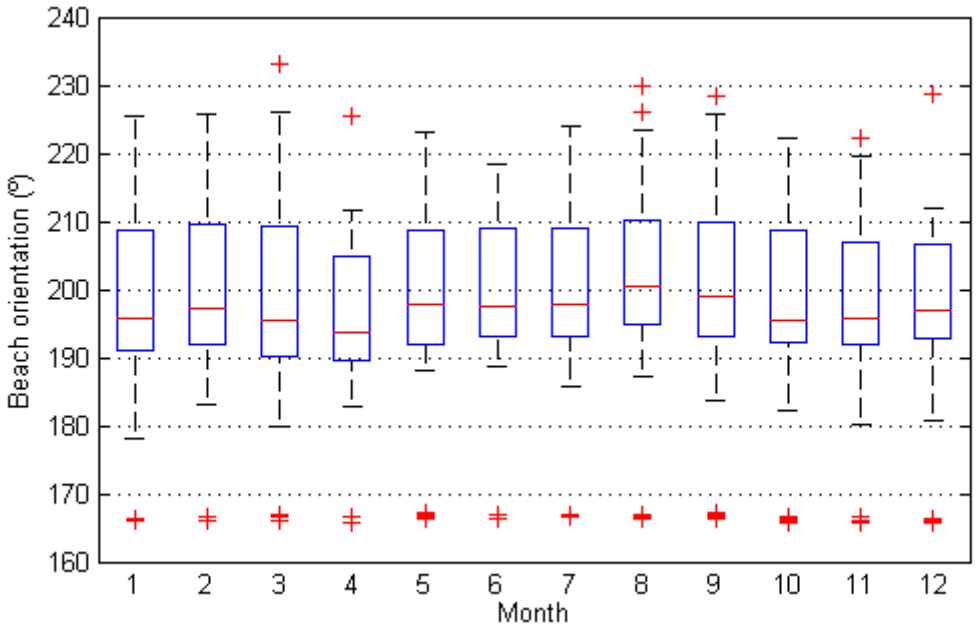

Figure 3.13. Monthly beach planform rotation for the period under analysis (April 2013 to December 2015). Boxes limits are the 25th and 75th percentiles, respectively; the mid-range is the median value; and whiskers extremes are 1.5 times the interquartile range.

The annual analysis show that, in 2014, the range of beach rotation was larger compared to the other years. However, it is important to notice that the smaller range observed in 2013 can be related with inexistence of data for the first trimester of this year (**Figure 3.14**).

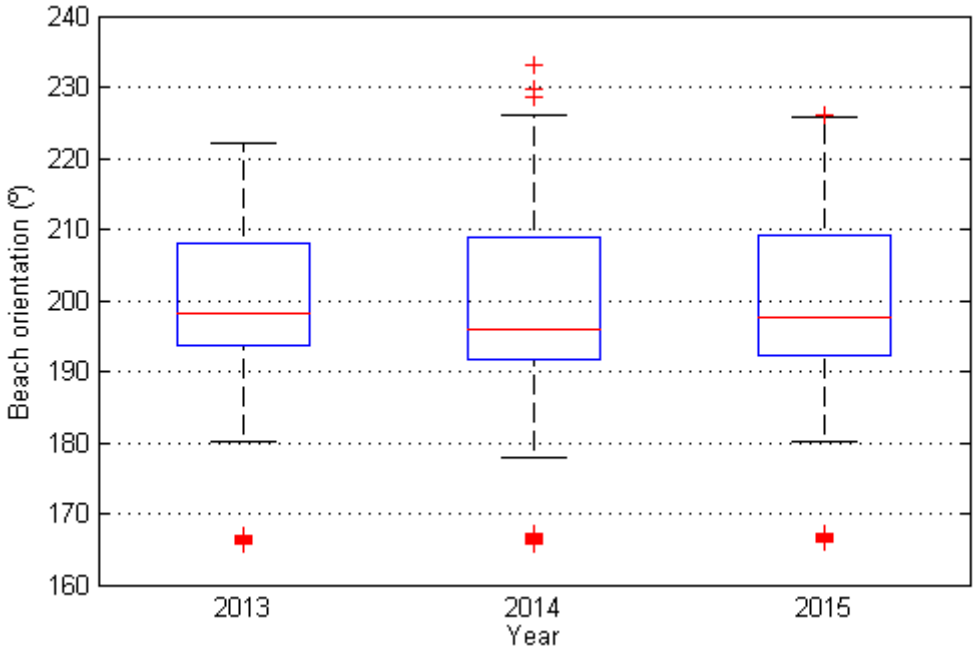

Figure 3.14. Annual beach planform rotation for the period under analysis (April 2013 to December 2015). Boxes limits are the 25th and 75th percentiles, respectively; the mid-range is the median value; and whiskers extremes are 1.5 times the interquartile range.

3.3.3 Beach cross-shore morphology

3.3.3.1 Profile morphology

Cross-shore morphology of the sta. Cruz beach was studied based on three profile: SCR1 at the northern sector, backed by a cliff; SCR2 at the central sector, backed by an artificialized dune; and SCR3 at the southern sector, backed by an artificial structure (**Figure 3.15**). During the monitoring period this beach often presented one or two well-developed berms with a crest elevation between 2.4 and 6 m. The berm was usually wider and higher in the southern sector, except in March/June 2011, when the northern sector presented a particularly well-developed berm. The seasonal variability of the beach is reflected mainly by the berm advance and retreat, although sometimes it was possible to observe a more dissipative morphology. The most notorious case occurred in March 2013, when all the beach profiles had a concave shape, typical of post-storm conditions. However, beach also showed a rapid recovery of its typical morphology in the following months. In April 2014, beach profiles showed again a considerable retreat and the northern and central sectors reached its minima elevation on the upper part.

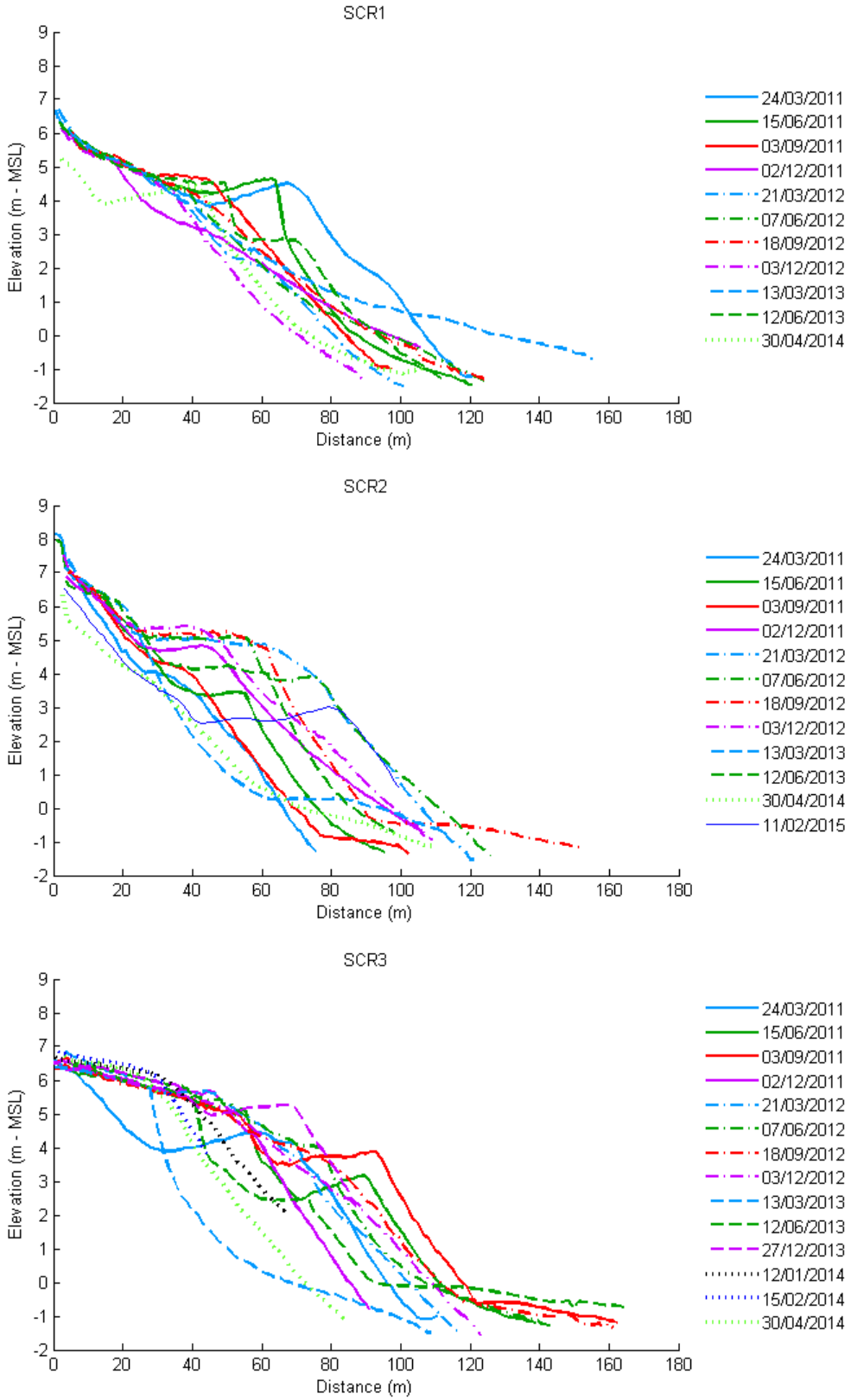

Figure 3.15. Sta. Cruz beach profiles: SCR1 at the northern sector, SCR2 at the central sector and SCR3 at the southern sector.

Coxos beach profile is backed by a cliff and between 2011 and 2013 presented a well-developed berm with a crest elevation between 4 and 5.6 m. During this period, the morphological changes were minor and related with the berm width and elevation. However, in January 2014, the beach profile presented a concave shape, typical of post-storm conditions, with a lowering of the topographic surface of about 3.5 m in the upper part. During the eighteen months afterward, it can be noticed the beach did not recover its previous volume (**Figure 3.16**).

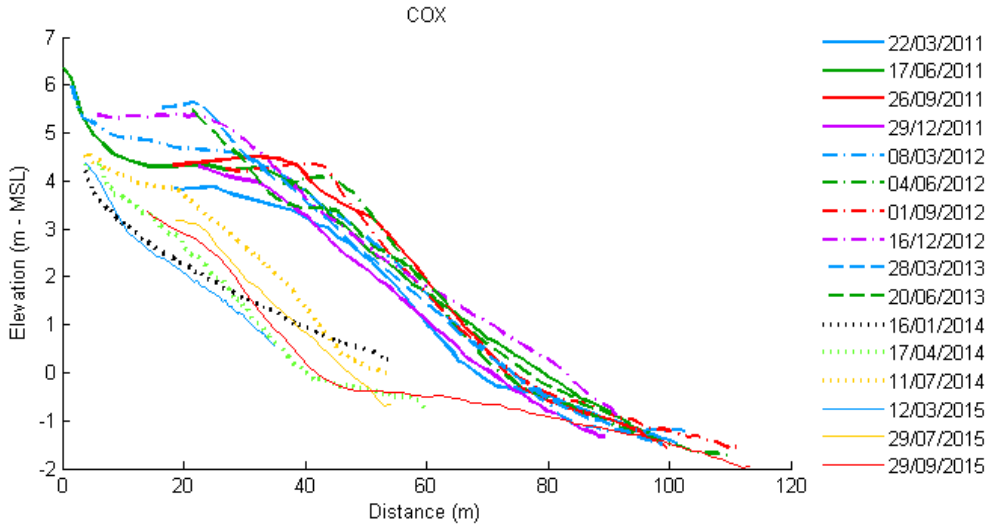

Figure 3.16. Coxos beach profiles.

Baleia beach is backed by an artificial structure in all its extension and showed a very stable behaviour during the monitoring period (**Figure 3.17**). The profiles showed that beach width increases from north (BAL1) to south (BAL2). At the northern sector, the beach was narrower and does not developed a berm, while the central and southern sectors exhibited a summer berm that was eroded in winter. Berm crest elevation reached 5 m, in the central sector, and 4 m, in the southern sector. However, it must be acknowledged that some of the morphological features are artificially reworked. For example, the berm of the central sector is artificially constructed at the beginning of summer season, as observed during the survey of June 2014. Central and southern profiles showed an increasing of the elevation in the spring/summer, while the northern profile slightly grows in the winter, suggesting a beach rotation process. The low-tide terrace of this beach often presented a roughness pattern related with the exposure of a rocky platform located just below mean sea-level.

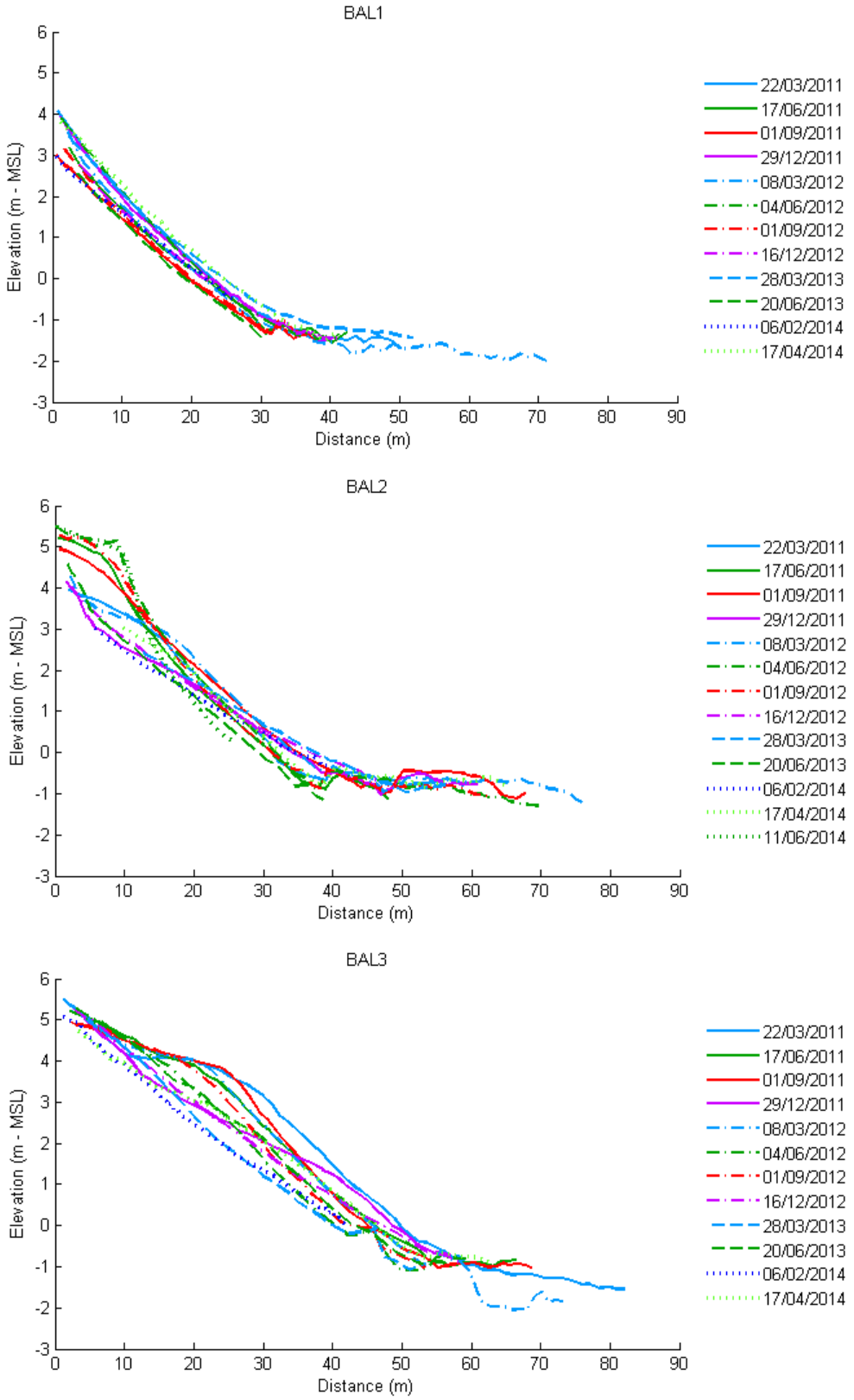

Figure 3.17. Baleia beach profiles: BAL1 at the northern sector, BAL2 at the central sector and BAL3 at the southern sector.

Foz do Lizandro profiles are backed by a dune, which was partially surveyed in the northern sector (LIZ1). This sector showed a lowering of the beach surface of about 2.5 m and a dune retreat of about 20 m, between February and April 2014. Southern profile (LIZ2) also showed lowering of the beach surface elevation of about 3 m, between January and June 2014. However, in June 2014, the northern sector of the beach already showed some recovering. In February 2015, both profiles showed an accretion with the development of two berms, in the northern sector, and one berm, in the southern sector, with elevations between 2.8 and 4.9 m (**Figure 3.18**).

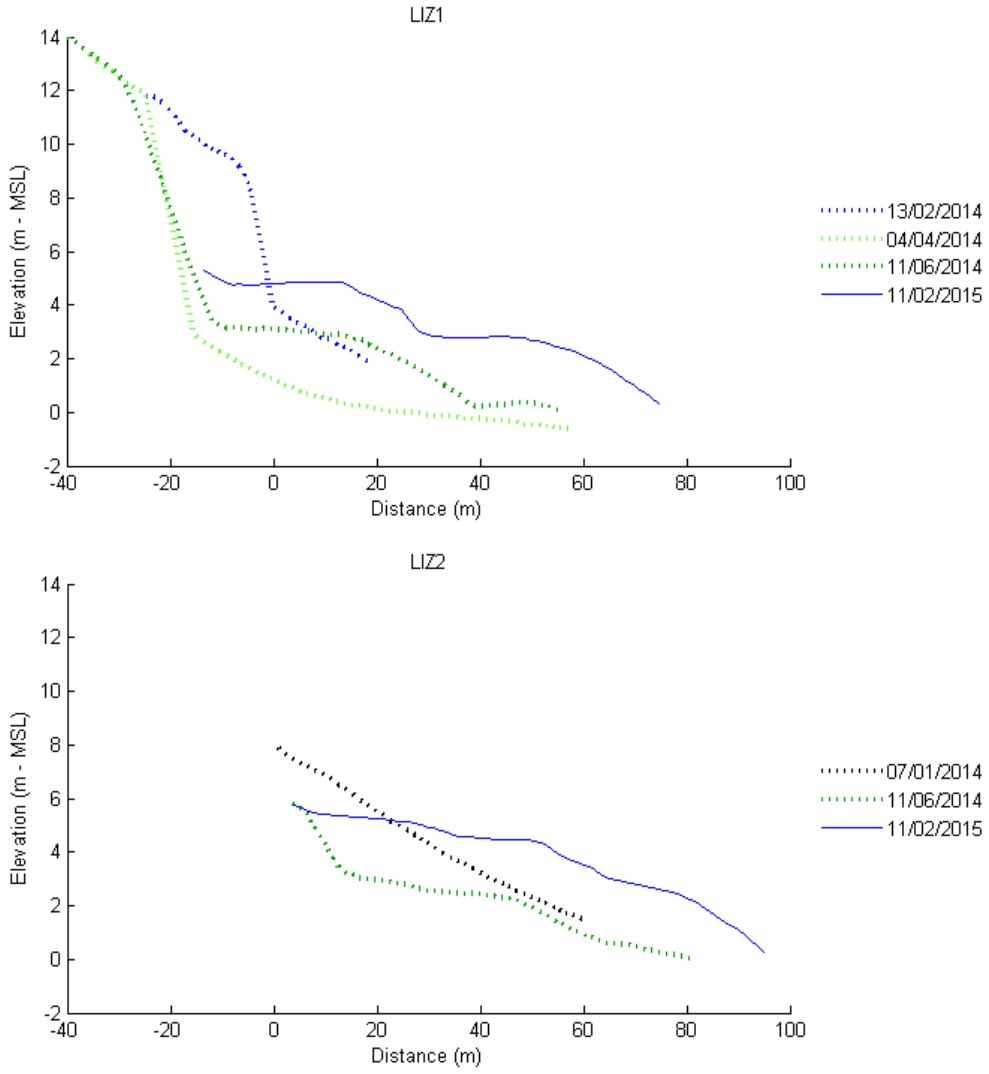

Figure 3.18. Foz do Lizandro beach profiles: LIZ1 at the northern sector and LIZ 2 at the southern sector.

Magoito beach profiles are backed by cliffs and, during the monitoring period, often showed a summer berm (with elevations between 2.3 and 3.5 m) that disappeared in the winter (**Figure 3.19**).

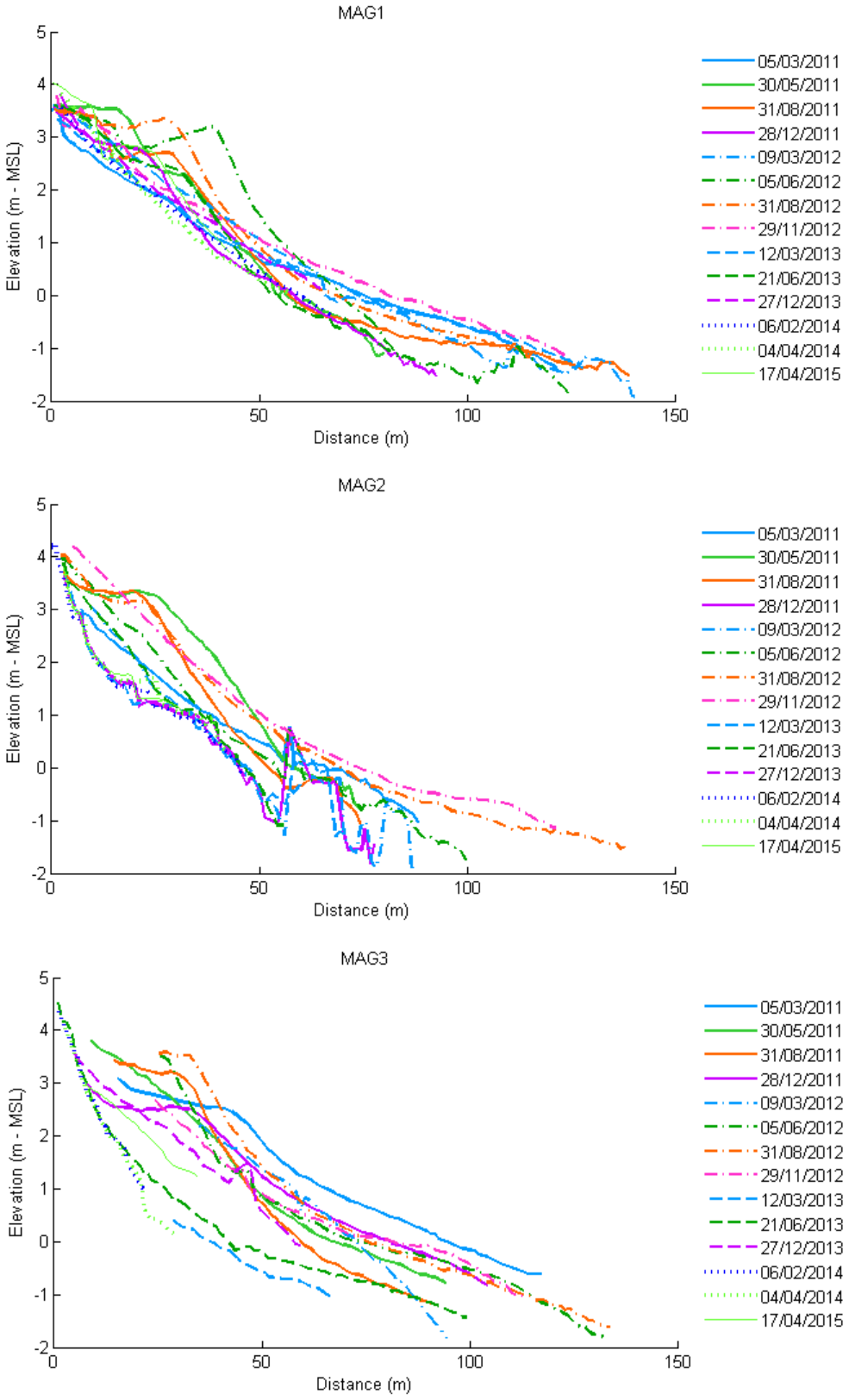

Figure 3.19. Magoito beach profiles: MAG1 at the northern sector, MAG2 at the central sector and MAG3 at the southern sector.

The high roughness observed in some profiles of Magoito beach was related with exposure of the rocky shore platform. Until March 2013, in the central sector (MAG2), the platform exposure only occurred in winter months. However, from this date onwards the rocky platform have been exposed or covered with a thin sandy layer on the upper part without berm development. In the southern sector (MAG3), it was also observed considerably retreat of the beach in March 2013. Despite the recovery observed by the end of the year, in January 2014 beach retreated again (**Figure 3.19**).

Maçãs beach is backed by a dune that was surveyed during field campaigns. In October 2012, the beach profile presented a wide berm (≈100 m) with a crest elevation of 4.5 m. At the beginning of 2014, a considerable beach retreat was observed with the berm obliteration, while dune showed a sand gain. In June 2014, dune presented a sand loss that according to the field observation, resulted from the artificial removal to nourish the upper beach. During the year of 2015, the beach gradually recovered and, in September 2015, a well-developed berm with a crest elevation of 4 m was observed. However, the beach volume observed in 2012 was not yet reached (**Figure 3.20**).

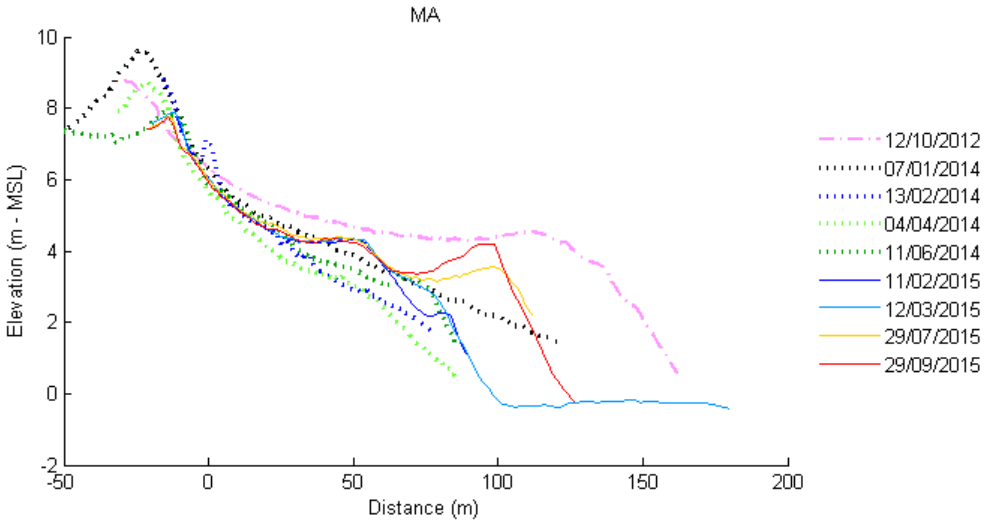

Figure 3.20. Maçãs beach profiles.

Grande beach is backed by an artificial structure at the northern (GRA1) and central (GRA2) sectors, and by a cliff, at the southern sector (GRA3). This beach show an overall accretionary trend between February 2014 and September 2015. In the summer period, presented a well-developed berm with elevations between 2 and 4.4 m; while in the winter, the berm was obliterated and the subaerial beach was represented by a flat beach face. The beach profiles acquired in September 2014 showed that the north and south sections of the beach

experimented an opposite behaviour (accretion of the northern sector and erosion of the central and southern sectors) related with the beach planform rotation process (**Figure 3.21**).

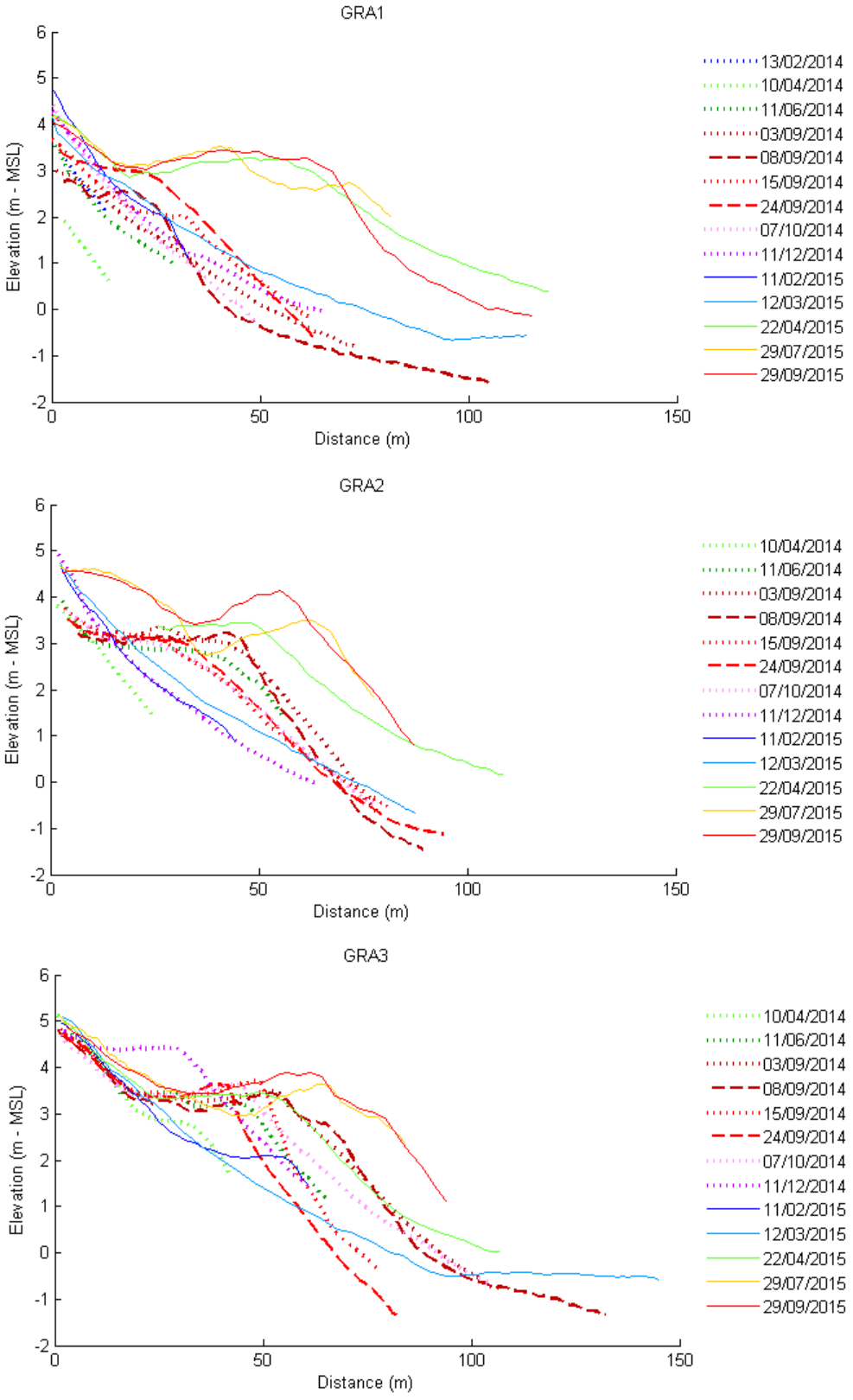

Figure 3.21. Grande beach profiles: GRA1 at the northern sector, GRA2 at the central sector and GRA3 at the southern sector.

Adraga beach profile, located in a stream mouth, showed an accretive trend during the monitoring period, presenting in all dates a well-developed berm with elevations ranging from 2.3 to 4.4 m (**Figure 3.22**).

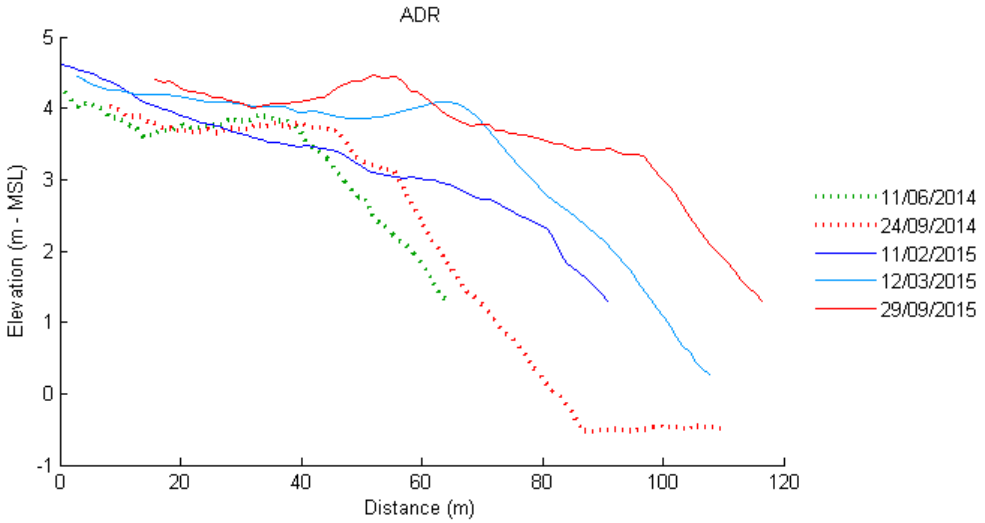

Figure 3.22. Adraga beach profiles.

Guincho beach is backed by dunes. In December 2009, this beach presented a typical winter morphology without berms. Three months later, the northern sector (GUI1) showed the same morphology, while the southern sector (GUI2) had experiment a significant erosion. In July 2014, beach presented a well-developed berm with an elevation of 2.7 m, in the northern sector, and 3.5 m, in the southern sector. However, beach surface was, in general, lower than the one observed four years before. In November 2015, beach showed an accretion with berm advance, in the northern sector, and the increase of the berm elevation and the development of a second berm, in the southern sector (**Figure 3.23**).

Figure 3.24 show the topographic profiles of several beaches: Azul (AZU), backed by dunes; Baío (BAI) and Pequena (PEQ), backed by cliffs; and São Lourenço (SLO) and Algodio (ALG), backed by artificial structures. The data acquired in February 2015 showed that São Lourenço and Agodio presented berms with crest elevations of 6 and 3.5 m, respectively; while Baío, Azul and Pequena beaches had flat shapes. The comparison of the topographic surveys performed in the summer of 2014 and winter of 2015, showed minor variations at São Lourenço beach, related with a slight erosion of the beach face and accretion of the berm. In the case of Pequena, beach surface presented higher elevations in the winter than in the summer.

The general aspect of the beaches, as well as some of the morphological aspect described above, can be seen through the beach photo-monitoring program (see Appendix A).

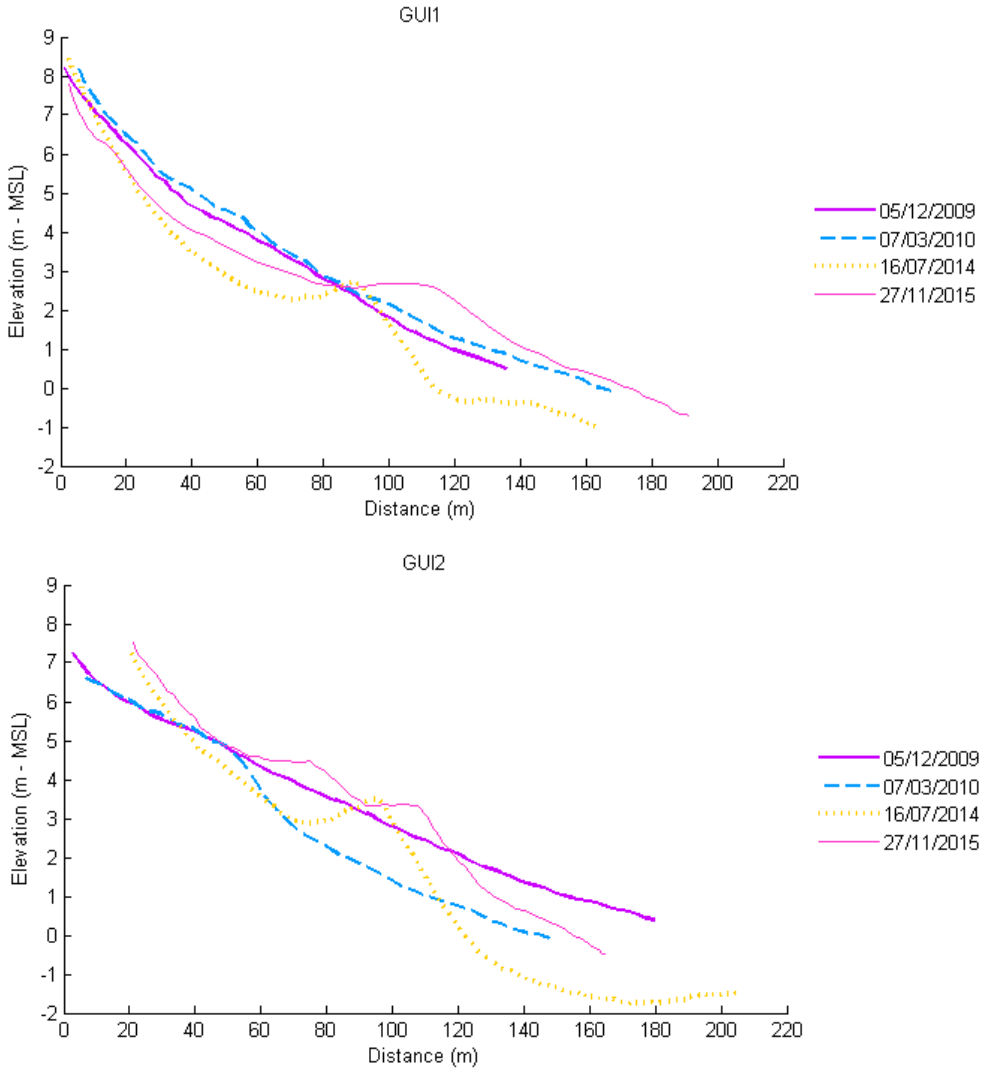

Figure 3.23. Guincho beach profiles: GUI1 at the northern sector and GUI2 at the southern sector.

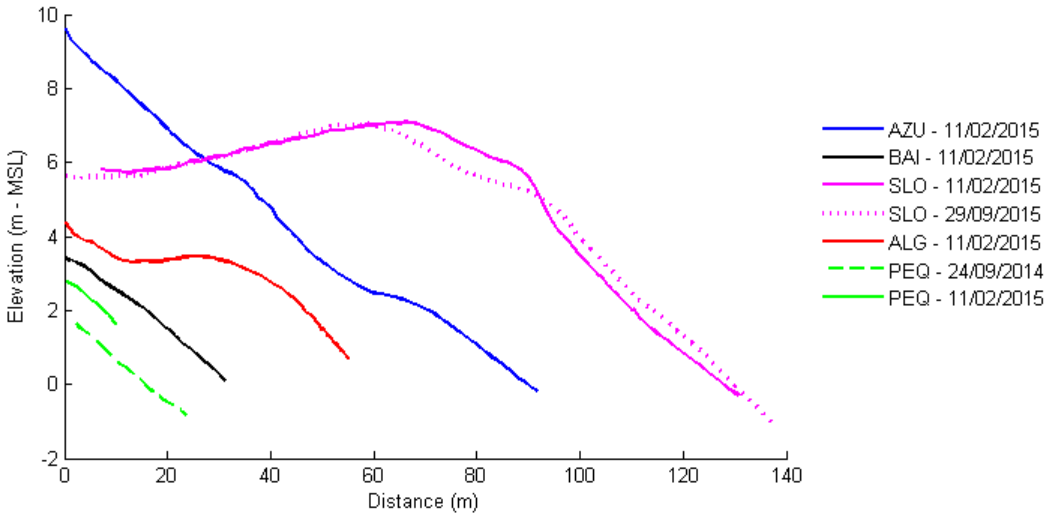

Figure 3.24. Azul (AZU), Baío (BAI), São Lourenço (SLO), Algodio (ALG) and Pequena (PEQ) beach profiles.

3.3.3.2 Beach face slope and berm crest elevation

Mean beach face slope and maximum berm crest elevation observed in each beach were compared in **Figure 3.25**. In the case of the beaches where more than one profiles were monitored, average values are assumed. Beach face slope ranges between 4° and 9°, being possible to noticed that beaches located north of Foz do Lizandro (LIZ) tend to have higher slopes, indicating that these are more reflective than the southern ones (**Figure 3.25A**). Berm crest elevation ranges between 3.6 m and 6 m relative to the MSL. The higher berm elevation correspond to the high-indented beaches of São Lourenço (SLO) and Coxos (COX), but any trend alongshore can be noticed (**Figure 3.25B**).

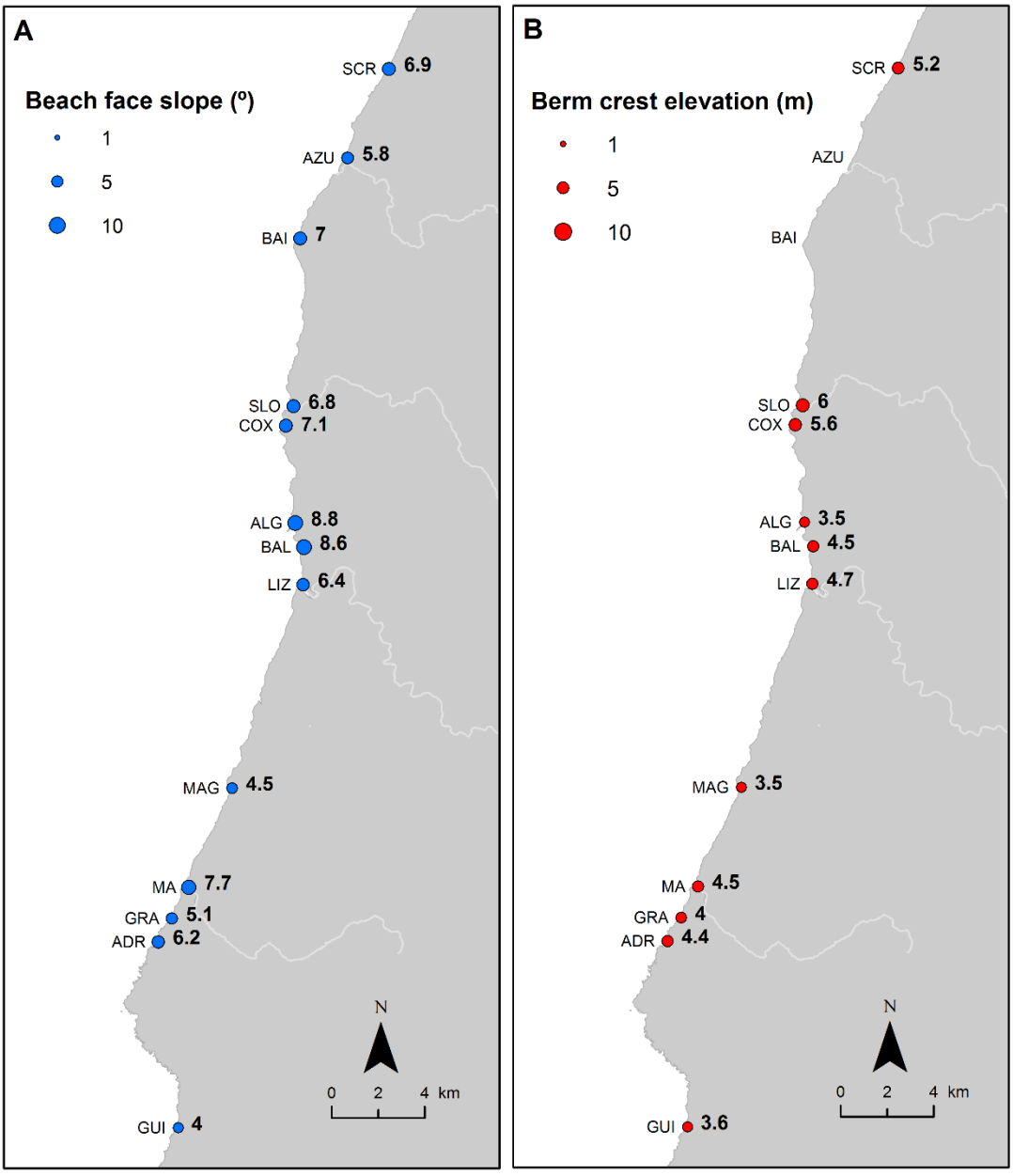

Figure 3.25. (A) Mean beach face slope (tan β) and (B) maximum berm crest elevation relative to MSL.

3.4 DISCUSSION AND CONCLUSIONS

The analysis of beach planform show that the longest and most exposed beaches are, in general, in the stretches with a NE-SW general orientation, being the sector between Paimôgo and Lamporeira the sandier. On the other hand, in the stretches with N-S and NW-SE general orientation, beaches tend to be shorter and less exposed to the dominant waves. Consolação beach is the exception to this trend, due to the sheltering effect of Peniche peninsula; it is the longest beach of the studied coast and is located in a NW-SE oriented stretch (**Figure 3.9** and **Figure 3.11**).

Beach orientation is, in general, similar to the general orientation of the coastal sectors where they are included. The most notorious exceptions are Samarra and Coxos beaches, which have an ENE-WSW orientation and a high-degree of embayment related with the local geomorphology. Both beaches developed on narrow indentations with an alignment NNW-SSE and NW-SE, respectively (**Figure 3.26**).

Beach embayment degree is conditioned by coastal geomorphology and do not have a direct relation with the others planform parameters (**Figure 3.11**).

Figure 3.26. Plainview of (A) Coxos beach and (B) Samarra beach (ortophotomaps of 2012 provided by *Direcção-Geral do Território* - DGT).

Planform rotation analysis show that beaches displays, in general, a clockwise rotation during summer (**Figure 3.13**), which can be related to the NW (less energetic) incident wave conditions. The persistence of these conditions induces an enlargement of the beach downdrift (southward) (**Figure 3.27**). This process can result in HSB through a continuous inner sandbar along the headland coast, which migrates downdrift in the surf zone and weld to the downdrift beach, as it can be seen in the example of the **Figure 3.28A**. In the winter, a counter-clockwise rotation is observed (**Figure 3.28B**). However, considering the wider distances observed between the beach berm and the northern headlands compared to the southern ones (**Figure 3.10**), and the less persistent W and SW incident wave conditions, HSB related with the beach rotation during winter, seems more unlikely.

Figure 3.27. Aspect of the Grande beach: (A) on 10th April 2014 (tidal level = 0.56 m MSL) and (B) on 31st August 2014 (tidal level = -0.66 m MSL). Tide levels were computed based on Cascais tide gauge data using the UTIDE model (Codiga, 2011).

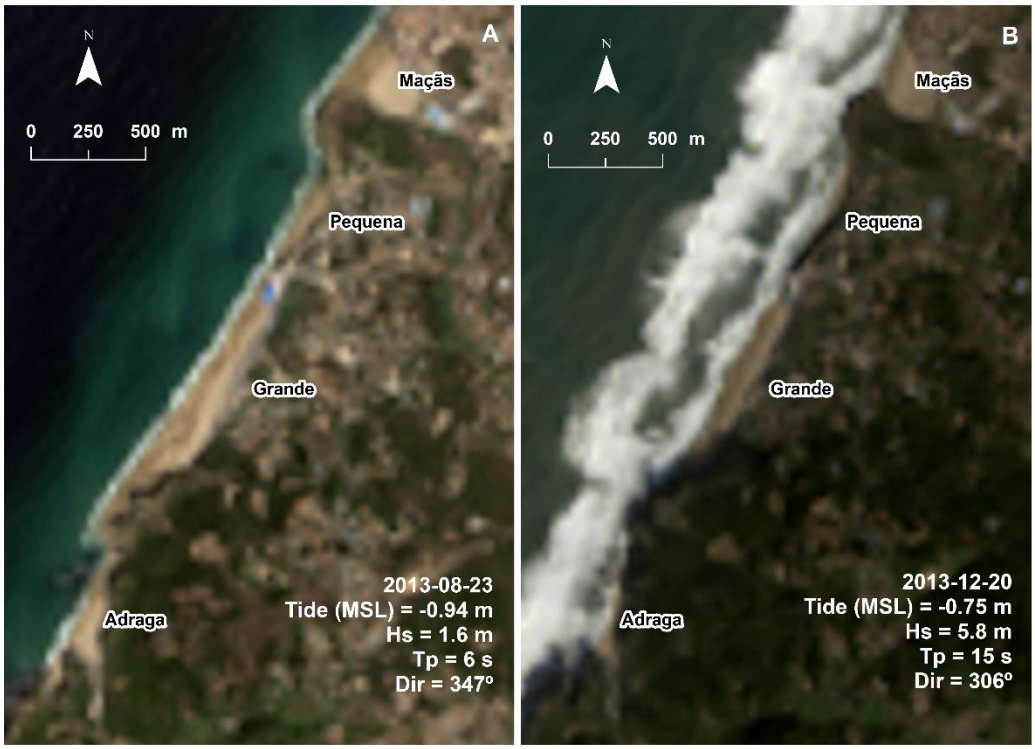

Figure 3.28. Aspect of the coastal strechet between Maçãs and Adraga beaches: (A) on August 23rd and (B) on December 20th 2013 (Landsat 8 images provided by NASA and USGS). Tide levels for the time of the image acquisition were computed based of Cascais tide gauge data using the UTIDE model (Codiga, 2011). The mean offshore wave conditions (Hs, Tp and Dir) for the 12 hours before the image acquisition, were obtained from the wave time-series numerically modeled, provided by Professor Xavier Bertin, University of *La Rochelle*.

Analysis of beach planform rotation also indicate that the beaches located north of Lamporeira headland have minor variations, while the southern beaches present larger rotations (**Figure 3.12**). However, in the case of Maçãs beach, the rotation seems abnormally high, being probably amplified by the influence of the Colares fluvial stream mouth on the shoreline orientation of this short beach.

Beach rotation increases with the decrease of the beach length (**Figure 3.29**), but is poor related with beach embayment (**Figure 3.30**) or exposure to the dominant waves (**Figure 3.31**). Thus, the differences between the beaches located north and south of Lamporeira headland, can only be explained by a faster response of the shorter beaches to the incident wave conditions compare to the longer ones. Despite the poor correlation between beach rotation and embayment degree, **Figure 3.11** shows that longer beaches (>1 km), have low-degree of embayment, being the case of all beaches located north of Lamporeira for which planform rotation was studied. The low-degree of embayment of these beaches can justify their small rotation given that retention capacity of the headlands is smaller. Under these conditions, the

active beach profile can easily reach the tip of headland, ceasing beach rotation due to the sediment bypass.

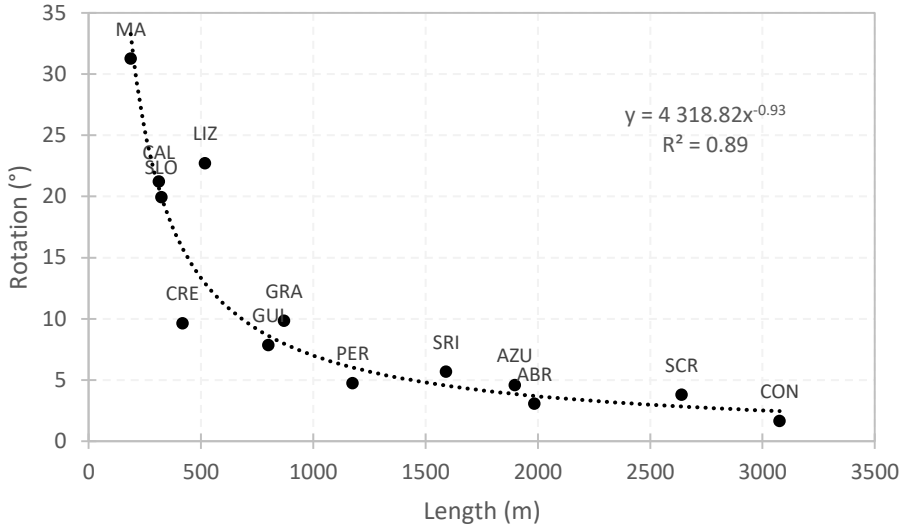

Figure 3.29. Relation between beach rotation (computed using the 25th and 75th percentiles values of beach orientation obtained from Landsat images) and beach length.

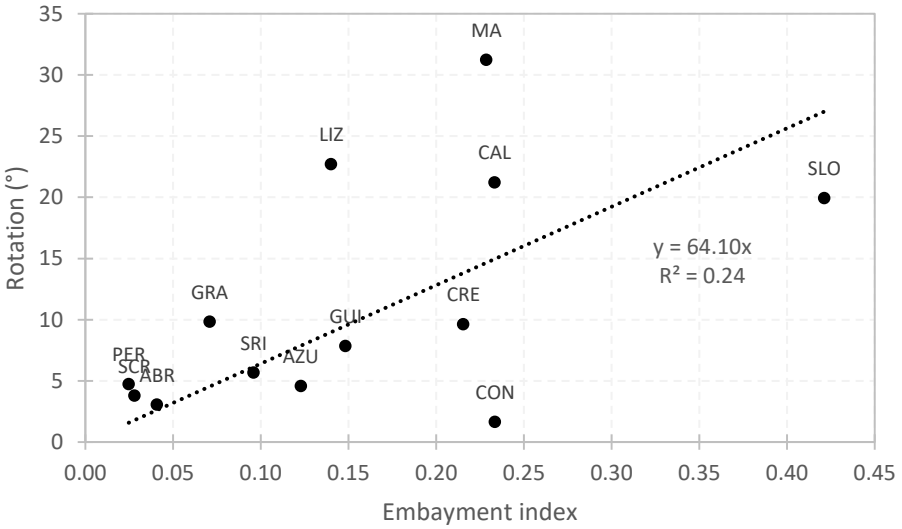

Figure 3.30. Relation between beach rotation (computed using the 25th and 75th percentiles values of beach orientation obtained from Landsat images) and beach embayment.

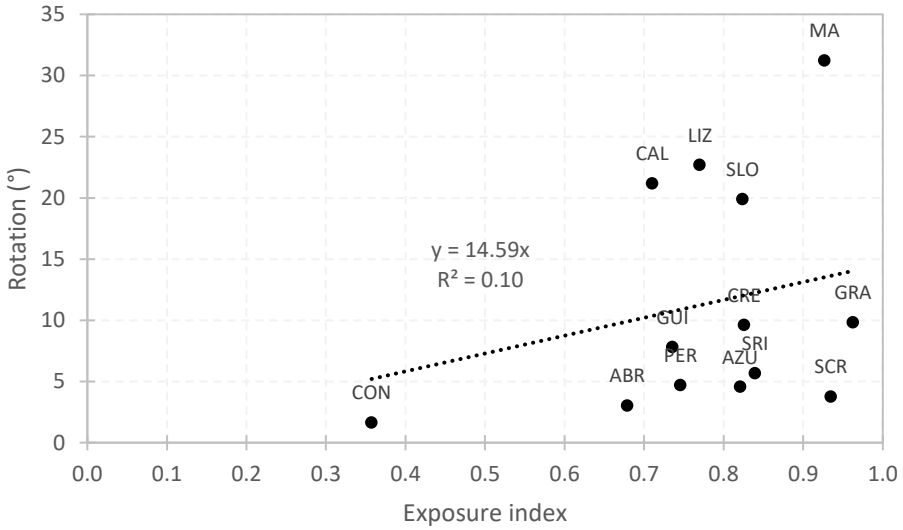

Figure 3.31. Relation between beach rotation (computed using the 25th and 75th percentiles values of beach orientation obtained from Landsat images) and beach exposure to the dominant waves.

The result of cross-shore morphological analysis show that beaches such as Baleia, Magoito and Grande, change between a convex shape, in the summer, due to a berm formation, and a concave shape, in the winter, when the berm is obliterated. Sta. Cruz, Coxos, Maçãs and Adraga beaches, on the other hand, usually present convex shapes and the seasonal changes are more related with the berm elevation and width. In latter cases, the concave shape are less frequent and seems to be related with winter storm events.

The variations of the beach face slope alongshore indicate that beaches located north of Foz do Lizandro, are more reflective than the southern ones. This could be an effect of the beach sediment grain-size, which tend to be coarse in the northern beaches (as shown in the Chapter 4), being in agreement with previous works (*e.g.* Bascom, 1951).

The monitoring of the beach profiles showed, in general, higher beach retreats during the year of 2013 and 2014. In fact, these two years were particularity energetic, presenting the higher frequencies of higher waves for the period under analysis (**Figure 3.7**). The most energetic events recorded during these years are related with the *Gong* storm occurred at January 19th 2013 (see Liberato, 2014) and *Christina* storm occurred at January 6th 2014 (see Diogo *et al.*, 2014). According to the offshore wave data the average Hs, Tp and Dir for these events were 8 m, 13 s and 295°, in the case of *Gong* storm, and 7 m, 19 s, 297°, in the case of *Christina* storm.

The morphological changes observed on beaches showed a variable response to these events. The *Gong* storm, in 2013, had strong impact on Sta. Cruz and Magoito beaches (**Figure 3.15** and **Figure 3.19**) and minor impact on the Baleia (**Figure 3.17**), while Coxos beach do not showed

significant changes, probably due to its higher degree of embayment (**Figure 3.16**). However, in the case of the *Christina* storm, in 2014, the impacts are visible in all beaches, including Coxos beach. The main difference between these two storms is the wave period, which was quite longer in case of *Christina* storm. This storm triggered the Foz do Lizandro dune retreat (**Figure 3.18**) and the lowering of topographic surface at the Coxos, Maçãs and Grande beaches (**Figure 3.16**, **Figure 3.20**, **Figure 3.21**). The impacts of this storm in these and other beaches are also reported by Diogo *et al.* (2014), Carapuço *et al.* (2014) and Bastos *et al.* (2015).

The morphological changes observed at Coxos beach, showed that on high-incised beaches, sediment can leave the embayment during particular extreme meteorological events. Under these conditions, waves induce strong erosion on the subaerial beach and a large volume of sediment is transported outside the embayment and, eventually, bypass the headlands.

The data obtained after storms showed a gradual recovery of the beaches with the increasing of the beach surface elevation or/and the berm advance. However, Coxos beach recovery seems to be slower when compare to the other beaches.

Table 3.2 shows the comparison between sand volumes estimated for Coxos and Maçãs beaches based on their beach profiles (above a common minimum elevation between surveys), before and after the storm events of 2014; and assuming that volume of the Maçãs beach, before the storms of 2014, was not significantly different to the one measure in 2012. Maçãs beach lost about 62 % of the initial sand volume, while Coxos lost about 78 %.

Table 3.2. Beach profile volume of Coxos and Maçãs beaches, before and after *Christina* storm in January 2014.

Beach	**Coxos**		**Macãs**	
Profile volume ($m^2.m^{-1}$) above 0.67 m (MSL)	2012-12-16	189	2012-10-12	690
	2014-04-17	37	2014-04-04	264
	2015-09-29	45	2015-09-29	464
Beach length (m)	112		187	
Beach volume pre-storm (m^3)	22×10^3		129×10^3	
Sand loss (Apr 2014)	78 %		62 %	
Sand gain (Sep 2015)	4 %		29 %	

The sand gain estimated for a period of approximately one year and a half shows a faster recovery at Maçãs (29 % of the initial volume). Although the Maçãs beach has been nourished with sand removed from the dune, as already mentioned, the beach profiles showed that larger part of sand volume was recovered through a natural process (**Figure 3.20**). The fast recovery of this beach can be then explained by its lower embayment, which allowed the capture of the sand bypassing near the shore, as explained previously (**Figure 3.28A**). On the contrary, the higher indentation of the Coxos beach is not favourable to this HSB process. In this case, the beach is feed by the sediment transport shoreward during low-energy wave conditions, which should have a low magnitude considering the rocky nature of adjacent inner shelf (see Chapter 2) and, justifies its slower recovering.

Chapter 4

Beach Sedimentology

4.1 INTRODUCTION

Sediment particles properties such as grain-size, shape and composition provide valuable information about sediment sources, transport processes and pathways. Clemens and Komar (1988), for example, used the heavy mineral content and the degree of grain rounding of sands to identify sediment sources, trace transport paths and to obtain additional information concerning the history of the sediment particles on the Oregon headland-bay coast (USA); Ferrari *et al.* (2014) used grain-size, composition and shape of sedimentary particles to trace sediment bypass between two adjacent gravel pocket beaches of the Ligurian Sea (Italy); and Cascalho *et al.* (2014) identified a sediment sorting during subaerial bypass at Nazaré headland (Portugal), based on the sediment grain-size.

Following these works, beach sediment grain-size and composition were used to get further insights on sediment sources and distribution processes in order to understand the headland sediment bypassing (HSB) processes. However, considering the large extension of the studied coast (about 100 km), the sediment sampling was focus in a shorter stretch, located between Sta. Cruz (Torres Vedras) and Guincho (Cascais) (**Figure 4.1**). The results obtained were discuss considering the sedimentological information of the previous works, which are listed in the **Table 4.1**.

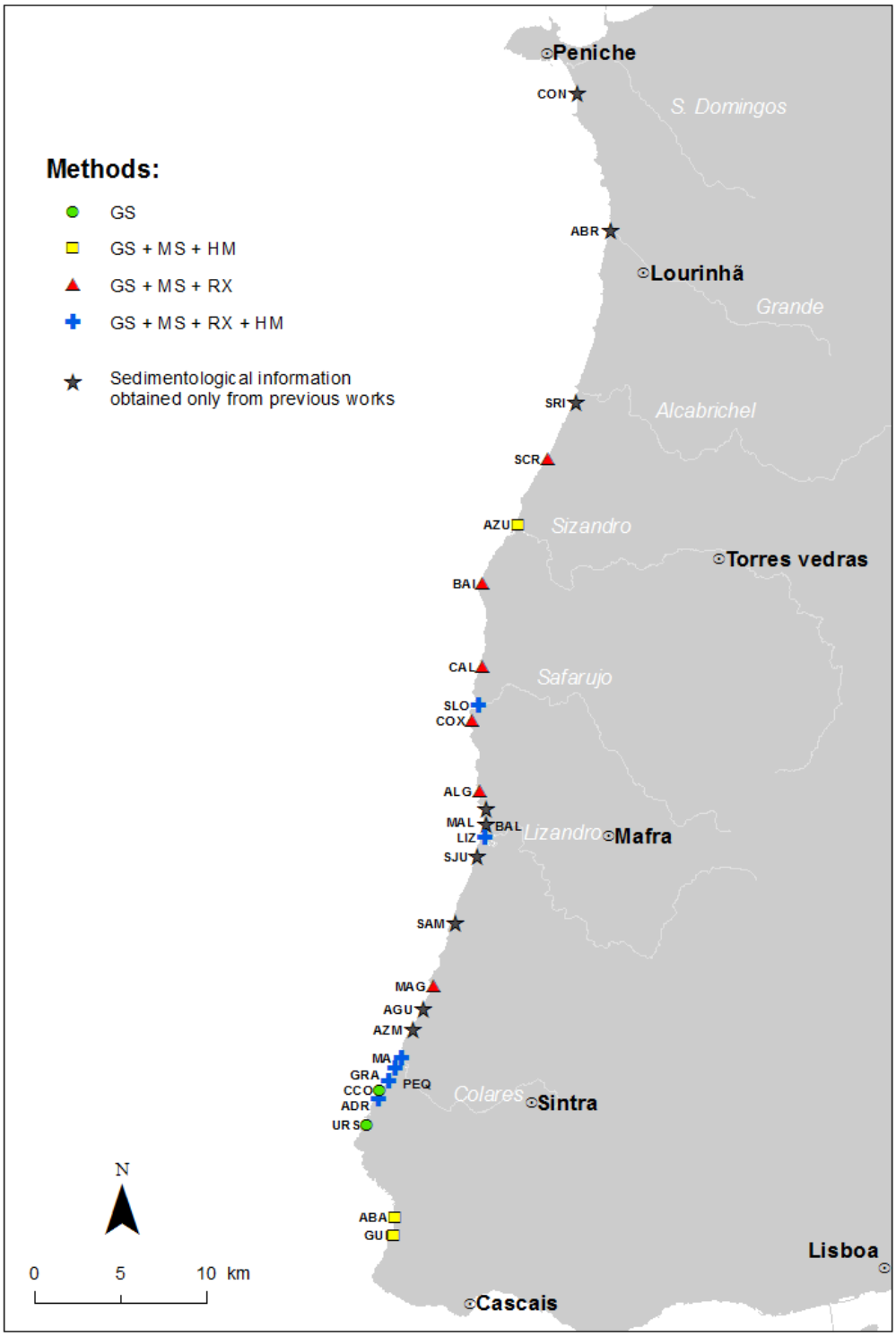

Figure 4.1. Geographic location of the beaches under analysis and the beaches studied under the scope of the previous works: Consolação (CON); Areia Branca (ABR); Sta. Rita (SRI); Sta.Cruz (SCR); Azul (AZU); Baío (BAI); Porto da Calada (CAL); São Lourenço (SLO); Coxos (COX); Algodio (ALG); Baleia (BAL); Malhadinha (MAL); Foz do Lizandro (LIZ); São Julião (SJU); Samarra (SAM); Magoito (MAG); Aguda (AGU); Azenhas do Mar (AZM); Maçãs (MA); Pequena (PEQ); Grande (GRA); Adraga (ADR); Abano (ABA); Guincho (GUI). Sediments were analyzed using several methods: grain-size analysis (GS); magnetic susceptibility (MS); heavy minerals analysis (HM); and X-ray diffractometry analysis (RX).

Table 4.1. Beach sedimentological information found in literature.

Reference	Beach acronym*[1]	Monitoring period	Sampling	Analysis
Trindade and Ramos-Pereira (2009)	SRC; SRI; AZU; LIZ	December 2005 to November 2006 (fortnightly)	Superficial sediment of the berm, beach face and low-tide terrace	Grain-size
Oliveira (2009)	SJU; SAM; MAG; AGU; AZM; MA; PEQ; GRA; ADR; URS	Not reported	Sediment of the beach face	Grain-size
Gusmão (2010)	MAL	January, February, March and June of 2009.	Sediment of the berm and beach face	Grain-size
Pires and Ribeiro (2010)	GUI	December of 2009	Superficial sediment of the berm and beach face	Grain-size
Balsinha *et al.* (2010)*[2]	CON; ABR; SCR; CAL; SJU	Not reported	Beach face sediment	Grain-size and composition
Silveira *et al.* (2013)	SCR; COX; BAL; MAG	March 2011 to June 2013 (quarterly)	Superficial sediment of the berm and beach face	Grain-size
Janardo (2016)	CON	Not reported	Not reported	Grain-size

*[1] Beaches names are presented in the legend of **Figure 4.1**.

*[2] Location and mean grain-size of the sediment samples were kindly provided by the authors.

4.2 METHODS

4.2.1 Field campaigns and data acquisition

Sediment sampling was carried out during several field campaigns that are summarized in **Table 4.2**. Most sediment samples correspond to the first centimetres of the surficial layer, however, superficial sediments correspond to the sedimentary particles that are in equilibrium with the effective wave conditions and might not be representative of the entire beach system. Thus, a sampling procedure that following the recommendations of the Beach Sand Code Project (2012) technical note, was also used in order to characterize the beach sediment average characteristics (composite sediment samples). These samples were collected at the beach face, using a PVC tube with 4.5 cm of diameter and 50 cm of length (**Figure 4.2A** and **Figure 4.2B**). The only exception was the sediment sampled at Grande beach on February 2014, which was manually collected and corresponds to the 32 cm of thickness of the heavy mineral deposit observed (**Figure 4.2C**).

Table 4.2. Sediment sampling campaigns.

Date	Beach	Beach profile zone	Sampling method	Nº of samples	Observations
2013-04-12	BAI; CAL	Beach face	Superficial layer	2	-
2014-02-13	GRA	Beach face	Composite	1	After storm events
2014-06-11	LIZ; MA; GRA; ADR; URS	Beach face	Superficial layer	5	-
2014-07-09	GUI	Beach face	Superficial layer	1	-
2014-09-08	GRA; CCO; ADR	Beach face and low-tide terrace	Superficial layer	6	Collected during a fluorescent tracer experiment (see Chapter 5)
2014-09-24	PEQ; GRA; ADR	Beach face and low-tide terrace	Superficial layer	9	-
2015-02-11	SCR; AZU; BAI; CAL; SLO; COX; ALG; LIZ; MAG; MA; PEQ; GRA; ADR	Beach face	Composite	13	-
2015-09-29	COX	Beach face, low-tide terrace and submarine beach	Superficial layer	3	Submarine sample was collected in alignment with the tip of the downdrift (southern) headland
2015-11-27	ABA; GUI	Beach face	Composite	2	-

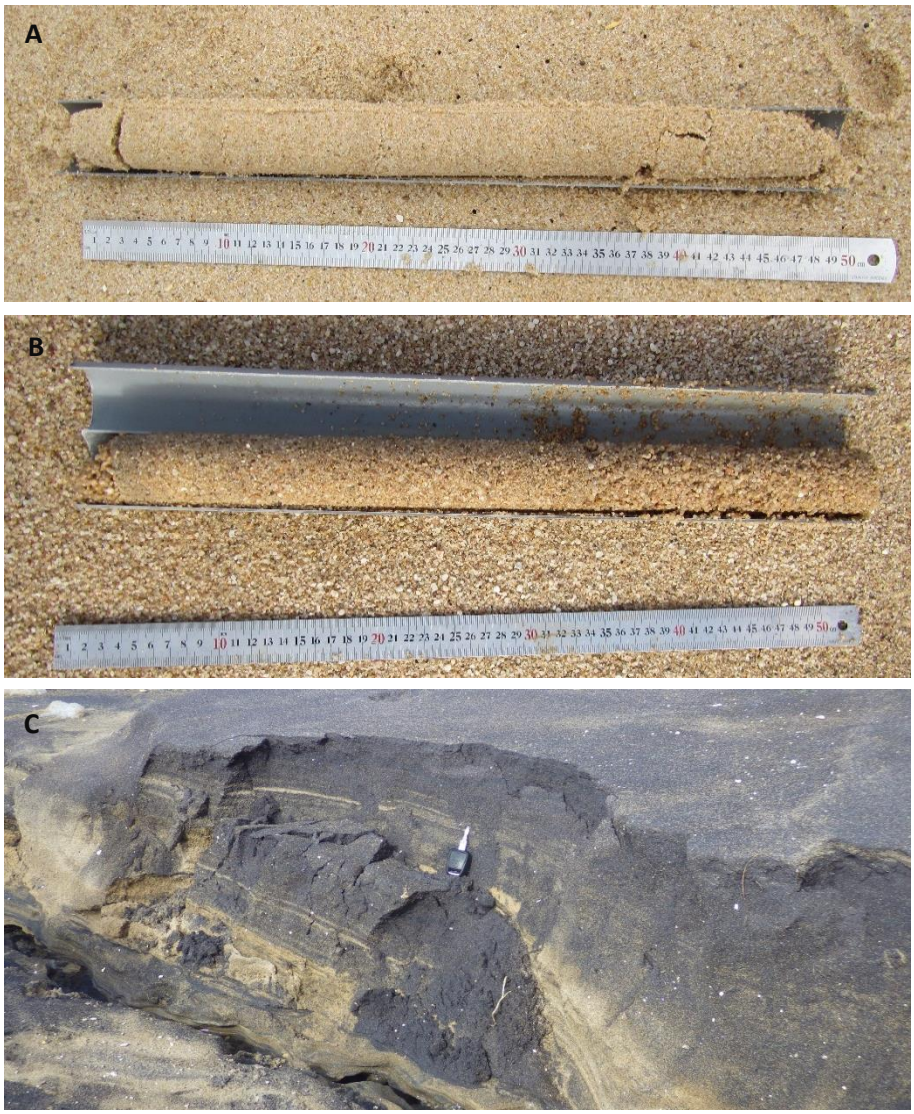

Figure 4.2. Vertical samples collected at (A) Sta. Cruz and (B) São Lourenço; and (C) placer deposit observed at Grande beach after the earlier storm events of 2014.

4.2.2 Laboratory work and data analysis

Grain-size analysis was performed in all samples, while compositional analysis were only performed for composite sediment samples as shown in **Figure 4.1**.

4.2.2.1 Grain-size analysis

Sediment grain-size analysis was taken by sieving method for the particles larger than 1 ϕ and by laser diffraction for particles smaller than 1 ϕ. Both methods were performed according to the internal protocols of *Instituto Hidrográfico*, which are based on the standards NP EN 933-1 and ISO 13320-1. The size grade scale adopted was the Wentworth scale modified by Krumbein (1934) and the statistic parameters of the grain-size distributions were computed through the method of moments described in Boggs (1995).

4.2.2.2 X-ray diffractometry analysis

X-ray diffractometry is a technique usually applied to obtain the mineralogy of silty-clay sediments. However, according to the works presented by Hein *et al.* (2013), Armstrong-Altrin *et al.* (2014) and Oliveira *et al.* (2015), this technique can be used as a first approach to get insights on the major mineral phases (> 2%) present in coarser sediment using a bulk of milled sample. Thus, sediment samples were milled to get a powder with a median grain-size of 100 μm (3.3 ϕ). The mineralogical analysis was performed using a PANalytical diffractometer, with a CuKα radiation. Scans were run between 4° and 60°, with a 0.02° per 2θ step and a counting time of 1 second. Mineral relative abundances was determined based on the x-ray diffractogram peak areas, being the basal reflections of the main minerals weighted by empirically factors following the criteria presented by Rocha (1993). Due to technical problems with diffractometer, the samples of Azul, Abano and Guincho beaches were not analysed.

4.2.2.3 Magnetic susceptibility analysis

Magnetic susceptibility is a fast and non-destructive assessment of the concentration of iron-bearing magnetic minerals that according to the work presented by Shankar *et al.* (1996), can be used as a *proxy* for heavy mineral content of the sediment. In mathematical terms, magnetic susceptibility (κ) is defined as the ratio between induced magnetization per volume unit of measured sample (M) and applied magnetic field intensity (H). Since M and H have the same SI units (Am^{-1}), κ is a dimensionless number (Dearing, 1999).

This technique was applied to get insights on sediment heavy mineral content of all composite samples. Before measuring magnetic susceptibility, sediment samples were washed with distilled water, dried and well mixed in plastic containers. The measurements were performed with the sediment inside plastic containers, using a Bartington MS2E sensor, which measures the magnetic susceptibility with a high spatial resolution (3.8 mm). To avoid anomalous values, 15 measurements at different points were taken for each sample and a median value was assumed.

4.2.2.4 Heavy minerals analysis

The heavy mineral analysis was performed on a subset of the composite samples (see **Figure 4.1**) to complement and validate the results of magnetic susceptibility. Heavy minerals are usually concentrated in the grain-size classes of medium to very fine sand. However, the sediments under analysis reveal low frequencies of very fine sand, thus the heavy mineral study was performed only for the grain-sizes ranging between medium and fine sand (1-3 ϕ). The

weight percentage of heavy fraction was firstly computed based on the ratio between heavy and light mineral weights and secondly was weighted on the total sediment weight.

The preparation of the samples included the elimination of carbonates using a 10 % solution of hydrochloric acid (HCl). After, sand fractions were washed and dried and, heavy and light minerals were separated using bromoform (density = 2.89). The required amount of grains for each microscopic slide was obtained using a micro-splitter and then mounted in Canada balsam on glass slides. Mineral particles identification and counting under the petrographic microscope was performed according to the ribbon method (Galehouse, 1971 *in* Mange and Maurer, 1992). The percentage of each mineral specie (in each sample) was computed based on the total number of grains counted (about 600 grains per sample).

4.2.2.5 Principal components analysis

Compositional data interpretation was supported by the principal components analysis (PCA). This analysis was applied in order to reduce the number of possibly correlated variables (*i.e.* mineral species) into a fewer uncorrelated variables (principal components) that are linear combinations of the original ones. The objective of this analysis is to reduce the number of variables of the data set, but retain as much of the original variability in the data as possible. Two PCA were performed using the STATISTCA software. The first one explore the major minerals phases of the sediment, while the second one explore the main transparent heavy minerals identified.

4.3 RESULTS

4.3.1 Beach sediment grain-size

The grain-size distributions of the composite samples show that beach sediment is mainly composed by coarse sand (1 ϕ to 2 ϕ) with a modal class of 0.75 ϕ, in the most cases, or 0.25 ϕ, in the cases of Calada and Coxos beaches. Exceptions are São Lourenço beach that is mainly composed by very coarse sand (0 ϕ to -1 ϕ) and present significant percentages of gravel (-1 ϕ to -2 ϕ); and the placer sediment (collected at Grande beach) that is mainly composed by medium sand (1 ϕ to 2 ϕ) (**Figure 4.3**).

The superficial sediment samples are also mainly composed by coarse sand with a model class of 0.75 ϕ. Nevertheless, Calada beach sediment presented, once again, a slightly coarser mode (0.25 ϕ). The sediment sampled at Adraga and Grande low-tide terrace and at Coxos submarine

beach showed higher percentages of medium sand particles (1-2 ϕ); in the latter case, it can be also noticed an increasing of fine sand particles (2-3 ϕ) (**Figure 4.4**).

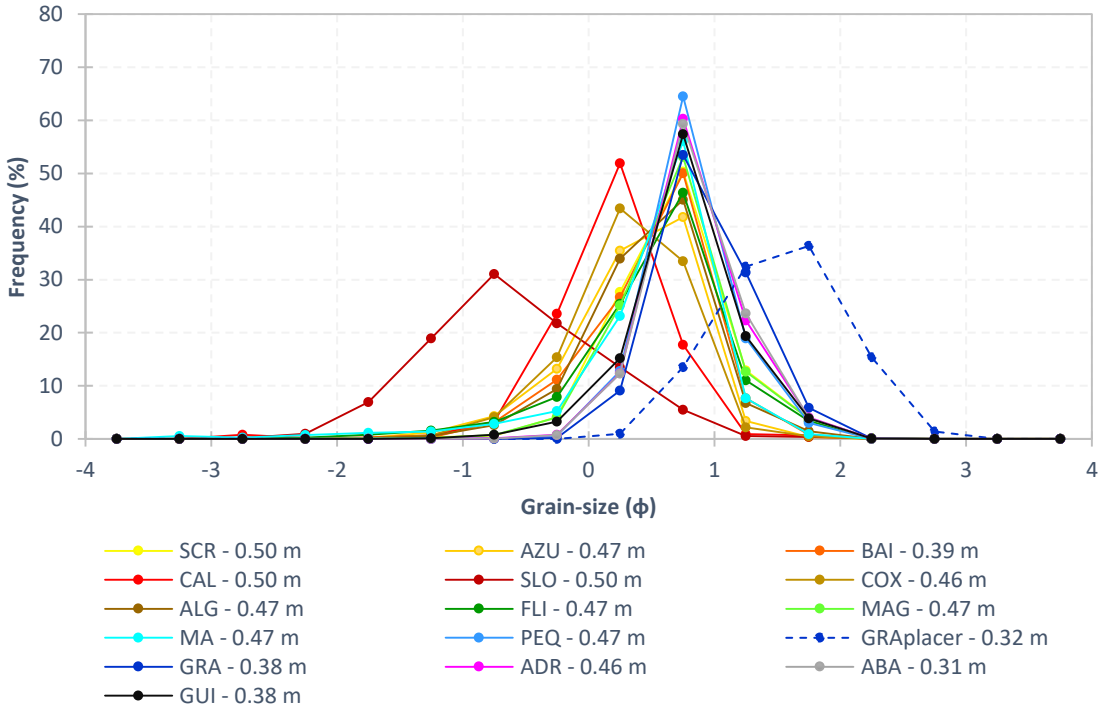

Figure 4.3. Grain-size distributions curves of the composite samples. The dashed line corresponds to the placer sample collected at Grande beach. The plot legend include the tickness of the sampled layer.

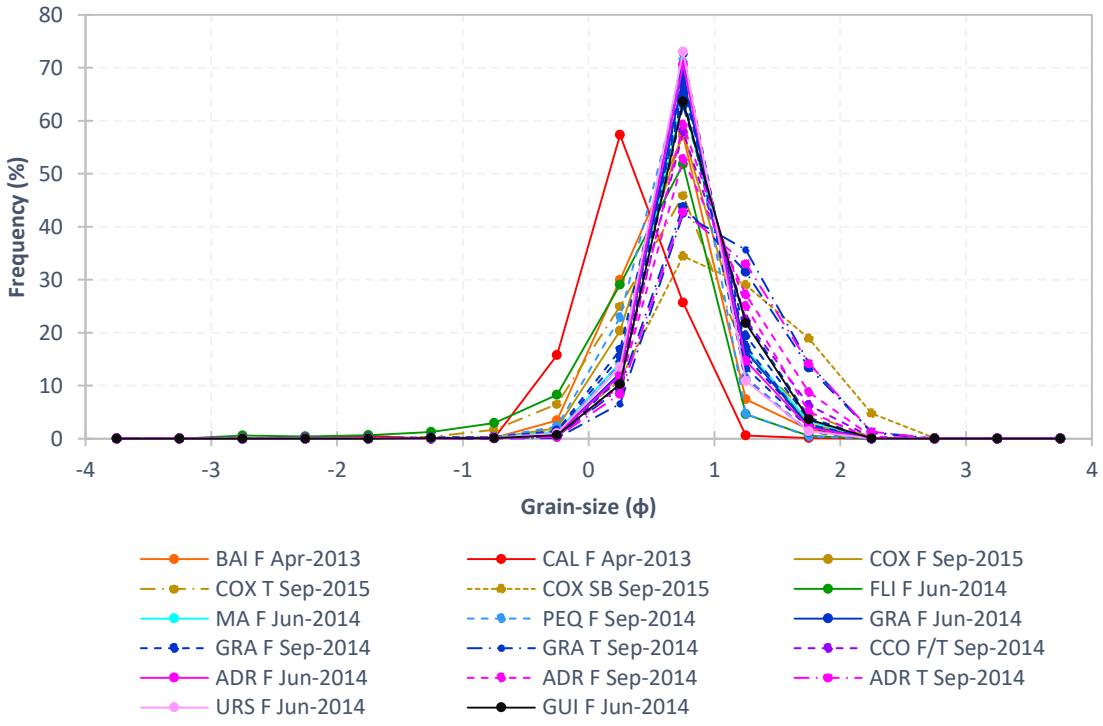

Figure 4.4. Grain-size distributions curves of the superficial sediment samples collected on beach face (F), low-tide terrace (T) and submarine beach (SB).

The relation between the mean, standard deviation and skewness of sediment grain-size shows that the southern beaches tend to be finer, well sorted and fine skewed than the northern beaches. In what concerns to the beaches where both sampling methods were applied, it can be noticed that, Baío, Calada, Coxos and Maçãs composite sediment is clearly coarser and less sorted than the superficial sediment, in opposition to Foz do Lizandro, Pequena, Grande, Adraga and Guincho, which have slightly differences. On the other hand, low-tide terrace sediment collected at Adraga and Grande beaches is finer and well sorted than the one collected at Coxos, but have a mean grain-size similar to the Coxos submarine beach sediment (**Figure 4.5**).

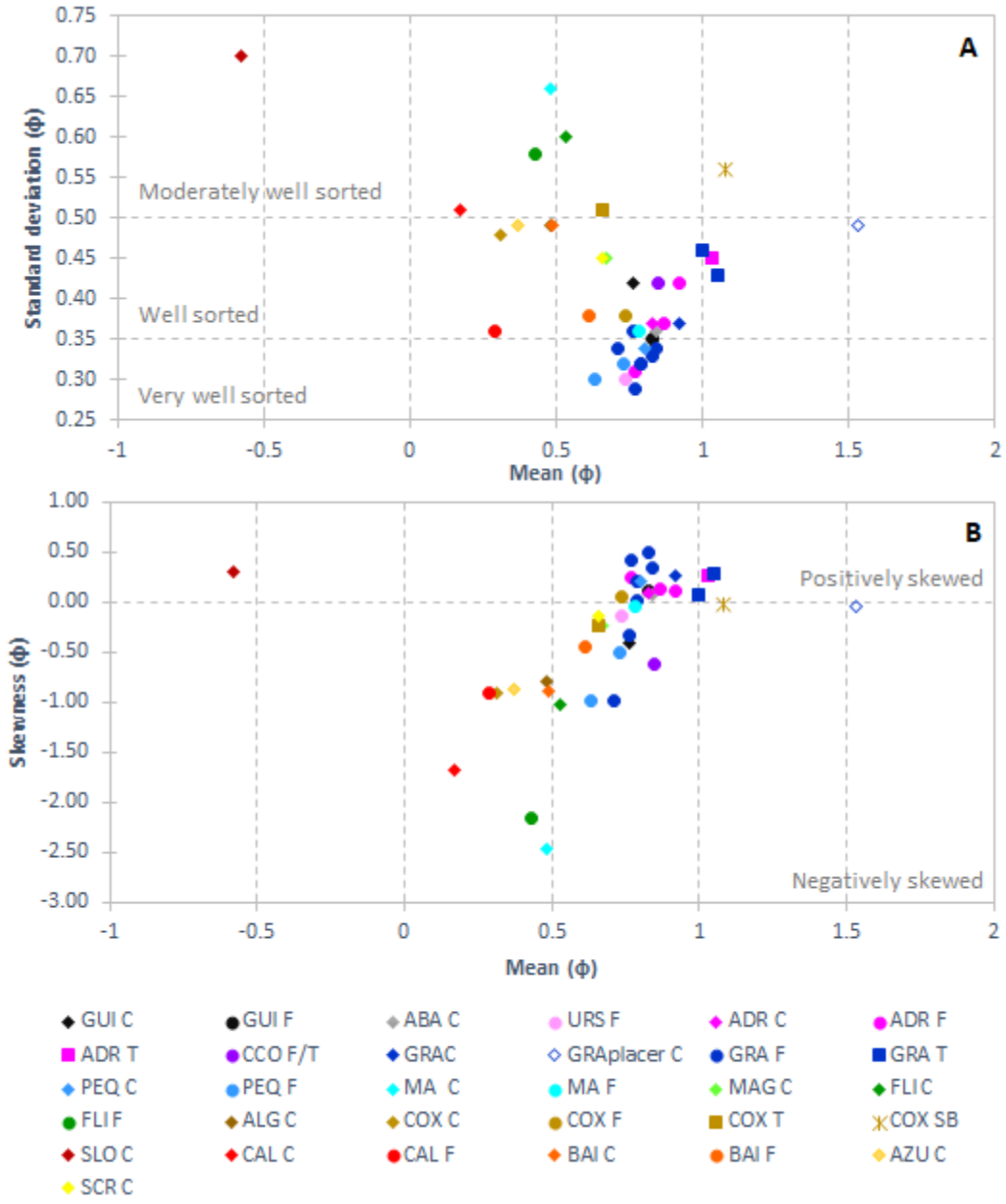

Figure 4.5. Relation between mean grain-size and standard deviation according to Folk and Ward (1957) classification; and (B) between mean grain-size and skewness (C - composite sample; F - superficial sample of the beach face; T- superficial samples of the low-tide terrace sample; SB – superficial samples of the submarine beach. In the lengend beaches are presented from south to north.

Considering the mean grain-size, most of sediment samples are classified as coarse sand; exceptions are the sample collected at São Lourenço, a very coarse sand, and the samples collected at the low-tide terrace of the Grande and Adraga beaches, at the submarine beach of Coxos and at placer of the Grande beach, classified as medium sand.

4.3.2 Beach sediment composition

4.3.2.1 Major minerals

X-ray diffractometry results show that the beach sediments under analysis are mainly composed by quartz, calcite and potassium feldspar, with median percentages above 17 %. Dolomite, aragonite, plagioclase and hematite have lower percentages that do not exceed 5 % (**Figure 4.6**). The placer sample collected at Grande beach has a peculiar mineral assemblage, mainly composed by heavy minerals, such as ilmenite (37 %), magnetite (30 %), hematite (12 %), garnet (8 %) and zircon (6 %), while light minerals such as potassium feldspar, calcite and quartz have residual percentages (≤ 3 %).

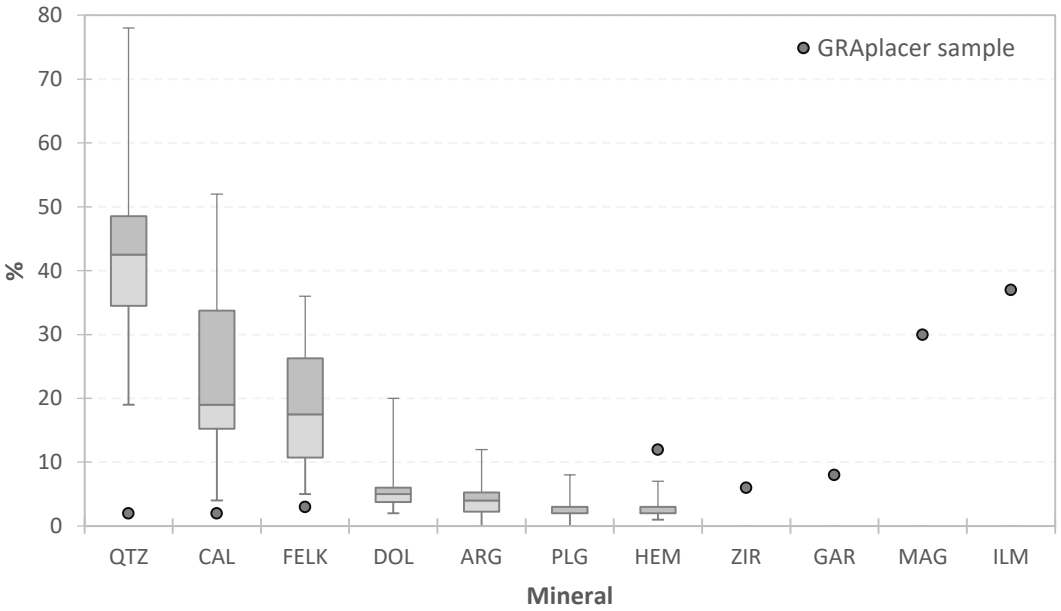

Figure 4.6. Major minerals of sediment (QTZ – quartz; CAL – Calcite; FELK - potassium feldspar; DOL – dolomite; ARG – aragonite; PLG – plagioclase; HEM – hematite; ZIR – zircon; GAR – garnet; MAG – magnetite; ILM – Ilmenite). The box-plots are divided by the 50th percentile, while its limits are the 25th and 75th percentiles; the whiskers represent the maximum and minimum values. The mineralogy of the placer sample collected at Grande beach is represented separately by dots.

The relative percentages of major minerals obtained for each beach show an increasing of carbonate content from north to south, mainly related with calcite and aragonite percentages. Calada and São Lourenço beaches stand out due to the highest percentages of quartz (60 % and

78 %, respectively) and dolomite (20 and 11 %, respectively). The results also put in evidence the significant differences between Grande beach sediment collected during modal (GRA sample) and after-storm conditions (GRAplacer sample). In the first case, sediment presents a mineralogical signature not much different from the adjacent beaches, dominated by light minerals, while in the second case the sediment is dominated by heavy minerals as previously mentioned (**Figure 4.7**).

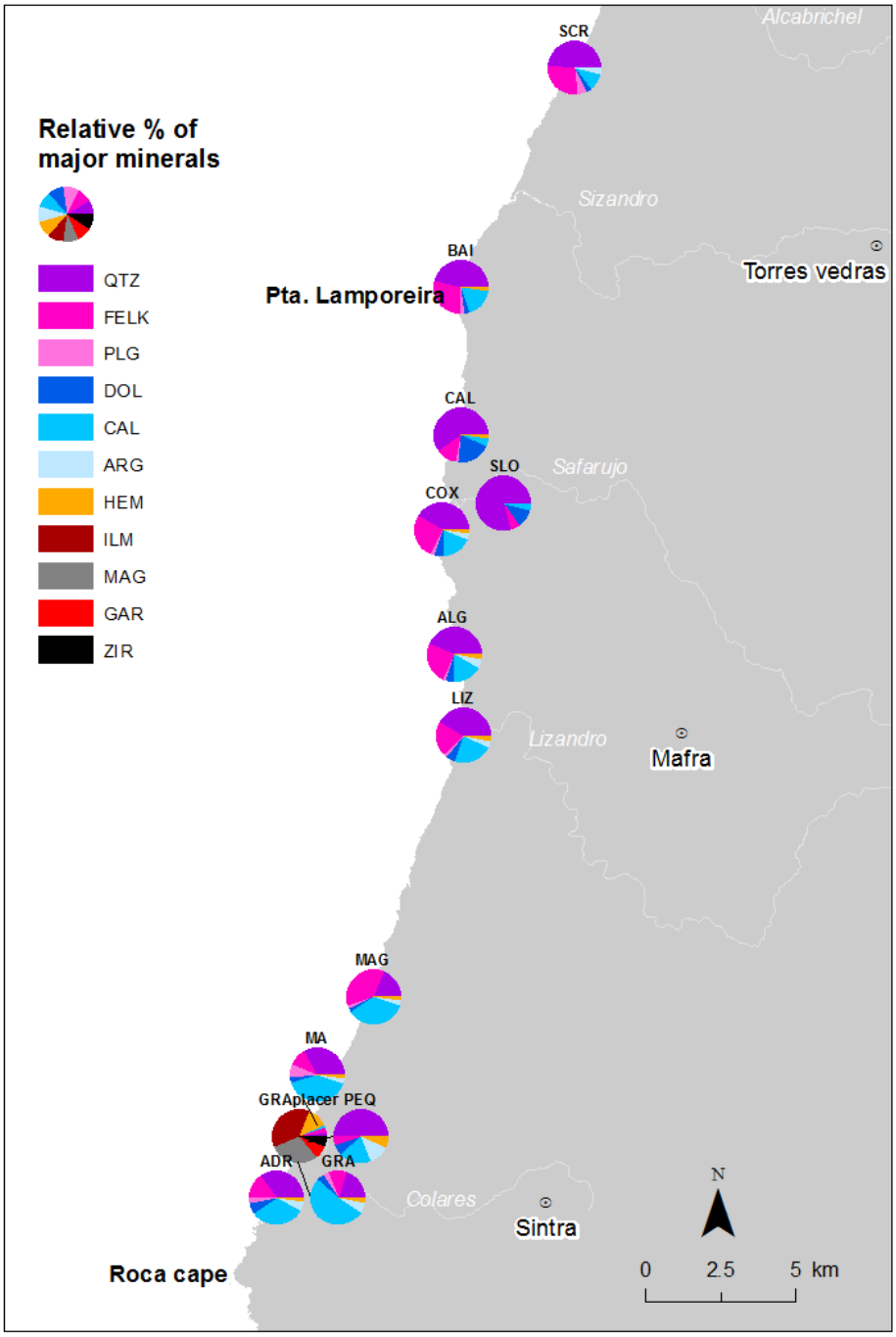

Figure 4.7. Relative percentage of the major minerals (QTZ – quartz; FELK - potassium feldspar; PLG – plagioclase; DOL – dolomite; CAL – Calcite; ARG – aragonite; HEM – hematite; ; ILM – Ilmenite; MAG – magnetite; GAR – garnet; ZIR – zircon).

4.3.2.2 Magnetic susceptibility

The results of magnetic susceptibility are quite consistent despite variations within each sample, related with the high spatial resolution of the sensor used. The beaches located north of Lamporeira headland (Sta. Cruz, Azul and Baío) have a magnetic signal almost null. South of this headland, magnetic signal tends to increase, reaching the highest values at Grande beach, which are up to two orders of magnitude higher. South of Grande beach magnetic signal back to decrease (**Figure 4.8A**). Placer sample have a magnetic signal extremely high with a median value of 7.1×10^{-1}, 30 times higher than the median value obtained for modal conditions (2.3×10^{-2}) (**Figure 4.8B**).

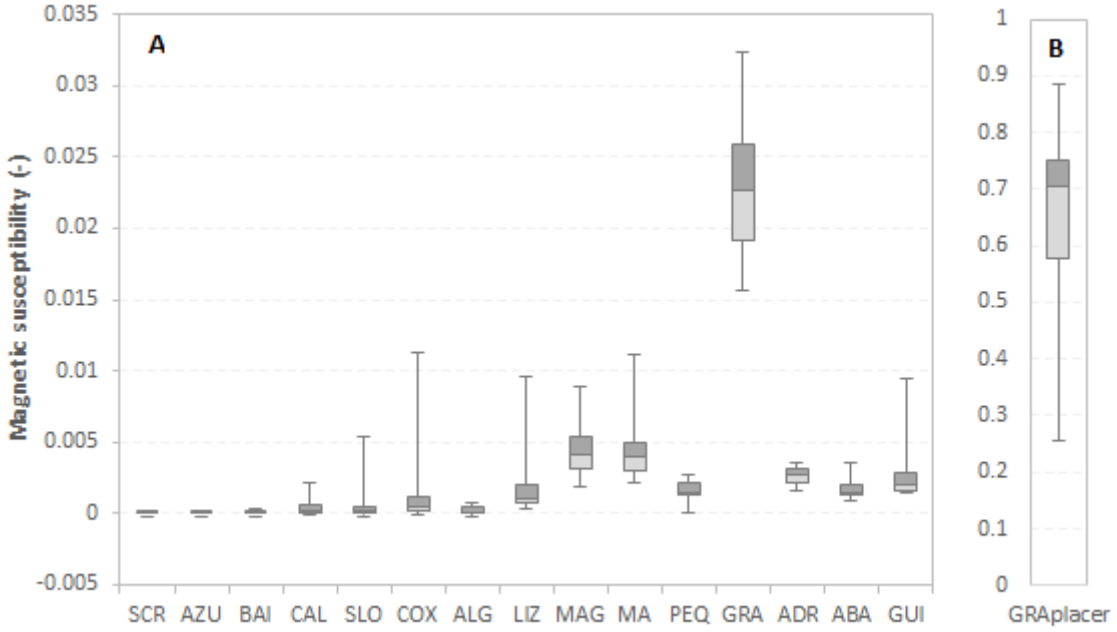

Figure 4.8. Magnetic susceptibility of beach sediment: (A) "regular" samples and (B) placer sample of the Grande beach. The box-plots are divided by the 50th percentile, while its limits are the 25th and 75th percentiles; the whiskers represent the maximum and minimum values.

4.3.2.3 Heavy minerals

Heavy mineral content (expressed in weight percentage) increases from Azul to Grande and decreases from Grande to Guincho. The heavy mineral percentages found at Grande beach are significantly higher than the ones observed at the other beaches. The placer sample collected in this beach reveal a heavy mineral concentration 25 times higher than the one found in the "regular" sediment sample (**Figure 4.9**).

The lower percentages of heavy mineral fraction found at Azul beach did not allow to obtain a number of heavy mineral particles with statistical significance. Thus, the results of heavy mineral

species of Azul beach were not considerate. Fourteen transparent heavy mineral species were identified under the petrographic microscope, but only half of these species have median percentages greater than 1 %. Those minerals are: tourmaline (24.5 %), clinopyroxene (21.3 %), garnet (18.4 %), staurolite (15.4 %), andaluzite (7.2 %), amphibole (5.0 %) and zircon (1.2 %). Epidote and rutile are less abundant (≤ 0.5 %) and apatite, titanite, biotite, cyanite and sillimanite are vestigial (**Figure 4.10**).

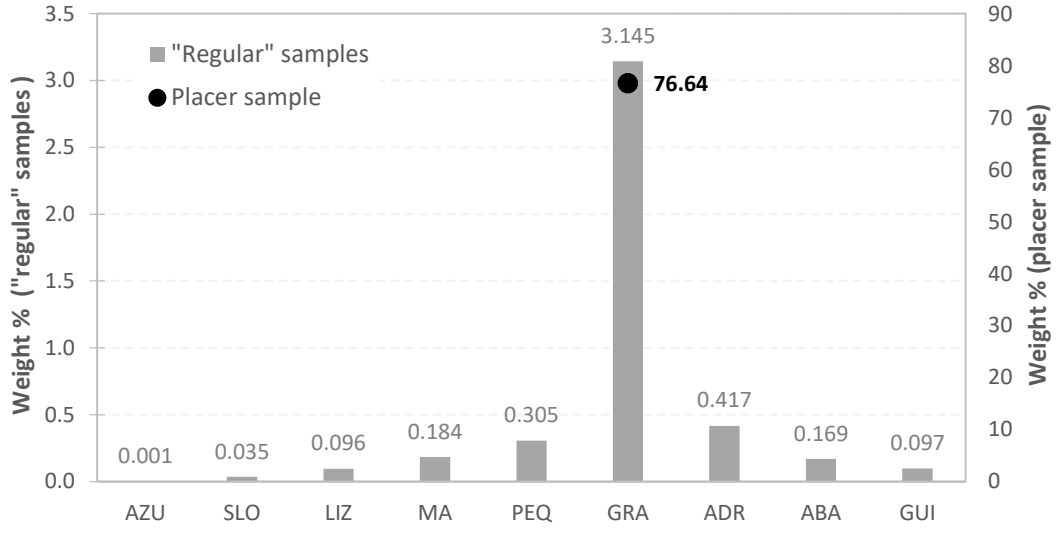

Figure 4.9. Heavy mineral weight percentage of each beach sediment sampled.

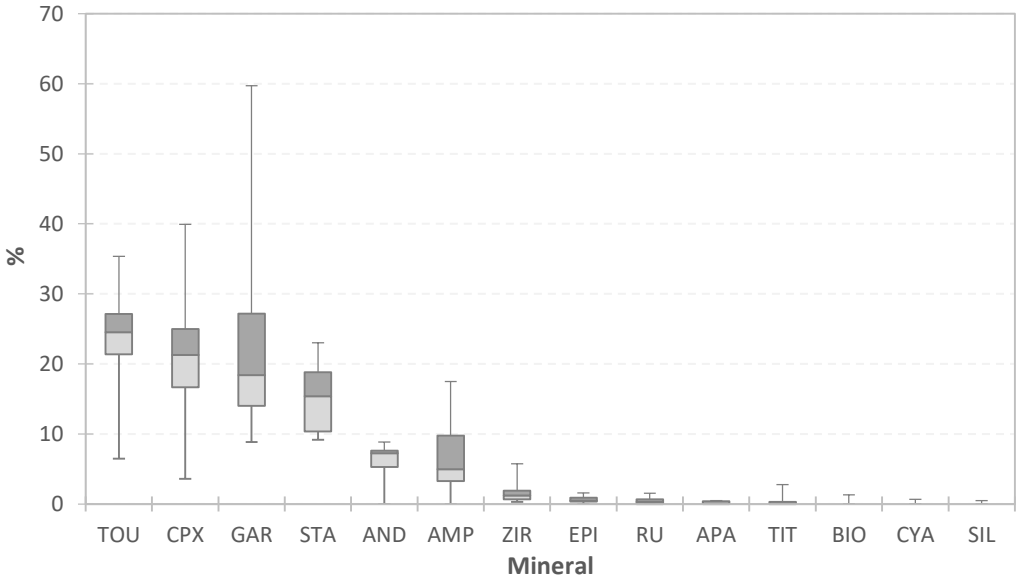

Figure 4.10. Transparent heavy mineral species identified under the petrographic microscope (TOU – tourmaline; CPX – clinopyroxene; GRA – granate; STA – staurolite; AND – andaluzite; AMP – amphibole; ZIR – zircon; EPI – epidote; RUT – rutile; APA – apatite; TIT – titanite (or sphene); BIO – biotite; CYA – cyanite; SIL – sillimanite). The box-plots are divided by the 50th percentile, while its limits are the 25th and 75th percentiles; the whiskers represent the maximum and minimum values.

The relative percentages of the main transparent minerals (>1 %) are shown in **Figure 4.11**. The results indicate that the beach heavy mineral signature is quite similar, despite some singularities found at São Lourenço beach (high percentage of amphibole and garnet), Foz do Lizandro beach (high percentage of clinopyroxene) and Grande beach (high percentage of garnet). The most exotic deposit was the placer of Grande beach which has a peculiar signature mainly composed by garnet (61 %), staurolite (23 %) and zircon (6 %).

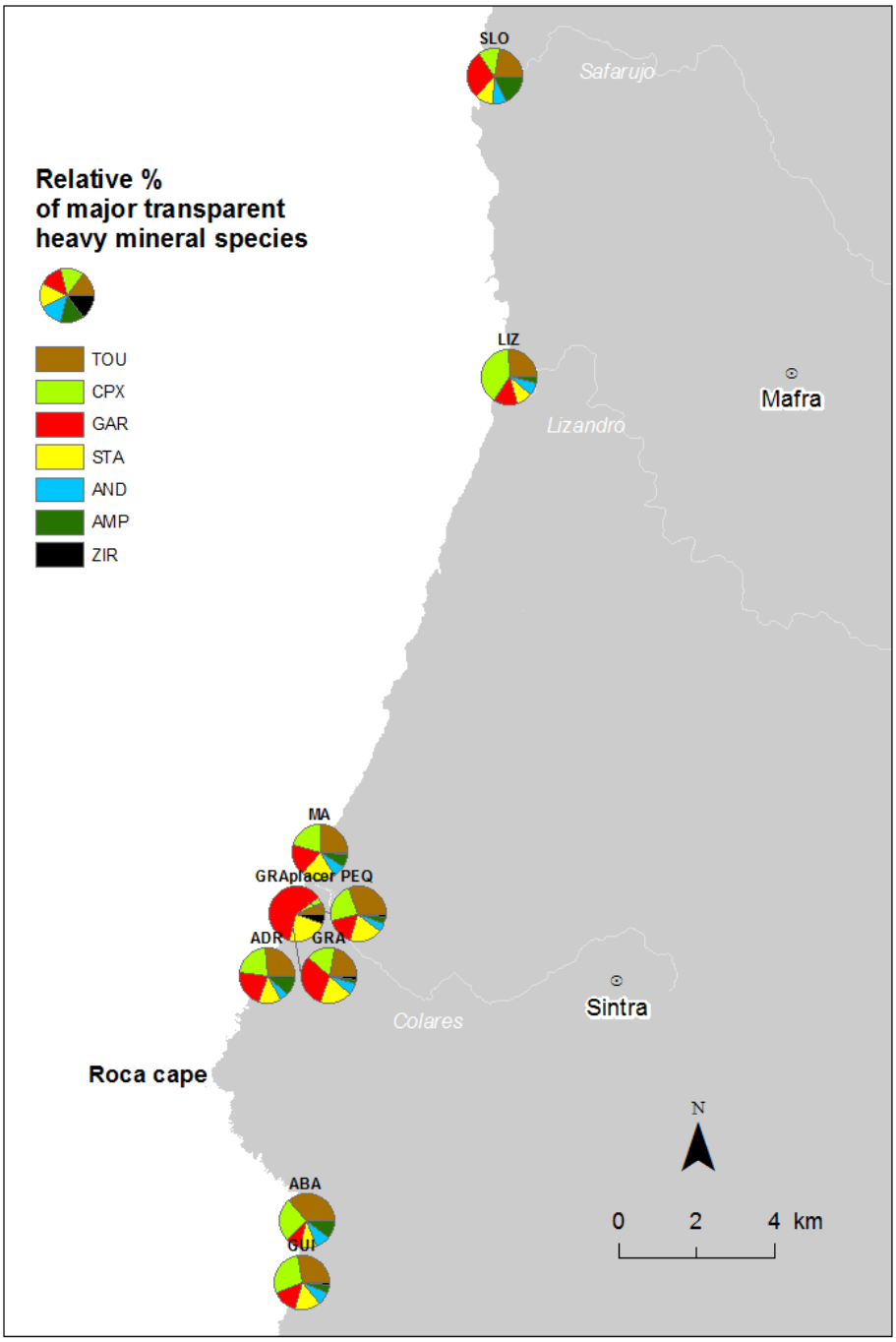

Figure 4.11. Relative percentage of major heavy mineral transparent species (TOU – tourmaline; CPX – clinopyroxene; GAR – garnet; STA – staurolite; AND – andaluzite; AMP – amphibole; ZIR – zircon).

4.3.2.4 Principal components

PCA applied to the major mineral species shows that 53 % of the total variance is explained by the component 1 that separates Grande placer sample from the other ones, based on the opposition between heavy and light mineral. The component 2 explains 21 % of the total variance and separate the Calada and São Lourenço beaches from the other ones, due to the higher percentages of quartz and dolomite presented by those beaches (**Figure 4.12**).

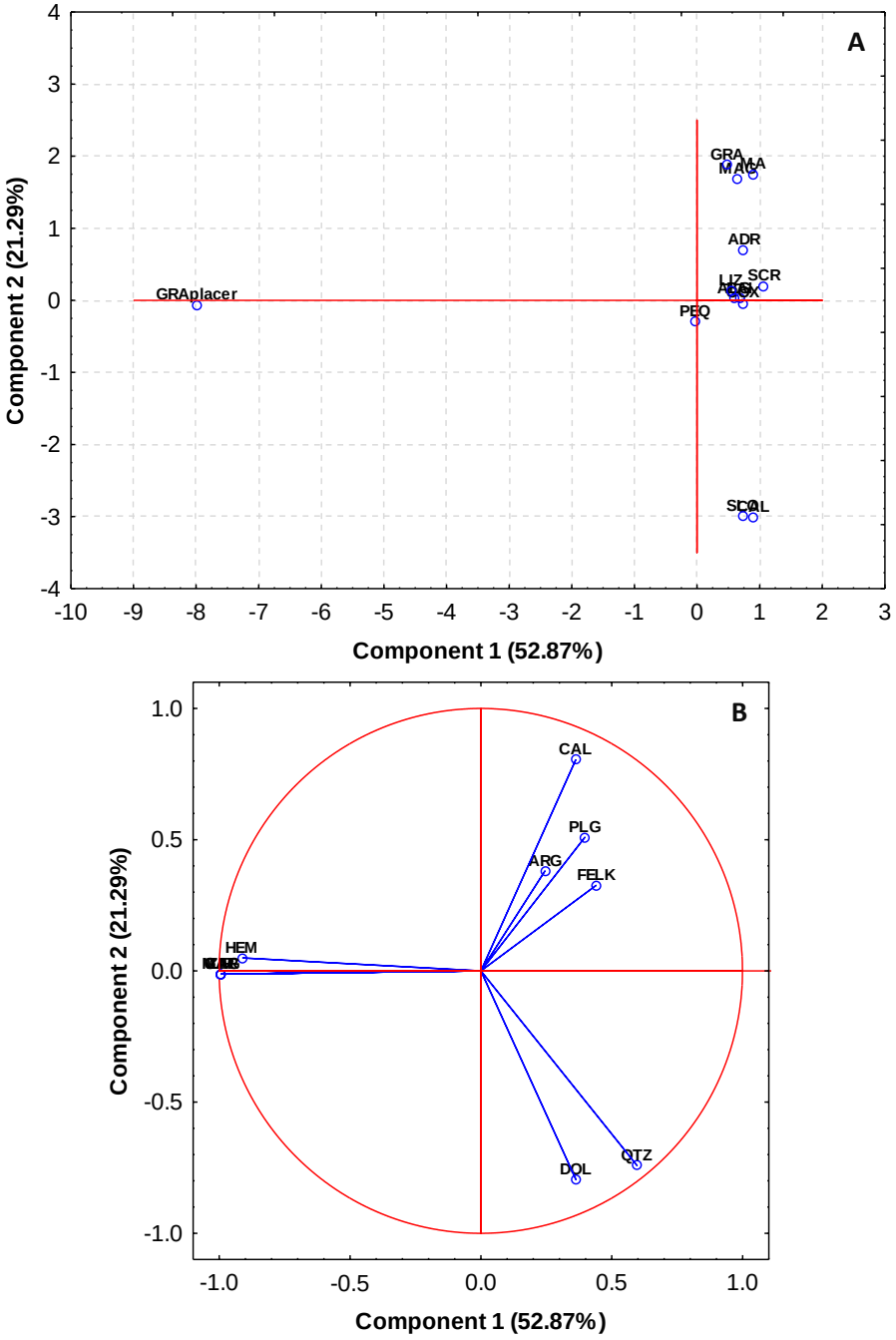

Figure 4.12. Principal components of analysis for the major minerals of sediment: (A) projection of the beach cases based on the two main components; (B) projection of the mineral variables based on the two main components.

In the case of main transparent heavy minerals, PCA results show that the two main components explain 90 % of the total variance. Component 1 explains 71 % of the total variance and separates both sediment samples collected at Grande beach from the other ones. This separation is related with the opposition between the denser mineral species such as staurolite, garnet and zircon from the other ones. Component 2 explains 17 % of the total variance and basically shows a slight detachment of the São Lourenço beach, mainly related with the amphibole values (**Figure 4.13**).

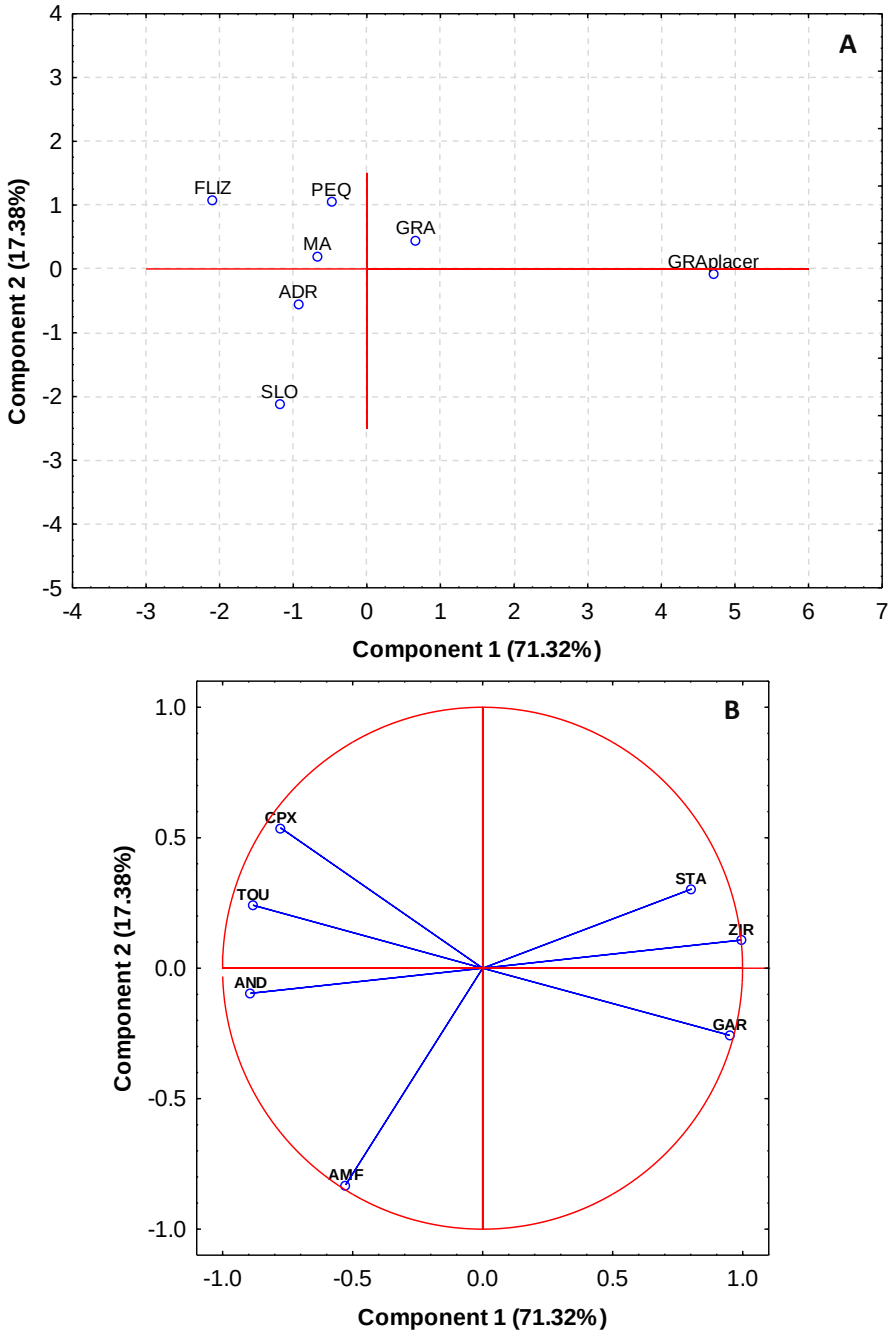

Figure 4.13. Principal components of analysis for the transparent heavy minerals of sand: (A) projection of the beach cases based on the two main components; (B) projection of the mineral variables based on the two main components.

4.4 DISCUSSION AND CONCLUSIONS

Sediment grain-size analysis shows that the studied beaches have, in general, mean grain-sizes of coarse sand. Exception are: (1) the very coarse sand of Lourenço beach; (2) the medium sands collected at low-tide terrace of the Grande and Adraga beaches and at the submarine domain of the Coxos beach; and (3) the medium sand of the Grande beach placer, collected after a major storm (**Figure 4.3**, **Figure 4.4** and **Figure 4.5**).

The sediment grain-size analysis was limited to the beaches located in the stretch between Sta. Cruz and Guincho. To have a wider view of the grain-size variations along the study coast, the mean grain-size of superficial beach face sediment samples was projected together with the mean grain-size of the beach face sediment analysed in previous works (**Figure 4.14A**). Despite the constrained imposed by the different number of samples used to estimate the average values of each beach, as well as the differences in the sediment sampling date and method, it can be noticed that coarser sediment are in the stretches with a N-S and NW-SE general orientation (the rockier inner shelf sectors as shown in the Chapter 2).

Composite sediments allowed a better characterization of the beaches alongshore, showing that beaches located north of the Foz do Lizandro, particularly, in the stretch between Lamporeira and Foz do Lizandro, tend to be coarser than the southern ones (**Figure 4.14B**). This trend is compatible with a selective sediment transport process southward, where finer particles bypass the headlands, while coarser ones are trapped inside the bays.

Previous assumption is also supported by the field observations at Ursa beach, where the rocks of the Sintra Igneous Complex contact with the Jurassic superior limestones. The cobbles and boulders particles resulting from the erosion of the referred rocks showed a weak mixture inside the bay, suggesting that gravel particles have low transport rates and are trapped inside the bays (**Figure 4.15**).

The sediment grain-size decreasing observed towards offshore, along the Coxos, Grande and Adraga beaches profiles also support the existence of a selective transport process. In the first case, sediment of the beach face and low-tide terrace was composed by coarse sand that gave place to medium sands at the submarine beach; while in the two latter cases, the coarse sands of beach face gave place a medium sand at the low-tide terrace. The medium sand found at the lower beach domains is in agreement with the inner shelf medium sand deposits mapped by IH (2010) up to 10/20 m depth, where they gave place to fine sands. These results indicate once again that coarser particles remain inside the bays, while finer ones are transported offshore and, eventually, bypass the headlands.

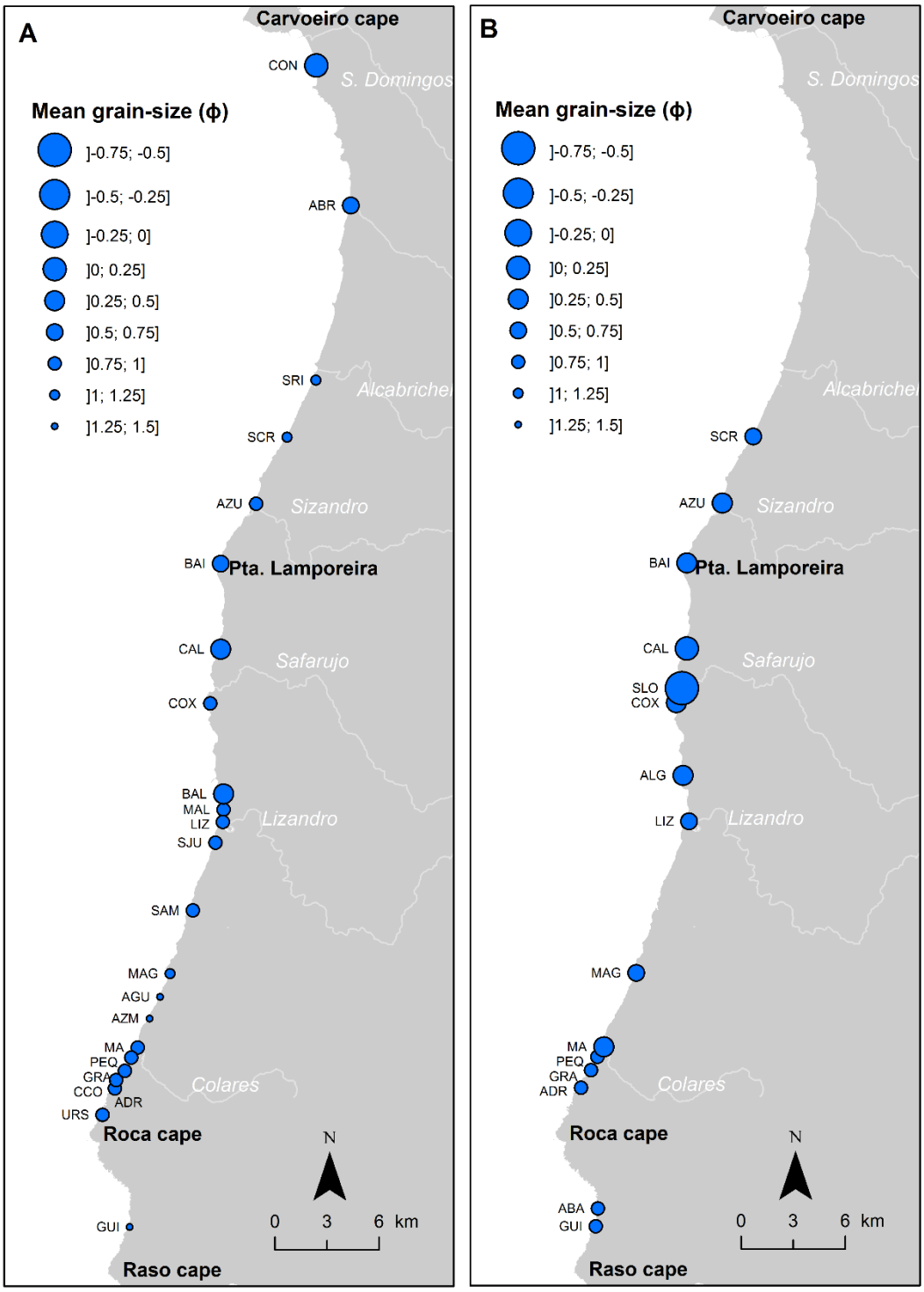

Figure 4.14. Longshore distribution of the beach sediment grain-size based on: (A) average of mean grain-size of the superficial sediment collected at the beach face in the scope of this and other works (Oliveira, 2009; Trindade and Ramos-Pereira, 2009; Balsinha *et al.*, 2010; Pires and Ribeiro, 2010; Gusmão, 2010; Silveira *et al.*, 2013); and (B) mean grain-size of the composite sediment samples.

Figure 4.15. (A) General aspect of the Ursa beach, located in the stretch between Adraga and Roca cape, at June 11th 2014: contact between the Jurassic limestones (northeast) and the rocks of Sintra Igneous Complex (southwest), and the respective, detrital deposits resulting from the cliffs erosion; (B) contact metamorphosed limestone (white cobbles), granite and syenite (pink cobbles) and gabbro and basalt (black cobbles); (C) aspect of the cobbles mixture at the low-tide terrace.

Despite the selective process identified alongshore, there are grain-size variations that should be related with geomorphological constrains and/or local sediment sources, being the most notorious case the São Lourenço beach (**Figure 4.14B**).

The mean grain-size of composite sediments was projected against the beach embayment index, but a weak relation was found (**Figure 4.16**), suggesting that the coarser sediment of São Lourenço can be directly provided by the Safarujo river. The same can be assumed for Maçãs beach, located at the Colares river mouth, that has a coarser sediment compared to the nearby beaches (**Figure 4.14B**).

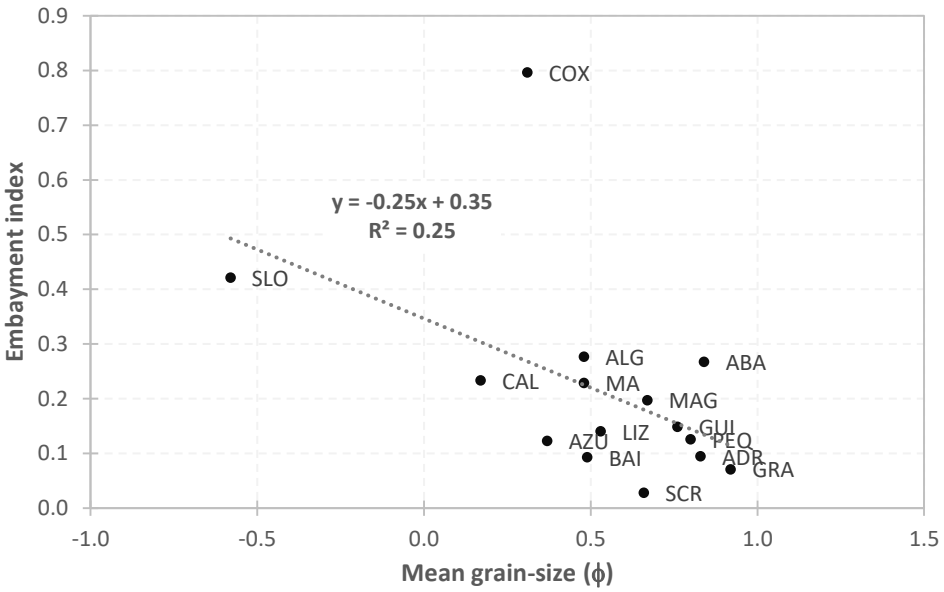

Figure 4.16. Relation between mean grain-size of composite sediments and beach embayment index.

The compositional analysis shows that beach sediment is mainly composed by quartz, feldspar and carbonate particles, except in the particular case of placer deposit. Despite some local variations, such as the higher percentages of quartz and dolomite of the Calada and São Lourenço beaches that could be related with the local sediment sources, the only trend observed alongshore is the increase of carbonate content southward, mainly calcite (**Figure 4.7**). However, the origin of the carbonate particles was not clarified, so it cannot be used for sedimentary dynamics proposes. Moreover, these results must be viewed with some caution, because they correspond to a first attempt to study the mineralogy of these sediments. The latter tests performed by Oliveira *et al.* (2016), show that median grain-size of the powder used in these analysis can lead to inaccuracies in the relative percentages of the mineral phases.

The transparent heavy mineral assemblages found in the beaches between São Lourenço and Guincho are quite similar and, are in agreement with mineral assemblages observed by Balsinha *et al.* (2010) in the beaches located between Peniche and Foz do Lizandro. This mineralogical homogeneity impedes tracing sediment sources and transport pathways. According to the work presented by Cascalho *et al.* (2016), held in conjunction with this work, the mineralogical homogeneity of these beaches can be explained by the great variety of lithological types (sedimentary, igneous and contact metamorphism rocks) found in the watersheds drained to the littoral.

Despite the few samples, the correlation between magnetic susceptibility and the weight percentage of heavy mineral was good, allowing the use of the magnetic signal as a proxy for

the heavy mineral concentration (**Figure 4.17**). Thus, according to the magnetic susceptibility results, heavy mineral concentration increases southward, reaching a maximum at Grande beach, for both modal ("regular" samples) and after-storm (placer sample) conditions (**Figure 4.8**). The high content of heavy minerals of the Grande beach sediment, compared to the other beaches, only can be explained by a long-term cumulative process promoted by the Calhau do Corvo headland at the downdrift limit of the beach. This headland is originated by the outcrop of Cretaceous limestone compact rocks exhibiting a subvertical stratification and a direction approximately perpendicular to the general orientation of the coastline, being a natural structural barrier to the longshore drift.

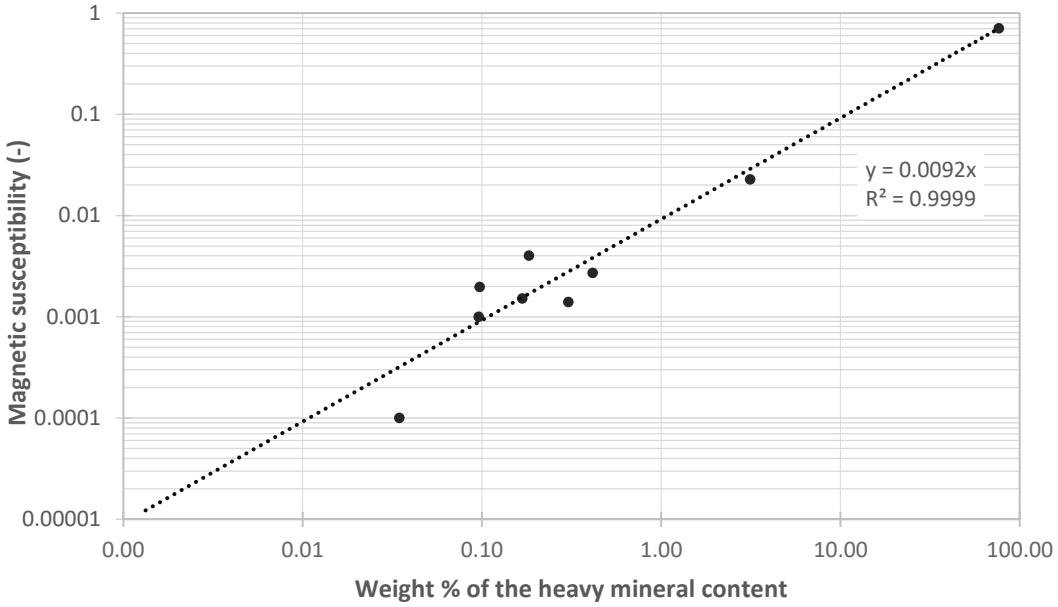

Figure 4.17. Relation between magnetic susceptibility (median value) and the weight percentage of heavy minerals.

The heavy mineral placer deposit observed at Grande beach resulted from an efficient grain density sorting induced by the storm events occurred in the begging of 2014 (also mentioned in Chapter 3). Nonetheless, the large size of this deposit and its peculiar mineralogy, which include high percentages of ilmenite, magnetite, hematite, garnet, staurolite and zircon, should result from the combination between the referred long-term cumulative process, promoted by the Calhau do Corvo headland, and a short-term process related with the sorting promoted by the storm event. This assumption is in agreement with the model proposed by Peterson *et al.* (1986), based on their observations at the headland-bay coast of Oregon (U.S.A). According to these authors, placers development is controlled by shoreline configuration, as the first-order factor, and seasonal variations of wave climate and longshore currents, as second-order factors.

These results show once again a selective bypassing process, where the heavier particles are trapped inside the embayment, while the lighter ones are transported offshore; once lighter particles reach the tip of the headlands, they can be entrained by the longshore flows and bypass the headlands. This selective process is particularity efficient during high-energy conditions.

Concluding, beach sediment textural and compositional analyses indicate that HSB is a selective process. According to the results its can assumed that coarser particles such gravel and very coarse sand tend to be trapped inside the embayments, being their bypass very low or negligible. Coarse sand bypass occur mainly at the subaerial beach, considering the high frequency of these particles in the beach face and low-tide terrace sediments. Their bypass should occur in relation with the beach rotation process, as explained in the previous chapter; except during major storm events, when the wave energy triggers an extreme efficient selective process, transporting the lighter sediment particles towards offshore (including coarser sands), originating heavy mineral placer deposits on subaerial beach. In the case of medium sand particles, headland bypass can occur either subaerial beach or inner shelf domain, depend on the wave energy; while fine sand bypass occur mainly at the inner shelf, considering the low frequency of these particles in the beach sediments and fine sand deposits of the inner shelf.

Chapter 5

Longshore Sediment Transport

5.1 INTRODUCTION

Longshore sediment transport or longshore drift plays a major role in coastal processes. Intense efforts have been made to estimate longshore drift with the development of empirical formulas based on laboratory tests and field experiments data (*e.g.* Komar and Inman, 1970; CERC, 1984; Kraus *et al*., 1988; Kamphuis, 1991), numerical models (Hanson, 1989; Larson *et al*., 2002; Trouw *et al*., 2012), and through field measurements, such as sediment accumulation rates in harbours or groins (see the database summarized by Schoonees and Theron, 1993), short-term sediment impoundment (Bodge and Dean, 1987), sediment tracers (Ingle, 1966; Komar and Inman, 1970; Duane and James, 1980; Kraus *et al.*, 1981; Taborda *et al*., 1994; Ciavola *et al*., 1997; Vila-Concejo *et al.*, 2004; Tonk and Masselink, 2005; Silva *et al.*, 2007; Fernández- Fernández *et al.,* 2015), streamer sediment traps (Kraus and Dean, 1987; Rosati *et al*., 1991; Wang *et al*., 1998; Tonk and Masselink, 2005), optical devices (Downing *et al*., 1981; Taborda *et al*., 1999; Aagaard *et al*., 2002; Tonk and Masselink, 2005) and acoustic sensors (Vincent and Green, 1990; Vincent *et al*., 1991). In the present work, longshore sediment transport was studied using two different but complementary approaches. The first one, targeted the understanding of short-term processes and was based on a tracer experiment, relating the longshore drift rate with the hydrodynamic conditions. The experiment was designed to study headland sediment bypassing (HSB) and selective sediment transport processes. The second one was addressed to macroscale processes

and aimed at understanding longshore transport patterns along the studied coastal stretch. This latter approach was supported by the evaluation of net longshore drift by an empirical formulation and using an extended wave time-series.

5.2 SHORT-TERM APPROACH

The tracer experiment was carried out at Grande beach, located 3.5 km north of the Roca cape (**Figure 5.1**). As shown in Chapter 3, Grande beach extends for about 1 km with a NNE-SSW orientation, has high exposure to the NW dominant waves and presents a low-degree of embayment (within the range values of the studied beaches). This beach displays a clockwise rotation during summer and a counter-clockwise rotation in the winter. The cross-shore morphology varies between convex shape due to the presence of a well-developed berm, in the summer, and concave shape due to the berm obliteration, in the winter. In the northern sector the mean beach face slope and maximum berm crest elevation observed were 4° and 3.5 m, receptively; while in the southern sector, were 6° and 4.4 m, respectively. Beach sediment is mainly composed by coarse sand that tends to gets finer seaward (see Chapter 4).

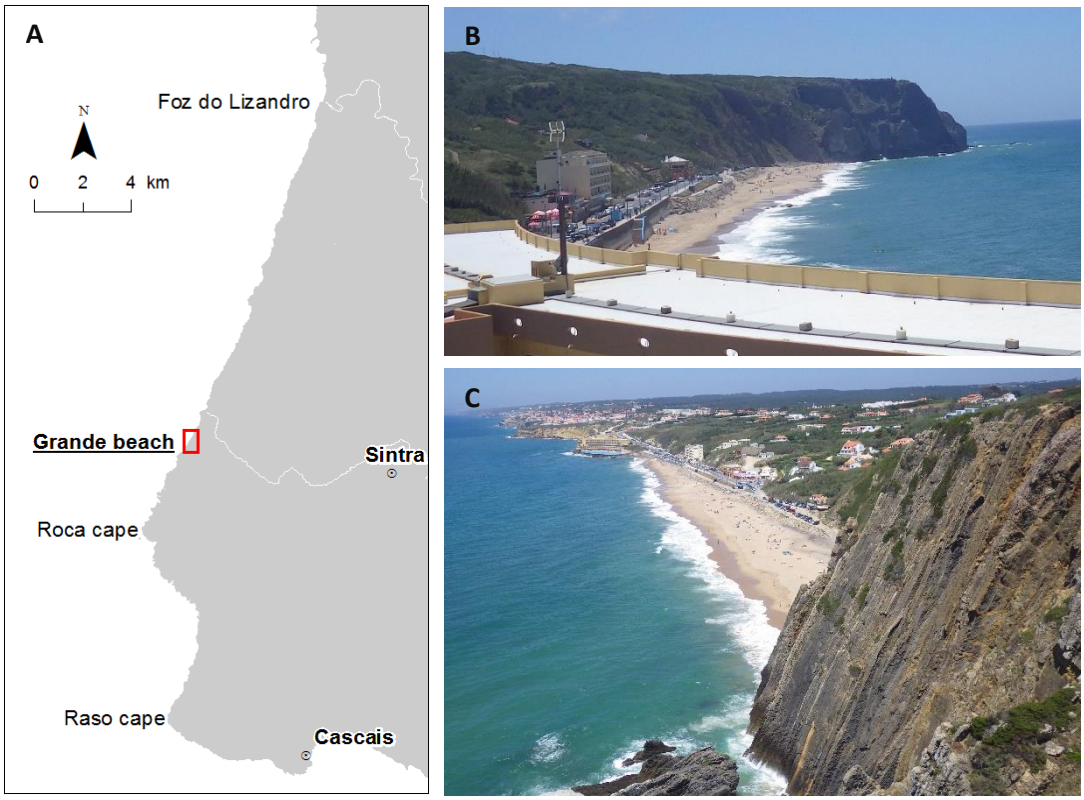

Figure 5.1. Grande beach: (A) geographic location; (B) north and (C) south views of the beach on June 11th 2014.

5.2.1 Methods

5.2.1.1 Tracer approach

The use of tracers to estimate longshore drift can be done through spatial integration method (SIM), time integration method (TIM) and continuous injection method (CIM) (Ingle and Gorsline, 1973; Madsen, 1987). In the present work, the CIM (also known as dilution method) was applied, injecting a known quantity of tracer at a given position, at a constant rate, over a given sufficient time to allow stabilization of the tracer flux rate downdrift, measured at one or more locations. The application of the principle of tracer mass conservation, assuming that a steady state can be reached, yields that the rate which the tracer is introduced into the transport system equals the rate that tracer leaves the transport system. Thus, longshore sediment transport (Q) can be given by:

$$Q = \frac{q}{\bar{c}_{eq}} \tag{5.1}$$

where $\overline{c}_{eq}$ is the steady state or equilibrium concentration measured at a point downdrift of the injection site and q is the volumetric tracer injection rate, which can be deduced from the tracer dry mass injection rate (q_{dm}) using the equation:

$$q = \frac{q_{dm}}{(1-p)\rho_s} \tag{5.2}$$

where ρ_s is the quartz density and p the sand porosity (assumed as 0.4).

CIM was selected due to the advantages point out by Duane and James (1980), namely: (1) tracer sampling can be accomplished at relatively few fixed locations and there is no need to monitor the entire spatial extent of the dispersing tracer cloud, thus minimizing attendant logistic difficulties and sampling problems associated with increasing dilution of tracer concentration with time; (2) problems associated with increasing dilution of tracer are not a factor because, theoretically, in steady state conditions, tracer concentration will increase throughout the experiment, until it reaches equilibrium; (3) it is not necessary to determine thickness of the active layer nor the width of the transport system, because demonstration of lateral constancy on the equilibrium concentration, across the transport system, is sufficient to validate the experimental results. The experimental results validation can be done by establishing sampling locations transverse to the transport zone, at several distances from the injection point.

If these experiments are performed during relatively short periods of time, the risk of wave changing conditions is reduced comparatively with TIM and SIM. Furthermore, it does not requires a vertical sampling (sediment cores), because it is not necessary to sample the entire

mixing layer. A superficial layer sample with approximately 1 cm is sufficient. In fact, sampling should not exceed mixing depth to avoid sampling sediment below the active layer that may lead to an underestimation of the tracer concentration.

5.2.1.2 Preparation of fluorescent tracer

The preparation of the tracer experience was carried out in conjunction with the tracer experiment of the Beach to Canyon project[4], in order to take advantage of the necessary logistics, which otherwise would be very heavy. For this reason the sediment used in the tracer experiment of Grande beach was non-native, being collected at Norte beach, located north of the study site (at Nazaré). Norte beach sediment is characterized by a wide grain-size range, with a median grain-size ranging from fine gravel (-2.6 ϕ) to medium sand (1.79 ϕ) (Cascalho *et al*., 2012), ideal to support the study of selective transport processes. On the other hand, it also include the grain-size range of Grande beach sediment (see Chapter 4).

From approximately 12 tons of sediment collected at Norte beach, 1.7 tons were used in the tracer experiment of Grande beach. The sediment tagging process included sediment washing, dryness and painting. For better adhesion of the ink on the grains surface the sediment was washed with running freshwater, inside of permeable big bags, until the salt particles were completely removed. The washed sediment was dispersed on the ground at a storehouse to dry, before being painted with a mixture of orange fluorescent ink and cellulose diluent. The ink and diluent quantities were estimated based on tests performed by Silva (2005) that suggests the use of a mixture composed by 40 % of ink and 60 % of diluent, and then, a 1:30 proportion of diluted ink and sediment. Painting was performed for sediment portions of 100 to 130 kg, using a concrete mixer in motion to minimize sediment aggregation during the drying process. Finally, the tracer was stored in portions of about 16 kg inside polyethylene bags (**Figure 5.2**).

[4] Beach to Canyon project website: http://beachtocanyon.fc.ul.pt/

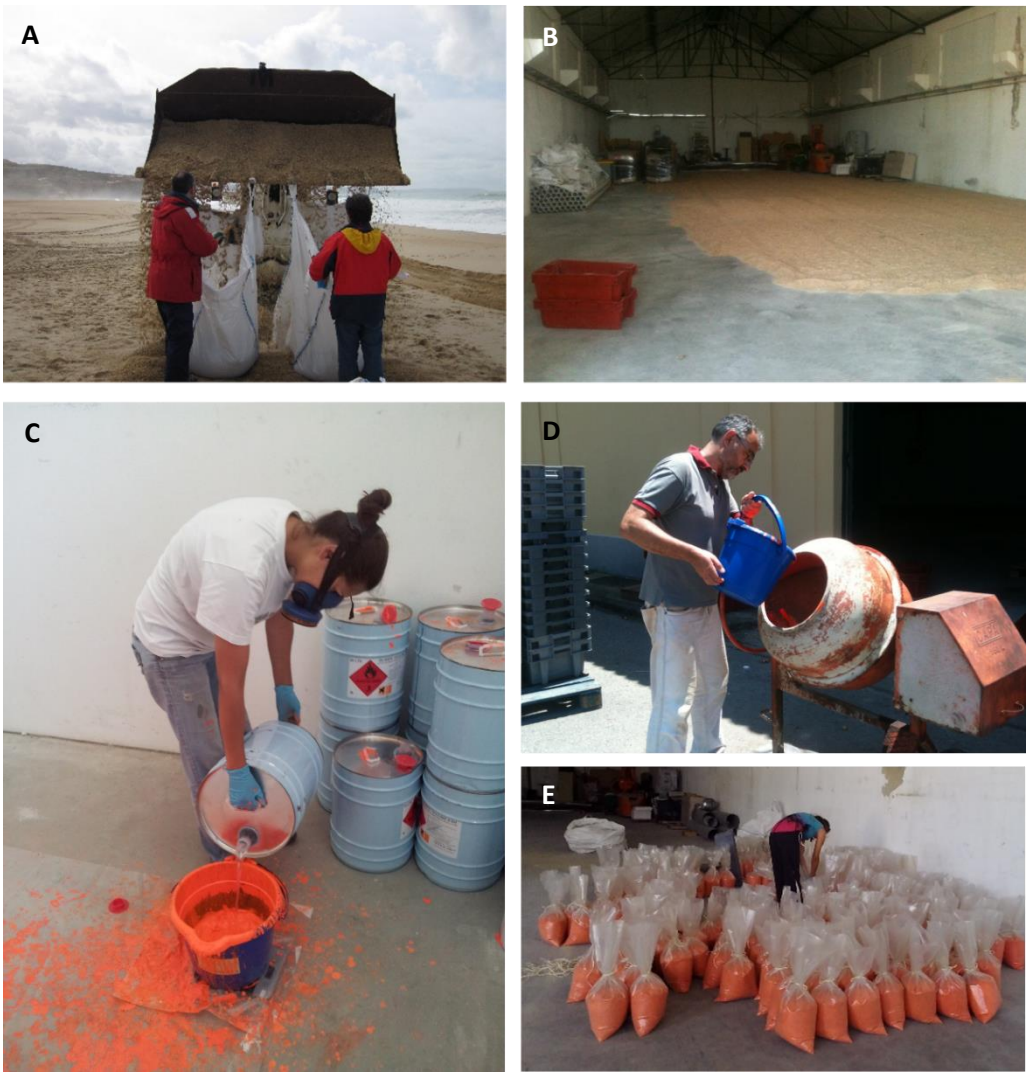

Figure 5.2. (A) Sediment collection at Norte beach; (B) drying of the washed sediment; (C) preparation of the diluted fluorescent ink; (B) painting process in a concrete mixer; and (G) storage of the fluorescent tracer.

5.2.1.3 Fieldwork and data acquisition

The tracer experiment was scheduled for the end of summer season, considering that the maximum beach rotation occurs during the summer, due to the persistent NW low-energy wave conditions (Chapter 3), which are favourable to the HSB. Few days before the field campaign, wave forecasting indicated a change in wave direction that was not favourable to the southward sediment transport. However, taking into account the scheduling and logistics constraints inherent in fieldwork it was not possible to postpone the experiment until favourable HSB conditions so, experiment was carried out on September 8th of 2014.

A northward longshore drift current was confirmed in the experiment day with floating devices (oranges) tossed into the breaker zone. Thus, injection point and sampling sites were defined according to these conditions, as shown in **Figure 5.3**.

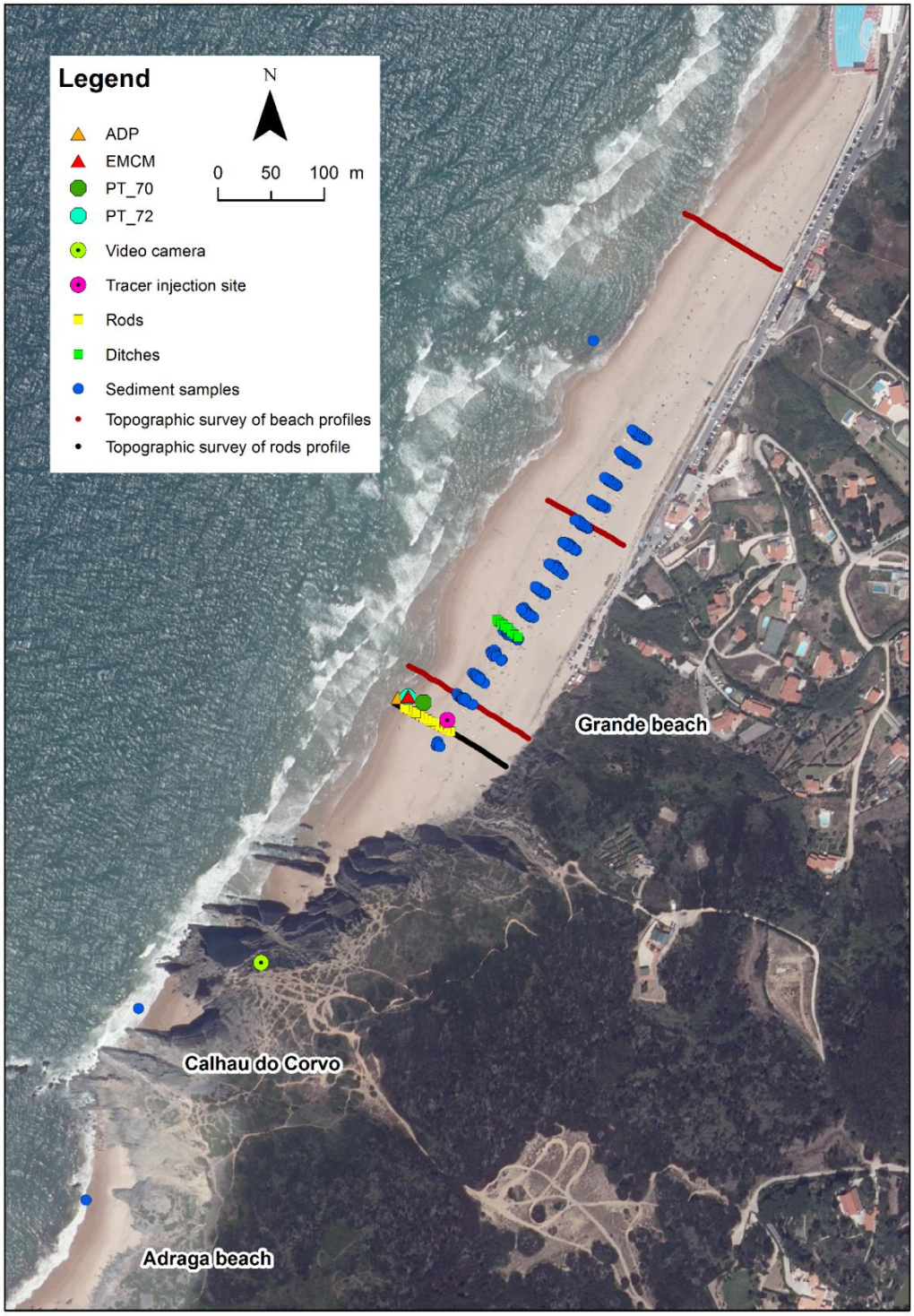

Figure 5.3. Location of the tracer injection point; oceanographic sensors; sediment sampling and mixing depth (rods and ditches) monitoring sites; and beach topographic surveys (background image: orthophotomap acquired on June 2012, provided by *Direcção-Geral do Território* - DGT).

Morphological changes were monitored on three cross-shore beach profiles with a GPS-RTK, during low tide levels before and after the tracer experiment. Although it was not necessary for the tracer dilution method, the thickness of the active layer was measured during the low tide subsequent to the tracer experiment, based on sediment thickness deposited above the washers

on the rods. However, only 6 rods (on the low-tide terrace) remained from the initial 13, thus thickness of the mixing layer in the beach face was obtained from the tracer vertical displacement observed at 6 ditches opened along a cross-shore profile downdrift the tracer injection site (**Figure 5.3**).

Oceanographic conditions (tide, waves and currents) were monitored along a cross-shore profile, at approximately 29 m, 43 m and 51 m offshore the tracer injection point (**Figure 5.3**). The first monitoring point included a pressure transductor (PT70), the second one included a pressure transductor (PT72) and an electromagnetic current meter (EMCM), and the third one included an acoustic doppler current profiler (ADP). The acquisition frequency of the PTs and EMCM was 2 Hz, while for the ADP was 1 Hz. Once these sensors were offshore the breaking zone during the tracer injection, direction and magnitude of the longshore drift current, were also estimated using floating devices (oranges) tossed into the breaker zone. These estimations were done at several locations along the sediment sampling stretch. The wave direction was monitored using a video camera placed at Calhau do Corvo headland (**Figure 5.3**).

The tracer experiment was carried out around the high-tide level, when the surf zone was narrower and the waves were plunging at the beach face, avoiding therefore a great dispersion of the tracer on the low-tide terrace and the rip currents, which are more active during lower tide levels. Tracer was injected at the inferior limit of the swash zone, at a 16 $kg.min^{-1}$ rate, during 1 hour and 46 minutes (from 14:09 to 15:55). Superficial sediment samples (≈1 cm thickness) were collected along 13 downdrift cross-shore profiles spaced by 25 m, from the injection site (**Figure 5.3** and **Figure 5.4**). Sediment sampling was also performed along one updrift cross-shore profile, located 25 m from the injection site, to check for any inversion in the longshore drift during experiment. Sampling began 10 minutes after the beginning of tracer injection and extended for about 1 hour and 10 minutes after the injection ended. Sediment sampling cycle over all profiles lasted about 20 to 30 minutes, but due to the limited number of persons, it was not performed synchronously.

Even with the northward longshore drift, two sediment samples southward of injection point were collected after the tracer experiment, one at Adraga beach (20:15) and another one at the tip of Calhau do Corvo headland (20:30). Sediment of the inner sandbar was also sampled at about 400 m downdrift of the injection point (21:50). The grain-size analysis of these sediment was already presented in Chapter 4, but is presented and discussed in this chapter together with the tracer results.

Figure 5.4. Tracer experiment: (A) 106 bags with 16 kg of tracer each one; (B) and (C) tracer injection at the inferior limit of swash zone; and (D) sediment sampling.

5.2.1.4 Data processing and analysis

Oceanographic data

Wave parameters (height and period) were computed for 10 minutes interval, from the spectral analysis of the pressure transducers records, accounting for pressure attenuation according to Kamphuis (2000). The magnitude of cross-shore and longshore currents measured by the EMCM were averaged for each 10 minutes interval, while current data acquired by the ADP were processed for a 30 minutes interval, using *SonTek ViewADP* software. The wave direction and wave breaking angle were obtained from the video images, which were corrected and rectified using a set of ground control points acquired during the image acquisition, following the work of Taborda and Silva (2012).

Sedimentological data

The sediment grain-size analysis was performed for a sub-set of the samples collected during the experiment (23 from 286 samples), in order to compare the grain-size distribution of the Grande beach sediment and the tracer sediment. The analysis was performed according to the method described in section 4.2.2.1 of the previous chapter.

Tracer data

Sediment samples collected for the tracer analysis were washed with freshwater and dried in an oven at 100°C; afterwards each sample was well mixed and spread on black boards, in a way

that the sediment completely covered the board, before being photographed with white and ultraviolet (UV) light using a digital camera (**Figure 5.5**).

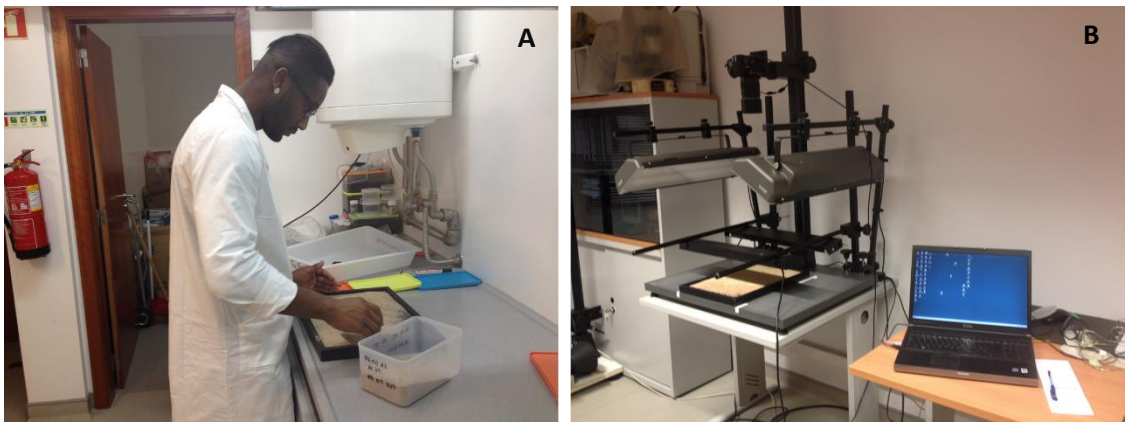

Figure 5.5. (A) Spreading of a portions of sediment sample in a black board and (B) image acquisition system.

Tracer particles detection and counting were done by image analysis using a MATLAB toolbox (*SedPhoto2* toolbox – see Appendix B). This toolbox converts, originally acquired RGB images into Lab colour space images (Hunter labs, 1996) and, identifies the area occupied by each tracer particle through image segmentation (image binarization). The image segmentation process is defined based on threshold values for *a* and *b* (colour-opponent dimensions) obtained from the spectral signature of the tracer particles, and based on an adjustment of *L* (lightness). This procedure can be done using the UV light images only; however, as some shells particles reflected in the same spectral range of tracer particles, white light images were also used to differentiate shells from tracer (under white light, shells display a white colour while tracer displays an orange colour).

Based on the area of tracer particles computed with *SedPhoto2*, it was possible to perform a grain-size analysis, assuming an equivalent diameter. Tracer particles were grouped in 1 ϕ classes and the individual frequency of each class was estimated, allowing the computation of a mean grain-size of tracer for each sample.

The tracer concentration, or dilution, was obtained through the ratio between the area occupied by the tracer particles and the image area. To estimate a longshore drift rates, these relative dilutions were converted into mass dilutions using a calibration curve. This curve was developed based on standard dilutions obtained with controlled masses of the tracer relatively to the natural beach sediment. The standard dilution samples were, equally, photographed and processed with the *SedPhoto2* toolbox. The relation between the relative area dilutions (Dr) and the standard mass dilutions (Dm), was obtained by a least square linear fitting forcing the

regression line to pass though the origin (**Figure 5.6**). The tracer dilution of each sediment sample was then computed considering all tracer particles and for each tracer grain-size class.

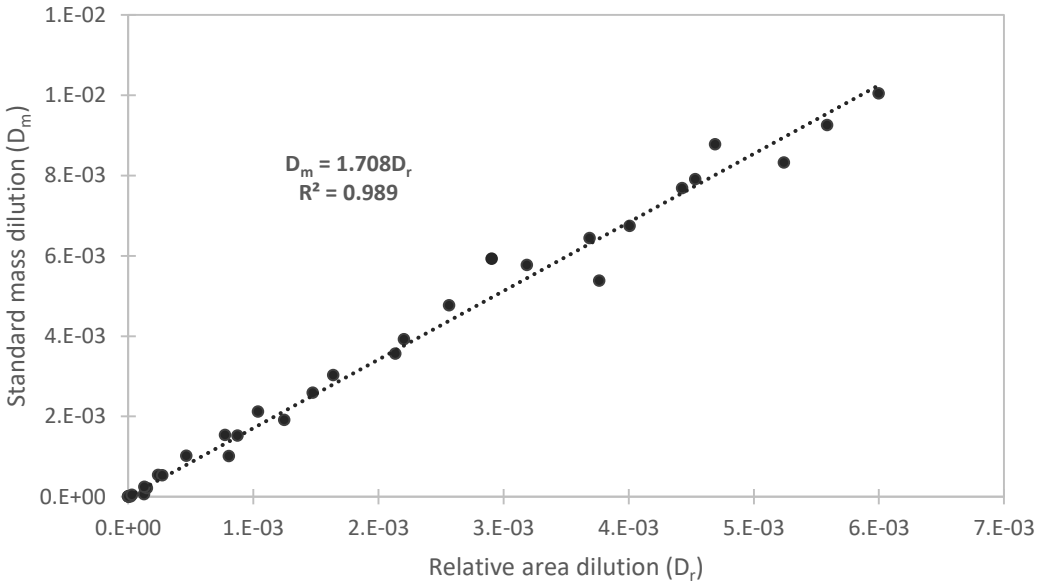

Figure 5.6. Relation between standard mass dilution (D_m) obtained from controlled masses of tracer and relative area dilution (D_r) obtained from the image analysis.

5.2.1.5 Tracer concentration modelling

Tracer dilution is a consequence of advection and diffusion processes. Thus, an analytical solution of advection-diffusion equation (ADE) was used to model the tracer concentrations observed alongshore over the time. According to Socolofsky and Jirka (2005), 1D ADE is given by expression:

$$\frac{\partial c}{\partial t} + v_a \frac{\partial c}{\partial x} - D \frac{\partial^2 c}{\partial x^2} = 0 \qquad (\mathbf{5.3})$$

where c is the concentration, D is the diffusion coefficient, v_a is the advection velocity, x is the coordinate in the flow direction and t is the time. If an initial concentration (c_0) is assumed, the analytical solution of 1D ADE for an instantaneous concentration at a point is given by:

$$c(x,t) = \frac{c_0}{2} erfc\left[\frac{x - v_a t}{\sqrt{4Dt}}\right] \qquad (\mathbf{5.4})$$

where $erfc$ is the error function.

To fit the aforementioned model to the data, an unconstrained nonlinear optimization algorithm (*fminsearch* function of MATLAB) was applied to find a v_a and D local minimums of the scalar function $c(x,t)$, starting at an initial estimated which in this case was the steady state concentration ($c_0 = \bar{c}_{eq}$).

5.2.1.6 Longshore sediment transport

The longshore drift rate was computed from the equation (5.1), based on the tracer equilibrium concentration ($\bar{c}_{eq}$), and on the volumetric tracer injection rate (16 kg.min^{-1}). The rate obtained was compared with the rate estimated by the Bagnold (1963) approach that relates the immersed weight sediment transport with the wave energy flux and the longshore drift current. According to the simplifications proposed by Komar (1998) based on the wave linear theory, this approach can be given by:

$$I_l = K' E_b \frac{\bar{v}_l}{0.5\gamma_b} \quad (\mathbf{5.5})$$

where $\bar{v}_l$ is the mean longshore current velocity; $E = 1/8\,\rho g H_b^2$ is the total wave energy (ρ is the sea water density (1025 kgm^{-3}), g is the gravitational acceleration (9.81 ms^{-2}) and H_b is the breaking wave height); K' dimensionless empirical coefficient, assumed as 0.28 according to Komar and Inman (1970), when root mean square wave height at the breaking is used to compute the total wave energy.

The immersed weight transport rates were converted into volumetric sediment transport rates (Q) by the relation $I_l = (\rho_s - \rho)(1-p)gQ$, where ρ_s is the sediment density (quartz density was assumed 2650 kgm^{-3}), and p is the sand porosity (0.4).

5.2.2 Results

5.2.2.1 Beach morphology

Topographic profiles show that the beach had a steep beach face ($tan\beta = 0.12$) with a low-gradient tide terrace ($tan\beta = 0.03$) and that the berm width and elevation increased from north to south. The comparison of the profiles surveyed during low-tide before and after the experiment, revealed no significant morphological changes (**Figure 5.7** to **Figure 5.9**).

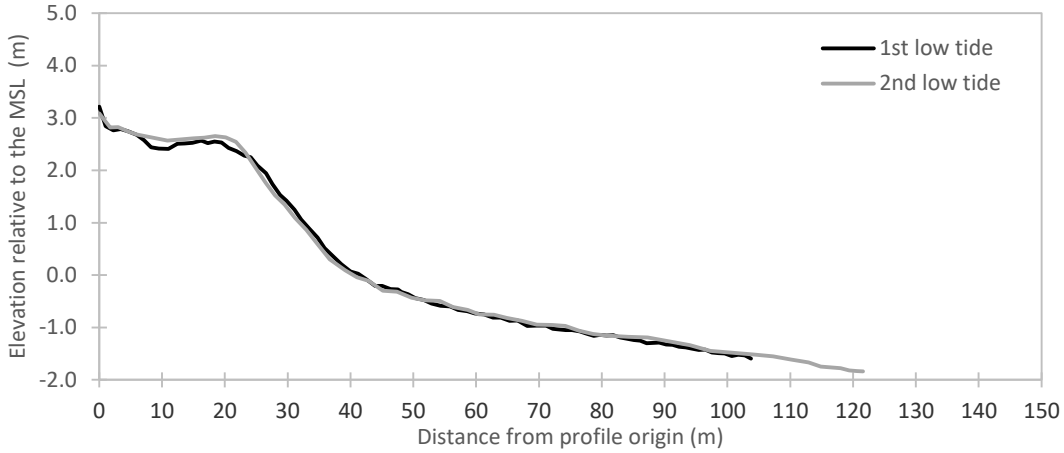

Figure 5.7. Topography of the beach cross-shore profile at the northern sector.

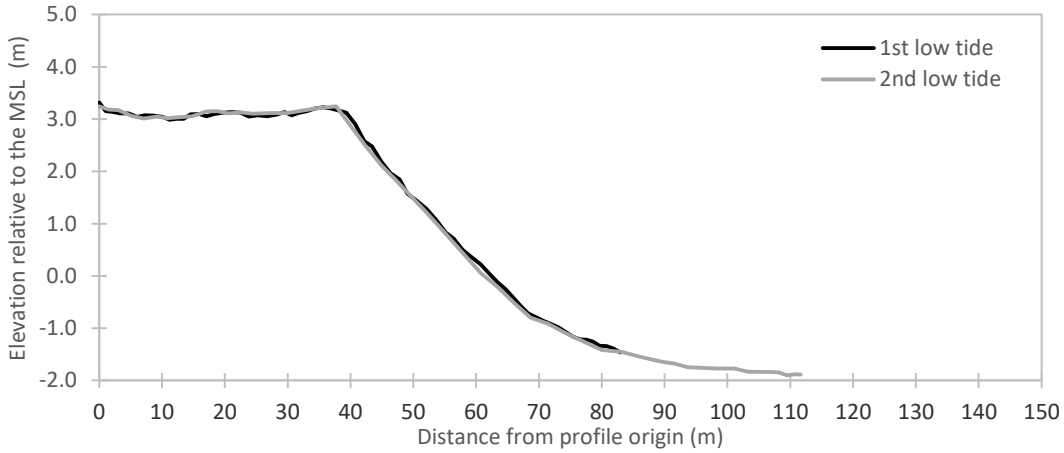

Figure 5.8. Topography of the beach cross-shore profile at the central sector.

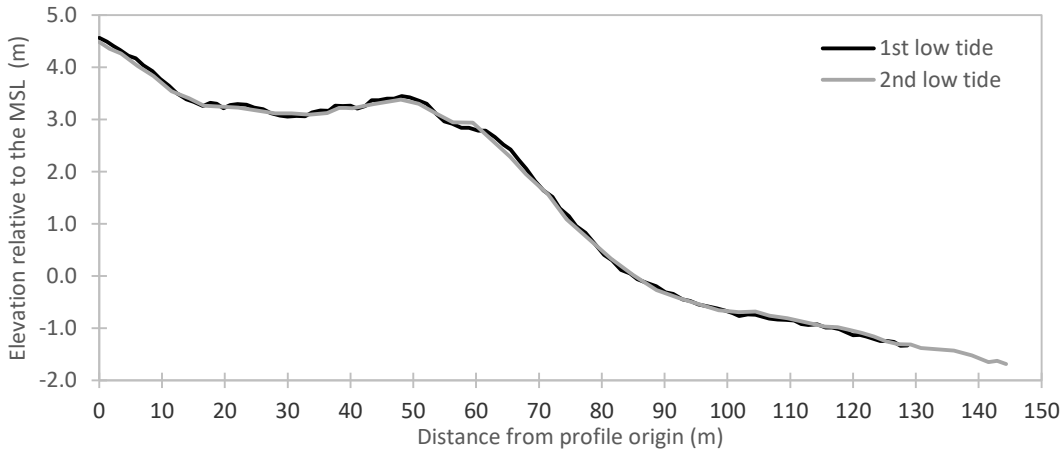

Figure 5.9. Topography of the beach cross-shore profile at the southern sector.

5.2.2.2 Oceanographic conditions

The variation of water level measured at the three monitoring sites is presented in **Figure 5.10**; it can be noticed that water level measured by ADP is higher than PTs, which can be explained by a sinking of the ADP structure relative to the initial position. The tracer experiment began 35 minutes before the high-tide and ended 2 hours and half afterwards, during this period water level variation was about 1.2 m.

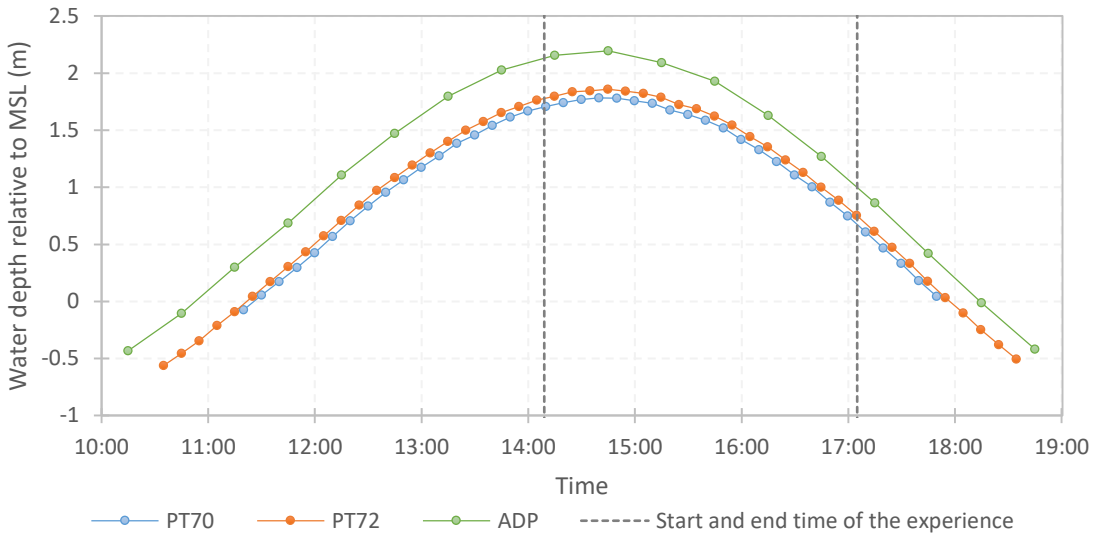

Figure 5.10. Water level relative to the MSL measured by ADP and PTs.

The wave parameters obtained from the two PTs records are in agreement. The mean significant wave height (Hs) and mean zero crossing wave period (Tz) were 0.7 m and 6 s, respectively (**Figure 5.11** and **Figure 5.12**).

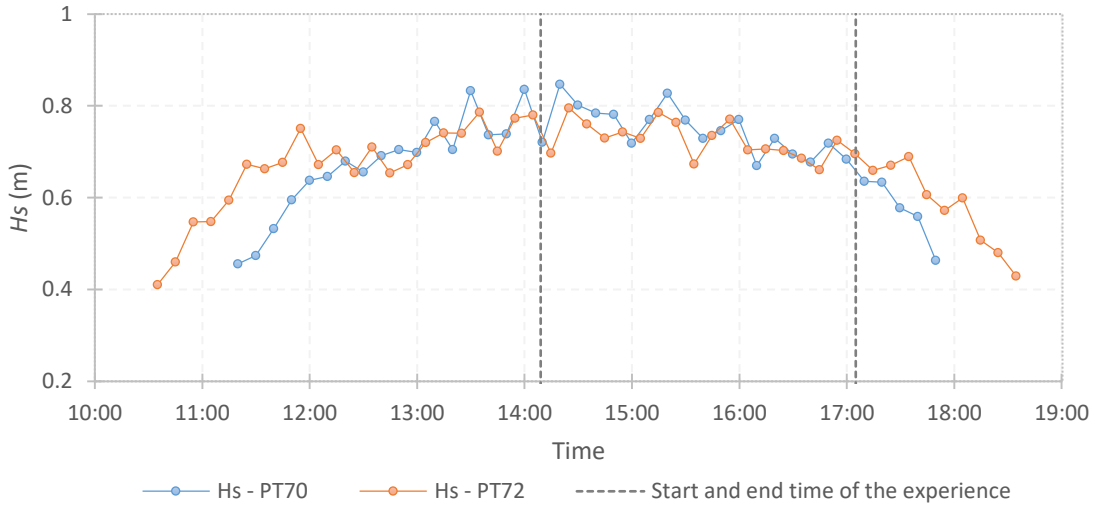

Figure 5.11. Significant wave height (Hs) computed from pressure transducers records.

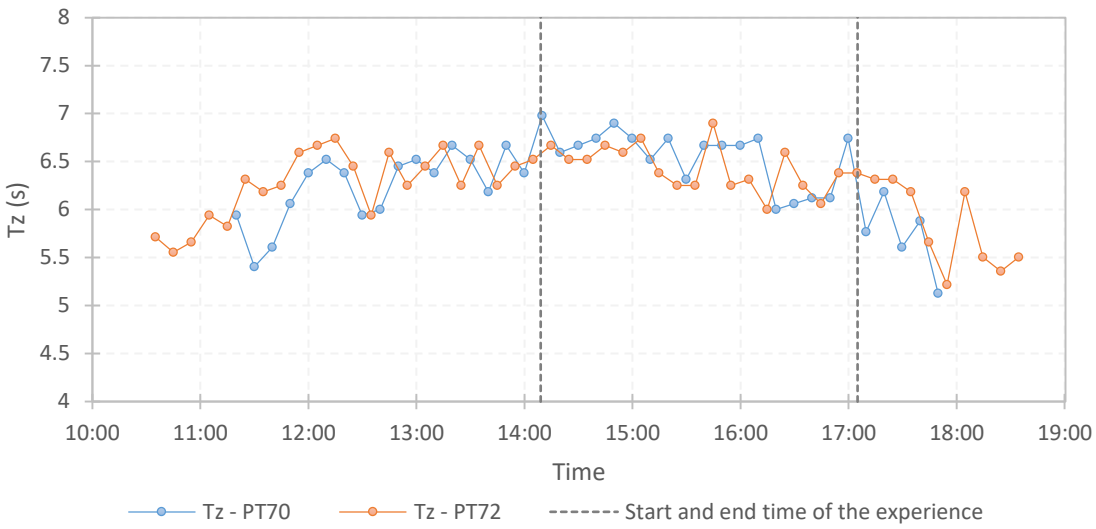

Figure 5.12. Wave zero crossing period (Tz) computed from pressure transducers records.

The video images show a crossed sea state during the field experiment (**Figure 5.13**). Two wave sets can be observed, one coming from W with directions approximately between 270° and 280°, the other one coming from NW with directions approximately between 310° and 320°. The analysis of rectified images shows a negative wave breaking angle, *i.e* northward. However, the angles measured on the images vary alongshore. For example, the angle measured south of the injection point (21°, see **Figure 5.14A**) is considerably larger than the one measured northward of this point (7° in **Figure 5.14A** and 6° in **Figure 5.14B**).

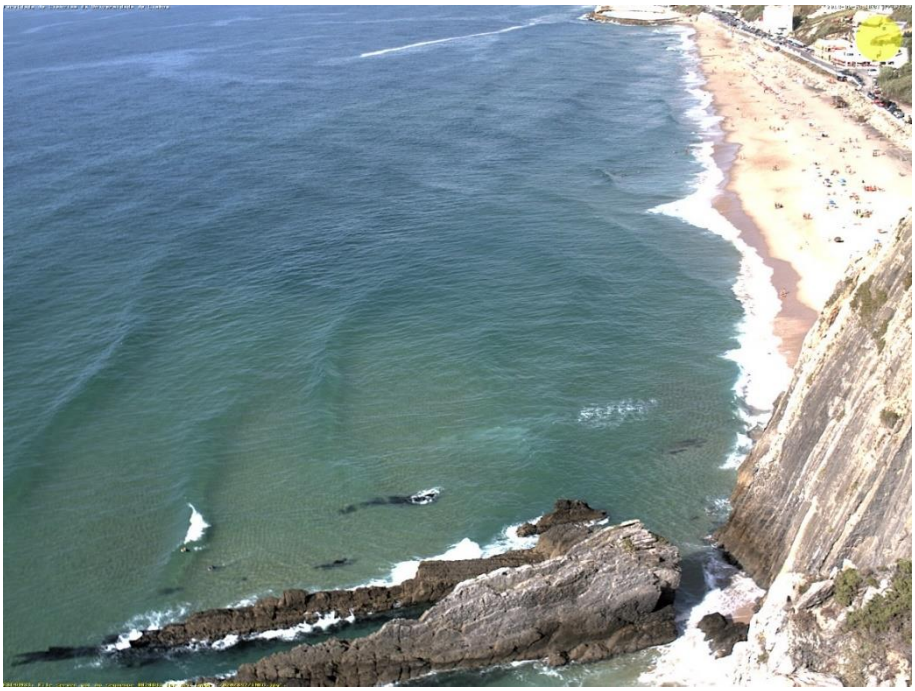

Figure 5.13. Cross sea state observed from Calhau do Corvo (video image acquired at 17:00).

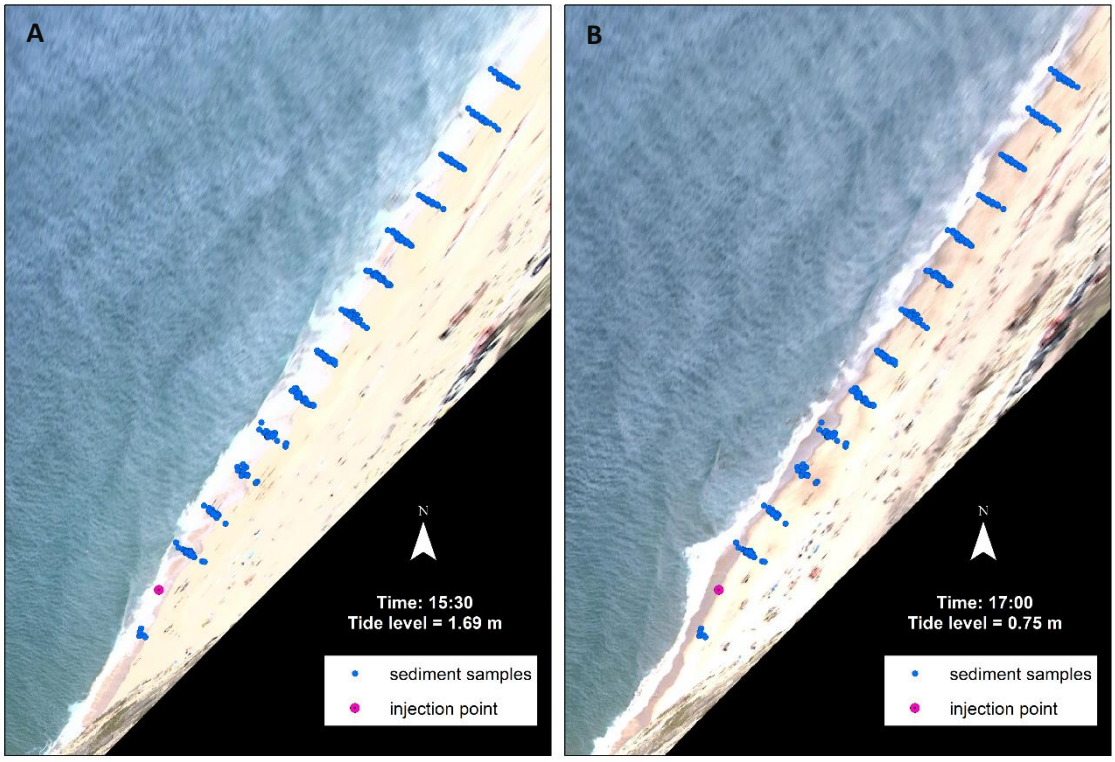

Figure 5.14. Wave direction and incident angle at the breaking observed from the video images aquired at: (A) 15:30 with a tide level of 1.69 m (MSL) and (B) 17:00 with a tide level of 0.75 m (MSL).

The depth-average velocity measured by ADP reached the highest magnitudes when the waves were breaking closer to the sensor, with maximum values of 0.64 and 0.47 $m.s^{-1}$ at the beginning and the end of the record, respectively. Under these conditions, the flow was northward. During the tracer experiment period, the water column above the sensor was higher (offshore the breaking zone), being the flow magnitude lower (< 0.1 $m.s^{-1}$) and southward (**Figure 5.15**).

The longshore current velocity measured by EMCM present a similar pattern, despite the slightly lower maximum magnitudes in the beginning and end of the record (0.54 and 0.42 $m.s^{-1}$, respectively). On the other hand, the cross-shore current measured by EMCM present negative values that, considering the sensor position, indicate a flow towards offshore with magnitudes ranging between 0.003 and 0.12 $m.s^{-1}$ (**Figure 5.15**).

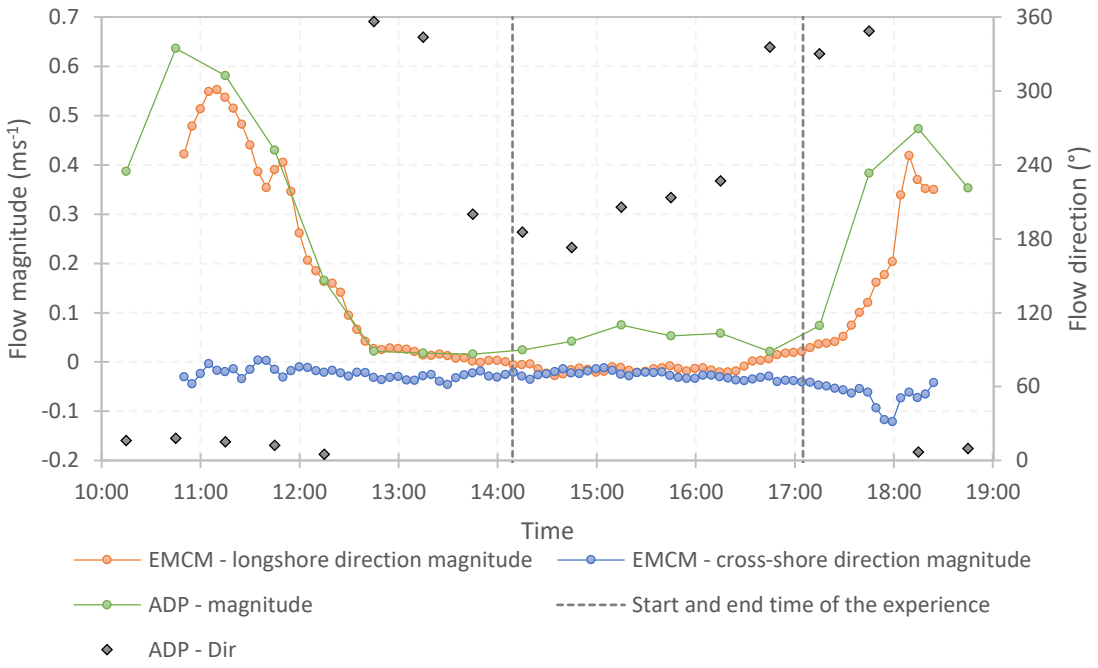

Figure 5.15. Depth-average velocity and current direction meausred by ADP, and lonsghore and cross-shore current measured by the EMCM at 0.41 m from the bottom. In the EMCM case, positive values in longshore direction correspond to a northward flow and positive values in cross-shore direction correspond to a shoreward flow.

The results of the measurements with floating devices show that longshore drift during the tracer experiment was northward, being possible to notice an increase of the current magnitude over time. The magnitudes measured using this method reached values significantly higher ($\approx$ 2 m.s^{-1}) compared to the sensors. However, the mean value was 0.79 m.s^{-1}, close to the magnitudes measured by the sensors under the breaking wave conditions. Furthermore, no clear relation between magnitudes and alongshore position was found (**Figure 5.16**).

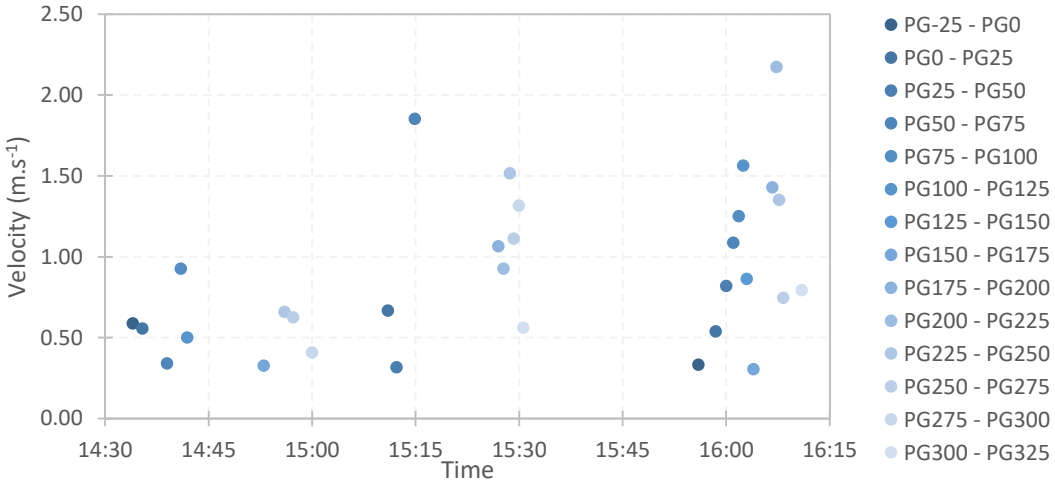

Figure 5.16. Longshore current drift estimated with floating devices at several alongshore positions, between profiles PG-25 and PG325.

5.2.2.3 Thickness of sediment active layer

The thickness of active layer was measured based on sediment deposited on rods and from the tracer vertical displacement (**Figure 5.17**). It should be noted that despite the overlapping representation of the profiles, these were located at distinct positions along the coast. Rod's profile was located close to the tracer injection point, while ditches profile was located 150 m downdrift the injection point and corresponded to the beach face domain.

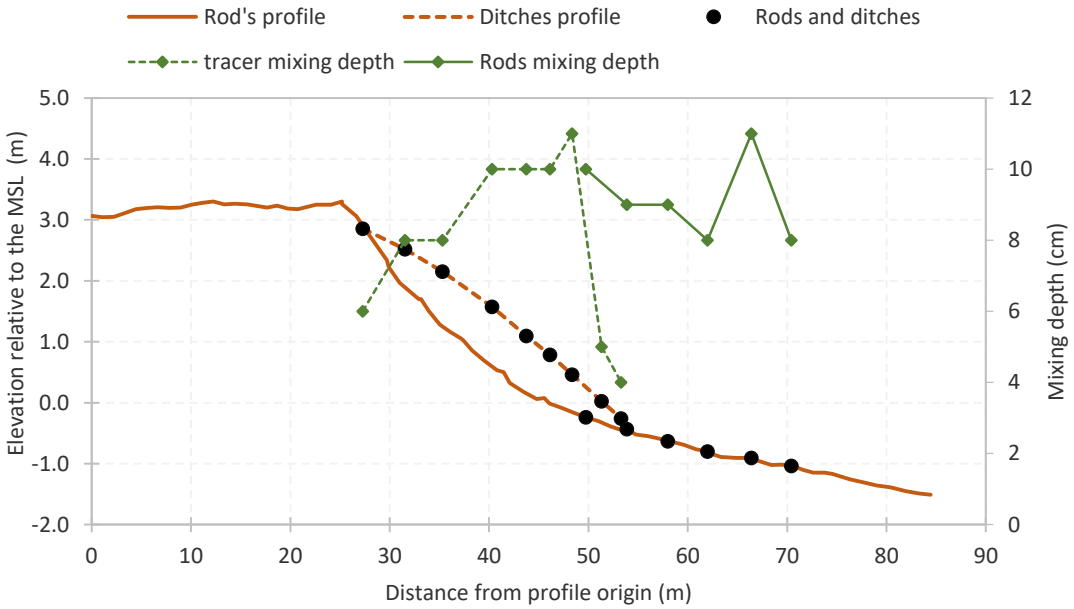

Figure 5.17. Thickness of the active layer measured on ditches through the tracer vertical mixing and on sediment deposition measured on rods.

The results show that the mixing depth increased from 6 to 11 cm from berm crest to the base of the beach face, while at the transition zone, between beach face and low-tide terrace (around 50 m from the profile origin), mixing depths were smaller than the ones obtained with rods. These differences can be related with measurement inaccuracies due to the presence of water and to differences of profile morphology, especially when in presence of cusps systems, as can noticed by the concave and convex shape of the two profiles. The mixing depth at the low-tide terrace varied between 8 and 11 cm.

5.2.2.4 Grain-size of the tracer particles and beach native sediment

Grain-size distributions obtained from laboratorial analysis show that sediment samples collected at the beach face and berm of Grande beach had mean grain-sizes between 0.60 ϕ and 0.9 ϕ (coarse sand), with standard deviations inferior to 0.38 ϕ (well to very well sorted). The sediment used to trace transport, on the other hand, had mean grain-sizes between - 0.06 ϕ and 0.44 ϕ (very coarse to coarse sand), and standard deviations between 0.68 ϕ and 0.80 ϕ

(moderately to moderately well sorted). Despite the differences in grain-size distributions of the tracer and the beach native sediment, tracer grain-size range covers the entire grain-size range of Grande beach (**Figure 5.18**).

The sediment collected at Calhau do Corvo and Adraga beach presents a grain-size distribution similar to the sediments collected at beach face and berm of Grande beach; although, in the case of Adraga, a slight enrichment in medium sand is observed. On the other hand, the sediment collected at the inner sandbar is clearly finer compare to the beach face and berm of the Grande beach.

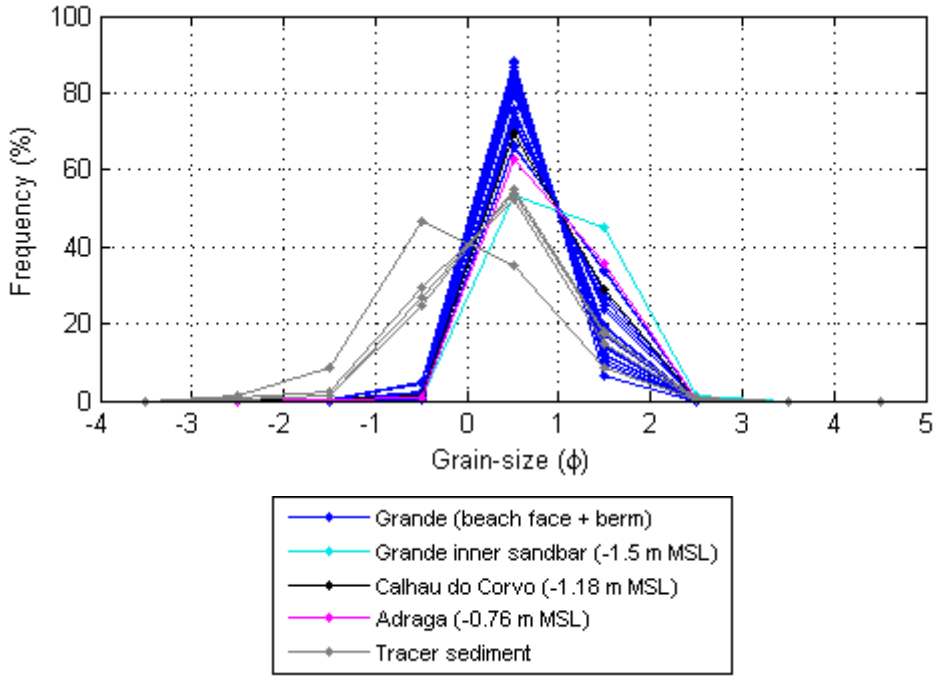

Figure 5.18. Grain-size distribution of beach native sediment and tracer samples, obtained from laboratory analysis.

The grain-size analysis of tracer particles found in sediment samples collected during the tracer experiment (computed by image analysis), show three main grain-size modal classes: very coarse sand (-1 ϕ to 0 ϕ), coarse sand (0 ϕ to 1 ϕ) and medium sand (1 ϕ to 2 ϕ). The results also show the existence of particles smaller than 3 ϕ that, according to the laboratory grain-size analysis of the tracer sediment, had null percentages (**Figure 5.19**).

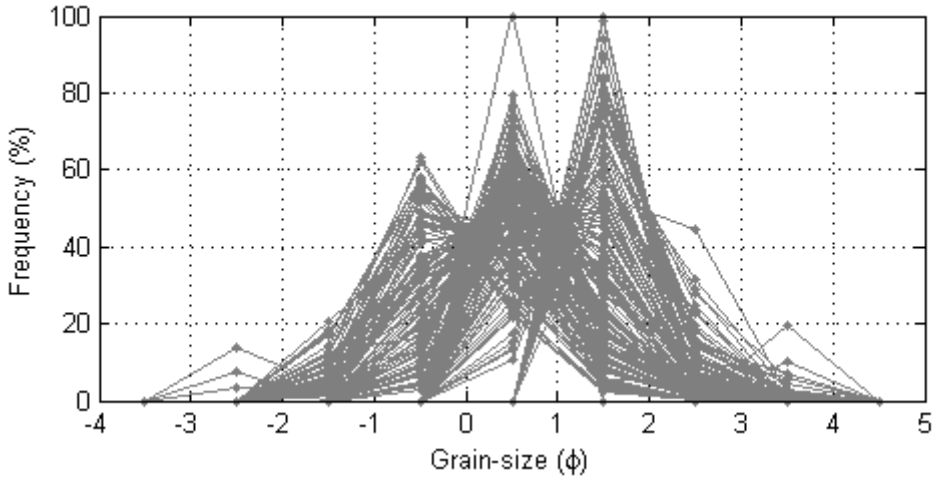

Figure 5.19. Grain-size distributions of tracer particles on the sediment samples obtained from image analysis.

The spatial analysis of the tracer particles show that mean grain-size decreased with the longshore distance to the injection point. In the cross-shore direction, the mean grain-size decreasing occurred from the lower to higher elevations, correspondingly from lower beach face to upper beach face (**Figure 5.20**).

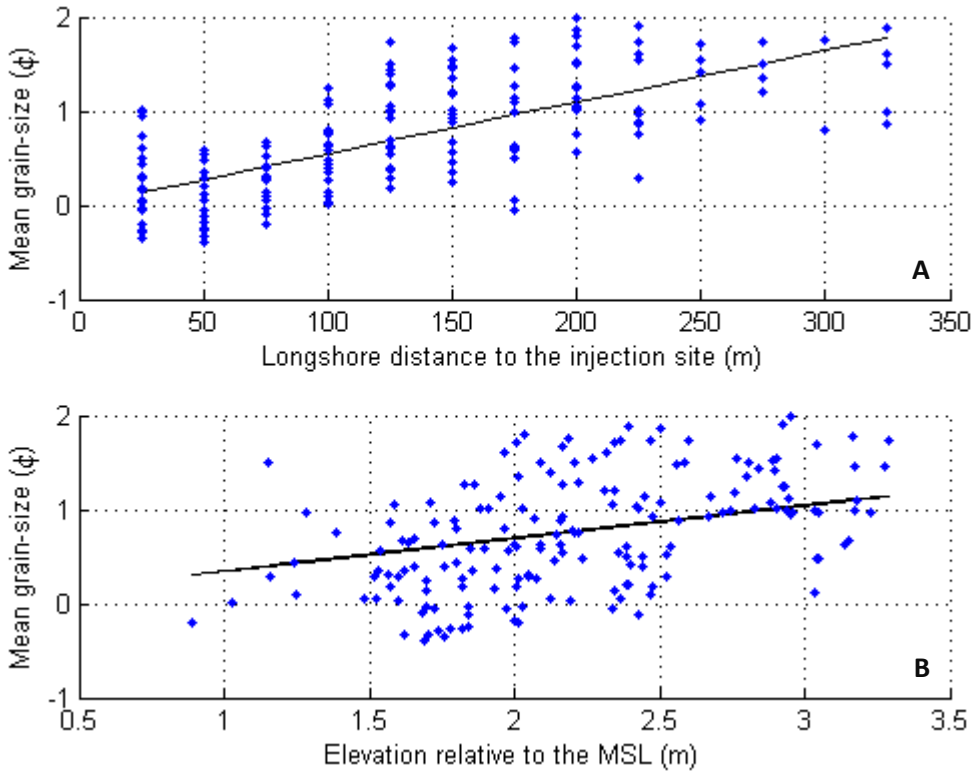

Figure 5.20. (A) Relationship between mean tracer grain-size and longshore distance from the injection site; and (B) relationship between mean tracer grain-size and sample elevation relative to mean sea-level.

5.2.2.5 Tracer dilution

Tracer concentrations of each sediment sample were computed, first, considering all tracer particles, and then separately for each grain-size class (**Figure 5.21**). Updrift of the injection site (-25 m), concentrations were null; while downdrift, as expected, tracer concentration decreased with the distance. The exception is the medium gravel, which has a small significance and did not show any distribution pattern. Up to 50 m downdrift, tracer concentration show large variations along the sampling profiles and an abrupt decreasing in a short time after the tracer injection ended, mainly for coarser particles. Between 75 and 100 m downdrift, it is possible to observe that concentration increased and then then became steadier. This is particularity evident for the finer particles (medium to very fine sand), which reached the steady state earlier. In the case of coarser particles, as well as in the case where all tracer particles were considered, the steady state condition is not so evident. For distances greater than 100 m, concentration increased slower, mainly for coarse sediments, and steady state was not reached.

The sediments collected at the inner sandbar, Calhau do Corvo tip and Adraga beach did not reveal any tracer particle.

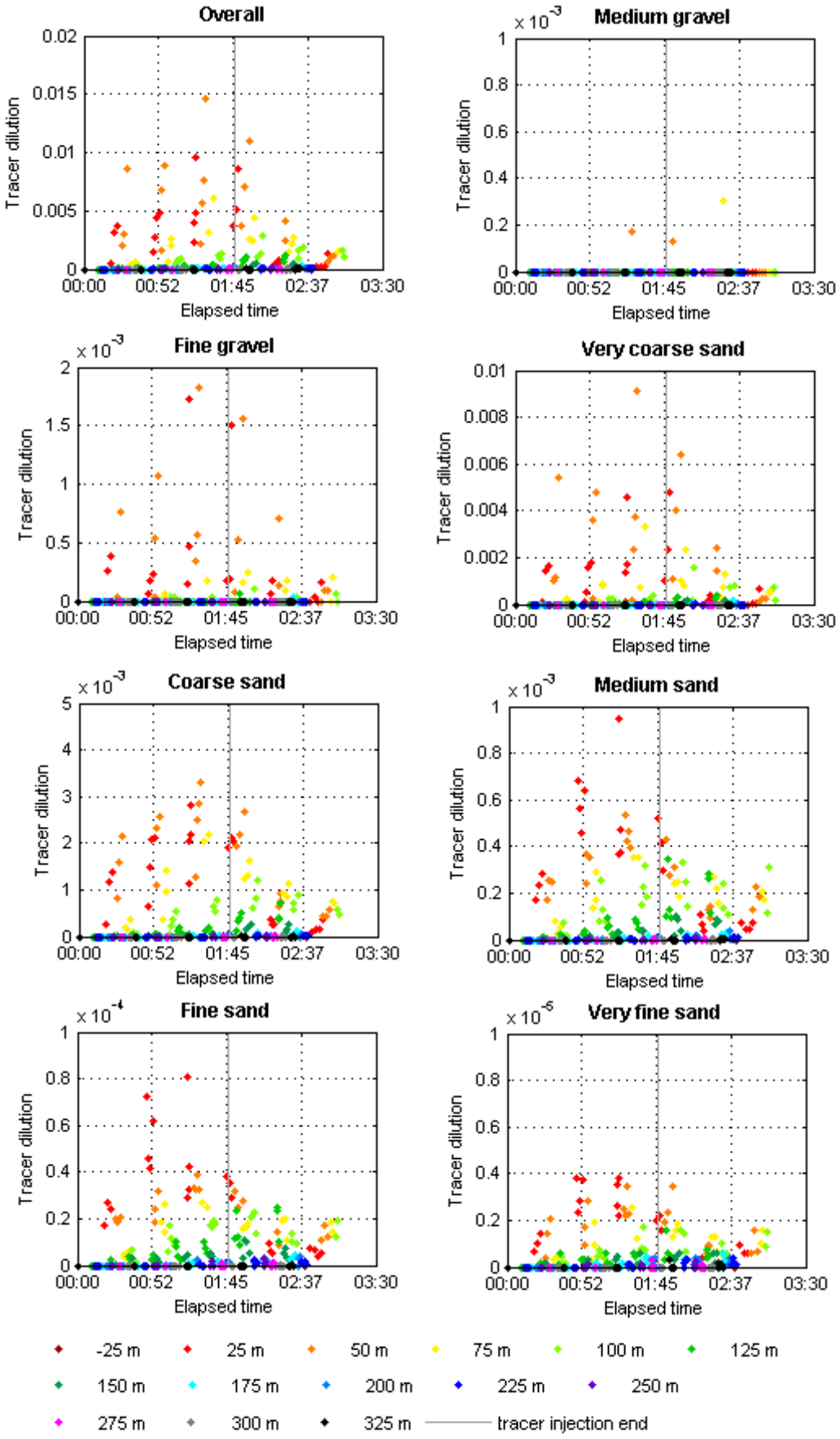

Figure 5.21. Tracer concentration distributions considering all grain-sizes and each grain-size class separately, the colours correspond to the sampling alongshore from the injection site.

The relationship between the tracer dilution and the topographic elevation show that the highest concentrations occurred between 1.5 and 2.5 m (MSL), and that coarser particles (fine gravel and very coarse sand) tended to concentrate below 2 m (**Figure 5.22**).

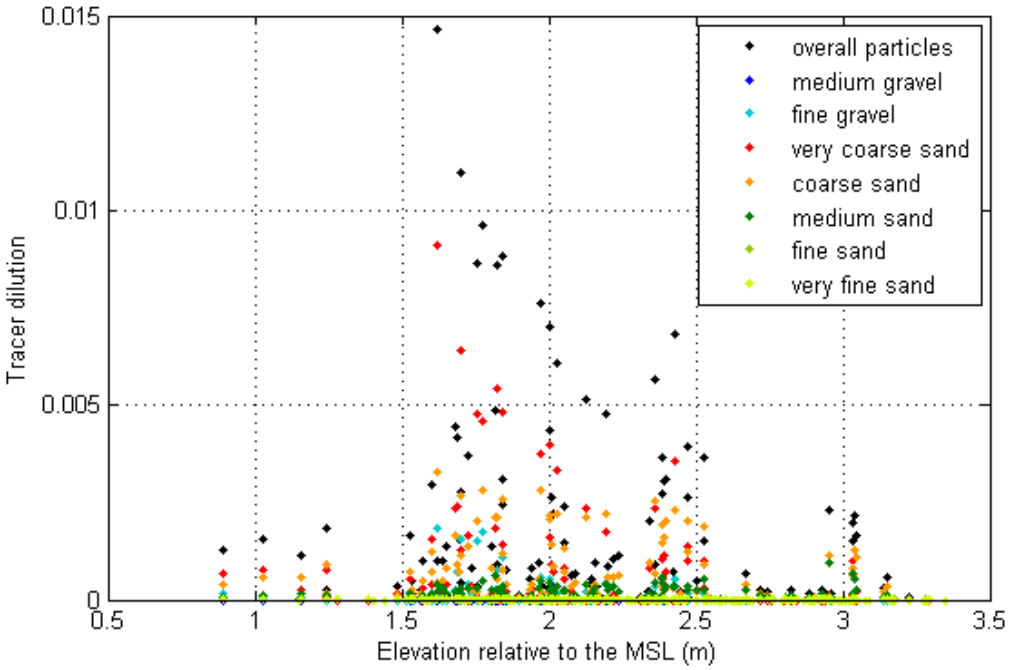

Figure 5.22. Relation between tracer concentration and topographic elevation relative to the mean sea level (MSL).

5.2.3 Discussion

5.2.3.1 Beach morphology and oceanographic conditions

During the tracer experiment (September 8th 2014), Grande beach presented a well-developed berm, a steep beach face and a low-gradient tide terrace (**Figure 5.7** to **Figure 5.9**). Under these conditions, the tracer experiment had to be carried out during high-tide, when the surf zone was narrower and the waves were plunging at the beach face, avoided tracer dispersion on the low-tide terrace.

This fact, led that oceanographic sensors staying most of the time offshore the breaking zone, explaining the low magnitude of the longshore current during high-tide level. However, at the beginning and end of the current records, when the waves were breaking on the sensors, the measured flow was clearly northward and had a magnitude between 0.42 and 0.64 m.s^{-1} (**Figure 5.15**). The mean longshore current measured with floaters was higher (0.79 m.s^{-1}), due to the higher speeds (2 m.s^{-1}) measured at the end of the experiment that seem too high and should

be an effect of sea breeze (**Figure 5.16**). Thus, in the following sections an average value of 0.62 m.s^{-1}, estimated from the previous three values, was considered.

The incident waves were coming from W and NW directions and were characterized by an average Hs of 0.7 m and average Tz of 6 s. The northward longshore current indicate that the flow was dominated by the waves coming from W. However, the interpretation of the incident wave angles at the breaking seem difficult, considering the variations alongshore due to the topo-bathymetric spatial variability and wave interference (**Figure 5.13** and **Figure 5.14**).

5.2.3.2 Tracer dilution modelling and longshore drift

Tracer concentration distributions presented in **Figure 5.21** show a great variation along sampling profiles located at 25 and 50 m downdrift the injection point, as well as an abrupt decay of concentration after the end of the injection, mainly for the coarser particles. This suggest that at these distances tracer was not completely mixed within the active beach transport system. Between 75 and 100 m away from the injection point, steady state concentration of finer particles ($\leq 1\phi$) is clearly observed. For coarser particles this state is not so evident, meaning that the tracer injection should have been extended in time either by using more tracer or through a lower injection rate. Tide level variation during the tracer experiment (approx. 1.20 m) is also a factor that does not match steady state condition.

Nevertheless, the application of the advection-diffusion model to simulate tracer dilution revealed, in general, a reasonable fit to data, supporting the equilibrium concentration identified from the tracer dilutions. Model results for overall tracer particles and for very coarse, coarse, medium and fine sand particles are presented in **Figure 5.23** to **Figure 5.27**, for distances between 75 and 150 m. The results for the remaining distances can be seen in the Appendix C.

Due to the deficient mixture of coarser particles at 25 and 50 m from the injection point, the tracer dilution of the coarse and very coarse sand, as well as the ones obtained considering all tracer particles, at these distances, were not use in the nonlinear optimization to find advection velocity and diffusion coefficient.

Medium gravel was excluded from the analysis due to the inexistence of a coherent dilution pattern; as well as fine gravel, because the results gave an advection velocity almost null and a diffusion coefficient one order of magnitude higher than the ones found for the other grain-sizes, which appears to be unrealistic and deserves further investigation. These results can be explained by the lower frequency of these particles in the tracer sediment (averaging 4 %) and their lower transport rates.

Very fine sand was also excluded because the laboratory grain-size analysis of tracer sediment indicate absence of these particles (**Figure 5.18**). The low percentages of very fine sand obtained from image analysis, should be an effect of particles overlapping, which is more problematic in the case of finer particles, because they tend to fall into spaces between the larger particles.

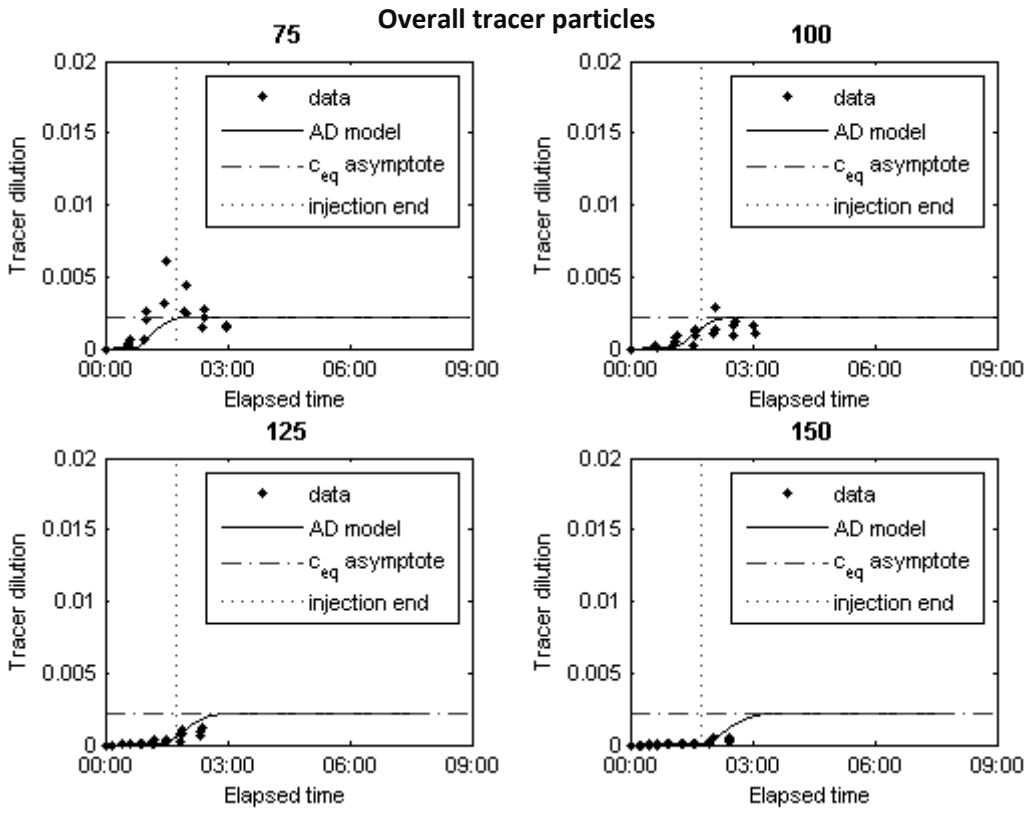

Figure 5.23. Advection-diffusion model for overall tracer particles (75 to 150 m downdrift).

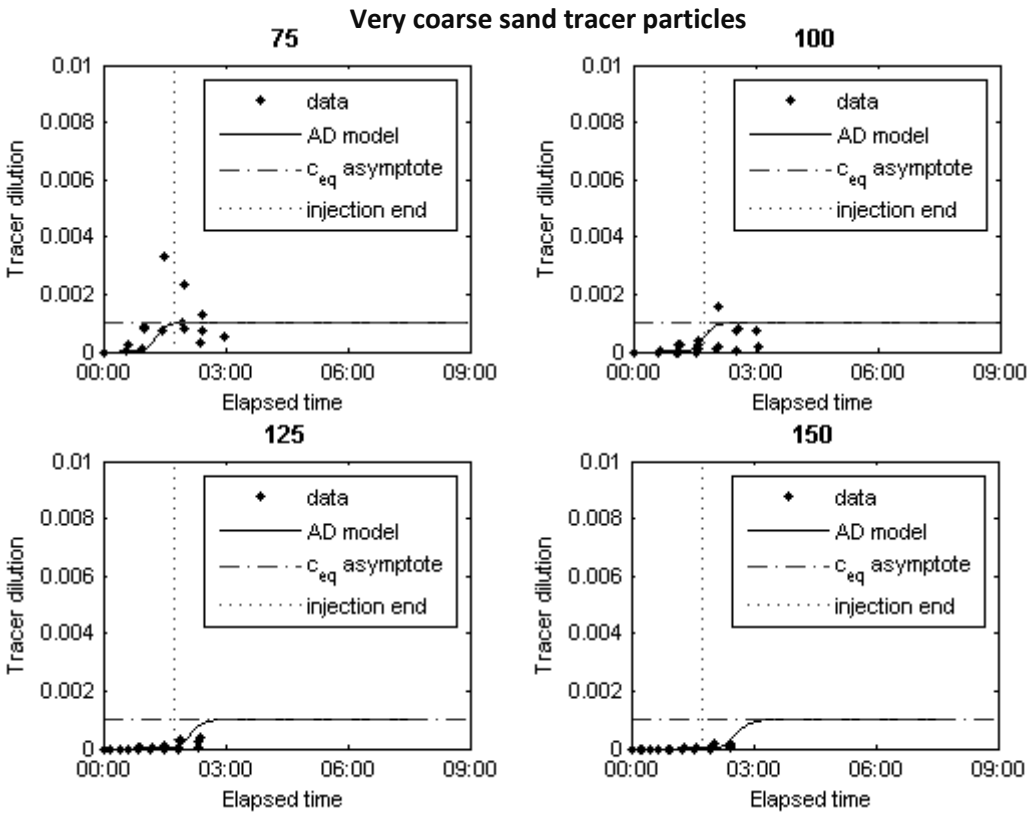

Figure 5.24. Advection-diffusion model for very coarse sand tracer particles (75 to 150 m downdrift).

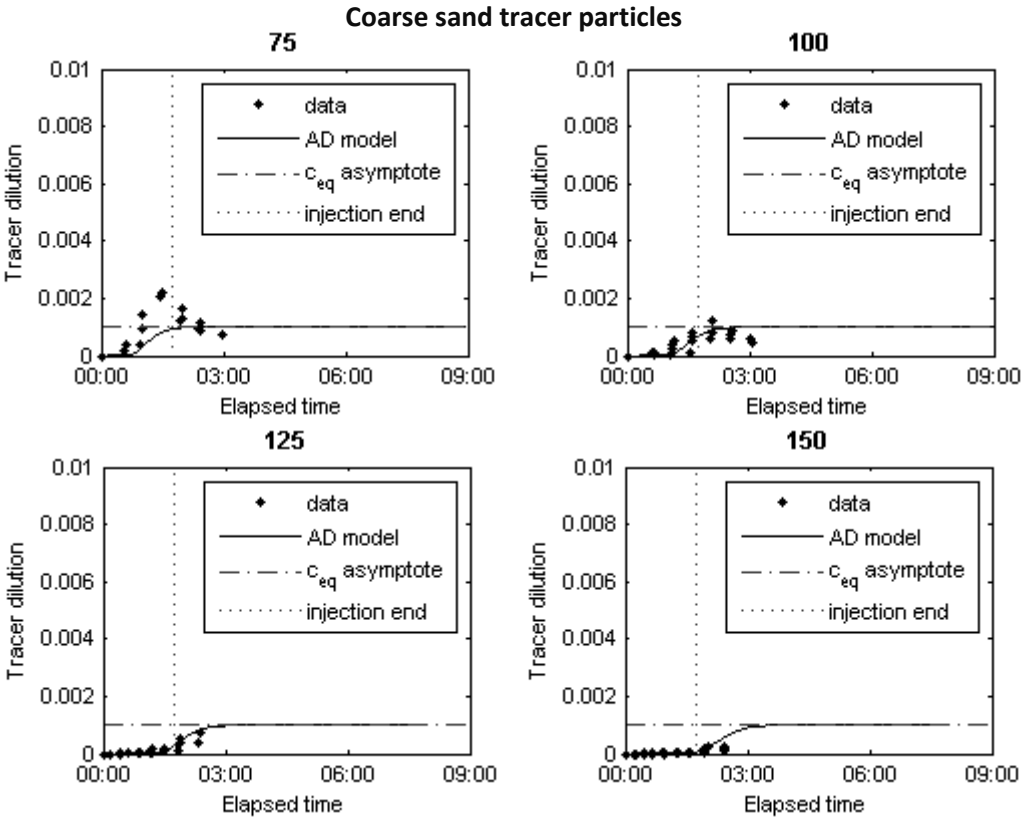

Figure 5.25. Advection-diffusion model for coarse sand tracer particles (75 to 150 m downdrift).

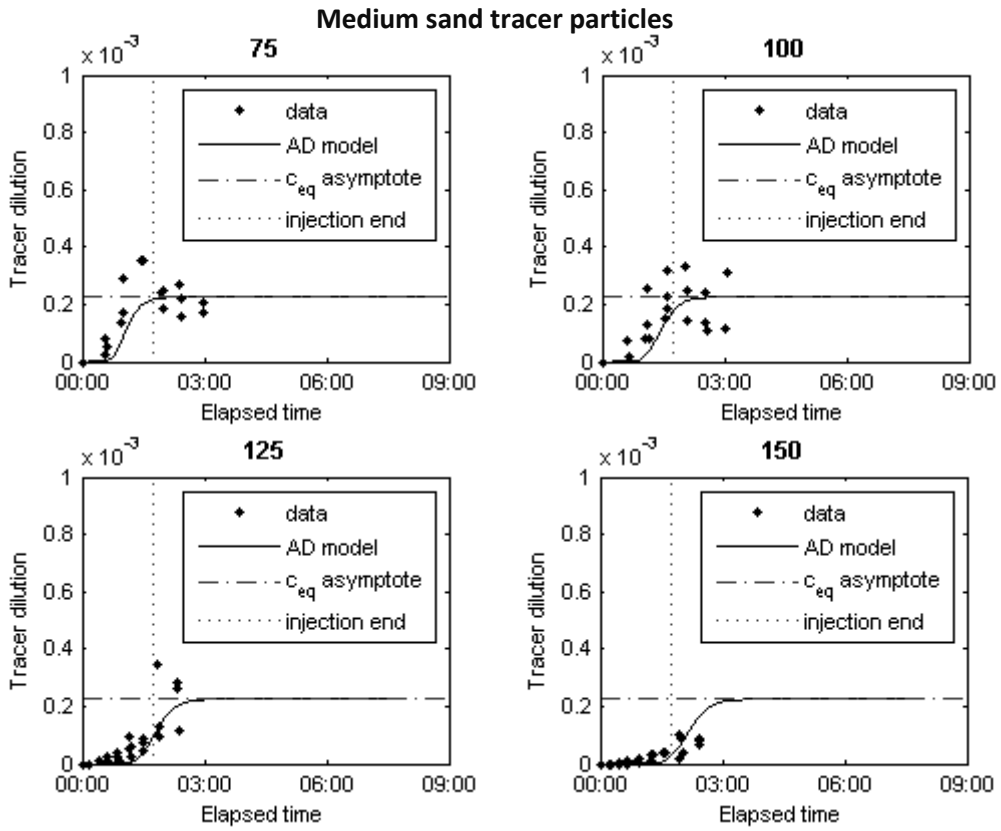

Figure 5.26. Advection-diffusion model for medium sand tracer particles (75 and 150 m downdrif).

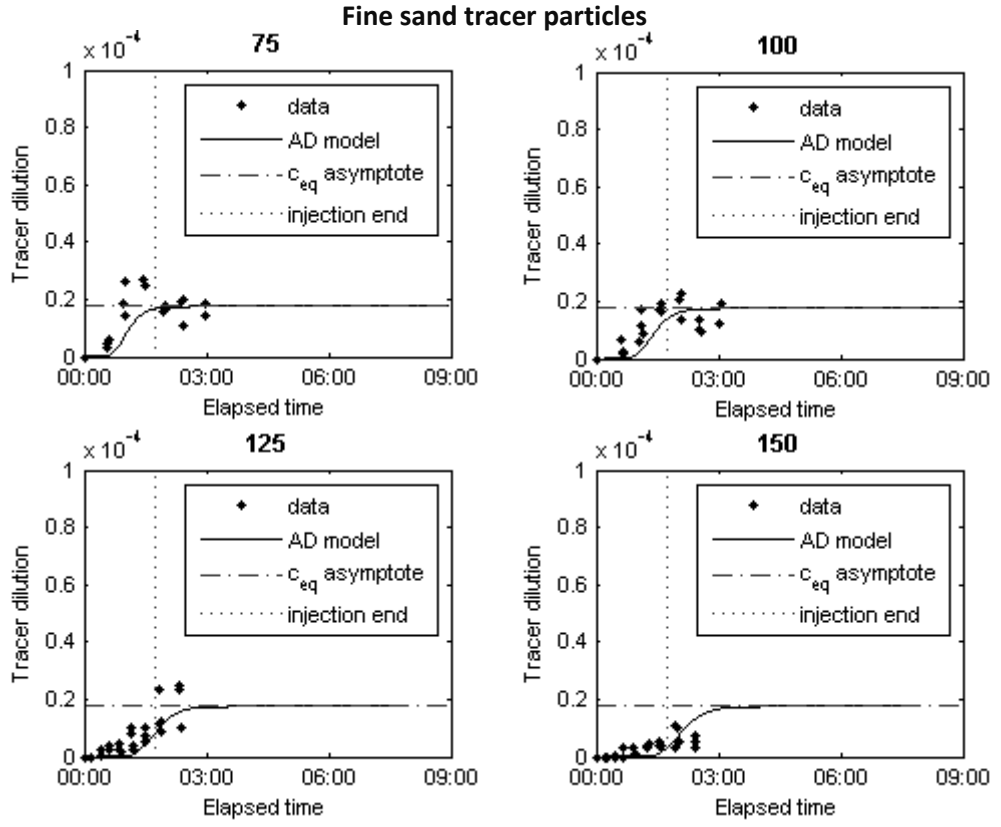

Figure 5.27. Advection-diffusion model for fine sand tracer particles (75 and 150 m downdrif).

Equilibrium concentrations, advection velocities and diffusion coefficients used to fit the model are summarized in **Table 5.1**. The results show that sediment diffusion and advection velocity increase from the coarser to the finer particles. The average advection velocity and transport rates of the grain-size classes present similar values to those obtained based on overall tracer particle. This means that the velocity and volume of the sediment transport alongshore depend upon the relative amount of particles of each grain-size class within the entire distribution, which is in agreement with the observations performed by Komar (1977). On the other hand, this also means that grain-size classes with lower frequencies have little significance in the sediment transport rate. Thus, taking in account that Grande beach native sediment is essentially composed by very coarse, coarse and medium sand, a transport rate of 8.15×10^{-2} $m^3.s^{-1}$ was estimated based on the average rate of these three grain-size classes (**Table 5.2**).

Table 5.1. Equilibrium concentration ($\bar{c}_{eq}$), advection velocity (v_a) and diffusion coefficient (D) used to fit model to the data; mean frequency of grain-size in the tracer ($\overline{fi}$); tracer mass injection rates (IR) and transport rates (Q).

Grain-size	$\bar{c}_{eq}\times10^{-3}$	$v_a\times10^{-2}$ ($m.s^{-1}$)	$D\times10^{-2}$ ($m^2.s^{-1}$)	$\overline{fi}$ (%)	IR* (kg.min¹)	$Q\times10^{-2}$ ($m^3.s^{-1}$)
Very coarse sand	1	1.61	1.33	31.92	5.11	5.36
Coarse sand	1	1.76	4.63	48.91	7.82	8.20
Medium sand	0.225	1.92	5.04	14.63	2.34	10.9
Fine sand	0.0175	1.97	6.62	0.43	0.7	4.19
Mean	-	1.82	4.41	-	-	7.16
Overall	2.3	1.72	4.18	100	16	7.29

* The tracer injection rate of each grain-size class was estimated based on its individual frequency in the tracer sediment, assuming an average value estimated from the samples presented in **Figure 5.18**.

Table 5.2. Longshore transport rates estimated by different methods.

Method	$Q\times10^{-2}$ ($m^3.s^{-1}$)	Parameters
Tracer dilution (CIM)	8.15	Average rate of grain-sizes between -1ϕ to 2ϕ presented in **Table 5.1**
Tracer advection and cross-sectional transport area of beach active profile	7.99	v_a = 1.76×10^{-2} $m.s^{-1}$ area = 4.54 m^2
Bagnold aproach (1963) - equation (**5.5**)	1.44	v_l = 0.62 $m.s^{-1}$ d_{50}= 0.76 ϕ

Under the uncertainties related with the image analysis technique, which can led to an overestimation of the equilibrium concentrations, together with the fact that the concentration of each grain-size class was calibrated using the linear correlation obtained from standard concentrations containing all tracer particles, it was decided estimate the longshore drift using another approach and compare the results.

Considering that the advection velocity obtained from the model depends on the concentration distribution patterns but, at same time, is independent of the concentration values, this characteristic can be used to estimate the transport rate independently. Therefore, the mean advection velocity estimated based on the three main grain-sizes classes of Grande beach was multiplied by the transport cross-sectional area, deduced by the thickness of the active layer measured along the beach profile and the width of the zone under the influence of breaking waves (see **Figure 5.17** and **Table 5.2**).

The estimated longshore transport rate was 7.99×10^{-2} $m^3.s^{-1}$, a magnitude similar to the previously estimated. However, the width of the transport section considered (beach face + low-tide terrace) is wider compared to the narrow breaking zone, during the tracer experiment (beach face). This suggests that the longshore transport under spilling breakers (at the low-tide terrace) is lower than under plunging beakers (at the beach face), which can be explained by a smaller mixing depth induced by this breaking type. In the study case, mixing depth at the low-tide terrace may even be overestimated due to the water in the mixing layer that difficult the measurement through the washers sinking.

The longshore drift estimated using tracer data were also compared with the rate computed using Bagnold's (1963) approach (**Table 5.2**). The rate obtained was 1.44×10^{-2} $m^3.s^{-1}$, which is 5.5 times lower than the rates measured from the tracer experiment. This means that the dimensionless empirical coefficients (K') proposed Komar and Inman (1970) is not adequate to estimate the sediment transport under plunging breakers, in this case, the K' obtained was 1.5. In fact, previous works carried out on the Portuguese reflective beaches reported that the longshore transport formulas tend to underestimate the total transport rate when applied to steep beaches under plunging breakers and that the differences between the two methods are usually one order of magnitude (Ciavola *et al*., 1997; Taborda *et al*., 1994; Silva *et al*., 2007).

The ration between advection velocity and average longshore drift current was 0.028, similar to the ratios obtained in previous authors (0.021-0.024 in Ciavola *et al*., 1997; 0.017 in Taborda *et al*., 1994 and 0.010 in Silva *et al*., 2007), supporting the hypothesis that the high transport rates

are mostly linked with high cross-sectional area of the transport system, due to the high mixing depth observed in steep beaches under plunging breakers.

5.2.3.3 Selective sediment transport

The grain-size analysis of the tracer particles show that coarser particles tend to concentrate at the lower beach face, while the finer ones are transported up to the upper beach face (**Figure 5.20B** and **Figure 5.22**), suggesting a transport of the coarser particles towards offshore. However, the finer sediment found at the inner sandbar indicate that coarser particles are trapped at the base of the beach face. This observation is in agreement with previous works, which have been shown that sediment grain-size is generally coarser within the wave plunge point at the base of the beach face, decreasing both up to the foreshore slope and towards offshore, sometime with a second sediment coarsening at the offshore bar (see the synthesis about this subject in Komar, 1998).

This sediment sorting can explain the absence of tracer in the sediment collected 400 m downdrift of the injection point at the inner sandbar, considering that sediment use to tracer had high percentages of coarse particles (< 1 ϕ).

The longshore variations, on the other hand, show a decrease of the tracer mean grain-size with distance to the injection point, which can be explained by the fact that finer particles remain longer in suspension and thus travel farther in a shorter time.

The longshore transport rates estimated from the equilibrium concentrations increase from the very coarse to medium sand. In fact, several works have recognised the sediment grain-size effect on the magnitude of sediment transport, showing that an increase in the median grain- size will decrease longshore transport rates (*e.g.* del Valle *et al*., 1993; King, 2005).

Komar (1977) observed an opposite behaviour in a tracer experiment carried out on a steep beach face (β = 8°) under plunging breakers (H_b = 0.42 m; T = 3.4 s; θ_b = 27°), where the advection velocity decreased from the very coarse to medium sand with larger differences (between 3.1×10^2 and 0.6×10^2 m.s^{-1}). The same author justifies that the finer grains swash high up the beach face, where they move alongshore more slowly than the coarser grains, which remain near the breaker zone and are transported by stronger longshore currents. However, his analysis was based on five sediment samples collected alongshore at the same elevation level, which limits the data interpretation and comparison. Still, even that finer particles remain longer at the same position, once entrained by waves, they can be transported, in suspension, for longer distances.

5.2.3.4 Headland sediment bypassing

Despite the northward longshore drift observed, Grande beach presented a morphology that was favourable to the HSB southward, *i.e.* a wider southern sector and a continuous inner sandbar along the Calhau do Corvo headland coast (**Figure 5.28**).

This morphology should result from the previous incident wave condition that induced the beach clockwise rotation and HSB through the low-tide terrace, which is compatible with the enrichment of medium sand observed at Adraga beach and at the inner sandbar, compare to the berm and beach face sediment of Grande beach.

As the HSB occurs at the low-tide terrace under spilling breakers, its magnitude should be lower than the longshore drift estimated from the tracer experiment under plunging breakers. Even so, a significant sediment volume can bypass the headland during a tide cycle, under low-energy wave conditions, considering the advection velocity of the tracer and the mixing depth observed at the low-tide terrace.

Figure 5.28. Grande beach at September 8th 2014: (A) northern view during the rising tide; (B) southern view from the top of Calhau do Corvo headland during low tide; (C) aspect of the sandbar at Grande beach, near to Calhau do Corvo, during low tide; (D) tip of Calhau do Corvo headland tip during low tide. The arrows point to the comum features on the images.

5.3 LONG-TERM APPROACH

5.3.1 Methods

The breaking wave conditions used to estimate potential longshore drift were obtained from the 56-years offshore wave time-series reconstructed by Dodet *et al.* (2010) that was presented in **Figure 1.7** of Chapter 1.

The offshore waves were propagated up to 15 m depth using the SWAN (Simulating Waves Nearshore) model, which is a spectral third-generation wave model developed by Delft University of Technology (Booij *et al.*, 1999). The SWAN model was implemented using a bathymetry built based on three data sources: (1) European Marine Observation and Data Network (EMODnet) with a 428 m resolution, available online at: http://www.emodnet-hydrography.eu/; (2) *Instituto Hidrográfico* with 250 m resolution, available online at: http://www.hidrografico.pt/download-gratuito.php; and (3) the LiDAR data provided by *Direção-Geral do Território* with 2 m resolution. The model computational domain was discretized by a rectangular grid with 89×189 km dimension and 500 m resolution. The boundary conditions were imposed by the mentioned 56-years wave time-series of integral parameters (wave significant height, peak period and peak direction) with a time interval of 6 hours. The spectra shape was Jonswap, with a spectral directional resolution of 10°, while the discretization in the frequency-space was made using 31 intervals between 0.04 to 1 Hz. No currents, wind or tidal levels were used, therefore, nonlinear quadruplet wave interactions were disabled and a mean sea water level was considered. The model output parameters were significant wave height (Hs), mean absolute wave period ($Tm01$) and mean wave direction (Dir).

For the period under analysis there is no wave data near to the coast to validate the model results. However, the validation results presented by Ribeiro (2013), for the SWAN model performance at the Portuguese west coast, showed a root mean square of 0.42 m for Hs and 9° for Dir, consistent with the errors presented in other works for the Portuguese west coast (*e.g.* Rusu *et al.*, 2008; Silva *et al.*, 2009). This validation was performed with the data of an ADCP moored at 28 m depth north of Peniche.

From 15 m depth to the breaking point, waves were propagated based on the wave linear theory and on the Snell law, using the Larson *et al*. (2010) approach to estimate breaking wave parameters.

The longshore drift induced by each wave was computed with the CERC formula proposed by Rosati *et al.* (2002), which relates longshore component of the energy flux at the breaking and the longshore sediment transport through the equation:

$$Q = K\left(\frac{\rho\sqrt{g}}{16{\gamma_b}^{\frac{1}{2}}(\rho_s-\rho)(1-p)}\right)Hs_b^{\frac{5}{2}}\sin(2\theta_b) \quad (\mathbf{5.6})$$

where γ_b is the wave breaking criteria (0.78); ρ is the sea water density (1025 kgm^{-3}); ρ_s is the quartz density (2650 kgm^{-3}); g is the gravitational acceleration (9.81 ms^{-2}); p is the assumed sand porosity (0.4); Hs_b is the wave significant height at breaking; θ_b is the wave breaker angle, and K is an empirical coefficient (0.39, according to CERC, 1984).

The longshore drift estimated corresponds to a potential value that should not correspond to the effective longshore drift considering the sediment starving observed in the studied coast. Under these circumstances, the use of the K parameter estimated from the tracer experiment would not improve the results. However, the goal of this approach was to get insights on the net longshore drift patterns, which are independent of the transport magnitude.

5.3.2 Results

5.3.2.1 Breaking wave conditions

The results show that breaking waves have a mean Hs between 1.5 and 2.3 m and a time-averaged power between 11 and 27 k.Wm^{-1}. For both parameters, the lowest values occur in the stretches sheltered by Carvoeiro and Roca headlands, as well as in the vicinity of Foz do Lizandro where an inflection in the coastline orientation is observed. In these stretches the ratio between nearshore and offshore wave power show a large wave power reduction. In the other stretches, Hs and wave power are higher and the ratio between nearshore and offshore wave power indicate a small wave power reduction, mainly in the vicinity of Lamporeira headland. Mean Dir and mean wave power direction are, in general, orthogonal to the coastline due to wave refraction (**Figure 5.29**).

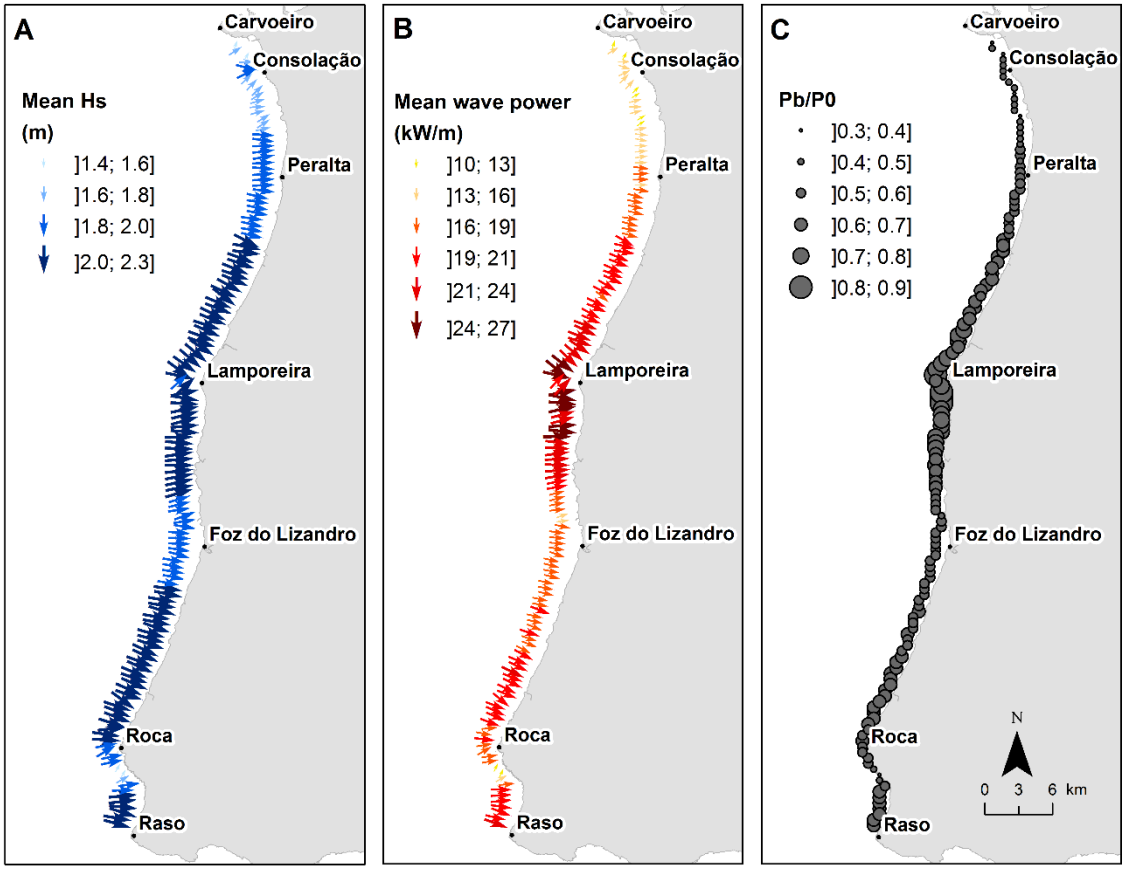

Figure 5.29. (A) Mean wave significant height and direction at the breaking; (B) mean wave power and power direction at the breaking; and (C) ratio between nearshore (P_b) and offshore (P_0) wave power. The mean wave direction and mean wave power direction are represented by the arrows orientation.

5.3.2.2 Potential net longshore drift

The annual potential net drift is shown **Figure 5.30**; negative values correspond to a southward transport, while positive values correspond to a northward transport. The potential transport have lower magnitudes in the sectors NE-SW oriented, while the sectors NW-SE and N-S oriented present a higher potential transport. The sediment transport is preferably southward, however, in some circumscribed areas potential net drift is northward. The most notable cases are the stretches immediately north of the Consolação, Lampoeira, Roca and Raso headlands, where northward component show higher magnitudes and frequencies.

The analysis of seasonal potential net drift show that the higher transport magnitudes occur during autumn (October-December) and winter (January – March) seasons. The asymmetry in the transport magnitude between sectors with different orientation, is higher during autumn/winter when compared to spring/summer seasons. Further, it can be noticed that at NW-SE stretches, the northward transport component is particularly significant during

autumn/winter seasons. In the spring, the northward component weakens, and in the summer, rarely can counterweight the southward component (**Figure 5.31**).

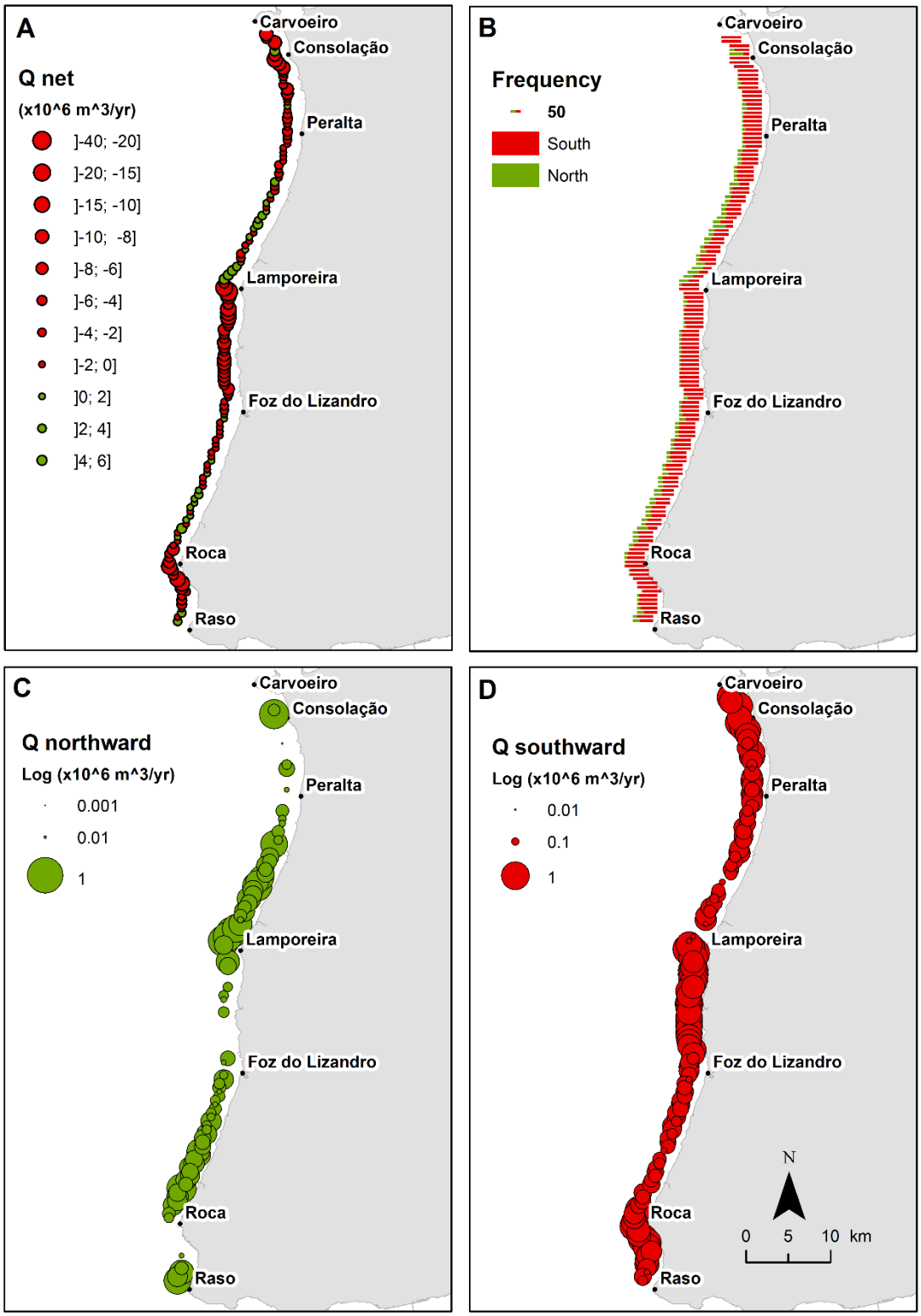

Figure 5.30. (A) Annual potential net drift (negative values correspond to the south-directed transport, while positive values are the north-directed transport); (B) relative frequency of transport directions; and (C) north and (D) south components of the annual potential net drift.

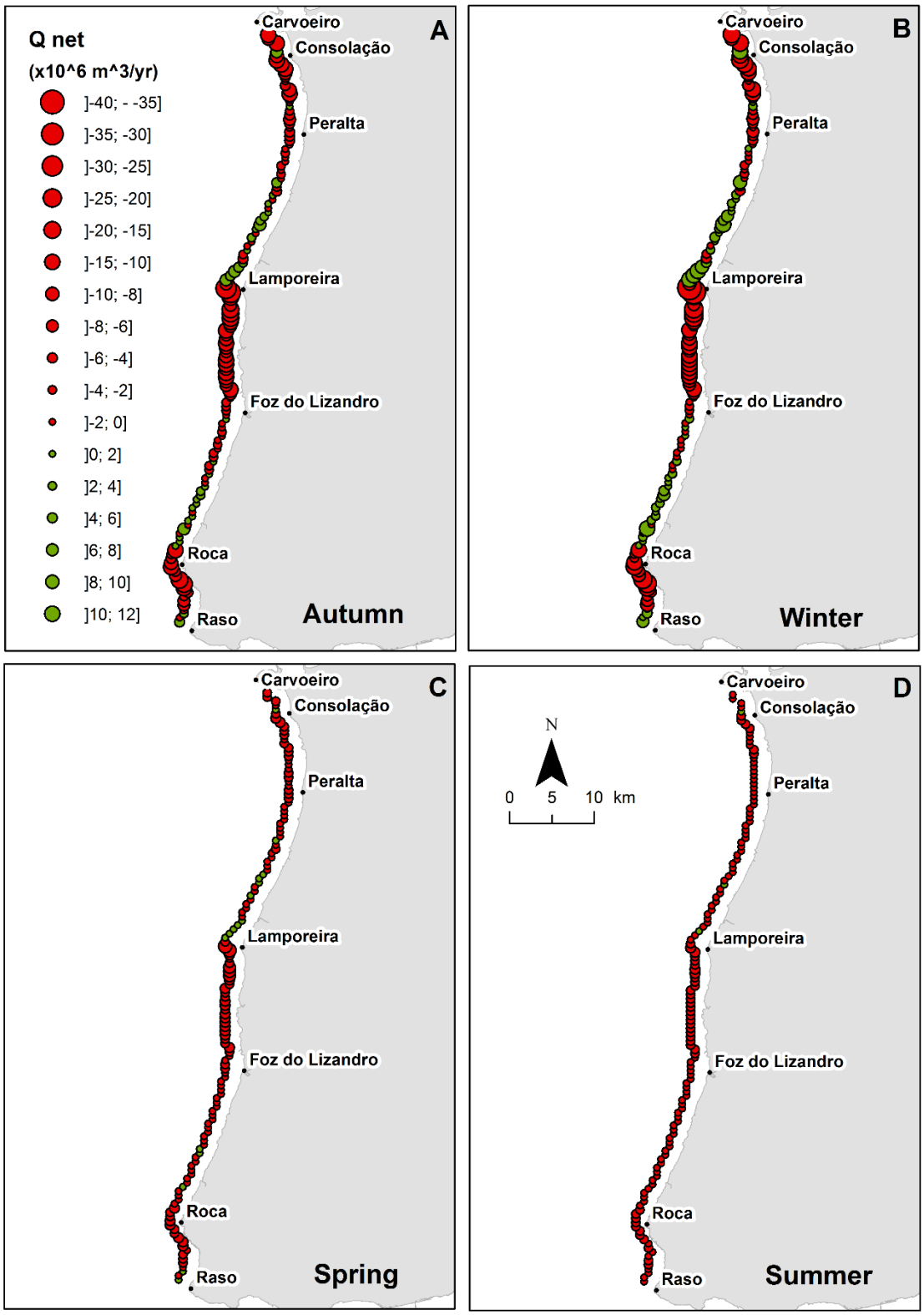

Figure 5.31. Seasonal potential net drift: (A) Autumn; (B) Winter; (C) Spring; and (D) Summer (negative values correspond to the south-directed transport, while positive values are the north-directed transport).

5.3.3 Discussion

The magnitude of the potential net drift estimated, reach 2×10^7 $m^3.yr^{-1}$ at Lamporeira headland, one order of magnitude higher than the one estimated by Silva *et al.* (2012a), for a NE-SW oriented coastal stretch located north of the studied site (Mondego cape – Nazaré headland). However, the sediment starving observed in the studied coast indicate that the effective net drift is significantly lower than the potential net drift. Moreover, as the goal of this analysis was to understand the transport patterns, is the relative alongshore variation that is relevant, a pattern that is independent of the absolute transport values.

It should be noted that the potential net drift estimated in the vicinity of the Peniche peninsula is not consistent, considering the 500 m grid resolution used for the wave propagation modelling, which cannot properly represent the complex bottom morphology of this area. Thus, the wave refraction in this region should be greater and the potential net drift southward smaller than the estimated.

The annual net drift put in evidence the role of Carvoeiro, Consolação, Lamporeira, Roca and Raso headlands as major boundaries in the transport pattern. In the N-S and NW-SE oriented stretches, south of these headlands, net transport is higher and permanently southward; while in the NE-SW oriented stretches, north of these headlands, the southward component weakens and is counterweighed by the northward one that reduces the net dominant drift. In some places, the aforementioned process can revert the direction of the net longshore drift (*i.e.* northward). The northward transport component reach its higher magnitudes in the vicinity of the headlands, weakening northward. The seasonal analysis shows that this pattern is induced by the high-energy autumn/winter waves. In the spring, on the other hand, due to the decline and clockwise rotation of wave energy, transport magnitudes decrease and the northward component of transport weakens, being overcame by the southward component in summer along almost the entire coast.

The persistence of the southward longshore drift in summer, can led to a sand accumulation at the updrift (north) side of the headlands, as shown in Chapter 3, and sand bypass can occur. On the other hand, in the autumn/winter the opposite direction of the net drift in the both side of the headlands, inhibits the sand bypassing. This analysis confirms that nearshore sediment bypassing of the aforementioned headlands can only occur southwards, during summer low-energy wave conditions.

These longshore drift patterns justify the sandy and rocky nature of the inner continental shelf showed in Chapter 2. In the stretches N-S and NW-SE stretches the sediment is sweep southward

by the high longshore transport rates, while in the NE-SW sectors the balance between south and north transport components, generates a sediment recirculation within these sectors, allowing sand to accumulate.

5.4 CONCLUSIONS

The results presented in this chapter gave important insights on HSB processes. The presence of a continuous inner sandbar that crossed the tip of the Calhau do Corvo, suggests that HSB occurs at the low-tide terrace under spilling breakers, having a magnitude lower than longshore drift measured on the beach face, under plunging breakers. Notwithstanding, tracer advection velocity and the mixing depth measured at the low-tide terrace, suggest that a significant HSB can occur during one tide cycle, under low-energy wave conditions.

The sediment sorting observed during the tracer experiment showed that coarser particles are trapped in the base of the beach face, while the finer ones are transported up to the upper beach face or, towards offshore, considering the finer sediment found in the low-tide terrace. Thus, the slightly enrichment of medium sand observed from the Grande beach to Adraga beach, is compatible with a selective HSB through the low-tide terrace. These results are in line with the results presented in the Chapter 4.

The longshore transport patterns obtained from the potential net longshore drift suggest that studied coast can be segmented into four sediment circulation sub-cells: the northern one corresponds to the 3 km long beach-bay located between the Peniche peninsula and Consolação headland, while the other three are the macro scale embayments between Consolação, Lamporeira, Roca and Raso headlands. The opposite direction of the net longshore drift in the vicinity of the aforementioned headlands indicate that these boundaries only can be crossed in a single direction (southward), corresponding to gated boundaries. This behaviour can be explained considering that the net drift in the southern stretches is permanently southward directed, so all the sediment that bypass these headland cannot reverse its path.

Chapter 6

Headland Sediment Bypassing and Shoreline Evolution

6.1 INTRODUCTION

Headland sediment bypassing (HSB) is a key process in the headland-bay beaches development and evolution and, in this context, shoreline evolution modelling can be a useful tool. Several analytic and numerical models have been proposed to describe changes in shoreline based on analysis of the balance of sediment volumes over a certain time period, assuming an equilibrium beach profile (*e.g.* Pelnard-Considère, 1956; Hanson, 1989; Dabees and Kamphuis, 1998; Steetzel *et al*., 2000; Coelho *et al*., 2004). These models are based on the assumption that the beach profile shape remains constant; the shoreward and seaward vertical limits of the profile are constant and there is an adequate sand supply, *i.e.* an infinite supply of sand is assumed (Thomas and Ashley, 2013). However, in headland-bay coasts as the study one, the equilibrium profile assumption up to the closure depth is not valid due to the sediment scarcity and to the presence of cliffs and rocky shore platforms.

In this chapter a new shoreline evolution model – SEM-PLAT, developed to simulate shoreline changes on coastal stretches where beaches develop over a rocky platform, is presented and applied to understand the role of the HSB in the beaches development and evolution.

SEM-PLAT model was applied to study, in particular, the HSB occurring in subaerial beach domain. This model was firstly applied to the stretch between Maçãs and Adraga (Taborda and Ribeiro, 2016), being now extended northwards up to Magoito beach (**Figure 6.1**). In the northern sector of this coastal stretch, beaches are a thin layer of sand that covers a rocky shore platform. The wide sand accumulation found in the north edge, results from the shelter promoted by the Magoito headland to the NW dominant waves; southward, narrow beaches are found at Aguda and Azenhas do Mar. In the southern sector, are the Maçãs and Adraga beaches, which usually present a well-developed berm and are located in fluvial stream mouths. Between the theses beaches, occur the Pequena and Grande beaches, the first one is usually narrow, while the second one present large variations, changing between a winter concave morphology and a summer well-developed berm.

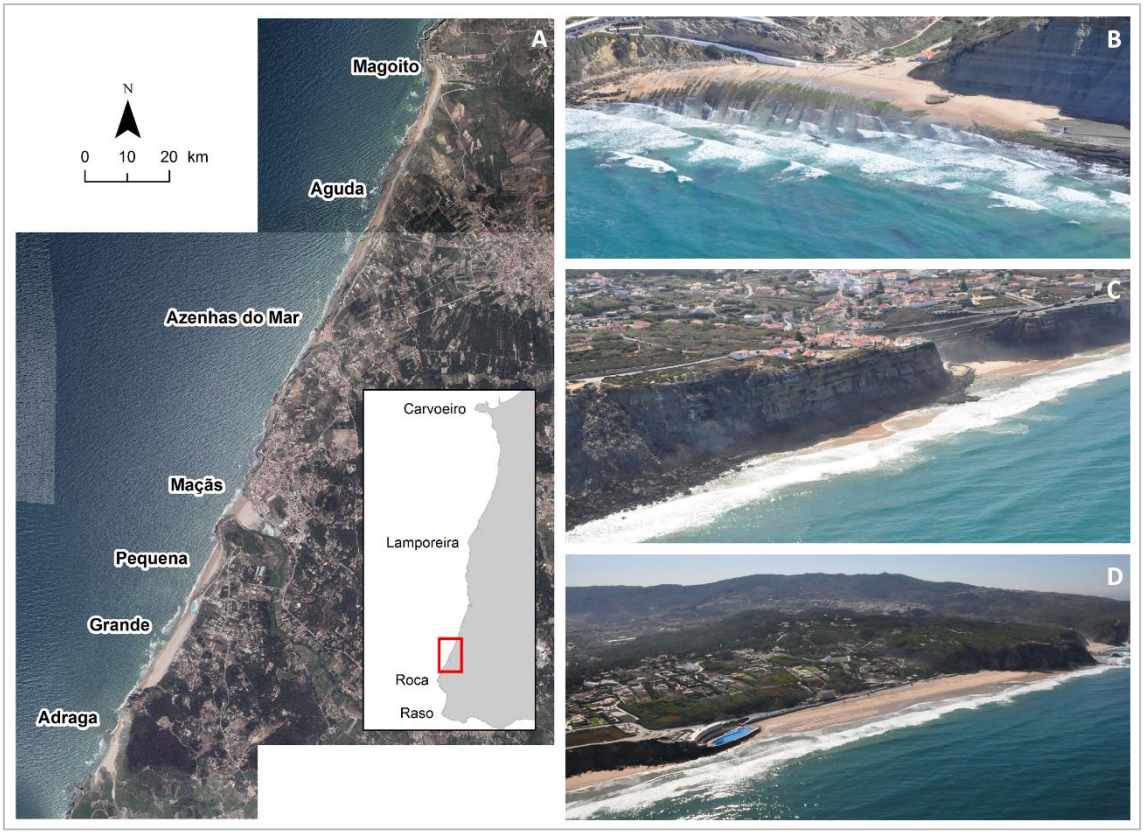

Figure 6.1. (A) Coastal stretch between Magoito and Adraga (background image: orthophotomap acquired on June 2012 and provided by *Direcção-Geral do Território* - DGT); (B) Magoito beach; (C) Azenhas do Mar; (D) Pequena, Grande and Adraga beaches (oblique aerial photographs taken in september 22nd 2009, provided by *Sistema de Administração do Recurso Litoral* – SIARL and available online at: http://www.siarl.igeo.pt, accessed Mar. 2017).

6.2 MODEL DESCRIPTION

SEM-PLAT is a one-line numerical model for modelling shoreline evolution on platform beaches as the result of wave-driven longshore sediment transport. The model is based on the standard conservation of sand volume equation that governs most shoreline evolution models:

$$\frac{\partial V}{\partial t} + \frac{\partial Q}{\partial x} = 0 \qquad \textbf{(6.1)}$$

where x is the distance alongshore, t is the time, Q is the longshore sediment transport rate and V is the volume of the active profile. This equation shows that profile change rate ($\partial V/\partial t$) is directly related to the alongshore gradients in longshore drift ($\partial Q/\partial x$).

In finite difference form, the conservation of sediment mass for each coastal section can be expressed as:

$$\Delta V = \frac{\left(Q_{in} - Q_{out}\right)\Delta t}{\Delta x} \qquad \textbf{(6.2)}$$

where Q_{in} is the sediment that enters in a coastal section and Q_{out} is the volume leaving the coastal section (**Figure 6.2**).

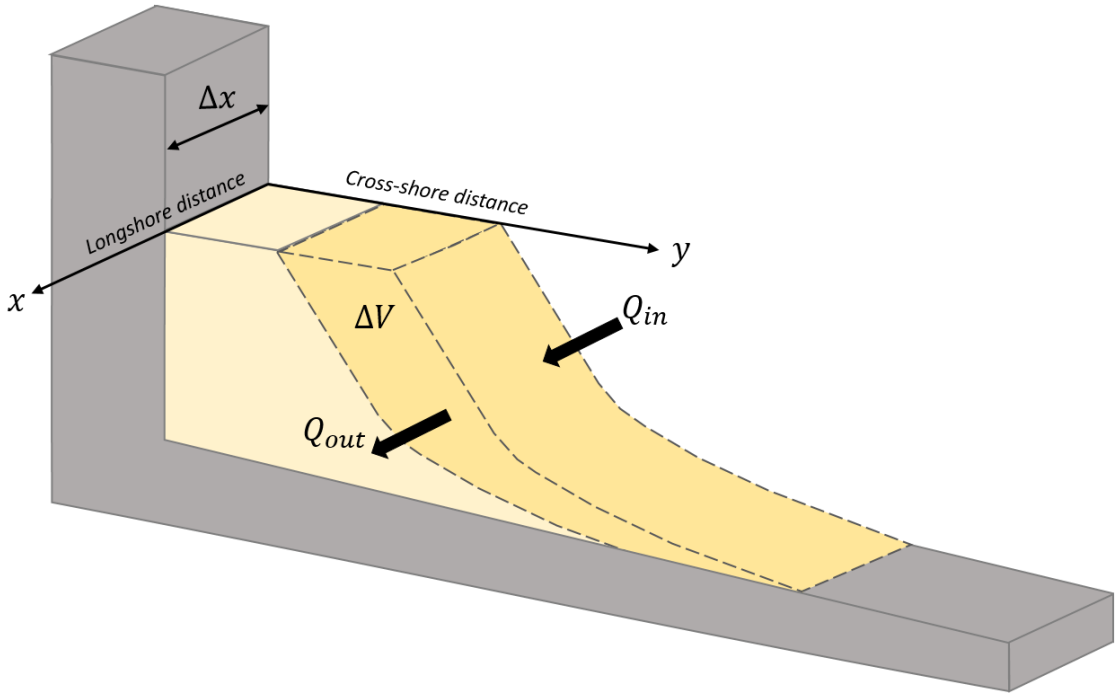

Figure 6.2. Definition of standard conservation of sediment volume for shoreline change calculation in a control section.

The equation (**6.2**) can be solved numerically, using finite difference methods over a discretized coastline domain knowing the longshore drift and boundary conditions. In the case of SEM-PLAT,

an explicit method is used. In order to establish the convergence of the finite-difference approximation, the model uses an adaptative time step, *i.e.* the minimum time step between the value defined by the user and the value computed based on the courant condition ($Courant\ number = Q\Delta t/\Delta x$). By default the Courant number adopted by the model is 0.5.

The model setting include the definition of the computational grid, profile model, offshore waves and boundary conditions. For each time step, a new shoreline is computed according to the flowchart presented in **Figure 6.3**.

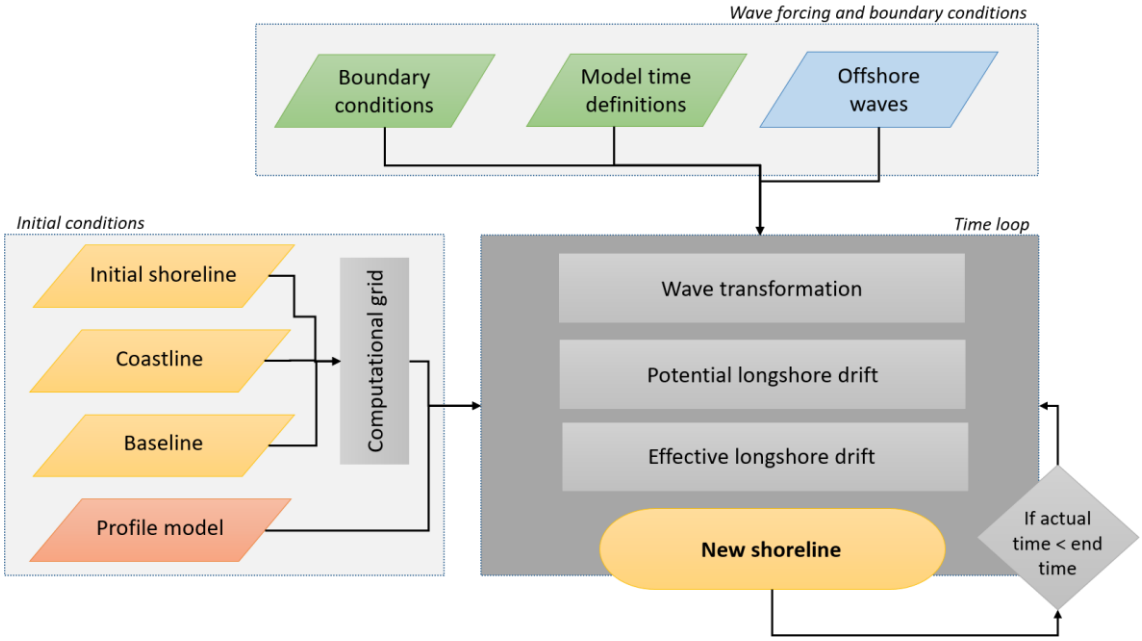

Figure 6.3. SEM-PLAT model flowchart.

6.2.1 Computational grid

The computational grid is built from an initial shoreline, a coastline and a baseline (**Figure 6.4**). The shoreline (x_s, y_s) corresponds to the beach berm crest and the coastline (x_c, y_c) to the cliff or dune foot. The baseline (x_b, y_b) is a reference line that can be curved and represents the trend of the shoreline, similar to the one proposed by Roelvink and Reniers (2012). The main advantage of using a curved baseline is related to the possibility of modelling non-straight coastal stretches, as is generally the case of headland-bay coasts. The grid consists of n cells defined by $n + 1$ cell boundaries, with uniform or variable alongshore resolution. SEM-PLAT is based on a staggered grid where the shoreline positions (n_i) are defined at the center of the grid cells and, the longshore drift (Q_i) and the azimuth of the normal to the shoreline (φ_c) are defined at the cell boundaries. The left boundary is located at grid cell 1, and the right boundary is at cell n.

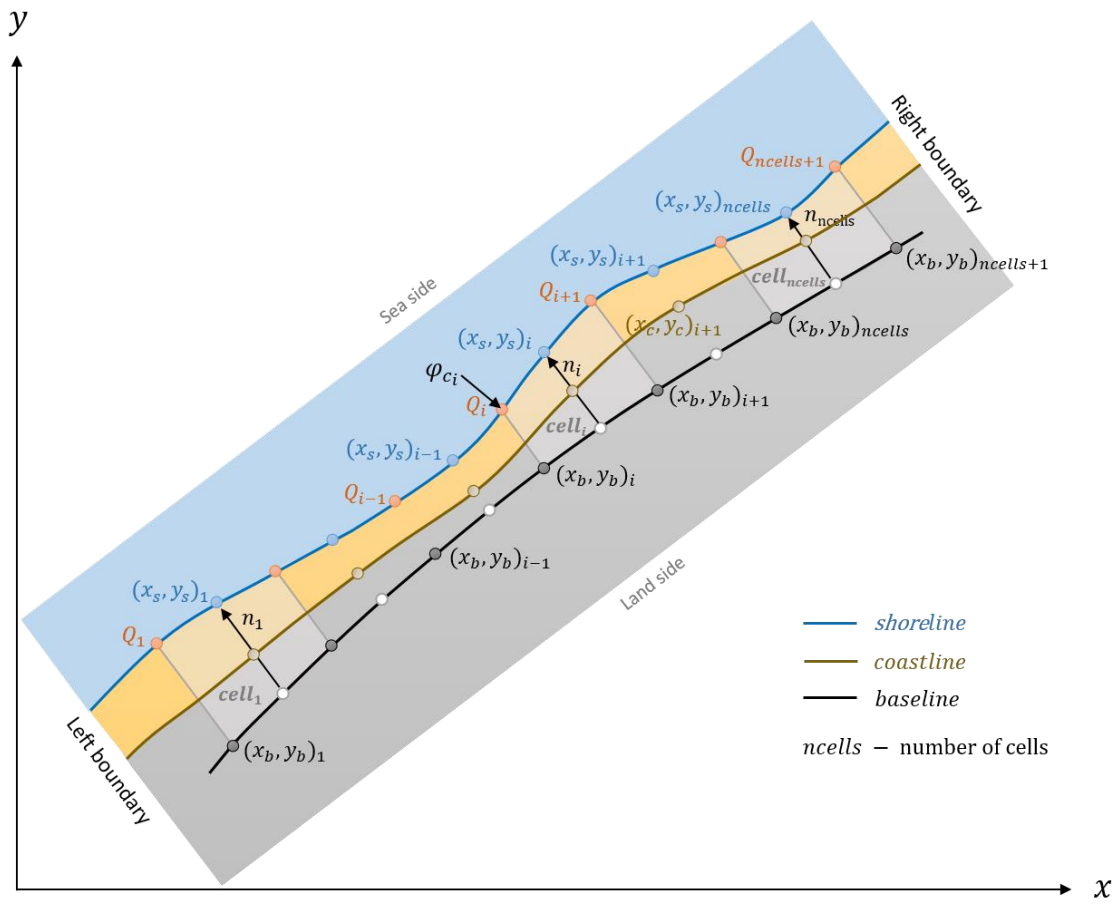

Figure 6.4. Finite difference staggered grid, where (x_s, y_s) are the shoreline coordinates, (x_b, y_b) are the coastline coordinates, (x_b, y_b) are the baseline coordinates, n_i is th the distance between the baseline and shoreline (normal to the baseline), Q_i is the longshore drift at cells boundaries and φ_c is the azimuth of the normal to the shoreline.

6.2.2 Profile model

SEM-PLAT profile model assumes a two dimensional profile cut in a hard rock substrate over which a sandy beach develops. The model is similar to the one proposed by Taborda and Ribeiro, (2015) where the beach overlays a flat, gently-sloping, shore platform. Beach profile is segmented in three domains: (1) a berm, (2) a beach face, and (3) a nearshore zone (**Figure 6.5**). The berm and beach face have constant slopes and the nearshore zone is based on the Dean's equilibrium profile (see for example Dean *et al*., 2002), considering that at the origin of the Dean's profile, the slope is equal to the beach face slope. The theoretical profile extends up to a specified closure depth, however, the beach domain ends where the theoretical profile intercepts the shore platform. The model assumes that the rocky shore platform has a constant slope.

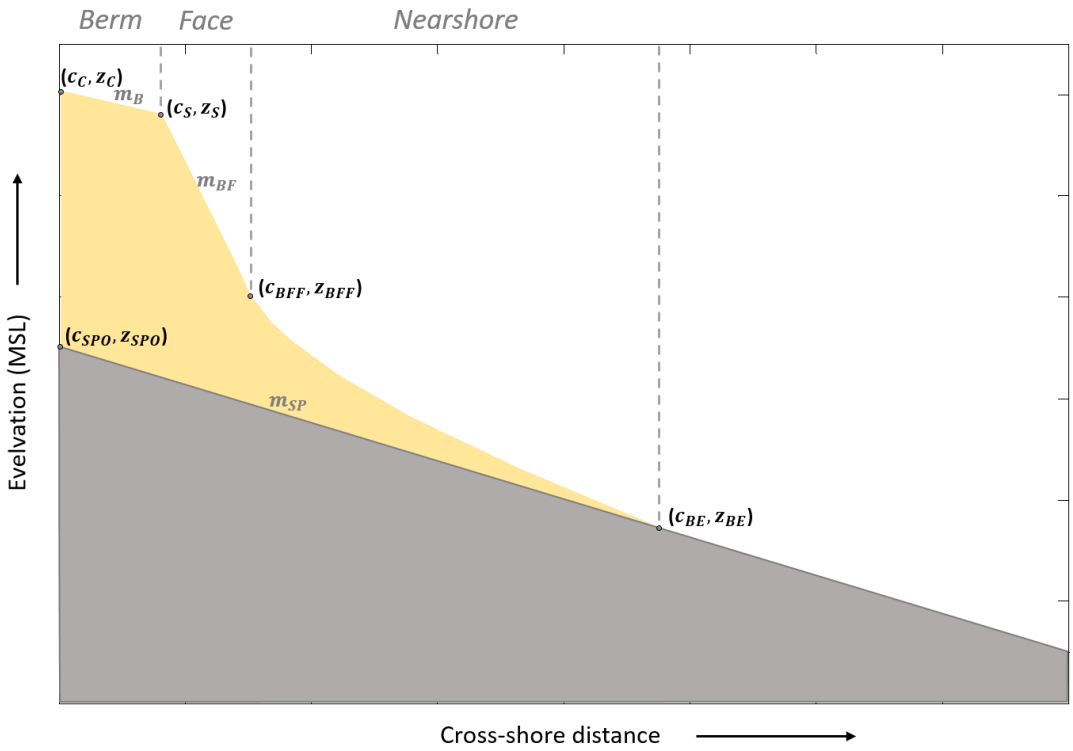

Figure 6.5. Schematic representation of the beach profile (yellow) and rocky platform (gray). Black dots represent the positions of the coastline (c_C, z_C); shoreline (c_S, z_S); beachface foot (c_{BFF}, z_{BFF}); beach end (c_{BE}, z_{BE}); and shore platform origin/landward limit (c_{SP0}, z_{SP0}). m_B is the berm slope; m_{BF} is the beachface slope; m_{SP} is the shore platform slope.

6.2.3 Boundary conditions

SEM-PLAT allow two options for the boundary conditions: closed and open. If an open boundary condition is chosen, sediment is transported freely across the boundary (default boundary condition). When a closed boundary condition is specified, means no sediment is transported across the boundary. The sediment transport across the left and right boundaries are computed according to the flowing conditions:

- If left boundary is open $\Rightarrow\ Q(1) = Q(2)$;
- If left boundary is closed $\Rightarrow Q(1) = 0$;
- If right boundary is open $\Rightarrow Q(ncell + 1) = Q(ncell)$
- If the right boundary is closed $\Rightarrow Q(ncell + 1) = 0$

6.2.4 Wave transformation

Wave transformation is based on the wave linear theory and Snell's law. Wave propagation from offshore to the closure depth (or other depth computed from a numerical wave propagation model) is computed considering a regional bathymetry, with an orientation that does not change

in time. From the defined depth to the breaking depth the transformation is performed considering (time varying) normal direction to the shoreline between adjacent cells (**Figure 6.4**). The propagation in this domain follows the explicit approach present in Larson *et al.* (2010) targeting to optimize the computation time.

6.2.5 Potential longshore drift

The potential longshore sediment transport induced by the waves is computed using the CERC formula proposed by Rosati *et al.* (2002), represented by the equation (**5.6**), in the section 5.3.1 of the previous chapter.

6.2.6 Effective longshore drift

In headland-bay coasts the effective longshore drift is generally much lower than potential transport, because the magnitude of sediment distribution processes (potential longshore drift) is in general much larger than the sediment supply. The consideration of a sediment starving coast is a cornerstone of the SEM-PLAT model development. SEM-PLAT first computes longshore sediment transport rates along the coastal stretch assuming that there is no sediment deficit (potential longshore drift). Then, considering sediment availability, which depends not only on the sediment in cell but also on the updrift ones, it estimates effective longshore drift. To identify updrift cells, SEM-PLAT computes a sediment accumulation vector which is a cumulative count of the number of cells that naturally drains into each cell (analogous to the flow accumulation tool used in hydrology). After this, the model, sweeps the cells, from updrift to downdrift adjusting the longshore transport magnitude to the available sediment, according to the following conditions (**Figure 6.6**):

(1) If the ΔV computed is positive or negative and smaller than the initial volume of the cell, the effective transport at the cell boundary is equal to the potential transport.

(2) If the ΔV computed is negative and greater than the initial volume of the cell, the longshore transport magnitude at the cell boundaries must be adjust. In this case:

- if sediment leaves the cell through one boundary, the effective transport is the sum of the initial volume of the cell and the volume that enters in the cell;
- if the sediment output occur through both cell boundaries, the effective transport at each boundary is 50% of the initial volume of the cell.

Cell number	Closed boundary	1	2	3	4	5	6	7	8	9	10	11	Open boundary
Q direction		→	→	→←	←	←	←	←→	→	→	→	→	
Cell accumulation		0	1	6	3	2	1	0	1	2	3	4	
Initial volume		70	60	40	40	50	50	100	70	90	60	20	
New volume		**10**	**60**	**160**	**40**	**50**	**40**	**0**	**60**	**90**	**60**	**20**	

Figure 6.6. Scheme of the update volume at each cell based on the effective longshore drift, considering a hypotetical potential longshore drift of 60 at each cell boundary and that left model boundary is closed and rigth model boundary is open.

6.2.7 Beach profiles update and shoreline position

For each time step, the sediment retained in each cell is redistributed within the beach profile according the following rules:

(1) if the ΔV is positive $\Rightarrow$ beach accrete and the sediment volume is added to the berm;

(2) if the ΔV is negative $\Rightarrow$ beach erode and the sediment volume is subtracted:

- if $V_{berm} + \Delta V > 0 \Rightarrow$ berm retreat;
- $V_{berm} + \Delta V < 0$ and $V_{beach} + \Delta V > 0 \Rightarrow$ berm obliteration and profile retreat from beach face;
- if $V_{beach} + \Delta V \leq 0 \Rightarrow$ complete obliteration of the beach profile.

The shoreline position depends on the berm width, so when the berm is completely obliterated the shoreline evolution ceases although the beach profile can still change.

6.3 MODEL SETTING

Model computational domain was extended from northern sector of Magoito beach to the mid of Adraga beach and discretized in 79 cells with approximately 100 m length (**Figure 6.7**). The coastline was defined as the base of the cliff for most of the domain, except at small stretches were the dune foot (Maçãs beach) or artificial structure foot (Grande beach) were considered.

As the goal was the study of HSB occurring in the subaerial beach, the model was set to account the effective longshore drift occurring between the coastline and the elevation of – 1 m (MSL) that corresponds to the rocky shore platform elevation observed in the Magoito beach (see Chapter 3). The beach face slope (0.09) and berm crest elevation (4 m) were also chosen based

on mean values of the observed beach profiles. Berm and shore platform were considered horizontal (**Figure 6.8**).

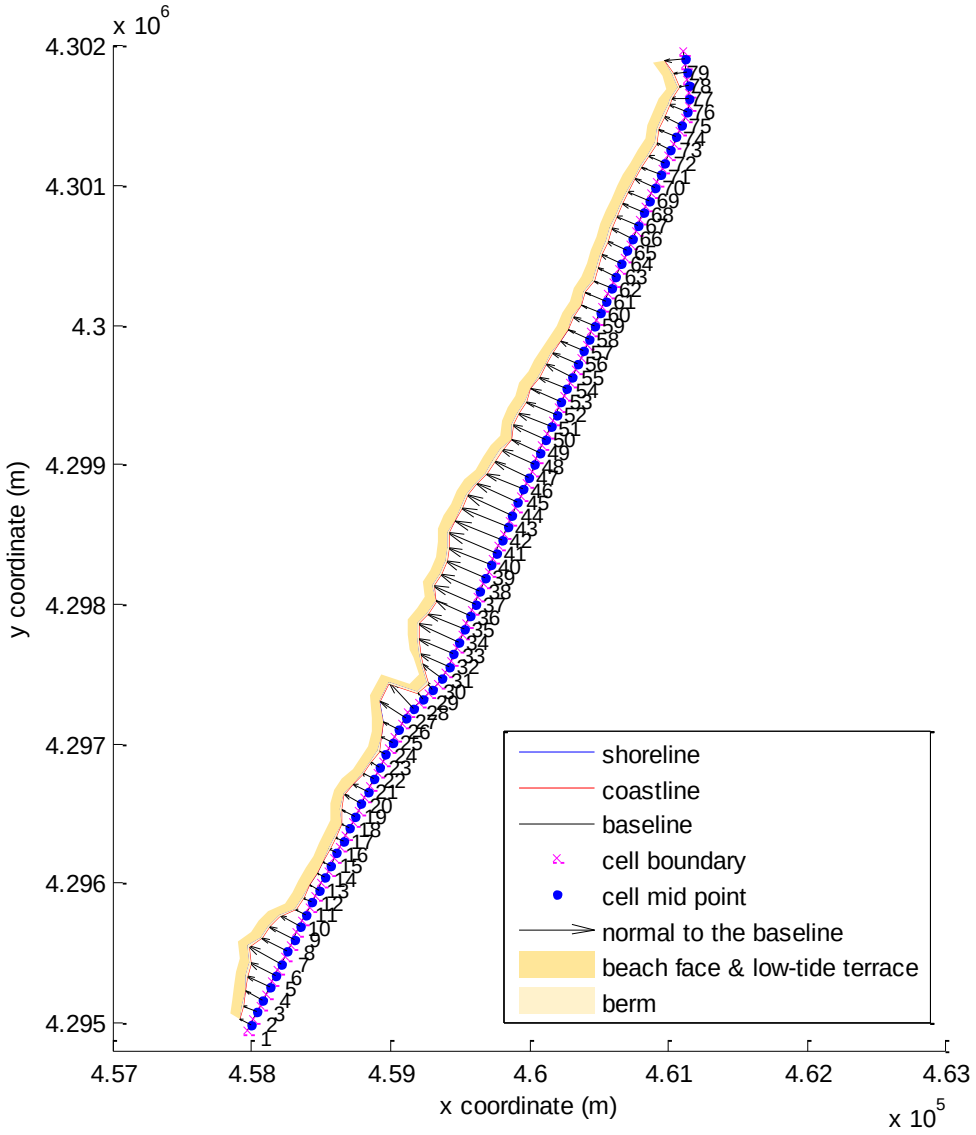

Figure 6.7. Model grid and initial shoreline that corresponded to a hypothetical scenario where all the coast was fulfilled with a continuous beach extending for the entire domain (coordinate system: WGS 84 / UTM zone 29N).

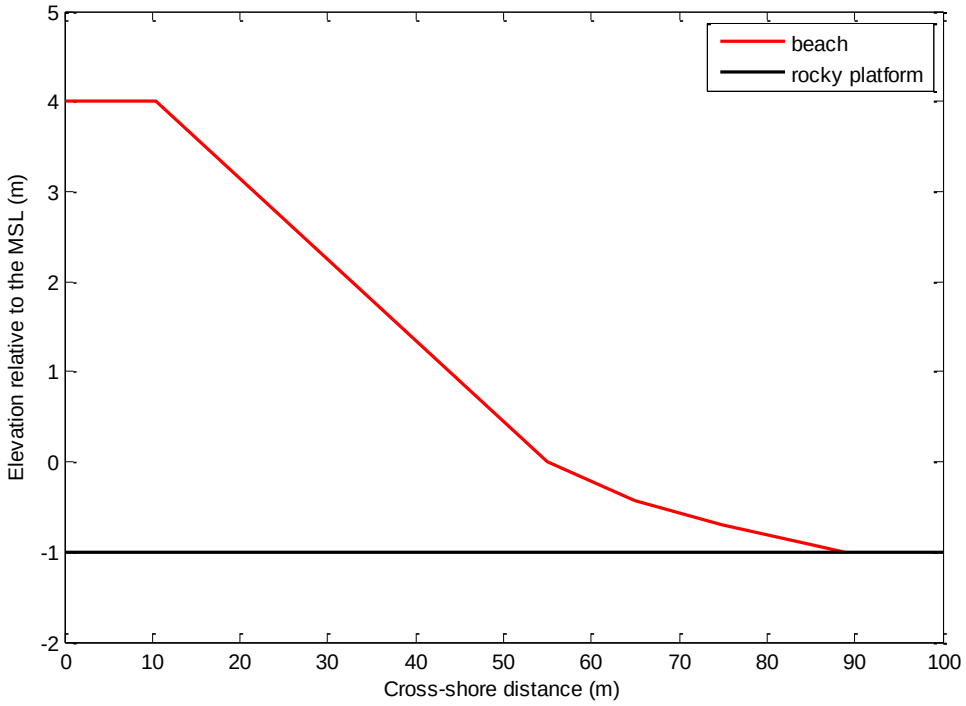

Figure 6.8. Initial beach profile and shore platform profile along the entire study coast.

Three simulations were conducted under constant wave forcing representative of the annual (Hs = 2 m; Tp = 11 s and Dir = 308°), summer (Hs = 1.4 m; Tp = 9 s and Dir = 314°) and winter (Hs = 2.7 m; Tp = 12 s and Dir = 302°) time-averaged conditions, estimated from the hindcast wave time-series presented in Chapter 1 (Dodet *et al.*, 2010).

Taking into account the counter-clockwise rotation of the bathymetry observed near Magoito, which certainly influence the wave propagation, the offshore waves were propagated up to 5 m depth assuming the direction of this contour, *i.e* 281° near Magoito (cell 70 to 79) and 295° for the remaining domain.

In the simulation S1 (annual), the initial shoreline corresponded to a hypothetical scenario where all the coast was fulfilled with a continuous beach extending for the entire domain, as shown in **Figure 6.7**. The northern boundary was set closed and the southern one open, allowing sediment leave the system until it reach the equilibrium. The simulation S2 (summer) starts from the shoreline position obtained from the simulation S1 and the boundary conditions were maintained; while the simulation S3 (winter) starts from shoreline position obtained from the simulation S2 and both boundaries were set closed to avoid that an unrealistic quantity of sediment get in the system through the southern boundary. The simulation S1 was conducted for a time-period of two years considering the large sediment volume in the system, while the other two correspond to a time-period of one year.

6.4 MODEL RESULTS AND DISCUSSION

The model results for annual time-averaged wave conditions show a sand redistribution pattern in the southern sector close to the one observed in the **Figure 6.1**. In this sector the model was able to reproduce: 1) the shape of Grande beach, with a berm that is slightly wider at the southern sector; 2) the narrow berm of Pequena beach; and 3) the wider extent of Maçãs beach with a well-developed berm (**Figure 6.10**).

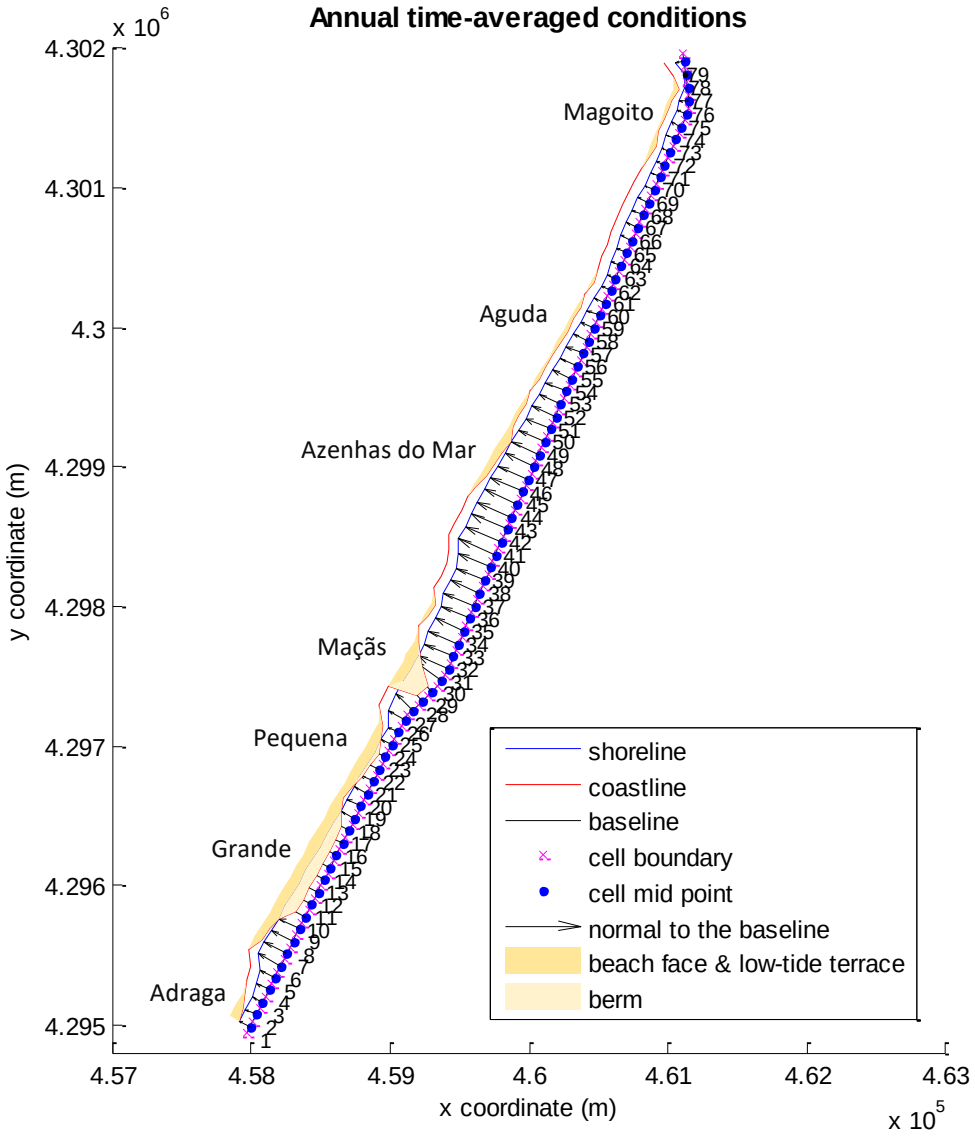

Figure 6.9. Model results for annual time-averaged wave conditions (Hs = 2 m; Tp = 11 s; Dir = 308°).

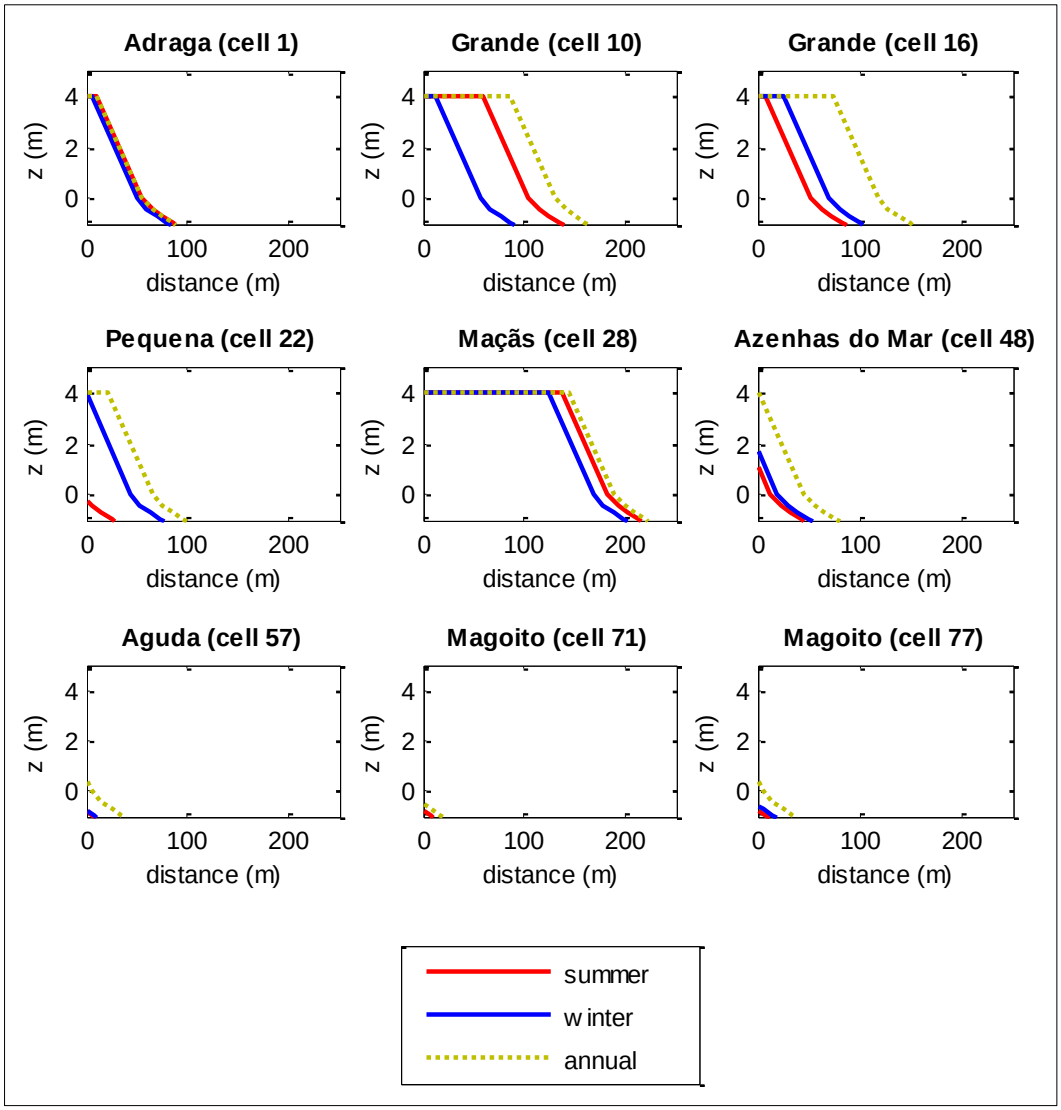

Figure 6.10. Modelled beach profiles for time-averaged overall (Hs = 2 m; Tp = 11 s; Dir = 308°), summer (Hs = 1.4 m; Tp = 9 s; Dir = 314°) and winter (Hs = 2.7 m; Tp = 12 s; Dir = 302°) wave conditions.

In the case of the Adraga beach, the sand redistribution originated a beach narrower than the one observed in **Figure 6.1**, which can be related with the large rocky outcrops in the northern sector of this beach, affecting nearshore wave propagation and sediment retention that were not accounted by the model.

In the northern sector, model results do not follow observations so closely. The model was able to reproduce the narrow beaches at Aguda and Azenhas do Mar, that mainly correspond to an intertidal domain, but in the case of Magoito, model do not match entirely with the observations, as the beach was reduce to a narrow face without berm (**Figure 6.10**). As shown in the **Figure 6.1** and by the results of Magoito beach morphology presented in Chapter 3, beaches in this sector are characterized by a thin sand deposit covering the rocky shore platform that is often exposed. Under these circumstances, the local bathymetric changes related with

the shore platform can be a major factor that constrain nearshore wave propagation and sand retention. Despite the use of a different bathymetry direction close to Magoito, the irregularities of the shore platform can explain the poorest model results for this sector.

The sand redistribution patterns for summer and winter time-averaged wave conditions are shown in the **Figure 6.11** and **Figure 6.12**; while the respective beach profiles are presented and compared in the **Figure 6.10**.

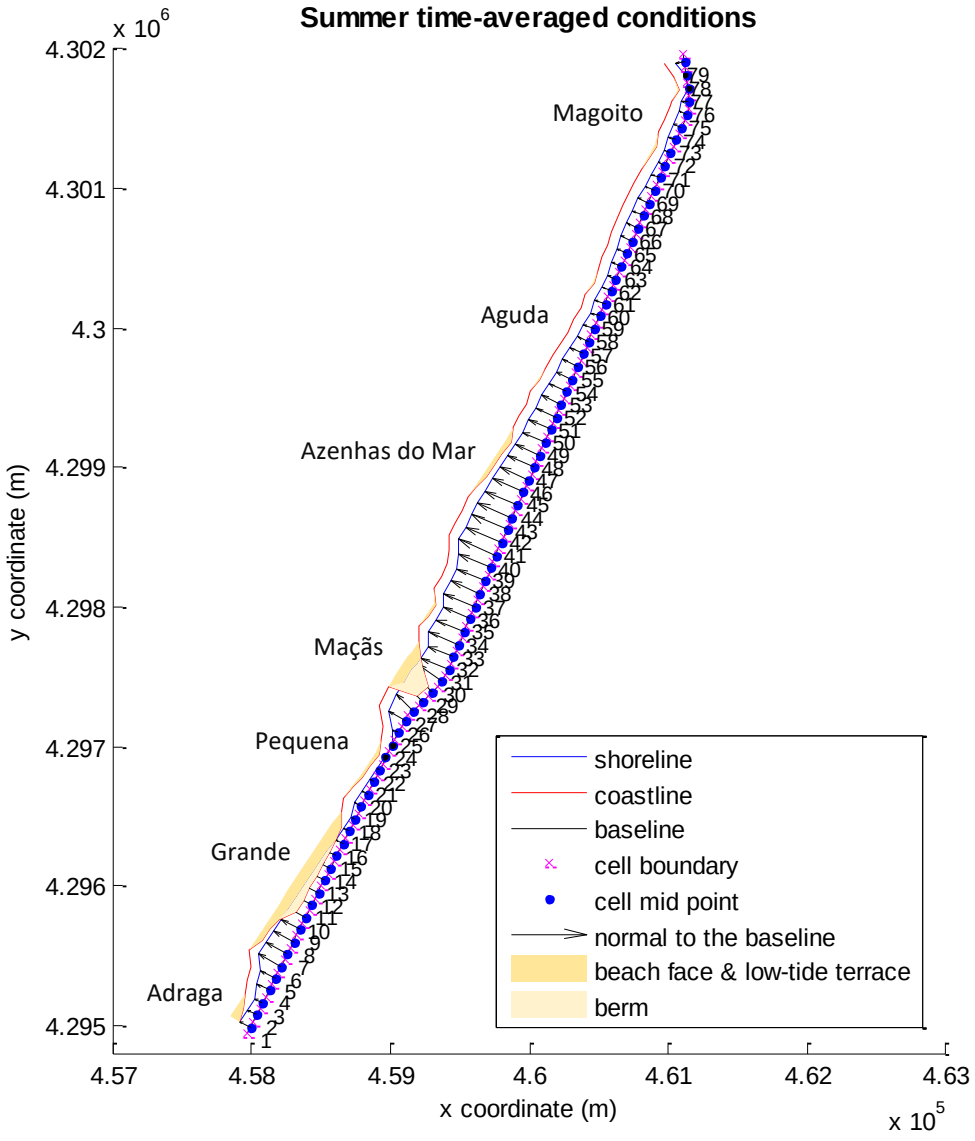

Figure 6.11. Model results for summer time-averaged wave conditions (Hs = 1.4 m; Tp = 9 s; Dir = 314°).

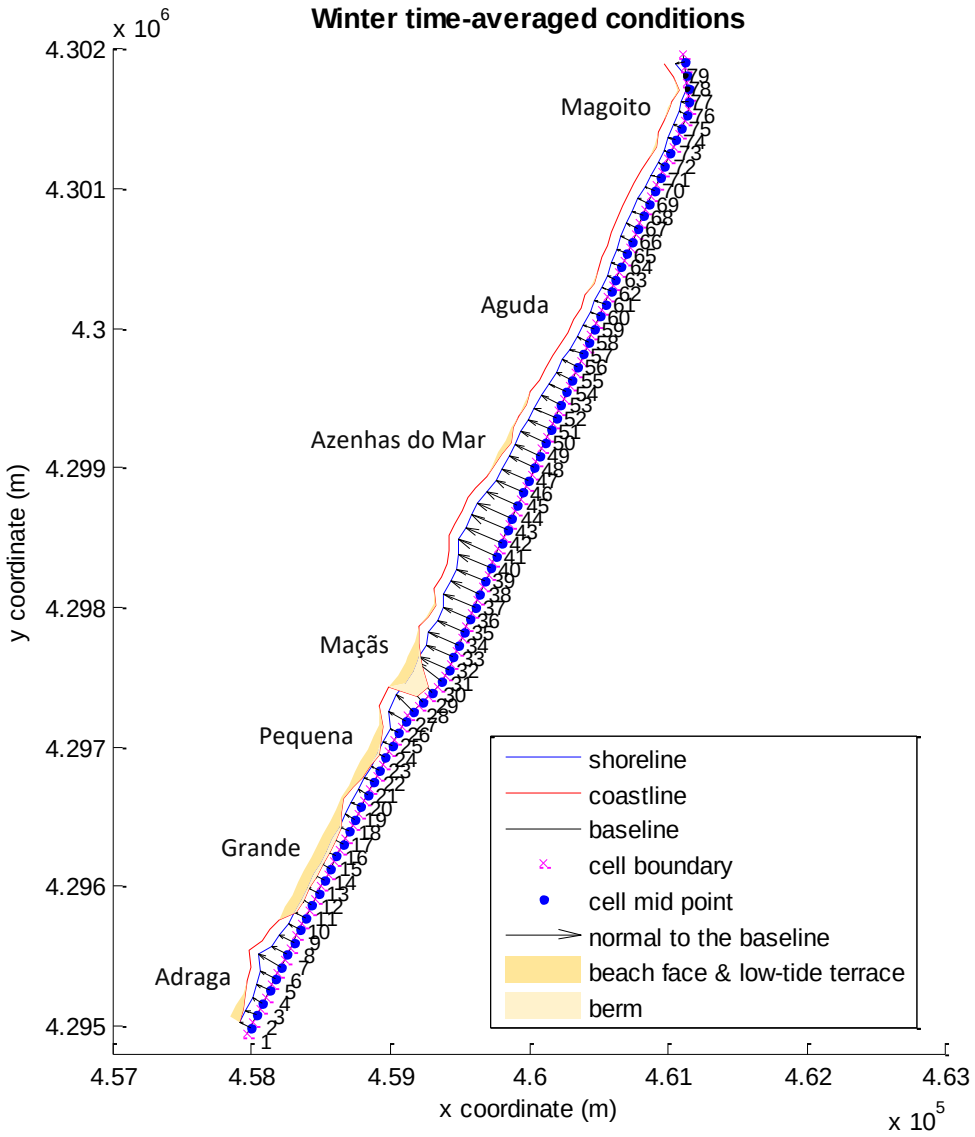

Figure 6.12. Model results for winter time-averaged wave conditions (Hs = 2.7 m; Tp = 12 s; Dir = 302°).

In the case of model forced with a typical summer wave, sediment sweep along the northern coast was more pronounce when compared to the annual time-averaged conditions. The sand accumulations are almost imperceptible and are located in the most indented zones of the coastline. In the southern stretch, beaches show a retreat relatively to the annual time-averaged conditions. This retreat is more evident at Pequena beach and in the northern sector of Grande beach, where the berm was obliterated (**Figure 6.11** and **Figure 6.10**). In latter cases, beach configuration closely matches the observed one in the satellite image obtained in the summer of 2014 (**Figure 6.13A**). This configuration with a larger berm in the southern sector of Grande beach and, the retreat at the northern sector and at Pequena beach, are compatible with beach planform rotation observed during the summer months (in Chapter 3).

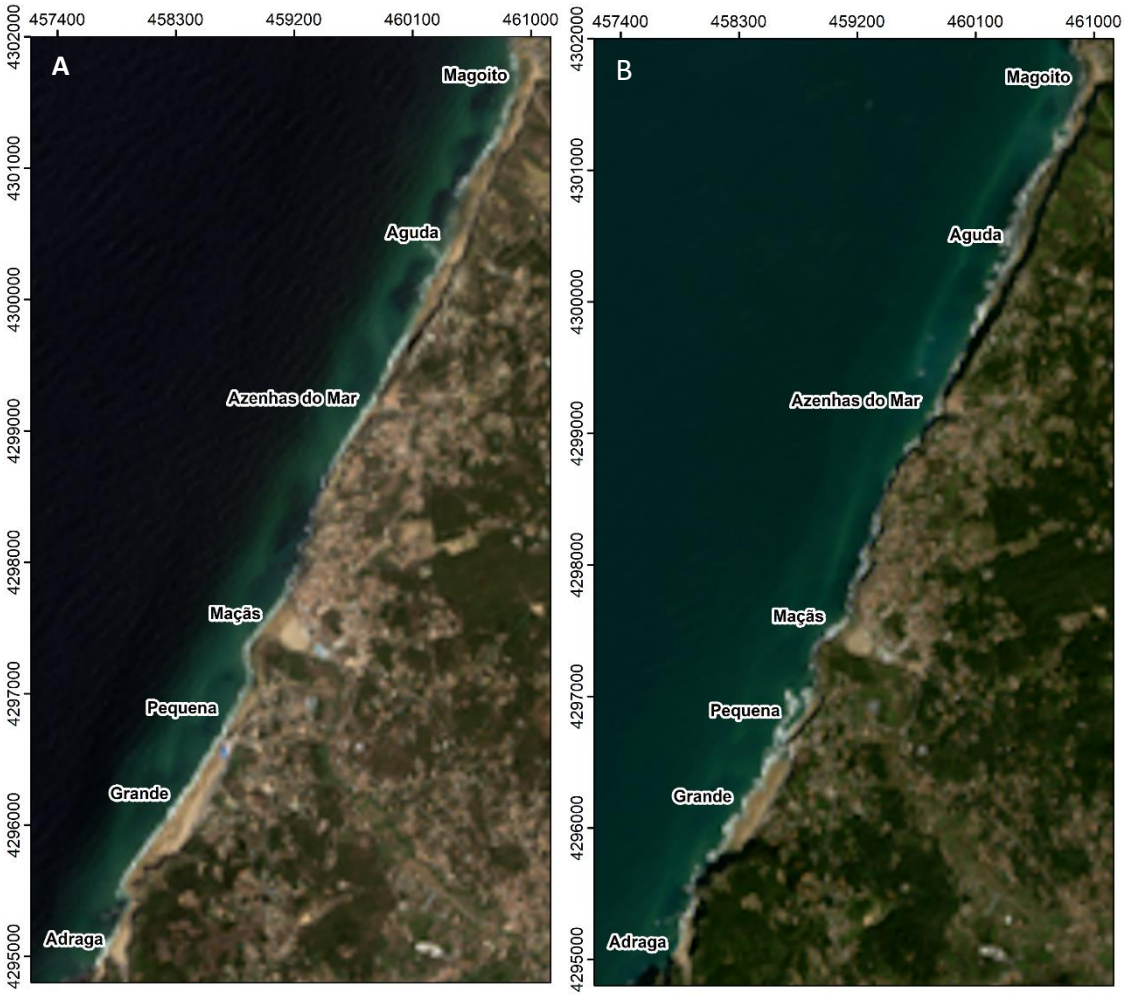

Figure 6.13. Landsat 8 satellite images (provided by NASA and USGS) of the studied coastal stretch during: (A) summer (August 23rd 2013, tide level = -0.95 m (MSL)) and (B) winter (February 9th 2015, tidel level = -0.80 m (MSL)). The tide level at the time of the image acquisition was computed based on Cascais tide gauge data using the UTIDE model (Codiga, 2011).

The model results for typical winter wave, show a berm retreat, mainly at Grande Beach, in agreement with the observed in the satellite image obtained in the winter of 2015 (**Figure 6.13B**). The retreat of the southern sector of the Grande beach occurs in relation with the enlargement of its northern sector and the adjacent Pequena beach, which is in agreement with summer and winter Pequena beach profiles presented in Chapter 3 (**Figure 3.24**). The beach enlargement is mainly related with the intertidal zone (face and terrace) and can be also observed at Maçãs beach. In the case of Adraga, the model cannot reproduce the expected count clockwise rotation because the southern boundary was defined on this beach. Despite the northward longshore drift, the northern stretch present a sand distribution pattern similar to the one obtained for summer wave condition, corroborating the assumption that HSB north-directed is more difficulty (**Figure 6.12** and **Figure 6.10**).

These results are in agreement with beach planform rotation presented in Chapter 3 and with transport patterns obtained in Chapter 5*, i.e*. during summer low-energy wave conditions, the net sediment transport is southward, inducing a beach clockwise rotation; while during winter high-energy wave conditions, the net sediment transport is northward, inducing a counter clockwise beach rotation.

6.5 CONCLUSIONS

SEM-PLAT model results are quite encouraging and suggest that it can be a useful tool to understand some key processes in headland-bay coasts such as HSB and beach rotation.

The model results reproduced quite well the beach characteristics along the southern coastal stretch, putting in evidence sand redistribution as a major mechanism of beach development, where the HSB occurring in the subaerial beach seems to plays an important role.

The poorest model results for the northern coastal stretch should be an effect of the local bathymetric changes related with the exposed shore platform (whose configuration was greatly simplified in the model) that constrain nearshore wave propagation. Moreover, the differences between model results and the observations can be also justified by the use of stationary wave conditions, which obviously is a simplification of the wave forcing.

The planform beach rotation induced by the summer and winter time-averaged waves, indicate that seasonal (and interannual) changes in the incident wave climate can significantly affect the beach configuration or even its development, putting in evidence the delicate dynamic equilibrium of these beaches. This also means that the wave climate rotation (in relation to climate changes) can have strong impacts on evolution of these beaches.

Chapter 7

Sediment Budget

7.1 INTRODUCTION

Headland sediment bypassing (HSB) plays a major role in the definition of coastal sediment budget, particularly, on headland-bay coasts, as is the case of the coast between Carvoeiro and Raso capes. However, sediment budget of a littoral cell depends not only on the longshore sediment transport, but also on other sediment sources and sinks as schematized in **Figure 7.1**.

The coastal stretch between Carvoeiro and Raso capes has been considered as a single littoral cell of sediment circulation, assuming a negligible wave-driven HSB at north and south boundaries (Santos *et al*., 2014), which is supported by the geomorphological and sedimentological analysis presented in the Chapter 2 and by the distinct heavy mineral signatures found by Balsinha *et al.* (2010), in the fluvial streams and beaches located north and south of Carvoeiro cape.

The sediment sources and sinks of the studied coast, found in literature, are summarized in **Figure 7.2** and described below.

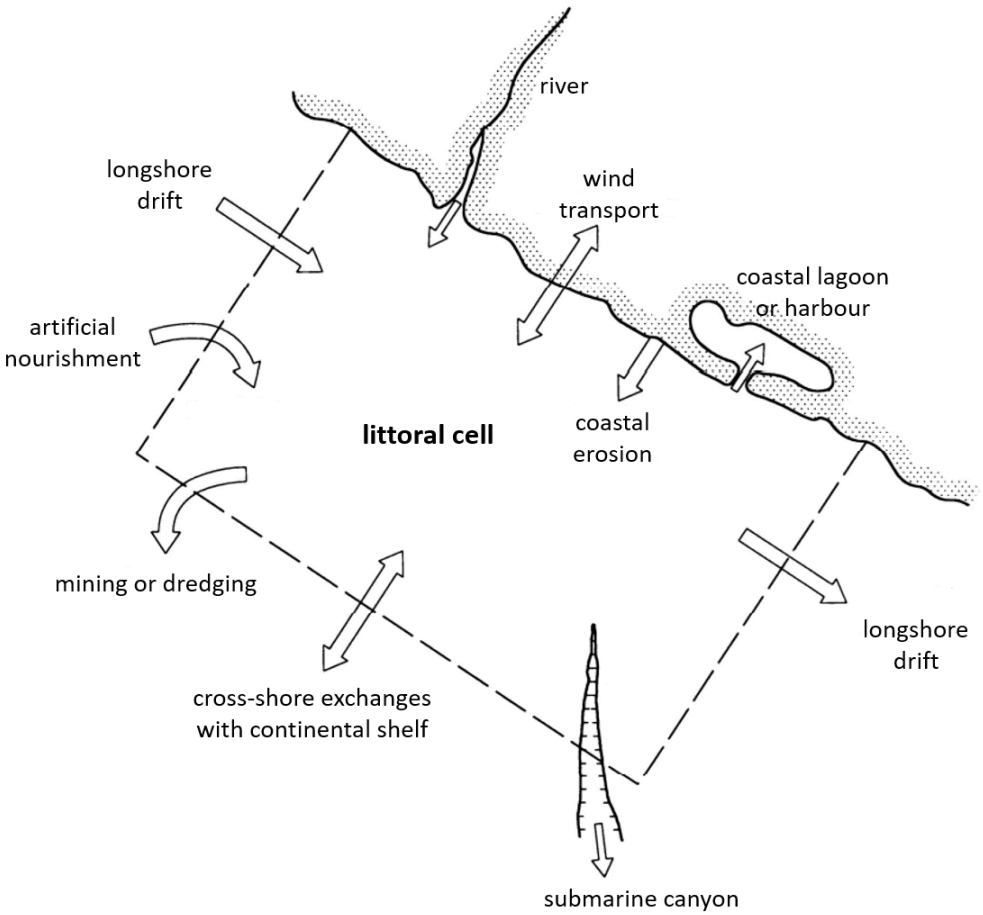

Figure 7.1. Schematic representation of the sedimentary sources and sinks of a littoral cell (adapted from van Rijn, 2010).

The main sediment sources are the fluvial streams and the coastal erosion; the latter one should be mainly from cliffs, considering that these represent 81 % of the coastline (Marques *et al.*, 2013).

The work presented by Lira *et al.* (2013), showed that the São Domingos, Alcabrichel, Sizandro and Lizandro rivers provide 37×10^3 $m^3.yr^{-1}$ of sediment, but only 10 to 40% (*i.e.* 3.7×10^3 to 14.8×10^3 $m^3.yr^{-1}$) of this sediment is compatible with the beach sediment. The sedimentary contribution of the smaller fluvial streams could not be discretised from the referred work, since that they were grouped with other small fluvial systems that do not drain to the study area.

Andrade *et al.* (2009), Oliviera (2009) and Taborda *et al.* (2010), estimated both fluvial and cliff erosion contribution for the Sintra and Cascais coasts and, according to their results, sediment supply for the littoral downdrift of Foz do Lizandro does not exceed 6×10^3 $m^3.yr^{-1}$.

The sediment supply from fluvial streams can be reduce due to dam's construction, as is the case of São Domingos river. The study presented by Janardo (2016), showed that São Domingos dam's reservoir is a very efficient trap for sand, interrupting its transport downstream. According

to this author, before the dam's construction (started in 1988, as reported at: http://www.cm-peniche.pt/, accessed Mar. 2017), sediment supply for the littoral was between 1.2×10^3 and 2.7×10^3 $m^3.yr^{-1}$. Currently, sediment supply should be much lower, considering that 87 % of the sediment yield is capture by the dam.

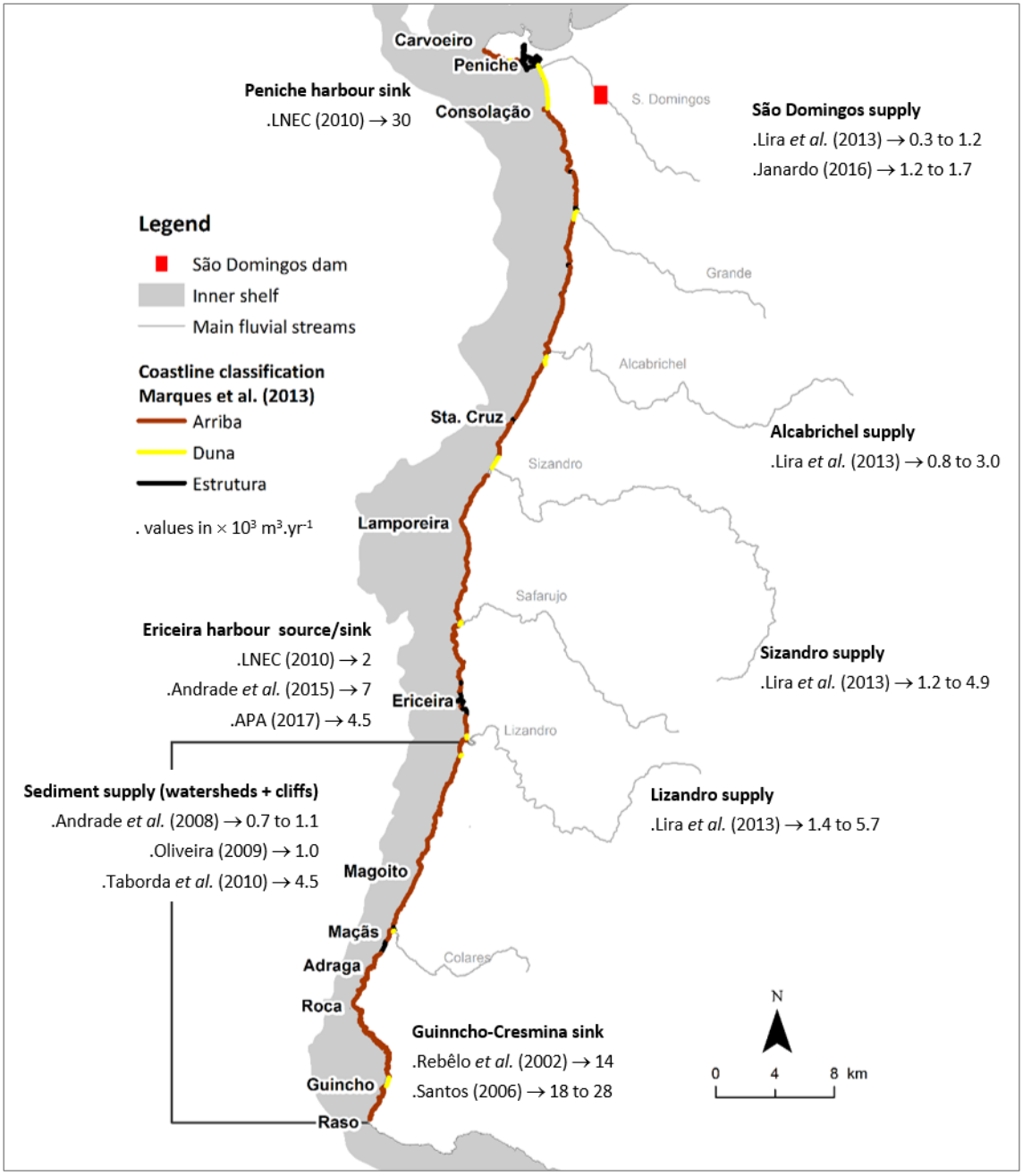

Figure 7.2. Main sediment sources and sinks of the studied coast based on previous works (values in $\times10^3$ $m^3.yr^{-1}$).

The sediment exchange of beach-dune systems, promoted by aeolian transport, is also a possible sediment source and sink as shown in **Figure 7.1**. However, beach-dune systems occupy

only 6 % of the studied coast (Marques *et al*., 2013), occurring near to stream mouths and presenting, in most of the cases, poor-developed dune fields.

The larger dune fields are the Consolação and Guincho-Cresmina, located near the northern and southern limits of the studied coast, respectively. The first one is relatively stabilized by vegetation, while the second one, it is an active and extremely unstable system due to the constant drifting of sand particles. According to Rebêlo *et al.* (2002), the Guincho-Cresmina dunes belong to a vaster and complex dune system, known as the Guincho-Oitavos and classified as a headland bypass dune field. Guincho-Cesmina dunes should therefore considered a major sediment sink, while the sediment exchanges by aeolian transport of the other dune fields should have a small significance in the sediment budget of the studied coast. The aeolian transport at Guincho-Cresmina dune was estimated by Rebêlo *et al.* (2002), based on topographic data acquired between 2000 and 2001, with a magnitude of 14×10^3 $m^3.yr^{-1}$. For the same dune system and based on topographic maps and aerial images, Santos (2006) estimated an aeolian transport of 28×10^3 $m^3.yr^{-1}$, between 1974 and 1981, and 18×10^3 $m^3.yr^{-1}$, for the periods 1981-1990 and 1974-1990.

At the northern boundary of the studied coast, aeolian sand transport is a possible sediment source, considering the proximity of the Baleal beach-dune system, located at the north side of the Peniche isthmus. However, currently, this should be reduced due to the urban structures on the isthmus.

The cross-shore exchange between littoral and the continental shelf should be reduce and related with extreme storm events, but no reference about this subject was found for the studied area. Also, there are no morphological evidence of submarine canyons on the studied inner shelf (Vanney and Mogenout, 1981; Badagola, 2008); therefore, there is no significant sediment losses for deeper continental shelf.

The sediment retention related with the sea-level rise (SLR), is also a sediment loss that is not quantified for the study coast.

According to the harbours dredging plan presented by LNEC (2010), Peniche and Ericeira harbours should capture, 30×10^3 $m^3.yr^{-1}$ and 2×10^3 $m^3.yr^{-1}$ of sediment, respectively, mainly composed by sand. More recently, Andrade *et al*. (2015) presented a value of 7×10^3 $m^3.yr^{-1}$ for the Ericeira harbour, based on information provided by DGRM (*Direcção-Geral de Recursos Naturais, Segurança e Serviços Marítimos*). LNEC (2010) refer that only two maintenance dredging operations at Peniche harbour were carried out in the period 2000-2010, corresponding to a sediment volume of 6.6×10^3 m^3, dredged in 2004. In the case of Ericeira

harbour, one dredging was performed in 2003, but its volume is unknown. Despite the recommendations presented in this report for the use of the uncontaminated sediment dredged from the harbours in the beach nourishment, there is no information about the operations carried out in the Peniche harbour after 2010. In the case of Ericeira harbour, about 9×10^3 m^3 of sand were dredged in the last two years, which were used to nourish the Algodio beach located north of the harbour (personal communication of the Dr. Fernando Magalhães of the *Agência Portuguesa do Ambiente*). Based on this volumes the sediment capture of this harbour can be estimated in 4.5×10^3 $m^3.yr^{-1}$.

The coastline evolution presented by Lira *et al.* (2016), based on foredune toe location observed from aerial images (1958-2010), suggest a non-significant long-term evolution for the coastal stretch between Carvoeiro and Raso capes, compared to other sectors of the Portuguese western coast. The signal and magnitude of the changes are site-specific and the main trends observed were erosion at Consolação, north sector of Foz do Sizandro and Guincho (-0.49, -0.22 and -0.65 $\pm$0.2 $m.yr^{-1}$), and accretion at Areia Branca, Santa Rita and south sector of Foz do Sizandro (+0.74, +1.06 and +0.23 $\pm$0.2 $m.yr^{-1}$, respectively). The other dune fields had changes that are within the method uncertainty ($\pm$0.2 $m.yr^{-1}$). The authors concluded that the measured changes essentially reflect the coastal system's natural variability, assuming that anthropogenic influence in sediment supply are negligible.

The work presented by Carapuço (2016)[5], based on historical postcards dated from the early 20th century to the present, suggests that the western beaches of Cascais (*i.e.* Abano, Guincho and Cresmina beaches, located north of Raso cape) are relatively stable. This author assumes that shoreline changes are related with seasonal to interannual variations in oceanographic forcing, excluding a perceptible long-term trend. Furthermore, the photo-monitoring carried out by the same author at the same beaches, during approximately one year, illustrate well the seasonal changes occurring in these beaches.

According to the longshore sediment transport patterns presented in Chapter 5, this coast can be segment into four sub-cells: (1) Carvoeiro-Consolação; (2) Consolação-Lamporeira; (3) Lamporeira-Roca; and (4) Roca-Raso. The main goal of this chapter is to define a comprehensive sediment budget for the studied coast and respective sub-cells, based on the main sediment sources and sinks identified (**Figure 7.2**) and, on the information obtained from previous chapters.

[5] See also the website: http://beachphotomonitoring.campus.ciencias.ulisboa.pt/

As existing information about the main sediment sources is spatially limited (*i.e.* is not available or discretize along the entire coast) and because estimates were obtained through different methods, new estimates are presented in this chapter. Moreover, the sediment loss related with the SLR and the long-term evolution of the studied beaches were also investigated.

7.2 METHODS

7.2.1 Estimation of sediment volume from cliff erosion

The estimation of sediment volumes resulting from cliffs erosion was based on a historical inventory of cliff instabilities carried out by Penacho *et al.* (2013). This inventory was based on the comparison of aerial photographs covering the period between 1942-47 and 2010. The volume displaced (V) from each retreat movement detected was computed based on the mean cliff height ($\bar{h}$), mean retreat of the cliff crest ($\bar{R}$) and length of the affected cliff (L) available in the inventory, using the following expression:

$$V = A_c \times L \quad (\mathbf{7.1})$$

where A_c is the affected cross-sectional area of cliff, assuming that cliffs have vertical faces and landslide as a triangular area: $A_c = \left(\bar{h} \times \bar{R}\right)/2$. According to Professor Fernando Marques of the University of Lisbon (personal communication) this approach can underestimate the volumes when landslides have cross-sectional areas with trapezoidal shapes or when cliffs present less steep faces, and overestimated volumes when landslide does not affect the entire cliff height. Nonetheless, the same author noted that most of the cliffs of the study area have very steep faces, therefore this approach can be considered acceptable. Sediment yield rates from cliff erosion were then computed by dividing the estimated volume by monitoring time period of each landslide event.

7.2.2 Estimation of sediment yield from watersheds

Sediment yield from watersheds was estimated based on the soil erosion potential. Watersheds limits were defined based on the ASTER GEDM 2 digital elevation map (≈30 m resolution), release in 2011 by Japan's Ministry of Economy, Trade, and Industry – METI and U.S. National Aeronautics and Space Administration – NASA (available online at: https://gdex.cr.usgs.gov/gdex/, accessed Feb. 2013), using the Hydrology toolbox of ArcGIS software.

The soil erosion was estimated using an empirical model - Revised Universal Soil Loss Equation (RUSLE) model (Renard *et al*., 1997), which is a revision and update of the widely used Universal Soil Loss Equation (USLE) model (Wischmeier and Smith, 1978). According to the RUSLE model, potential soil erosion is computed through the equation:

$$A = R \times K \times L \times S \times C \times P \quad (\mathbf{7.2})$$

where A is the average soil loss (mass/area/year), R is the rainfall-runoff erosivity factor, K is the soil erodibility factor, L is the slope length factor, S is the slope steepness factor, C is the cover-management factor, and P is the support practices factor.

For the present case study, the rainfall-runoff erosivity factor R was extracted from the rainfall-runoff erosivity map of the *Atlas da Água*, for precipitation episodes that have exceeded 25.4 mm (available online at: http://sniamb.apambiente.pt/, accessed Oct. 2015).

The soil erodibility factor K was obtained from Soil Map of *Atlas do Ambiente*, which follows the Food and Agricultural Organization of the United Nations (FAO) classification system (available online at: http://sniamb.apambiente.pt/, accessed Oct. 2015). The relation of the factor K values with the FAO classification follow the systematization proposed in Pimenta (1998) for the Portuguese territory.

The cover-management factor C was obtained from the CORINE Land Cover 2006 map (Caetano *et al*., 2009) (available online at: http://www.dgterritorio.pt, accessed Oct. 2015). The relations between C values and the CORINE land cover level 1 classes follow the systematization proposed by Tomás and Coutinho (1993) for the Portuguese territory.

To make the RUSLE model suitable at the catchment scale, L and S factors were merged into a single topographic factor (LS) following the equation proposed by Mitasova *et al*. (1996, 2001), for computation of the factor at a point i on a hillslope:

$$LS_i = (m+1)\left(\frac{A_i}{22.13}\right)^m \left(\frac{\sin\theta_i}{0.0896}\right)^n \quad (\mathbf{7.3})$$

where A_i is upslope contributing area per unit contour width ($flow\ accumulation \times cell\ size$), θ_i is the slope, and m and n are parameters for a specific prevailing type of flow and soil conditions. The variables A_i and θ_i were computed based on digital terrain map used to limiting the watersheds areas (*i.e.* ASTER GEDM 2 with ≈30 m resolution), while m and n were assumed equal to 0.4 and 1.3, respectively, following the work presented by Lira *et al.* (2013) for an area that includes the studied watersheds.

Finally, the P factor was considered equal to 1 due to lack of information and impossibility of spatial discrimination (Cardoso, 1985; Lira *et al.*, 2013).

The transformation of soil erosion potential into sediment yield potential can be achieved by a multiplicative coefficient, known as Sedimentary Delivery Ratio (SDR). According to Cardoso (1985), when there are no objective measurements to determine a SDR coefficient, an empirical correlation between watershed area (A_w) and the SDR values proposed by Mitchell and Buzenzer (1980, *in* Cardoso, 1985) can be used. The correlation is given by the equation:

$$SDR = -0.052 \ln(A_w) + 0.374 \quad (\mathbf{7.4})$$

The sediment yield obtained in units of weight per year, were then converted into volumes, assuming a sediment dry unit weight. According to the relation between dry unit weight and the percentage of sand in the sediment accumulated in dam's reservoirs, proposed by Lane and Koelzen (1943, *in* Sousa, 1995), and considering sand percentages obtained by Oliveira (2009) and Janardo (2016) for the sediment resulting from watersheds erosion, the dry unit weight should be between 11 and 15 kN.m^{-3}, so a mean value of 13 kN.m^{-3} was assumed.

Data integration and computation of sediment yield was made with the ArcGIS software, using the toolbox created by Lira *et al.* (2013) for this purpose.

7.2.3 Estimation of littoral sediment supply

Littoral sediment supply corresponds to the sediment volume provided by the sediment sources that is compatible with beach systems. Considering the sandy nature of the studied beaches, sediment yield from watersheds and cliff erosion, useful for the littoral, should correspond approximately to the sand percentage in the total sediment yield. Thus, the quantification of the littoral sediment supply was based on grain-size compatibility factors between the sediment resulting from the erosion of the lithotypes that outcrop in the watersheds/cliffs and the beach sediment.

The analysis of each lithotype to get grain-size compatibility factor is a heavy task and time consuming. Since it is not the scope of this work, the compatibility factors were chosen based on information found in the works of Oliveira (2009), for the Sintra's watersheds, and Janardo (2016), for the São Domingos' watershed (Peniche) (**Table 7.1**).

According to the analysis presented by the authors mentioned above, the sand percentages of Jurassic and Cretaceous formations are quite variable due to the facies variation on limestones, marlstones and sandstones layers. Thus, sediment supply from these geological formations was estimated considering a range of values, between the minimum compatibility factor found for

the Jurassic-Cretaceous formations and the mean compatibility factor found for Jurassic superior formations, since these correspond to 70 % of the total area occupied by both Jurassic and Cretaceous formations.

Table 7.1. Grain-size compatibility factors presented by Oliveira (2009) and Janardo (2016), and the ones assumed in this work.

Geological formations*	**Grain-size compatibility factor**		
	Oliviera (2009)	***Janardo (2016)***	***This work***
Jurassic and Cretaceous sedimentary formations	0.10 (Jurassic) and 0.15 (Cretaceous)	0.15 to 0.60 (Jurassic)	0.10 to 0.35
Eocene-Oligocene sedimentary formations	0.35	-	0.35
Pleistocene and Pliocene sedimentary formations	-	0.75	0.75
Holocene sedimentary formations	0.60	0.76	0.76
Granitic rocks	0.85	-	0.85
Volcanic rocks	-	-	0.25

* see lithological description in section 1.5.1

The works mentioned above did not analysed the grain-size compatibility of volcanic sub-volcanic rocks that also outcrop in the studied watersheds, as shown by the geological map presented in Chapter 1 (see **Figure 1.6**). Basalts are the dominant lithotype and, according to analysis performed by Fedo *et al.* (2015), they can produce detrital material with 50 % of sand. However, this analysis was based on crushed basalt samples and did not account the strong chemical weathering affecting these rocks; thus, the sand percentage resulting from volcanic and sub-volcanic rocks should be lower, being assumed a compatibility factor of 0.25.

The littoral sediment supply was computed by multiplying the volume of total sediment yield and the grain-size compatibility factor. In the cliff case, this is a direct relation since each mass movements affected only one of the geological formations defined in the **Table 7.1**. In the case of watersheds, the estimated volumes were adjust by a mean compatibility factor ($\bar{C}$):

$$\bar{C} = \frac{\sum_1^i C_i \,.\, Al_i}{A_w} \qquad (\mathbf{7.5})$$

where C_i is the grain-size compatibility of each lithotype, Al_i is the outcrop area of each lithotype (based on the Geological Map of Portugal at a 1:500 000 scale, presented in **Figure 1.6**); A_w is the watershed area; i is the number of lithotypes.

7.2.4 Estimation of sediment retention related with the sea-level rise

The sediment retention related with the SLR was estimated assuming some of the assumptions of the model proposed by Taborda and Ribeiro (2015) to estimate the impact of the SLR in platform beaches, which considers that headland-bay beaches are usually limited to the upper section of the profile and beach face is limited by a rocky shore platform. This model develops on the assumption that the beach profile (including berm elevation and face slope) is in equilibrium with mean sea-level (MSL) and wave climate. In response to sea- level rise, the model assumes that the profile will preserve the shape but the berm will be raised by the same amount as the rise in sea-level. If the system is assumed closed (*i.e.* beach volume is invariant) the thickness of sediment deposited over the berm must be compensated by the erosion of the beach face and landward migration of the berm crest.

However, considering the results presented in previous chapters, the studied beaches are not closed systems and the sediment deposited over the berm must be compensated by the HSB. Under these conditions, the sediment volume retained by the berm rising can be estimated multiplying the beach berm area and SLR. The estimation was performed considering the SLR rate of 2.5 $mm.yr^{-1}$, estimated by Antunes and Taborda (2009) for first decade of the 21st century. The berm area of each beach was computed from the beach length (presented in the Chapter 3) and average beach width. The average beach width was estimated based on the distance between the berm crest line (*S* line, see section 3.2.2.1) and the coastline (*i.e.* dune, cliff or structure toe), using the Digital Shoreline Analysis v4.3 software (Thieler *et al*., 2009).

7.2.5 Historic and recent ground-photographs analysis

Historic and recent ground-photographs were used to get insights on long-term beach evolution, through a simple comparison. Most of the historic images were extracted from the antique postcards website *Delcampe* (https://www.delcampe.net/), but also from the blogs *Notícias de Colares* (http://freguesiacolares.blogspot.pt/) and *Rio das Maçãs* (http://riodasmacas.blogspot.pt/). The images date is unknown in most of the cases, but the postmarks, on the back of the postcards, helped to constrain a minimum date. The recent photographs were acquired during the field work or kindly provided by colleagues. These images had as first intent the photo-monitoring of the studied beaches, therefore, camera location and direction angle are not exactly the same of the historic images. The image comparison was performed only for few beaches once it is very difficult to find historical photographs for the most of them. The beaches were Sta. Cruz, Baleia (Ericeira), Magoito, Maçãs, Grande and Adraga (see location in **Figure 7.2**).

7.3 RESULTS

7.3.1 Sediment volume from cliff erosion

The spatial distribution of the landslides identified by Penacho *et al.* (2013) shows that this are more frequent in the stretch between Consolação and Ericeira (60 %), but its magnitude is quite variable alongshore (**Figure 7.3A**). The sediment volume magnitude varies between 6.5 and 1.8×10^5 m^3, but only 22 % exceed 1×10^3 m^3 (**Figure 7.3B**). For the period under analysis (1942- 2010), cliff erosion provided a total of 6.8×10^5 m^3 of detrital material, which correspond to a sediment yield of 1.4×10^4 $m^3.yr^{-1}$.

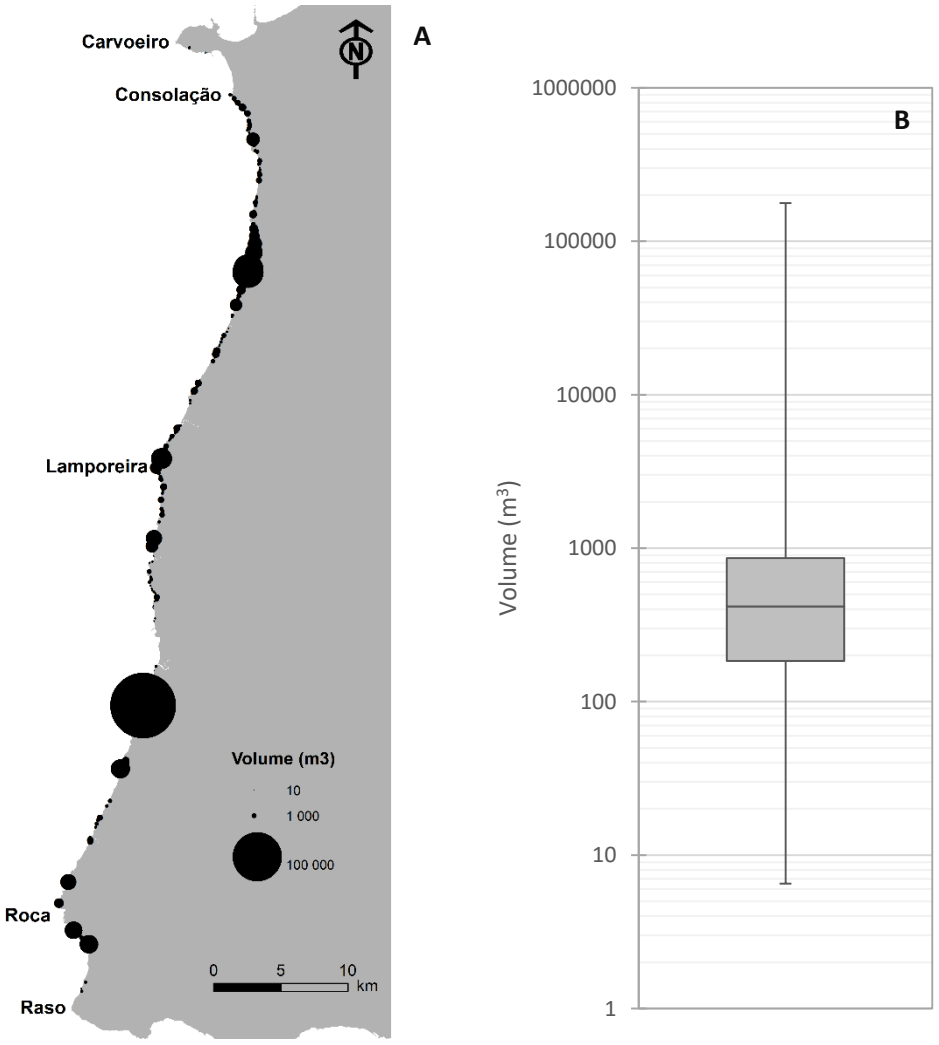

Figure 7.3. (A) Spatial distribution of landslides identified by Penacho *et al.* (2013), for the period between 1942/47 and 2010, and their respective magnitudes. (B) Total sediment yeild from cliffs erosion; Quartile 1 and quartile 3 of the boxes diagrams are the 25th and 75th percentiles of the samples, respectively; the mid-range is the median sample; and whiskers extremes are maximum and minimum values.

7.3.2 Sediment yield from watersheds

Sediment yield from watersheds is shown in **Figure 7.4**, where smaller watersheds are represented in a single class – coastal streams, despite being independent water systems. On the whole, fluvial streams release 7×10^4 $m^3.yr^{-1}$ of sediment. Lizandro and Sizandro rivers are the main sources, with 14×10^3 and 12×10^3 $m^3.yr^{-1}$, respectively; followed by Alcabrichel (7×10^3 $m^3.yr^{-1}$), Grande (6×10^3 $m^3.yr^{-1}$), Safarujo (6×10^3 $m^3.yr^{-1}$), Cuco (5×10^3 $m^3.yr^{-1}$), Colares (4×10^3 $m^3.yr^{-1}$) and São Domingos (3×10^3 $m^3.yr^{-1}$). The coastal streams present individual values lower than 3×10^3 $m^3.yr^{-1}$, but together contribute with 12×10^3 $m^3.yr^{-1}$ of sediment.

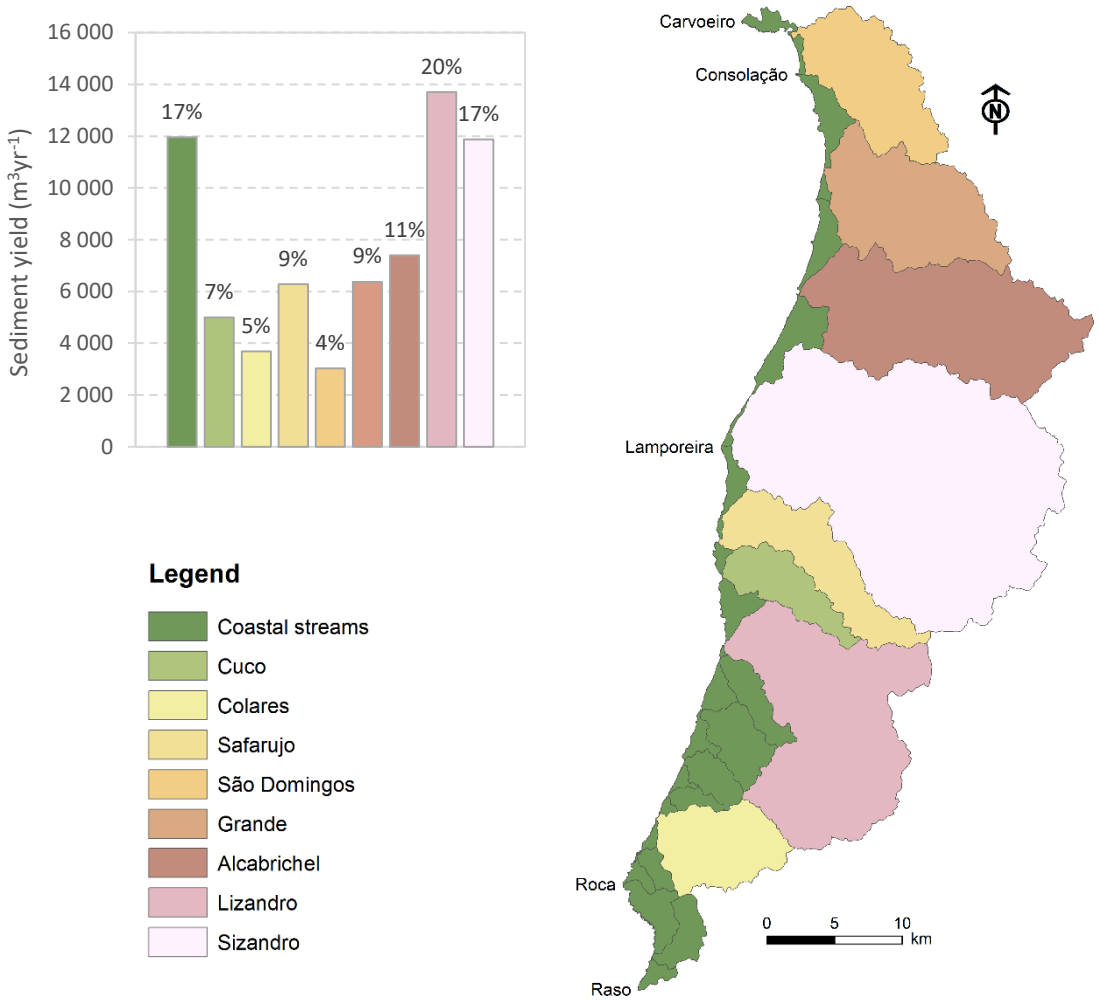

Figure 7.4. Sediment yield estimated by RUSLE model (at the left) and geographical area (at the right) of each watershed.

7.3.3 Littoral sediment supply

The application of grain-size compatibility factors indicate that sediment supply should be between 1.6×10^4 and 3.3×10^4 $m^3.yr^{-1}$, considering the minimum and maximum compatibility

factors assumed for the Jurassic and Cretaceous sedimentary formations. These values correspond to 19 and 40 % of the total sediment yield provided from both watersheds and cliff erosion (**Figure 7.5A**). The sediment contribution from watersheds was estimated between 1.4×10^4 and 2.8×10^4 $m^3.yr^{-1}$, and is one order of magnitude higher than the one from cliff erosion (1.9×10^3 to 5.3×10^3 $m^3.yr^{-1}$) (**Figure 7.5B**).

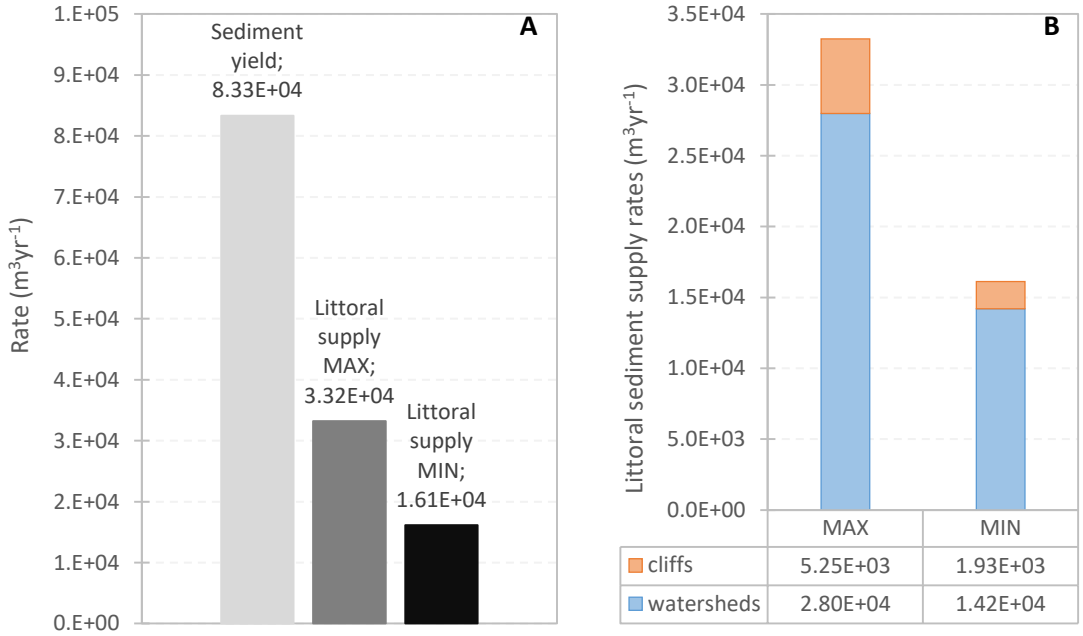

Figure 7.5. (A) Sediment yield from watersheds and cliff erosion and minimum and maximum littoral sediment supply estimated based on the grain-size compatibility factors; and (B) littoral sediment supply from watersheds and cliff erosion.

7.3.4 Long-term beach evolution

Historic and recent photographs of the beaches are shown in **Figure 7.6** and **Figure 7.7**. Most of historic photographs were acquired during the first half of 20th century, except in the case of Adraga, acquired in mid-50's, and probably Magoito (prior to 1967). Despite the possible differences on tide level and wave conditions, the simple comparison of the historic and recent images shows that the general configuration of these beaches did not have significant change over the last century. The main differences observed are related with human development, such as the concrete wall of Grande beach and the small groin in the mid of Baleia beach.

Sta. Cruz beach

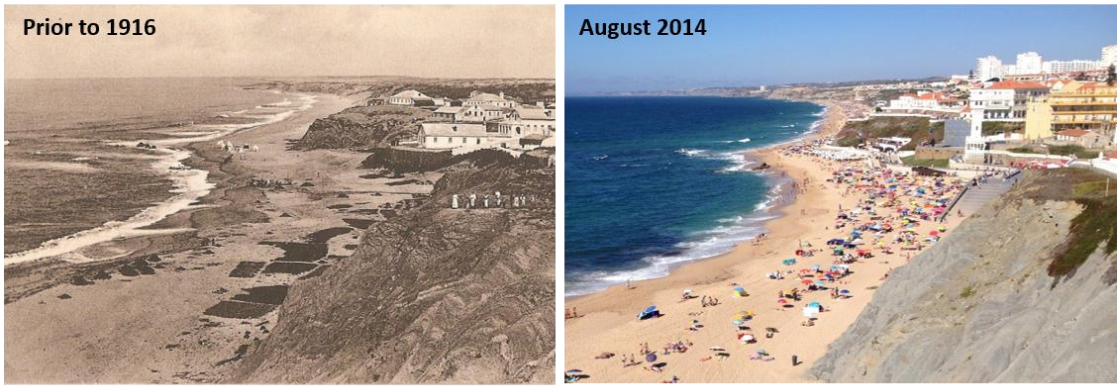

Baleia beach

Magoito beach

Figure 7.6. Sta. Cruz beach in the early 20th century and in August 2014; Baleia beach in first half of 20th century and in July 2014; and Magoito beach before 1967 and in July 2014 (historic images avaliable in https://www.delcampe.net/, accessed in Feb. 2017).

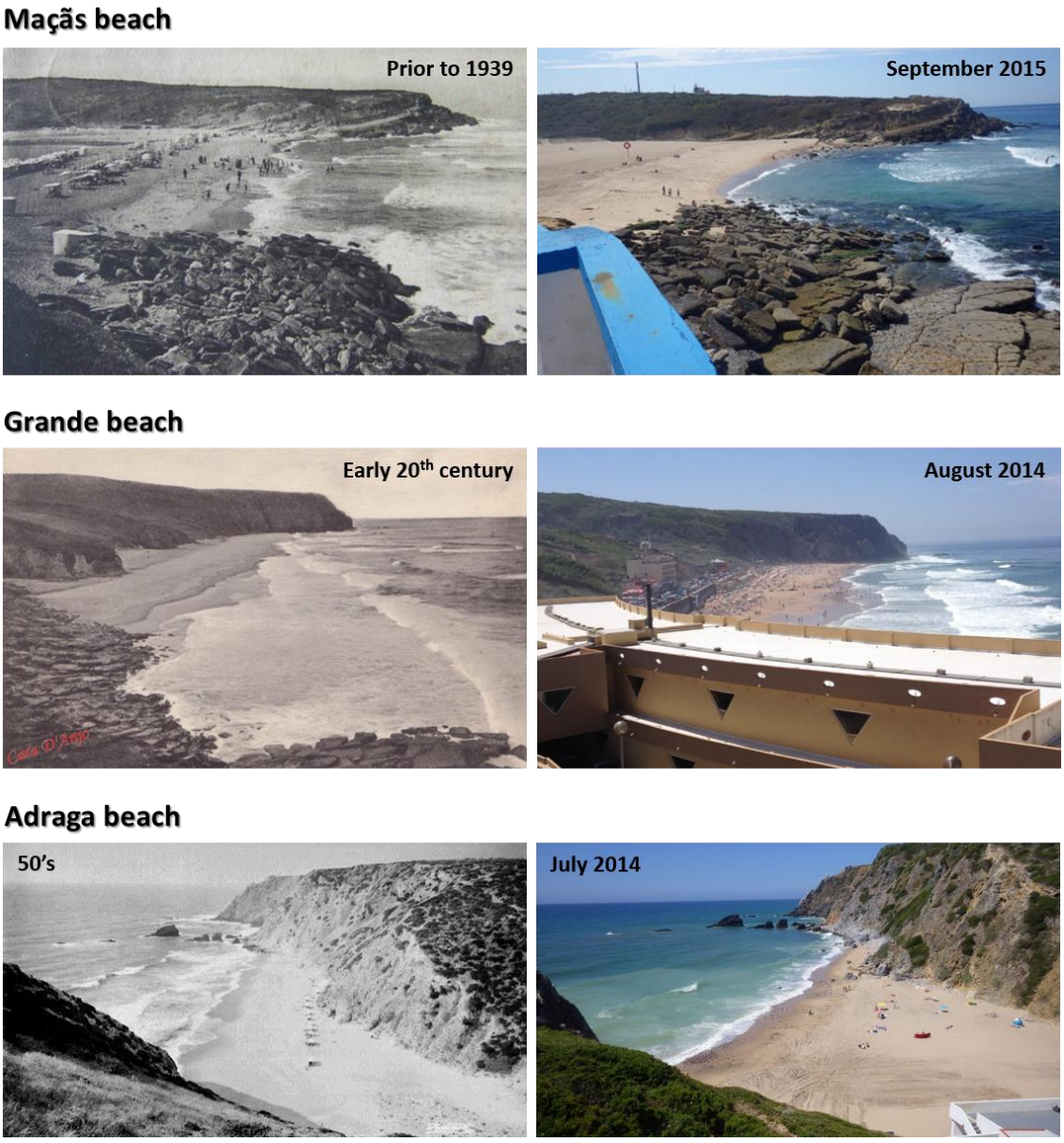

Figure 7.7. Maçãs beach before 1939 (avaliable online at https://www.delcampe.net/, accessed in Feb. 2017) and in September 2015; Grande beach in early 20th century (avaliable online at http://freguesiacolares.blogspot.pt/, acessed in Feb. 2017) and in August 2014; and Adraga beach in 50's (António Passaporte photo, available online at http://riodasmacas.blogspot.pt/, accessed in Feb. 2017) and in July 2014.

7.4 DISCUSSION AND CONCLUSIONS

The comparison between historic and recent ground-photographs did not show any long-term trend, suggesting that the studied beaches are stable. The changes observed on the beaches can be explained by the seasonal and interannual wave variability, as shown by the beach morphological analysis and photo-monitoring (see Chapter 3). These observations are in agreement with coastline evolution of the short low-lying sandy stretches presented by Lira *et al.* (2016) and with the study of Carapuço (2016) in the western beaches of Cascais.

The sediment retention related with the SLR was estimated in 4.7×10^3 $m^3.yr^{-1}$ (for a berm area of 1.9×10^6 m^2), one order of magnitude lower than the main sediment sources (1.6×10^4 to 3.3×10^4 $m^3.yr^{-1}$). This added retention does not have significant impacts on the shoreline position, corroborating the assumption that HSB is the main driver of beach dynamics and evolution. However, considering the expected sea-level change scenarios in relation to climate change, is plausible that this sediment sink will have a greater impact on the sediment budget of this coast.

The longshore sediment transport patterns presented in Chapter 5, showed that the studied coast is segment into four sub-cells: (1) Carvoeiro-Consolação; (2) Consolação-Lamporeira; (3) Lamporeira-Roca; and (4) Roca-Raso. The transport patterns also showed that the headlands that separate this sub-cell are gated boundaries, where the net HSB only occurs in the southward direction.

The sediment supply provided by fluvial streams and cliff erosion and, the sediment retention related with the SLR of each sub-cell, are presented in **Figure 7.8**. It can be noticed that sub-cell 3 receives between 9×10^3 and 1.7×10^4 $m^3.yr^{-1}$ of sediment (more than half of the sediment supply estimated for the entire coast), followed by sub-cell 2 with a sediment supply of 5.3×10^3 to 1.3×10^4 $m^3.yr^{-1}$; while in the sub-cells 1 and 4, sediment supply do not exceed 2×10^3 $m^3.yr^{-1}$. Despite the larger source area of the sub-cell 1, sediment supply for the sub-cell 4 is higher, which should be the effect of the geology and geomorphology.

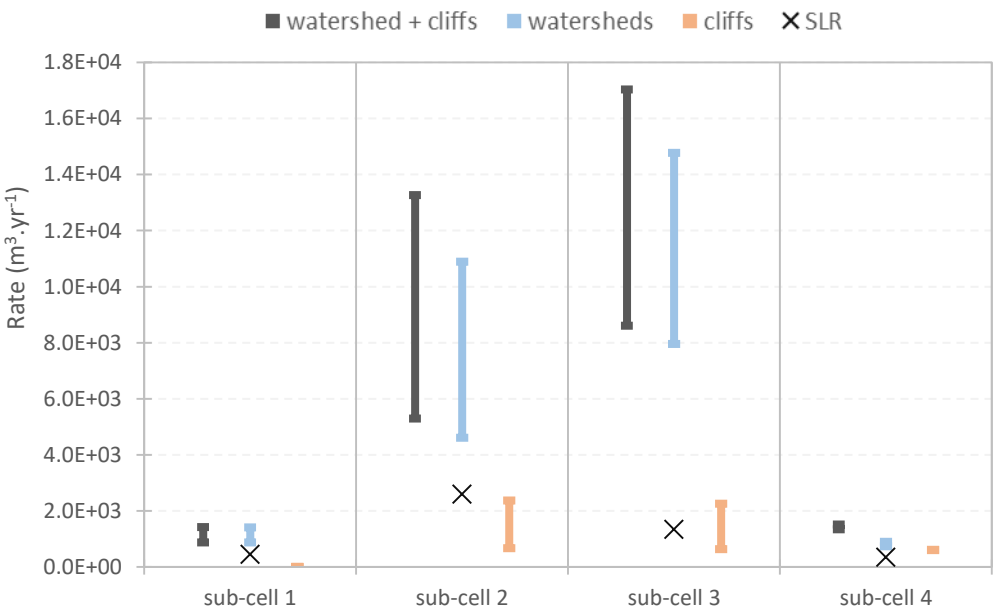

Figure 7.8. Sediment supply (from fluvial streams and cliff erosion) and sediment loss related with the SLR, for each sub-cell: (1) Carvoeiro-Consolação; (2) Consolação-Lamporeira, (3) Lamporeira-Roca and (4) Roca-Raso. The bars represent the range of values between maximum and minimum estimates.

The results also show that sediment supply provided by fluvial streams is higher than the one provided by cliff erosion, mainly in the sub-cell 2 and 3, where the differences can reach one order of magnitude. It should also be noticed that sediment supply for the sub-cell 1 is provided almost in totality by fluvial stream and corresponds to the reference condition, taking into account the current sediment retention in São Domingos dam's reservoir.

The sediment loss related with the SLR have higher magnitudes in the sub-cell 2 (2.6×10^3 $m^3.yr^{-1}$) and sub-cell 3 (1.4×10^3 $m^3.yr^{-1}$) due to longer beach extensions (see Chapter 3); while sub-cells 1 and 3 have sediment losses that do not exceed 500 $m^3.yr^{-1}$ (**Figure 7.8**).

Based on the magnitude of the sediment sources and sink here presented and the ones obtained from previous studies, as well as on the information obtained in the previous chapters, a sediment budget for the studied littoral and its sub-cells is proposed (**Figure 7.9**):

SUB-CELL 1 (CARVOEIRO - CONSOLAÇÃO)

Considering that: (1) the Carvoeiro cape is a closed boundary, (2) the sediment bypass northward at Consolação cannot occur, and (3) most of the sediment provided from São Domingos river is retained in the dam's reservoir, sediment supply for this cell is negligible.

Sediment sinks of this sub-cell are the Peniche harbour with a magnitude of 3×10^4 $m^3.yr^{-1}$ (LNEC, 2010) and the SLR that is two orders of magnitude lower (447 $m^3.yr^{-1}$).

Under this scenario, this sub-cell presents a sediment deficit consistent with the erosive trend observed by Lira *et al.* (2016). However, the same authors considered that the coastline changes have a low magnitude that can be explained by the natural variability of the beach system. Notwithstanding, it was decided to confirm the compatibility of the eroded volumes with the sinks. The volume was estimated through a simple approach[6], based on the LiDAR data of 2011 provided by *Direcção-Geral do Território* and the data provide by Lira *et al.* (2016). The dune erosion rate obtained was 2.4×10^3 $m^3.yr^{-1}$, one order of magnitude lower than sediment sinks, suggesting that harbour sedimentation rate proposed by LNEC (2010) is overestimated. These dune erosion is more compatible with the sedimentation rate of 1.7×10^3 $m^3.yr^{-1}$ (estimated based on volume of the maintenance dredging presented by the same authors), or even with sediment loss related with the São Domingos dam (9×10^2 to 1.4×10^3 $m^3.yr^{-1}$).

[6] The coastline position (dune toe) for 2011 and 2012 were computed assuming the retreat rate (0.49 $m{\cdot}yr^{-1}$) and the coastline position in 2010 (Lira *et al.*, 2016). The projection of the coastline obtained for 2011 on the DTM acquired in the same year, coincides with the dune toe position observed from DTM (between 5 and 7 m elevations (MSL)). Thus, considering that dune toe is at least 5 m, a sand volume eroded between 2011 and 2012 was computed based on the DTM.

The sediment deficit due to the source suppression, plus the weakening of the southward component of longshore drift due to the sheltered promoted by the Peniche peninsula to the dominant NW waves, suggests that southward sediment bypassing at Consolação headland is negligible and, this sub-cell can be assumed as a small closed system. Moreover, if the sediment dredged in the harbour since 2010, had been used to nourish the beach, the system should have be in equilibrium.

SUB-CELL 2 (CONSOLAÇÃO – LAMPOREIRA)

The main sediment sources of the sub-cell 2 are fluvial streams and cliff erosion ($A \approx 5.3\times10^3$ to 1.3×10^4 $m^3.yr^{-1}$), given that HSB from updrift sub-cell and dune erosion are negligible. The sediment sinks are the sediment retention due to the SLR ($B \approx 2.6\times10^3$ $m^3.yr^{-1}$) and the Lamporeira sediment bypassing (A-B).

SUB-CELL 3 (LAMPOREIRA – ROCA)

Sediment sources of the sub-cell 3 are the HSB from the updrift sub-cell (A-B) and the fluvial streams and cliff erosion ($C \approx 8.6\times10^3$ to 1.7×10^4 $m^3.yr^{-1}$). The sediment sinks are the SLR ($D \approx 1.4\times10^3$ $m^3.yr^{-1}$) and the Roca sediment bypassing (A-B+C-D), because according to the most recent information, the sediment captured by the Ericeira harbour ($\approx 4.5\times10^3$ $m^3.yr^{-1}$) has been dredged and used in the nourishment of the updrift beach (Algodio beach).

SUB-CELL 4 (ROCA – RASO)

This sub-cell is supplied by the HSB from the updrift sub-cell (A-B+C-D) and by fluvial streams and cliff erosion ($E \approx 1.4\times10^3$ to 1.5×10^3 $m^3.yr^{-1}$). Considering that Raso cape is a closed boundary, the sediment sinks are the Guincho-Cresmina dune filed ($F \approx 1.4\times10^4$ to 2.8×10^4 $m^3.yr^{-1}$; Rebêlo *et al.*, 2002; Santos, 2006) and the SLR ($G \approx 353$ $m^3.yr^{-1}$) that compared to the previous sink has low significance in the sediment budget (A-B+C-D+E-F-G).

Under the previous assumptions and considering all the scenarios (*i.e.* maximums and minimum values) the sediment budget of this sub-cell varies between -2×10^4 and $+1\times10^4$ $m^3.yr^{-1}$. This result is obviously conditioned by the uncertainties of the sediment sources and sink estimates, such as the uncertain related with resolution and temporal validity of the background information used in the RUSLE model; the simplification of the grain-size compatibility factors applied; and the interannual variability of the system, as for example, the aeolian transport rates estimated by Rebêlo *et al.* (2002) and Santos (2006) for different time-intervals. Nevertheless, the magnitude range of the Guincho sink is in agreement with magnitude range of the Roca sediment bypassing ($\approx 1\times10^4$ to 3×10^4 $m^3.yr^{-1}$).

The sediment budget indicate that sediment sources balance the sinks and that this littoral is in equilibrium, which is supported by the long-term stability of the studied beaches. Furthermore, the results obtained also helped to define the magnitude of the net HSB at Lamporeira and Roca headlands, in the order of 10^4 $m^3.yr^{-1}$.

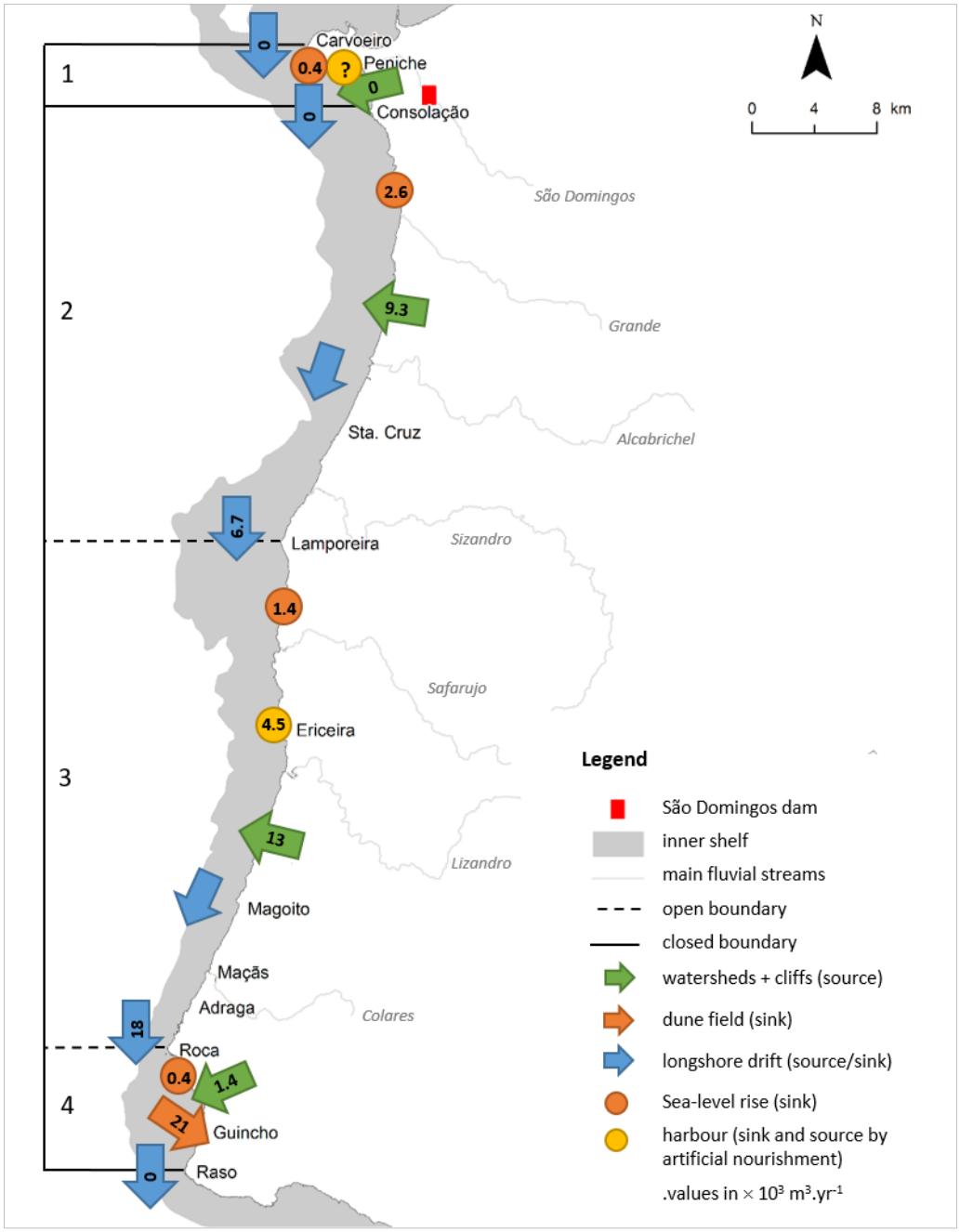

Figure 7.9. Sediment budget of the littoral between Carvoeiro and Raso capes (values in $\times 10^3$ $m^3.yr^{-1}$). The magnitude of the sediment sources and the Guincho dune field sink, are represented by a mean value, but they can vary in the interval of values described in the text.The offshore limit of the inner shelf was defined based on the bathymetric contour of 40 m provided by Vanney and Mougenot (1981).

Chapter 8

Synthesis and Conclusions

8.1 INTRODUCTION

This thesis addresses the study of headland sediment bypassing (HSB) processes. These processes play an important role in the definition of the littoral sediment budget, having particular relevance on headland-bay coasts. However, headland-bay beaches research has been focus on the beach planform stability and rotation, since these beaches are generally regarded as fairly closed systems. On the other hand, although there are several references to the natural HSB in literature, few are those that focus on a detail description and conceptualization of these processes. For these reasons and taking into account that rocky coasts encompass more than half of the world's coastline, the present study aimed to improve the current understanding of HSB.

To archive this goal, the 100 km rocky coastal stretch between Carvoeiro and Raso capes, located at the Portuguese western coast, was chosen as a case study. This stretch includes headlands of several sizes and a set of beaches with variable length, orientation, embayment degree and exposure to the NW dominant waves. To identified and characterized the HSB processes occurring in this coast, it was fundamental to investigate depth, direction, frequency and magnitude of these processes, as well as the characteristics of the sediment that bypass the headlands. The research was based on morphological, sedimentological and oceanographic data

analyses, a tracer field experiment and processes modelling. The results obtained were also used to define the sediment budget of the studied coast, supported by the analyses of the sediment sources/sinks and the long-term change trends of the beaches.

The HSB processes identified are presented in this chapter through conceptual models and, discussed considering the conceptual models described in the literature. This chapter includes also a discussion about the sedimentary dynamics of the study coast considering the results presented in the previous chapters, the general conclusions and the guidelines for further research.

8.2 CONCEPTUAL MODELS OF HEADLAND SEDIMENT BYPASSING

The literature review shows that currently there are three conceptual models to describe HSB: (1) the headland sandbar bypassing proposed by Short and Masselink (1999), which assumes that the seaward beach rotation results in a sub-aqueous sand wave along the headland coast that migrates downdrift and weld to the downdrift beach; (2) the sand strand bypassing described by Smith (2001), where sediment that bypass the headlands is transported across the downdrift embayment following a strand at an angle that depend on the null point of the wave refraction orthogonal; and (3) the model described by Storlazzi and Field (2000), in which beach sediment is carried outside the embayment by the strong offshore flows during major storm events, allowing it to be transported alongshore and feed the downdrift beach during low-energy swells.

In the studied coast, a process similar to the one presented by Short and Masselink (1999) was identified. It was observed that the persistence of NW, low-energy wave conditions, typical of the summer season, induced beach rotation. In the low-degree embayments, beach planform rotation resulted in a continuous inner sandbar along the headland coast that migrates downdrift and weld to the downdrift beach. However, beach rotation it is not necessarily related with low-energy waves, being the persistence of a wave direction the main trigger mechanism of this process. The shoreline evolution modelling demonstrates that this process is clearly dominated by the longshore drift, occurring mainly in the intertidal zone and, eventually, in very shallow depths of the inner shelf. As this process is typical of the subaerial beach domain, was named as Beach headland Sediment Bypassing (BSB) (**Figure 8.1**). The sedimentological data show that BSB is mainly related with coarse to medium sand.

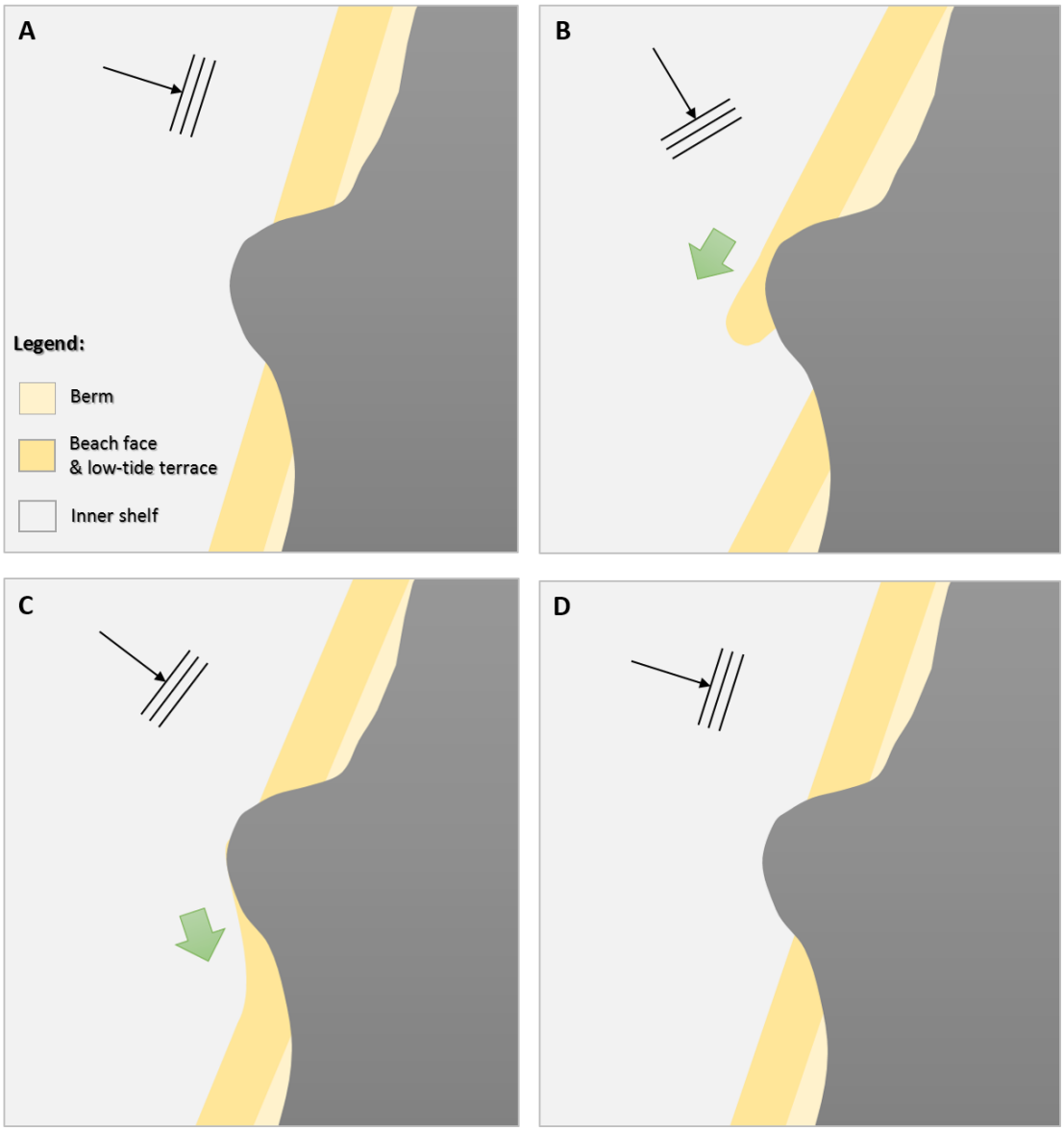

Figure 8.1. Conceptual model of the beach headland sediment bypassing (BSB): (A) initial condition; (B) beach rotation induced by a persistent wave direction and resulting inner sandbar; (C) merging of the inner sandbar with the downdrift beach; (D) slightly accretion of the downdrift beach.

In the case of high-embayed beaches, the process described above cannot induce HSB, since the active beach profile does not reach the tip of the headland. In these cases, the results obtained suggest that sediment only can leave the embayment during high-energy wave conditions. During major storm events a severe beach erosion was observed, as result of the cross-shore sediment transport induced by strong seaward currents, in agreement with the Storlazzi and Field (2000) model. The sediment that leaves the embayment is then distributed on the inner shelf and eventually transported alongshore, bypassing the headlands. When wave energy start to diminish the sediment is slowly transported onshore and start to merge with downdrift beaches. This process is not exclusive of high-indented beaches and its frequency increases from

high- to low-degree embayment, *i.e.* as higher the embayment degree, the higher has to be the wave energy need to transport the sediment outside the bay. This HSB process is clearly triggered by the increase of wave energy and, depends on both cross- and longshore transport components, occurring at deeper waters, being named as inner Shelf headland Sediment Bypassing (SSB) (**Figure 8.2**). The spatial distribution of the inner shelf sedimentary deposits indicate that SSB is related with medium to fine sand. Although, during major storm events, the wave conditions can trigger an extremely effective selection process, as demonstrated by the large heavy mineral placer deposit observed at Grande beach, capable to transport coarser particles offshore.

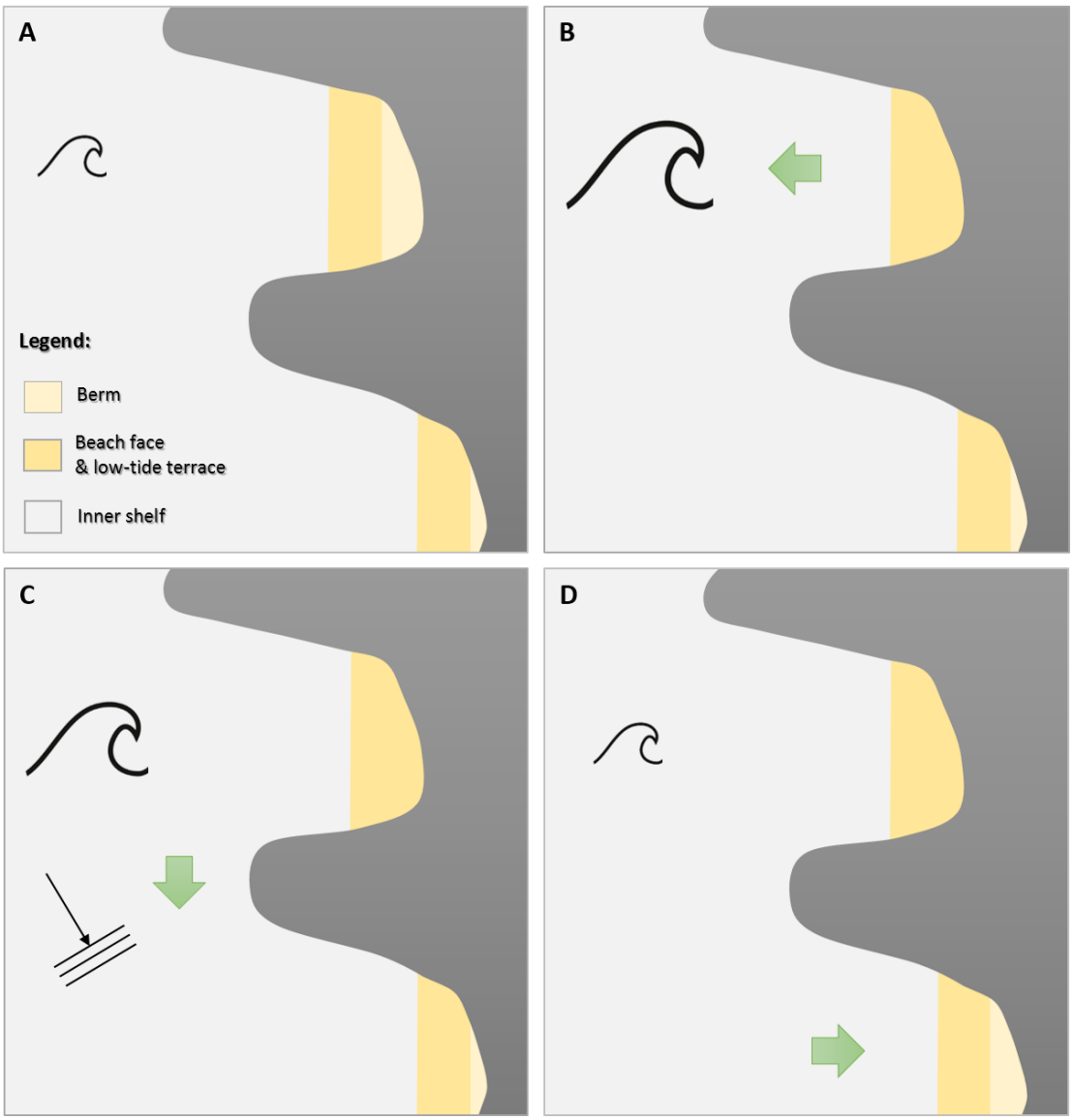

Figure 8.2. Conceptual model of the inner shelf headland sediment bypassing (SSB): (A) intial conditions; (B) beach erosion induced by the strong offshore flow during high-energy wave conditions; (C) sediment transport along the inner shelf; and (B) slow merge of the sediment that bypassed headland with the downdrift beach, during low-energy wave conditions.

The model proposed by Smith (2001), is not necessarily a different HSB process, but a model that focus on the geometry of the HSB at the downdrift side. In fact, the sand strand described by this author, is compatible with the offshore sandbar, shallow attached sandbar or elongated spit observed by Short and Masselink (1999). However, as stated by Smith (2001), strand bypassing cannot develop when the seabed is sand starving and/or the downdrift beach is highly curve in plan, because the projection of the strand along the wave refraction orthogonal may be impossible. This means that geometry of the HSB depends on both, coastal geomorphology and sedimentary availability. In the studied coastal stretch it was noticed that, in the sandier stretches, HSB manifest itself through well-defined path, *i.e.* continuous inner or outer sandbars along the headland coast. However, in the rockier stretches, the sediment spread on the rocky platform, should be transported alongshore as thin, discontinuous and patchy sand bodies, as observed and described by Storlazzi and Field (2000) and Hume *et al.* (2000).

8.3 IMPLICATIONS OF THE HEADLAND SEDIMENT BYPASSING IN THE SEDIMENTARY DYNAMICS OF THE STUDY COASTAL STRETCH

The results presented in the previous chapters show that studied coast is segmented in four sub-sedimentary cell: (1) Carvoeiro-Consolação; (2) Consolação-Lamporeira; (3) Lamporeira-Roca; and (4) Roca-Raso.

The first sub-cell comprises the beach located between Peniche harbour and Consolação headland, having particular characteristics due to shelter promoted by the Peniche peninsula to the NW dominant waves, which reduce significantly the longshore sediment transport southward. The magnitude of the sediment sources within this sub-cell is extremely reduced and the only sink is the Peniche harbour that should capture the sediment transported northward, during SW wave conditions. According to the sediment budget defined, this sub-cell corresponds to a small closed system.

The other three sub-cells are macro scale embayments, which have similar sedimentary dynamics. The northern sectors of these embayments have a NW-SE or N-S general orientation and the net longshore drift is southward for both winter and summer wave conditions. Thus, headlands in these sectors only can be crossed in a single direction (*i.e.* southward), independently of the HSB process. The southern sectors, on the other hand, have a NE-SW general orientation and the net longshore drift is southward, in the summer, and northward, in the winter. Considering the higher persistence of NW waves during summer, HSB should occur mainly through the BSB process. In winter, wave directional spreading is larger and wave energy

increases favouring the SSB. In low-indented beaches it is entirely possible that BSB and SSB occur simultaneously during storm conditions. However, the BSB northward is unlikely, considering the larger distances between the shoreline (beach berm) and the tip of the headland and the lower persistence of W and SW wave conditions.

The coexistence of the two HSB processes in the low-indented coastal stretches suggest that they are decoupled. This assumption is also supported by the shoreline evolution modelling, which demonstrate that BSB is sufficient to justify the shoreline configuration of low-indented coastal stretches, suggesting that in this case BSB is the dominant process. Otherwise, the shoreline configuration modelled should be significantly different from the observed one.

The balance between the longshore transport components within the southern sectors of the macro scale embayments, results in a sediment recirculation, which explains the sandy nature of inner shelf in these sectors. Otherwise, considering the lower magnitude of the sediment sources (in the order of 10^4 m^3yr^{-1}) compared to the longshore drift rate estimated based on the tracer experiment and numerical modelling (in the order of 10^6 m^3yr^{-1}), the inner shelf should be rocky, as the one in the northern stretches.

The sediment accumulation observed on the inner shelf of the southern sectors (of the macro scale embayments), is a consequence of the sediment recirculation described before, suggesting that sediment can have a relatively long residence time inside these sub-cells. However, once sediment cross the sub-cell boundaries cannot reverse its movement, considering that at the downdrift side of the most prominent headlands the net longshore drift is permanently southward. The frequency of the sediment linkage between the sub-cells depend on the seasonal and interannual wave climate variability, as shown by the beach morphological analysis. The magnitude, on the other hand, depends on the balance between the sediment sources and sinks of each sub-cell and was estimated in the order of 10^4 $m^3.yr^{-1}$.

According to the previous considerations a conceptual model for sedimentary dynamics of the study site is proposed and presented in **Figure 8.3**.

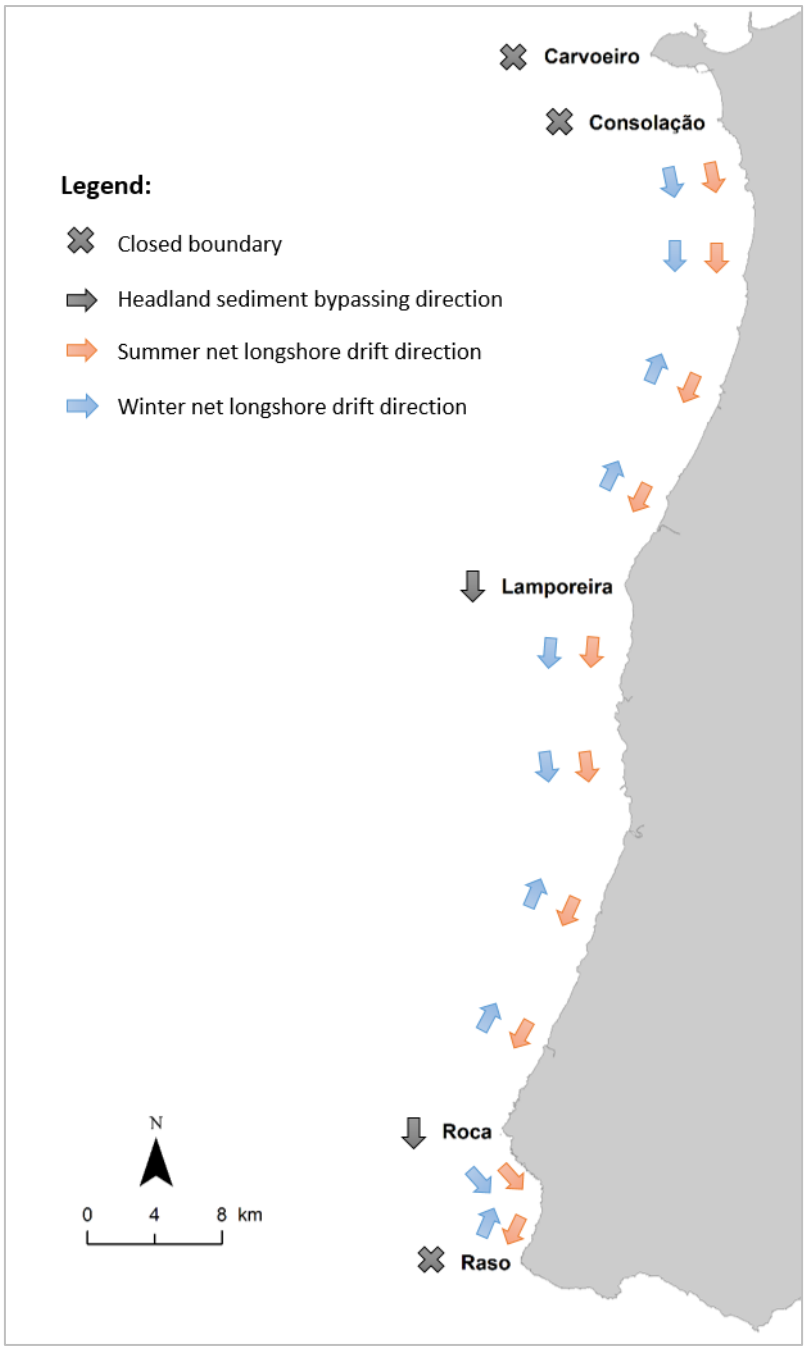

Figure 8.3. Conceptual model of the sedimentary dynamics for the studied coastal stretch. In the northern sectors, the sediment that leaves the embayments is sweeping southward, independently of the HSB process. In the southern sectors, the sediment is transported southward during the summer, bypassing the headlands through the BSB process, and northward, in the winter, though the SSB process (and eventually through the BSB).

8.4 GENERAL CONCLUSIONS AND FURTHER RESEARCH

The work carried out in the scope of this thesis contributes to the headland sediment bypassing research. The results obtained through several approaches allowed to classify dominant headland sediment bypassing processes in two main modes, which are in line with two of the existing conceptual models. The processes were classified according to the prevailing domain

where sediment bypass the headlands as: 1) beach headland sediment bypassing (BSB) – a processes that takes place mainly at the subaerial section of the beach, and 2) inner shelf headland sediment bypassing (SSB) – a processes that occurs on the submarine domain. BSB is triggered by the persistence of incoming wave direction, is dominated by the longshore drift and is typical of low-indented coasts, where it plays a major role on the beach development and evolution. SSB is triggered by high-energy wave conditions, depend of both cross- and longshore transport components and can occur in both low- and high-indented coasts. This latter process is particularly important in the development and evolution of high-indented beaches, where it is the only headland sediment bypassing process possible.

The sedimentological analysis and tracer experiment showed that headland sediment bypassing is a selective process. Coarser particles such gravel and very coarse sand tend to be trapped inside the embayments, being their bypassing very low or negligible. Coarse sand bypass occurs mainly in the subaerial beach, except during major storm events, when the wave energy triggers an extreme efficient selective process, transporting the lighter sediment particles offshore (including coarser sands), originating heavy mineral placer deposits. This selective process can generate large placer deposits due to a long-term enrichment in heavy mineral particles. In the case of medium sand particles, headland bypass can occur either subaerial beach or inner shelf domain, depend on the wave energy; while fine sand bypass should occur mainly in the inner shelf.

SEM-PLAT model results showed that headland sediment bypassing plays an important role in the beach development and evolution and that, seasonal (and interannual) changes in the incident wave climate can significantly affect the beach configuration, putting in evidence the delicate dynamic equilibrium of these beaches. Moreover, modelling also suggest that the exposed rocky shore platform can be a major factor in the wave propagation and, consequently, influence the beach configuration.

The analysis of the sediment sources and sinks, long-term beach evolution, potential net longshore drift patterns and bypassing constrains, allowed to define the sediment budget and sedimentary dynamics along the studied coast. The results indicate that beach systems between Carvoeiro and Raso capes are currently in equilibrium. The magnitude of the sediment bypassing at the most prominent headlands that segment the coast, depends on the balance between the sediment sources and sinks of each sub-cell and was estimated in the order of 10^4 $m^3.yr^{-1}$; while its frequency depends on the seasonal and interannual wave variability.

The linkage of the studied beaches, through the headland sediment bypassing processes, and their delicate dynamic equilibrium, indicate that climate changes can have strong impacts on their evolution, either through sediment retention induced by sea-level rise or changes in transport patterns due to wave climate rotation.

The conclusions of this study are constrained by the available data, in time and space, mainly in what concerns to the inner shelf, where data acquisition was more difficult. While BSB was clearly defined and relatively well-understood, the description of SSB is based on several assumptions that deserve further clarification and validation. Thus, future research should be focused on the sedimentary transport along the inner shelf, including the exchanges with the beach.

The modelling approach also deserves further development, as the SEM-PLAT is still focused on BSB. The model revealed as a useful tool in the study of BSB and beach rotation processes but it should be improved to account SSB. Furthermore, modelling approach can be also useful to forecast the impacts of climate changes, as well as in the management of headland-bay coastal stretches.

References

Aagaard, T., Black, K.P., Greenwood, B. (2002). Cross-shore suspended sediment transport in the surf zone: a field-based parameterization. *Marine Geology*, 185(3-4): 283-302.

Ab Razak, M. (2015). *Natural headland sand bypassing. Towards identifying and modelling the mechanisms and processes*. PhD Thesis, Delft University of Technology. CRC Press/Balkema, Netherlands, 187 p.

Acworth, C., Lawson, S. (2011). The Tweed Rive Entrance Sand Bypassing Project, ten years of managing operations in a highly variable coastal system. *Proceedings of 20th NSW Coastal Conference*, *Tweed Heads*, 23 p.

ADAPT (2015). *Dados do Programa ADAPT - Alterações Climáticas em Portugal*. Portal do Clima. Available at: http://portaldoclima.pt/. [Accessed 13 May 2017].

Andrade, C., Bizarro, A.R., Brito, P., Caldeirinha, V., Couto, A., Ferreira, A.S., Pina, C., Pinto, C.A., Portela, L.I., Ramos, L., Rodrigues, A., Taborda, R., Terrinha, P. (2015). *Grupo de Trabalho para os Sedimentos: relatório final*. Technical report, 31 p.

Andrade, C., Freitas, M.C., Cachado, C., Cardoso, A., Monteiro, J., Brito P., Rebelo, L. (2002). Coastal zones. In: Santos, F.D., Forbes, K. and Moita, R. (eds.), *Climate Change in Portugal: Scenarios, Impacts and Adaptation Measures – SIAM Project*. Gradiva, Lisbon, pp. 173-219.

Andrade, C., Taborda, R., Marques, F., Freitas, C., Antunes, C., Mendes, T., Carreira, D. (2009). *Plano Estratégico do Concelho de Sintra face às Alterações Climáticas - Zonas Costeiras*. Faculdade de Ciências da Universidade de Lisboa, 62 p.

Antunes, C., Taborda, R. (2009). Sea level a Cascais Tide Gauge: Data, Analysis and Results. *Journal of Coastal Research*, SI 56: 218-222.

Armstrong-Altrin, J.S., Nagarajan, R., Il Lee, Y., Kasper-Zubillaga, J.J., Córdoba-Saldañal, L.P. (2014). Geochemistry of sands along the San Nicolás and San Carlos beaches, Gulf of California, Mexico: implications for provenance and tectonic setting. *Turkish Journal of Earth Sciences*, 23: 533-558.

Badagola, A. (2008). *Evolução morfo-tectónica da plataforma continental do Esporão da Estremadura*. Master Thesis, Universidade de Lisboa, 171 p. (unpublished)

Bagnold, R.A. (1963). Mechanics of marine sedimentation. In: Hill, M.N. (ed.), The Sea: *The Earth Beneath the Sea History*. Interscience, New York, pp. 507–528.

Baker, B.B., Deebel, W.R., Geisenderfer, R.D. (eds.) (1966). *Glossary of Oceanographic Terms.* 2nd edition. U.S. Naval Oceanographic Office, Washington, DC, 204 p.

Balsinha, M. (2008). *Dinâmica sedimentar da plataforma continental portuguesa entre o desfiladeiro submarino da Nazaré e a Ericeira*. Master Thesis, Universidade de Lisboa, 174 p. (unpublished)

Balsinha, M., Rodrigues, A., Oliveira, A., Palma, C., Valença, M., Mil-Homens, M. and Taborda, R. (2010). Assinatura geoquímica das ribeiras no Esporão da Estremadura. *Actas das 1as Jornadas de Engenharia Hidrográfica*. Instituto Hidrográfico, Lisbon, pp. 137-140.

Barriolo, G., Cabella, R., Ferrari, M., Montefalcone, M. (2012). Sediment bypass from the littoral cell in gravel pocket beaches of the Ligurian Sea (NW Mediterranean). *Proceedings of International Conference on Marine and Coastal Ecosystems 2012*, *Tirana, Albania*, pp. 472-481.

Bascom, W.N. (1951). The relationship between sand size and beach-face slope. *Transactions, American Geophysical Union*, 32(6): 866-874.

Bastos, A.P., Lira, C., Taborda, R., Ribeiro, M., Andrade, C. (2015). Morphological storm threshold: an example from a pocket beach in the west Portuguese coast. *Livro de resumos da 3ª Conferência sobre morfodinâmica estuarina e costeira*. Universidade do Algarve, Faro, pp. 73-74.

Beach Sand Code Project (2012). *Beach sediment sampling and processing guidelines*. Technical note, 9 p. Available at: http://sandcode.fc.ul.pt/References/sampling%20guidelines.pdf [Accessed 27 Dec. 2013].

Bodge, K., Dean, R. (1987). Short-term impoundment of longshore transport. In: Kraus, N.C. (ed.), *Coastal Sediments '87: Proceedings of a Specialty Conference on Advances in Understanding of Coastal Sediment Processes, New Orleans, Louisiana*. American Society of Civil Engineers, pp. 468-483.

Boeyinga, J., Dusseljee, D.W., Pool, A.D., Schoutens, P., Verduin, F., van Zwicht, B.N.M., Klein, A.H.F. (2010). The effects of a bypass dunefield on the stability of a headland bay beach: A case study. *Coastal Engineering*, 57(2): 152-159.

Boggs, S. (1995). *Principles of sedimentology and stratigraphy*. 2nd edition. Prentice-Hall, Englewood Cliffs, New Jersey, 774 p.

Booij, N., Ris, R.C., Holthuijsen, L.H. (1999). A third-generation wave model for coastal regions: 1. Model description and validation. *Journal of Geophysical Research*, 104(C4): 7649-7666.

Boswood, P.K., Murray, R.J. (2001). *World-wide Sand Bypassing Systems: Data Report*. Conservation technical report No. 15. Queensland Government, Environmental Protection Agency, ISSN 1037–4701, 59 p.

Bowman, D., Guillén, J., López, L., Pellegrino, V. (2009). Planview Geometry and morphological characteristics of pocket beaches on the Catalan coast (Spain). *Geomorphology*, 108(3-4): 191-199.

Bruun, P., Willekes, G. (1992). Bypassing and Backpassing at Harbors, Navigation Channels, and Tidal Entrances: Use of Shallow-Water Draft Hopper Dredgers with Pump-out Capabilities. *Journal of Coastal Research*, 8(4): 972-977.

Caetano, M., Nunes, V., Nunes, A. (2009). *CORINE Land Cover 2006 for Continental Portugal*. Technical report. Instituto Geográfico Português.

Calado, M. (1994). *Da Ilha de Peniche*. Edição de autor, Peniche, 117 p.

Carapuço, A.M. (2016). *Improving the transfer of coastal scientific knowledge: from concept to implementation*. PhD Thesis, Universidade de Lisboa, 143 p. (unpublished)

Carapuço, M., Ribeiro, M., Taborda, R. (2014). Assessing beach morphodynamics through close-range photomonitoring. *Actas das 3as Jornadas de Engenharia Hidrográfica*. Instituto Hidrográfico, Lisbon, pp. 293-296.

Cardoso, J.L. (1985). A erosão de bacias hidrográficas e o assoreamento de albufeiras. Estudo piloto de um caso português. *O Geoténico.* Faculdade de Ciências e Tecnologias da Universidade Nova de lisboa, pp. 115-139.

Cascalho, J., Bosnic, I., Taborda, R., Ribeiro, M., Lira, C., Carapuço, M. (2012). Beach sediment grain size variability based on image analysis. *Actas das 2as Jornadas de Engenharia Hidrográfica*. Instituto Hidrográfico, Lisbon, pp. 287-290.

Cascalho, J., Duarte, J., Taborda, R., Ribeiro, M., Silva, A., Bosnic, I., Carapuço, M., Lira, C., Rodrigues, A. (2014). Sediment textural selection during sub-aerial headland bypassing. An example from Nazaré coastal system (Portugal). *Actas das 3as Jornadas de Engenharia Hidrográfica*. Instituto Hidrográfico, Lisbon, pp. 297-300.

Cascalho, J., Ribeiro, M., Taborda, R., Rodrigues, A., Reis, J., Duarte, J., Oliveira, A. (2016). Os minerais pesados da praia Grande do Rodízio (Colares, Sintra): da fonte ao depósito sedimentar. *Estudos do Quaternário / Quaternary Studies*, 14: 82-91.

CERC (1984). *Shore Protection Manual*. 4th edition. Department of the Army, Waterways Experiment Station, Corps of Engineers, Coastal Engineering Research Center, Vicksburg, MS.

Ciavola, P., Taborda, R., Ferreira, Ó., Dias, J.M.A. (1997). Field measurements of longshore sand transport and control processes on a steep meso-tidal beach in Portugal. *Journal of Coastal Research*, 13(4): 1119–1129.

Clemens, K.E., Komar, P.D. (1988). Tracers of sand movement on the Oregon coast. In: Edge, B.L. (ed.), *Proceedings of 21st Conference on Coastal Engineering, Costa del Sol-Malaga, Spain*. American Society of Civil Engineers, pp. 1338-1351.

Codiga, D.L. (2011). *Unified Tidal Analysis and Prediction Using the UTide Matlab Functions*. Technical Report 2011-01. Graduate School of Oceanography, University of Rhode Island, Narragansett, RI, 59 p.

Coelho, C., Taveira-Pinto, F., Veloso-Gomes, F., Pais-Barbosa, J. (2004). Coastal evolution and coastal works in the southern part of Aveiro lagoon inlet, Portugal. In: Smith, J.M. (ed.), *Proceedings of 29th Conference on Coastal Engineering, Lisbon, Portugal*. World Scientific, pp. 3914–3926.

Collier, J.S., Brown, C.J. (2005). Correlation of sidescan backscatter with grain size distribution of surficial seabed sediments. *Marine Geology*, 214(4): 431-449.

Congedo, L. (2016). *Semi-Automatic Classification Plugin Documentation Release 4.8.0.1*. Available at: https://fromgistors.blogspot.com/p/semi-automatic-classification-plugin.html [Accessed 15 May 2016].

Costa, M., Esteves, R. (2009). Clima de Agitação Marítima na Costa Oeste de Portugal Continental. *Comunicações das XI Jornadas Técnicas de Engenharia Naval - O Sector Marítimo Português*. Instituto Superior Técnico, Lisboa, 15 p.

Cowell, P.J., Hanslow, D.J., Meleo, J.F. (1999). The Shoreface. In: Short, A.D. (ed.), *Handbook of beach and shoreface morphodynamics*. John Wiley & Sons, Chichester, pp.39-71.

Dabees, M., Kamphuis, W. (1998). Oneline, a numerical model for shoreline change. In: Edge, B.L. (ed.), *Proceedings of 26th Conference on Coastal Engineering, Copenhagen, Denmark*. American Society of Civil Engineers, pp. 2668–2681.

Daly, C.J., Winter, C., Bryan, K.R. (2015). On the morphological development of embayed beaches. *Geomorphology*, 248: 252-263.

Davis, K.S., Slowey, N.C., Stender, I.H., Fiedler, H., Bryant, W.R., Fechner, G. (1996). Acoustic backscatter and sediment textural properties of inner shelf sands, northeastern Gulf of Mexico. *Geo-Marine Letters*, 16(3): 273-278.

Dean, R.G., Kriebel, D.L., Walton, T.L. (2002). Cross-shore sediment transport processes (Chapter III-3). In: *Coastal Engineering Manual 1110-2-1100.* U.S. Army Corps of Engineers, Washington, DC, 79 p.

Dearing, J.A. (1999). *Environmental Magnetic Susceptibility: Using the Bartington MS2 System*. Bartington Instruments Ltd. 43 p.

Del Valle, R., Medina, R., Losada, M. (1993). Dependence of coefficient K on grain size. *Journal of Waterway, Port, Coastal and Ocean Engineering*, 119: 568-574.

Dias, J.M.A (1987). *Dinâmica Sedimentar e Evolução Recente da Plataforma Continental Portuguesa Setentrional*. PhD Thesis, Universidade de Lisboa, 384 p. (unpublished)

Dias, J.M.A., Boski, T., Rodrigues, A., Magalhães, F. (2000). Coast line evolution in Portugal since the Last Glacial Maximum until present — a synthesis. *Marine Geology*, 170(1-2): 177-186.

Diogo Z., Bastos, A., Lira, C., Taborda, R., Freire de Andrade, C., Silveira, T.M., Ribeiro, M., Silva A.N., Carapuço, M.M., Pinto, C.A., Freitas, M.C. (2014). Morphological impacts of Christina storm on the beaches of the central western Portuguese coast. *Comunicações Geológicas*, 101, Especial III, 1445-1448.

Dodet, G., Bertin, X., Taborda, R. (2010). Wave climate variability in the North-East Atlantic Ocean over the last six decades. *Ocean Modelling*, 31(3-4): 120-131.

Downing, J.P., Sternberg, R.W., Lister, C.R.B. (1981). New instrumentation for the investigation of sediment suspension processes in the shallow marine environment. *Marine Geology*, 42(1-4): 19-34.

Duane, D.B., James, W.R. (1980). Littoral transport in the surf zone elucidated by an Eulerian sediment tracer experiment. *Journal of Sedimentary Petrology*, 50(3): 929–942.

Duarte, J., Taborda, R., Ribeiro, M., Cascalho, J., Silva, A., Bosnic, I. (2014). Evidences of sediment bypassing Nazaré headland revealed by a large scale sand at tracer experiment. *Actas das 3as Jornadas de Engenharia Hidrográfica*. Instituto Hidrográfico, Lisbon, pp.289-292.

Evans, O.F. (1944). The relation of the action of waves and currents on headlands to the control of shore erosion by groins. *Proceedings of the Oklahoma Academy of Science*, 24: 9-13.

Fedo, C.M., McGlynn, I.O., McSween, H.Y. (2015). Grain size and hydrodynamic sorting controls on the composition of basaltic sediments: Implications for interpreting martian soils. *Earth and Planetary Science Letters*, 423: 67-77.

Fernández-Fernández, S., Baptista, P., Martins, V.A., Silva, P.A, Abreu, T., Pais-Barbosa, J., Bernardes, C., Miranda, P., Rocha, M.V., Santos, F., Bernabeu, A., Rey, D. (2015). Longshore Transport Estimation on Ofir Beach in Northwest Portugal: Sand-Tracer Experiment. *Journal of Waterway, Port, Coastal, and Ocean Engineering*, 142(2): 04015017, doi:10.1061/(ASCE)WW.1943-5460.0000319.

Ferrari, M., Cabella, R., Berriolo, G., Montefalcone, M. (2014). Gravel sediment bypass between contiguous littoral cells in the NW Mediterranean Sea. *Journal of Coastal Research,* 30(1): 183-191.

FitzGerald, D.M. (1982). Sediment bypassing at mixed energy tidal inlets. In: Edge, B.L. (ed.), *Proceedings of 18th Conference on Coastal Engineering, Cape Town, South Africa.* American Society of Civil Engineers, pp. 1094–1118.

FitzGerald, D.M., Kraus, N.C., Hands, E.B. (2000). *Natural mechanisms of sediment bypassing at tidal inlets*. Coastal and Hydraulics Engineering Technical Note ERDC/CHL CHETN-IV-30. U.S. Army Engineer Research and Development Center, Vicksburg, MS, 10 p.

Folk, R.L., Ward, W.C. (1957). Brazos River bar: a study in the significance of grain size parameters. *Journal of Sedimentary Petrology*, 27(1): 3–26.

França, J.C., Zbyszewski, G., Almeida, F.M. (1960). *Notícia explicativa da Carta Geológica de Portugal na escala de 1/50 000, Folha 26-C, Peniche*. Serviços Geológicos de Portugal, Lisbon, 33 p.

França, J.C., Zbyszewski, G., Almeida, F.M. (1961). *Notícia explicativa da Carta Geológica de Portugal na escala de 1/50 000, Folha 30-A, Lourinhã*. Serviços Geológicos de Portugal, Lisbon, 27 p.

Freitas, M.C., Andrade, C., Cruces, A. (2002). The geological record of environmental changes in southwestern Portuguese coastal lagoons since the Lateglacial. *Quaternary International*, 93-94: 161-170.

Gao, B.C. (1996). NDWI - A normalized difference water index for remote sensing of vegetation liquid water from space. *Remote Sensing of Environment*, 58(3): 257-266.

George, D.A., Largier, J.L., Storlazzi, C.D., Barnard, P.L. (2015). Classification of rocky headlands in California with relevance to littoral cell boundary delineation. *Marine Geology*, 369: 137-152.

Goodwin, I.D., Freeman, R., Blackmore, K. (2013). An insight into headland sand bypassing and wave climate variability from shoreface bathymetric change at Byron Bay, New South Wales, Australia. *Marine Geology*, 341: 29-45.

Gusmão, M. (2010). *Evolução actual do litoral Foz do Lizandro – Malhadinha*. Master Thesis, Universidade de Lisboa, 128 p. (unpublished)

Hamouda, A., EL-Gendy, N., El-Gharabawy, S., Fekry, A. (2016). Geological implications of acoustic imagery of the recent seabed textures in the Eastern Harbor, Alexandria. *The Egyptian Journal of Aquatic Research*, 42(3): 249-259.

Hanson, H. (1989). Genesis - A generalized Shoreline Change Numerical Model. *Journal of Coastal Research*, 5(1): 1-27.

Harley, M.D., Turner, I.L., Short, A.D. (2015). New insights into embayed beach rotation: The importance of wave exposure and cross-shore processes. *Journal of Geophysical Research*, 120(8): 1470-1484, doi:10.1002/2014JF003390.

Harley, M.D., Turner, I.L., Short, A.D., Ranasinghe, R. (2011). A reevaluation of coastal embayment rotation: The dominance of cross-shore versus alongshore sediment transport processes, Collaroy-Narrabeen Beach, southeast Australia. *Journal of Geophysical Research*, 116: F04033, doi:10.1029/2011JF001989.

Hein, J.R., Mizell, K., Barnard, P.L. (2013). Sand sources and transport pathways for the San Francisco Bay coastal system, based on X-ray diffraction mineralogy. *Marine Geology*, 345: 154-169.

Hsu, J.R.C., Silvester, R., Xia, Y.M. (1989). Generalities on static equilibrium bays. *Coastal Engineering*, 12(4): 353-369.

Hsu, J.R.C., Yu, M.J., Lee, F.C., Benedet, L. (2010). Static bay beach concept for scientists and engineers: A review. *Coastal Engineering*, 57(2): 76-91.

Hume, T.M., Oldman, J.W., Black, K.P. (2000). Sediment facies and pathways of sand transport about a large deep water headland, Cape Rodney, New Zealand. *New Zealand Journal of Marine and Freshwater Research*, 34(4): 695-717.

Hunter Labs (1996). Hunter Lab Color Scale. *Insight on Color*, vol. 8, No.9. Hunter Associates Laboratories, Reston, VA, USA, 4 p.

Iglesias, G., López, I., Castro, A., Carballo, R. (2009). Neural network modelling of planform geometry of headland-bay beaches. *Geomorphology*, 103(4): 577-587.

IH (2010). *Carta sedimentológica: Cabo Carvoeiro ao Cabo da Roca, na escala de 1/50 000, Folha SED4*. 1st edition. Instituto Hidrográfico, Lisbon, Portugal.

Ingle, J.C. (1966). *The Movement of Beach Sand: an analysis using fluorescent grains.* Developments in Sedimentology, Vol. 5. Elsevier, Amsterdam, 221 pp.

Ingle, J.C., Gorsline, D.S. (1973). Use of fluorescent tracers in the nearshore environment. In: *Tracer techniques in sediment transport*. Technical Reports Series No. 145, International Atomic Energy Agency, pp. 125-148.

Inman, D.L., Nordstrom, C.E. (1971). On the Tectonic and Morphologic Classification of Coasts. *The Journal of Geology*, 79(1): 1-21.

Inman, D.L. (1953). *Areal and seasonal variations in beach and nearshore sediments at La Jolla, California*. Beach Erosion Board technical memorandum nº 39, U.S. Army Corps of Engineers.

IPMA (2015). *Normais Climatológicas*. Instituto Português do Mar e da Atmosfera. Available at: https://www.ipma.pt/pt/oclima/normais.clima/, [Accessed 12 Sep. 2015].

Janardo, C. (2016). *Caracterização geológica da bacia hidrográfica da albufeira de São Domingos e avaliação da compatibilidade textural entre áreas-fonte e depósitos sedimentares*. Master Thesis, Universidade de Lisboa, 96 p. (unpublished)

Kamphuis, J.W. (1991). Alongshore Sediment Transport Rate. *Journal of Waterway, Port, Coastal, and Ocean Engineering*, 117(6): 624-640.

Kamphuis, J.W. (2000). *Introduction to coastal engineering and management*. Advanced Series on Ocean Engineering, Vol. 16. World Scientific, Singapore, 437 p.

King, D. (2005). *Influence of grain size on sediment transport rates with emphasis on the total longshore rate*. Technical Note ERDC/CHL CHETN-II-48. U.S. Army Research and Development Center US Army Corps of Engineers Vicksburg, MS, 24 p.

Klein, A.H.F., Ferreira, Ó. Dias, J.M.A., Tessler, M.G., Silveira, L.F., Benedet, L., Menezes, J.T., Abreu, J.G.N. (2010). Morphodynamics of structurally controlled headland-bay beaches in southeastern Brazil: A review. *Coastal Engineering*, 57(2): 98-111.

Klein, A.H.F., Filho, L.B., Schumacher, D.H. (2002). Short-Term Beach Rotation Processes in Distinct Headland Bay Beach Systems. *Journal of Coastal Research*, 18(3): 442-458.

Klein, A.H.F., Menezes, J.T. (2001). Beach morphodynamics and profile sequence for a headland bay coast. *Journal of Coastal Research*, 17(4): 812-835.

Komar, P.D. (1977). Selective longshore transport rates of different grain-size fractions within a beach. *Journal of Sedimentary Petrology*, 47(4): 1444-1453.

Komar, P.D. (1998). *Beach processes and sedimentation*. 2nd edition. Prentice-Hall, Upper Saddle River, New Jersey, 554 p.

Komar, P.D., Inman, D.L. (1970). Longshore sand transport on beaches. *Journal of Geophysical Research*, 75(30): 5914-5927.

Kraus, N.C. (2000). Reservoir Model of Ebb-Tidal Shoal Evolution and Sand Bypassing. *Journal of Waterway, Port, Coastal, and Ocean Engineering*, 126(6): 305-313.

Kraus, N.C., Dean, J.L. (1987). Longshore sediment transport rate distribution measured by trap. . In: Kraus, N.C. (ed.), *Coastal Sediments '87: Proceedings of a Specialty Conference on Advances in Understanding of Coastal Sediment Processes, New Orleans, Louisiana*. American Society of Civil Engineers, pp. 881–896.

Kraus, N.C., Farinato, R., Horikawa, K. (1981). Field experiments on longshore sand transport in the surf zone. *Coastal Engineering In Japan*, 24: 171–194.

Kraus, N.C., Gingerich, K.J., Rosati, J.D (1988). Toward an improved empirical formula for longshore. . In: Edge, B.L. (ed.), *Proceedings of 21st Conference on Coastal Engineering, Costa del Sol-Malaga, Spain*. American Society of Civil Engineers, pp. 1183-1196.

Kraus, N.C., Larson, M., Wise, R.A. (1998). *Depth of Closure in Beach-fill Design*. Coastal Engineering. Technical Note CETN II-40, 3/98. U.S. Army Engineer Waterways Experiment Station, Coastal and Hydraulics Laboratory, Vicksburg, MS, 13 p.

Krumbein, W.C. (1934). Size frequency distributions of sediments. *Journal of Sedimentary Petrology,* 4(2): 65–77.

Lapa, N., Rodrigues, A., Taborda, R., J. Duarte, J., Pinto, J.P. (2012). The sedimentary processes of the Portuguese inner shelf of Almagreiro Beach (Peniche). *Actas das 2as Jornadas de Engenharia Hidrográfica*. Instituto Hidrográfico, Lisbon, pp. 279-282.

Larson, M., Hoan, L., Hanson, H. (2010). Direct Formula to Compute Wave Height and Angle at Incipient Breaking. *Journal of Waterway, Port, Coastal, and Ocean Engineering*, 136(2): 119-122.

Larson, M., Kraus, N.C., Hanson, H. (2002). Simulation of regional longshore sediment transport and coastal evolution - the Cascade model. In: Smith, J.M. (ed.), *Proceedings of 28th Conference on Coastal Engineering, Wales, United Kingdom.* World Scientific, pp. 2612-2624.

Liberato, M.L.R. (2014). The 19 January 2013 windstorm over the North Atlantic: large-scale dynamics and impacts on Iberia. *Weather and Climate Extremes*, 5-6: 16-28.

Lira, C., Silva, A.N., Taborda, R., Andrade, C.F. (2016). Coastline evolution of Portuguese low-lying sandy coast in the last 50 years: an integrated approach. *Earth System Science Data*, 8: 265–278, doi:10.5194/essd-8-265-2016.

Lira, C., Taborda, R. (2014). Advances in Applied Remote Sensing to Coastal Environments Using Free Satellite Imagery. In: Finkl, C.W. and Makowski, C. (eds.), *Advances in Coastal and Marine Resources: Remote Sensing and Modeling*. Springer, pp. 77-102.

Lira, C., Taborda, R., Andrade, C. (2013). *Estimativas de descarga sólida fluvial potencial*. Technical report 1.1.2.b of the project "Criação e implementação de um sistema de monitorização no litoral abrangido pela área de jurisdição da Administração da Região Hidrográfica do Tejo". FFCUL/APA, I.P., Lisbon, 22 p.

LNEC (2010). *Planos plurianuais de dragagens portuárias. Volume 2: Zona Centro*. Technical report ##/10-NEC. Laboratório Nacional de Engenharia Civil, Lisbon, 56 p.

Lord, D.B., van Kerkvoort, A. (1981). A Coastal Process Investigation, Coffs Harbour, NSW. *Proceedings of the Fifth Australian Conference on Coastal and Ocean Engineering*. Institution of Engineers Australia, Barton, A.C.T., pp. 150-154.

Loureiro, C., Ferreira, Ó., Cooper, J.A.G. (2012). Extreme erosion on high-energy embayed beaches: Influence of megarips and storm grouping. *Geomorphology*, 139-140: 155-171.

Madsen, O.S. (1987). Use of tracers in sediment transport studies. In: Kraus, N.C. (ed.), *Coastal Sediments '87: Proceedings of a Specialty Conference on Advances in Understanding of Coastal Sediment Processes, New Orleans, Louisiana*. American Society of Civil Engineers, pp. 424–435.

Mange, M.A., Maurer, H.F.W. (1992). *Heavy minerals in Colour*. Chapman and Hall, London, 147 p.

Mariani, A., Carley, J., Miller, B. (2010). Infilling and Sand Bypassing of Coastal Structures and Headlands by Littoral Drift. *Proceedings of 19th NSW Coastal Conference*, 8 p.

Marques, F.M.S.F., Penacho, N., Queiroz, S., Sousa, H., Silveira, T.M., Gouveia, L., Matildes, R., Redweik, P., Garzón, V., Bastos, A.P., Diogo, Z.S., Taborda, R., Andrade, C.F., Freitas, M.C. (2013). *Caracterização das principais unidades geológicas e da organização geomorfológica da faixa costeira*. Technical report 1.2.1.a of the project "Criação e implementação de um sistema de monitorização no litoral abrangido pela área de jurisdição da Administração da Região Hidrográfica do Tejo". FFCUL/APA, I.P., Lisbon, 36 p.

McFeeters, S.K. (1996). The use of the Normalized Difference Water Index (NDWI) in the delineation of open water features. *International Journal of Remote Sensing*, 17(7): 1425-1432.

McLachlan, A., Illenberger, W.K., Burkinshaw, J.R., Burns, M.E.R. (1994). Management Implications of Tampering with Littoral Sand Sources. *Journal of Coastal Research*, SI 12: 51-59.

McManus, D.A. (1975). Modern versus Relict Sediment on the Continental Shelf. *Geological Society of America Bulletin*, 86(8): 1154-1160.

Miranda, P.M.A., Coelho, F., Tomé, A.R., Valente, M.A., Carvalho, A., Pires, C., Pires, H.O., Pires, V.C., Ramalho, C. (2002). 20th Century Portuguese Climate and Climate Scenarios. In: Santos, F.D., Forbes, K. and Moita, R. (eds.), *Climate Change in Portugal: Scenarios, Impacts and Adaptation Measures – SIAM Project*. Gradiva, Lisbon, pp. 27-83.

Mitasova, H., Brown, W.M., Hohmann, M., Warren, S. (2001). *Using soil erosion modeling for improved conservation planning: A GIS-based tutorial*. Available at: http://www4.ncsu.edu/~hmitaso/gmslab/reports/CerlErosionTutorial/denix/denixstart.html [Accessed 10 Oct. 2015].

Mitasova, H., Hofierka, J., Zlocha, M., Iverson, R.L. (1996). Modeling topographic potential for erosion and deposition using GIS. *International Journal of Geographical Information Systems*, 10(5): 629-641.

Moreno, L., Kraus, N. (1999). Equilibrium shape of headland-bay beaches for engineering design. In: Kraus, N.C. and McDougal, W.G. (eds.), *Coastal sediments '99: Proceedings of the 4th International Symposium on Coastal Engineering and Science of Coastal Sediment Processes, Hauppauge, Long Island, New York*. American Society of Civil Engineers, pp. 860-875.

Moura, A., Sanches, P., Monteiro, C., Silva, M., Mariano, A. (2014). Integração dos dados LiDAR batimétrico na Cartografia Náutica. *Actas das 3as Jornadas de Engenharia Hidrográfica*. Instituto Hidrográfico, Lisbon, pp. 29-32.

Neuendorf, K.K.E., Mehl, J.P., Jackson, J.A. (eds). (2005). *Glossary of Geology*. 5th edition. American Geological Institute, Alexandria, VA, 779 p.

Niedoroda, A.W., Swift, D.J.P. (1981). Maintenance of the shoreface by wave orbital currents and mean flow: Observations from the Long Island Coast. *Geophysical Research Letters*, 8(4): 337-340.

Niedoroda, A.W., Swift, D.J.P., Hopkins, T.S. (1985). The Shoreface. In: Davis Jr., R.A. (ed.), *Coastal Sedimentary Environments*. 2nd edition. Springer, New York, pp. 533-624.

Nolet, C., Poortinga, A., Roosjen, P., Bartholomeus, H., Ruessink, G. (2014). Measuring and Modeling the Effect of Surface Moisture on the Spectral Reflectance of Coastal Beach Sand. *PLoS ONE*, 9(11): e112151, doi:10.1371/journal.pone.0112151.

Oliveira, A., Cascalho, J., Duarte, J., Ribeiro, M., Taborda, R. (2015). Sand beach bulk mineralogy potential use to deduce transport processes (Nazaré). *Livro de resumos da 3ª Conferência sobre morfodinâmica estuarina e costeira*. Universidade do Algarve, Faro, pp. 51-52.

Oliveira, A., Cabral, M., Duarte, J., Pombo, J. (2016). Preparação de amostras em pó para análise quantitativa por DRX. *Actas das 4as Jornadas de Engenharia Hidrográfica*. Instituto Hidrográfico, Lisbon, pp. 324-326.

Oliveira, F.S.B.F., Barreiro, O.M (2010). Application of empirical models to bay-shaped beaches in Portugal. *Coastal Engineering*, 57(2): 124-131.

Oliveira, L. (2009). *Estudo Morfodinâmico e Sedimentar das Praias do Concelho de Sintra*. Master Thesis, Universidade de Lisboa, 148 p. (unpublished)

Patterson, D.C. (2011). *Tweed River Entrance Sand Bypassing. Reassessment of Long Term Average Annual Net Sand Transport Rate*. Technical report R.B17328.002.02. BMT-WBM Pty Ltd.

Pelnard-Considére, R. (1956). Essai de theorie de l'evolution des forms de rivages en plage de sable et de galets. *Quatrieme journees de l'hydraulique, les energies de la mer*, *Question III*. Société hydrotechnique de France, pp. 289-298.

Penacho, N., Marques, F M.S.F., Queiroz, S., Gouveia, L., Matildes, R., Redweik, P., Garzón, V. (2013). *Inventário de instabilidades nas arribas obtido por fotointerpretação.* Technical report 1.2.2.1.a of the project "Criação e implementação de um sistema de monitorização no litoral abrangido pela área de jurisdição da Administração da Região Hidrográfica do Tejo". FFCUL/APA, I.P., Lisbon, 48 p.

Peterson, C.D., Komar, P.D., Scheidegger, K.F. (1986). Distribution, geometry, and origin of heavy mineral placer deposits on Oregon beaches. *Journal of Sedimentary Petrology*, 56(1): 67–77.

Pimenta, M.T. (1998). *Directrizes para a aplicação da equação universal de perda dos solos em SIG: factor de cultura C e factor de erodibilidade do Solo K*. Instituo da Água and Direcção de Serviços de Recursos Hídricos, 12 p.

Pinto, C.A., Taborda, R., Andrade, C., Teixera, S.B. (2009). Seasonal and Mesoscale Variations at an Embayed Beach (Armação De Pera, Portugal). *Journal of Coastal Research*, SI 56: 118-122.

Pires, A.R., Ribeiro, M.A. (2010). *Caracterização morfodinâmica da praia do Guincho*. Training report in the framework of Master in Environmental Geology, Geological Hazards and Spatial Planning, University of Lisbon, 26 p. (unpublished)

Ramalho, M., Pais, J., Rey, J., Berthou, P.Y., Alves, C.A., Palácios, T., Leal, N., Kullberg, M.C. (1993). *Notícia explicativa da Carta Geológica de Portugal na escala de 1/50 000, Folha 34-A, Sintra.* Serviços Geológicos de Portugal, Lisbon, 77 p.

Ramalho, M., Rey, J., Zbyszewski, G., Alves, C.A.M., Palacios, T., Almeida, F.M., Costa, C., Kullberg, M.C. (2001). *Notícia explicativa da Carta Geológica de Portugal na escala de 1/50 000, Folha 34-C, Cascais*. Serviços Geológicos de Portugal, Lisbon, 104 p.

Ranasinghe, R., McLoughlin, R., Short, A., Symonds, G. (2004). The Southern Oscillation Index, wave climate, and beach rotation. *Marine Geology*, 204(3-4): 273-287.

Rebêlo, L.P., Brito, P.O., Monteiro, J.H. (2002). Monitoring the Cresmina dune evolution (Portugal) using differential GPS. *Journal of Coastal Research*, SI 36: 591-604.

Reis, A.H., Gama, C. (2010). Sand size versus beachface slope — An explanation based on the Constructal Law. *Geomorphology*, 114(3): 276-283.

Renard, K.G., Foster, G.R., Weesies, G.A., McCool, D.K., Yoder, D.C. (coords.) (1997). *Predicting Soil Erosion by Water. A Guide to Conservation Planning With the Revised Universal Soil Loss Equation (RUSLE).* Agriculture Handbook nº 703. U.S. Department of Agriculture, 384 p.

Ribeiro, M.A. (2013). *Wave propagation modeling*. Training report in the framework of the Advanced Training Course in Geology, Universidade de Lisboa, 25 p. (unpublished)

Rocha, F. (1993). *Argilas Aplicadas a Estudos Litoestratigráficos e Paleoambientais na Bacia Sedimentar de Aveiro*. PhD Thesis, Universidade de Aveiro, 399 p. (unpublished)

Roelvink, J.A., Reniers, A. (2012). *A guide to modeling coastal morphology*. World Scientific, Singapore, 274 p.

Rosati, J.D., Gingerich, K.J., Kraus, N.C., Smith, J.M., Beach, R.A. (1991). Longshore sand transport rate distributions measured in Lake Michigan. In: Kriebel, D.L. , Gingerich, K.J. and Kraus, N.C. (eds.), *Coastal sediments '91: Proceedings of a Specialty Conference on Quantitative Approaches to Coastal Sediment Processes, Seattle, Washington*. American Society of Civil Engineers, pp. 156–169.

Rosati, J.D., Walton, T.L., Bodge, K. (2002). Longshore Sediment Transport (Chapter III-2). In: *Coastal Engineering Manual 1110-2-1100.* U.S. Army Corps of Engineers, Washington, DC, 113 p.

Rusu, L., Pilar, P., Soares, C. (2008). Hindcast of the wave conditions along the west Iberian coast. Coastal Engineering, 55(11): 906–919.

Santos, F.D., Lopes, A.M., Moniz, G., Ramos, L., Taborda, R. (2014). *Gestão da Zona Costeira. O Desafio da Mudança*. Technical report of the Grupo de Trabalho do Litoral, 237 p.

Santos, M. (2006). *Caracterização e quantificação do transporte eólico na duna da Crismina*. Training report in the framework of the Postgraduate Specialization in Applied Geology, Universidade de Lisboa, 55 p. (unpublished)

Scholar, D.C., Griggs G.B. (1997). Pocket beaches of California. Sediment transport along a rocky coastline. In: Ewing, L. and Sherman, D. (eds.), *Proceedings of the California's Coastal Natural Hazards*. University of Southern California Sea Grant Program, Santa Barbara, pp. 65–75.

Schoonees, J.S., Theron, A.K. (1993). Review of the field-data base for longshore sediment transport. *Coastal Engineering*, 19(1-2): 1-25.

Sexton, W.J., Hayes, M.O. (1982). Natural bar-bypassing of sand at a tidal inlet. In: Edge, B.L. (ed.), *Proceedings of 18th Conference on Coastal Engineering, Cape Town, South Africa.* American Society of Civil Engineers, pp. 1479-1495.

Shankar, R., Thompson, R., Prakash, T.N. (1996). Estimation of heavy and opaque mineral contents of beach and offshore placers using rock magnetic techniques. *Geo-Marine Letters*, 16(4): 313-318.

Short, A.D. (1985). Rip-current type, spacing and persistence, Narrabeen Beach, Australia. *Marine Geology*, 65(1-2): 47-71.

Short, A.D., Bracs, M.A., Turner, I.L. (2014). Beach oscillation and rotation: local and regional response at three beaches in southeast Australia. *Journal of Coastal Research*, SI 70: 712-717.

Short, A.D., Masselink, G. (1999). Embayed and Struturally Controlled Beaches. In: Short, A.D. (ed.), *Handbook of beach and shoreface morphodynamics*. John Wiley & Sons, Chichester, pp. 230-250.

Short, A.D., Trembanis, A.C. (2004). Decadal Scale Patterns in Beach Oscillation and Rotation Narrabeen Beach, Australia—Time Series, PCA and Wavelet Analysis. *Journal of Coastal Research*, 20(2): 523-532.

Silva, A. (2005). *Traçadores sedimentares aplicados ao estudo da deriva litoral*. Training report in the framework of the Graduation in Applied and Environmental Geology, Universidade de Lisboa, 100 p. (unpublished)

Silva, A.N., Taborda, R., Bertin, X., Dodet, G. (2012a). Seasonal to Decadal Variability of Longshore Sand Transport at the Northwest Coast of Portugal. *Journal of Waterway, Port, Coastal, and Ocean Engineering*, 138(6): 464-472.

Silva, A., Taborda, R., Rodrigues, A., Duarte, J., Cascalho, J. (2007). Longshore drift estimation using fluorescent tracers: New insights from an experiment at Comporta Beach, Portugal. *Marine Geology*, 240(1-4): 137-150.

Silva, G.V., Toldo, E.E, Klein, A.H.F., Short, A.D., Woodroffe, C.D. (2016). Headland sand bypassing - Quantification of net sediment transport in embayed beaches, Santa Catarina Island North Shore, Southern Brazil. *Marine Geology*, 379: 13-27.

Silva, M., Patrício, P., Mariano, A., Morais, M., Valério, M. (2012b). Obtenção de Dados LiDAR para as Zonas Costeiras de Portugal Continental. *Actas das 2as Jornadas de Engenharia Hidrográfica*. Instituto Hidrográfico, Lisbon, pp. 19-22.

Silva, F.S., Pinto, J.P. and Almeida, S. (2009). Operational Wave Forecasting System for the Portuguese Coast. Journal of Coastal Research, SI(56), pp.1055–1059.

Silveira, L.F., Klein, A.H.F., Tessler, M.G. (2010). Headland-bay beach planform stability of Santa Catarina State and of the Northern Coast of São Paulo State. *Brazilian Journal of Oceanography*, 58(2): 101-122.

Silveira, T.M., Diogo, Z.S., Taborda, R., Andrade, C.F., Sousa, H., Carapuço, A.M., Silva, A.N. (2013). *Caracterização da variabilidade morfodinâmica sazonal das praias-piloto representativas do litoral em estudo*. Technical report 1.2.3.e of the project "Criação e implementação de um sistema de monitorização no litoral abrangido pela área de jurisdição da Administração da Região Hidrográfica do Tejo". FFCUL/APA, I.P., Lisbon, 146 p.

Silvester, R., Ho, S. (1972). Use of Crenulate Shaped Bays to Stabilize Coasts. In: O'Brien, M.P. (ed.), *Proceedings of 13th Conference on Coastal Engineering, Vancouver, Canada.* American Society of Civil Engineers, pp. 1347–1365.

Smith, A.M., Mather, A.A., Bundy, S.C., Cooper, J.A.G., Guastella, L.A., Ramsay, P.J., Theron, A. (2010). Contrasting styles of swell-driven coastal erosion: examples from KwaZulu-Natal, South Africa. *Geological Magazine*, 147(6): 940-953.

Smith, A.W. (2001). Headland Bypassing. *Coasts & Ports 2001: Proceedings of the 15th Australasian Coastal and Ocean Engineering Conference and the 8th Australasian Port and Harbour Conference*. Institution of Engineers Australia, Barton, A.C.T., pp. 214-216

Smith, J.B. (1995). *Literature review on the geologic aspects of inner continental shelf cross-shore sediment transport*. U.S. Army Engineer Waterways Experiment Station, Vicksburg, MS, 161 p.

Socolofsky, S.A., Jirka, G.H. (2005). *CVEN 489-501: Special topics in mixing and transport processes in the environment*. 5th Edition. Coastal and Ocean Engineering Division, Texas A&M University, 172 p.

Sousa, A.A. (1995). *Subsídios para um melhor conhecimento da erosão hídrica em bacias hidrográficas e doa assoreamento da Albufeiras – Arade e Funcho – dois casos Portugueses*. Master Thesis, Universidade de Lisboa, 91 p. (unpublished)

Steetzel, H.J., de Vroeg, H., van Rijn, L.C., Stam, J.M. (2000). Long-term modelling of the Holland coast using a multi-layer model. In: Edge, B.L. (ed.), *Proceedings of 27th Conference on Coastal Engineering, Sydney, Australia*. American Society of Civil Engineers, pp. 2942–2955.

Storlazzi, C.D., Field, M.E. (2000). Sediment distribution and transport along a rocky, embayed coast: Monterey Peninsula and Carmel Bay, California. *Marine Geology*, 170(3-4): 289-316.

Taborda, R. (1999). *Modelação da Dinâmica Sedimentar na Plataforma Continental Portuguesa*. PhD Thesis, Universidade de Lisboa, 367 p. (unpublished)

Taborda, R., Andrade, C., Marques, F., Freitas, C., Rodrigues, R., Antunes, C., Pólvora, C. (2010). *Plano estratégico do concelho de Cascais face às alterações climáticas – Sector Zonas Costeiras*. Faculdade de Ciências da Universidade de Lisboa, 48 p.

Taborda, R., Ciavola, P., Ferreira, Ó., Dias J.M.A. (1999). Measurements of suspended sediment transport on a reflective mesotidal beach in southern Portugal. *Boletín do Instituto Español de Oceanografía*, 15(1-4): 29-241.

Taborda, R., Ferreira, Ó., Dias, J.M.A., Moita, P. (1994). Field observations of longshore sand transport in a high energy environment. In: Carvalho, S. and Gomes, V. (eds.), *Littoral 94: Proceedings of Second International Symposium European Coastal Zone Association for Science and Technology*. EUROCOAST, Lisbon, pp. 479–487.

Taborda, R., Ribeiro, M.A. (2015). A simple model to estimate the impact of sea-level rise on platform beaches. *Geomorphology*, 234: 204-210.

Taborda, R., Ribeiro, M. (2016). Shoreline evolution modelling on platform beaches. *Actas das 4as Jornadas de Engenharia Hidrográfica*. Instituto Hidrográfico, Lisbon, pp. 265-268.

Taborda, R., Silva, A.N. (2012). COSMOS: A lightweight coastal video monitoring system. *Computers & Geosciences*, 49: 248-255.

Thieler, E.R., Himmelstoss, E.A., Zichichi, J.L., Ergul, A. (2009). *Digital Shoreline Analysis System (DSAS) version 4.0 — An ArcGIS extension for calculating shoreline change*. U.S. Geological Survey Open-File Report 2008-1278.

Thomas, R., Ashley, E. (2013). *Shoreline change modeling using one-line models: General model comparison and literature review*. Coastal and Hydraulics Engineering Technical Note ERDC/CHL CHETN-II-55. U.S. Army Engineer Research and Development Center, Vicksburg, MS, 9 p.

Thomas, T., Phillips, M.R., Williams, A.T. (2010). Mesoscale evolution of a headland bay: Beach rotation processes. *Geomorphology*, 123(1-2): 129-141.

Tomás, P.P., Coutinho, M.A. (1993). *Erosão hídrica dos solos em pequenas bacias hidrográficas: Aplicação da Equação Universal de Degradação dos Solos*. CEHIDRO nº 7/93, Centro de Estudos e Hidrossistemas, Instituto Superior Técnico, 25 p.

Tonk, A., Masselink, G. (2005). Evaluation of Longshore Transport Equations with OBS Sensors, Streamer Traps, and Fluorescent Tracer. *Journal of Coastal Research*, 21(5): 915-931.

Trindade, J., Ramos-Pereira, A. (2009). Sediment textural distribution on beach profiles in a rocky coast (Estremadura – Portugal). *Journal of Coastal Research*, SI 56: 138-142.

Trouw, K.J.M., Zimmermann, N., Mathys, M., Delgado, R., Roelvink, D. (2012). Numerical modelling of hydrodynamics and sediment transport in the surf zone: a sensitivity study with different types of numerical models. In: Lynett, P. and Smith, J.M. (eds.), *Proceedings of 33rd Conference on Coastal Engineering, Santander, Spain*. Coastal Engineering Research Council, 12 p.

Turki, I., Medina, R., Gonzalez, M., Coco, G. (2013). Natural variability of shoreline position: Observations at three pocket beaches. *Marine Geology*, 338: 76-89.

Van Rijn, L.C. (2010). *Coastal erosion control based on the concept of sediment cells*. Report of the EU project Conscience - Concepts and Science for Coastal Erosion, 76 pp.

Vanney, J.R., Mougenot, D. (1981). La plate-forme continentale du Portugal et les provinces adjacents: analyse géomorphologique. *Memórias dos Serviços Geológicos de Portugal*, N.S. 28, 86 p.

Vila-Concejo, A., Ferreira, Ó., Ciavola, P., Matias, A., Dias, J.M.A. (2004). Tracer studies on the updrift margin of a complex inlet system. *Marine Geology*, 208(1): 43-72.

Vincent, C.E., Green, M.O. (1990). Field measurements of the suspended sand concentration profiles and fluxes and of the resuspension coefficient γ0 over a rippled bed. *Journal of Geophysical Research*, 95(C7): 11591-11601.

Vincent, C.E, Hanes, D.M, Bowen, A.J (1991). Acoustic measurements of suspended sand on the shoreface and the control of concentration by bed roughness. *Marine Geology*, 96(1-2): 1-18.

Walton, T.L. (2005). A review of inlet bypassing solutions with nomographs. *Coastal Engineering*, 52(12): 1127-1132.

Wang, P., Kraus, N.C., Davis, R.A (1998). Total rate of longshore sediment transport in the surf zone: field measurements and empirical predictions. *Journal of Coastal Research*, 14(1): 269-283.

Wischmeier, W.H., Smith, D.D. (1978). *Predicting rainfall erosion losses: guide to conservation planning*. Agriculture Handbook nº 537, U.S. Department of Agriculture, 58 p.

Wright, L.D. (1987). Shelf-surfzone coupling: diabathic shoreface transport. In: Kraus, N.C. (ed.), *Coastal Sediments '87: Proceedings of a Specialty Conference on Advances in Understanding of Coastal Sediment Processes, New Orleans, Louisiana*. American Society of Civil Engineers, pp.25-40.

Wright, L.D. (1993). Micromorphodynamics of the inner continental shelf: A Middle Atlantic Bight case study. *Journal of Coastal Research*, SI 15: 93-124.

Yasso, W. (1965). Plan Geometry of Headland-Bay Beaches. *The Journal of Geology*, 73(5): 702-714.

Zbyszewski, G., Almeida, F.M., Assunção, C.T. (1955). *Notícia explicativa da Carta Geológica de Portugal na escala de 1/50 000, Folha 30-C, Torres Vedras*. Serviços Geológicos de Portugal, Lisbon, 33 p.

Zbyszewski, G., Assunção, C.T. (1965). *Notícia explicativa da Carta Geológica de Portugal na escala de 1/50 000, Folha 30-D, Alenquer*. Serviços Geológicos de Portugal, Lisbon, 104 p.

Zbyszewski, G., Ferreira, O.V., Manuppella, G., Assunção, C.T. (1966). *Notícia explicativa da Carta Geológica de Portugal na escala de 1/50 000, Folha 30-B, Bombarral*. Serviços Geológicos de Portugal, Lisbon, 90 p.

Appendices

Appendix A – Beach photo-monitoring

The morphological changes of the studied beaches were monitored through digital photographs, which were compiled online using the Flickr application and can be seen in the web addresses presented in the table below. The images were acquired during the field work carried out in scope of this work or kindly provided by same colleagues and friends.

Beach	Web address
Sta. Cruz	https://www.flickr.com/search/?user_id=114969613%40N05&sort=date-taken-desc&view_all=1&text=Sta.Cruz_HBB
São Lourenço	https://www.flickr.com/search/?user_id=114969613%40N05&sort=date-taken-desc&view_all=1&text=S.Louren%C3%A7o_HBB
Coxos	https://www.flickr.com/search/?user_id=114969613%40N05&sort=date-taken-desc&view_all=1&text=Coxos_HBB
Ribeira d'Ilhas	https://www.flickr.com/search/?user_id=114969613%40N05&sort=date-taken-desc&view_all=1&text=Ribeirad%27Ilhas_HBB
Baleia	https://www.flickr.com/search/?user_id=114969613%40N05&sort=date-taken-desc&view_all=1&text=Baleia_HBB
Foz do Lizandro	https://www.flickr.com/search/?user_id=114969613%40N05&sort=date-taken-desc&view_all=1&text=Lizandro_HBB
São Julião	https://www.flickr.com/search/?user_id=114969613%40N05&sort=date-taken-desc&view_all=1&text=S.Juli%C3%A3o_HBB
Magoito	https://www.flickr.com/search/?user_id=114969613%40N05&sort=date-taken-desc&view_all=1&text=Magoito_HBB
Maçãs	https://www.flickr.com/search/?user_id=114969613%40N05&sort=date-taken-desc&view_all=1&text=Ma%C3%A7%C3%A3s_HBB
Grande	https://www.flickr.com/search/?user_id=114969613%40N05&sort=date-taken-desc&view_all=1&text=Grande1_HBB
	https://www.flickr.com/search/?user_id=114969613%40N05&sort=date-taken-desc&view_all=1&text=Grande2_HBB
Adraga	https://www.flickr.com/search/?user_id=114969613%40N05&sort=date-taken-desc&view_all=1&text=Adraga_HBB

Appendix B – *SedPhoto2* toolbox

The *SedPhoto2* is a MATLAB class based on the *SedPhoto* class originally created by Rui Taborda, João Duarte and João Cascalho (in 2014) for detection and counting of fluorescent tracer particles on digital images of sediment acquired under ultraviolet (UV) light. *SedPhoto2* is an updated version to detect and count tracer particles using images acquired under both UV and white (WT) light, avoiding problems related with the presence of shells particles that reflected in the same spectral range of tracer particles. Furthermore, a function to extract the threshold values of the tracer particles on L*a*b colour space was also add.

This appendix includes the source code of the toolbox, examples of scripts using the toolbox and an example the tracer particles detection on images.

Source code of *SedPhoto2*

```
classdef SedPhoto2 <handle
    % SedPhoto2 is MATLAB class to process sediment images.
        % Detects and count fluorescent tracer particles in sediment
        % images acquired under ultraviolet (UV) and white (WT) light,
        % through the parallelepipedic cutoff method.

    properties
        % Name of the input images
        nameUVPhoto
        nameWTPhoto

        % UV and WL images represented by RGB and L*a*b colour models
        RGBUVPhoto
        RGBWTPhoto
        LabUVPhoto
        LabWTPhoto

        % Thresholds for the parallelepipedic cutoff of
        % tracer particles (defined by the user)
        aTWT = 131
        bTWT = 153
        LTUV = 20
        aTUV = 132
        bTUV = 123

        % Segmented image where 1 represents pixels above
        % threshold level
        BWImage

        % Flat disk-shaped structuring elements with a radius of 2,
        % used to comprise all pixels whose centers are no greater
        % than 2 away from the origin
        erosionDilationStructuringElement = strel('disk', 2);

        % Tracer particles
        particles
```

```
    end

    methods
        %% Read UV and WL images
        function obj = SedPhoto2(filenameUV, filenameWT)
            if nargin == 1
                obj.nameUVPhoto = filenameUV;
                obj.RGBUVPhoto = imread(filenameUV);
            else
                obj.nameUVPhoto = filenameUV;
                obj.RGBUVPhoto = imread(filenameUV);

                obj.nameWTPhoto = filenameWT;
                obj.RGBWTPhoto = imread(filenameWT);
            end
        end

        %% Displays RGB image in Handle Graphics figure
        function imageShow(obj, photoType)
            if nargin == 1
                photoType = 'UV';
            end
            switch photoType
                case 'UV'
                    imshow(obj.RGBUVPhoto)
                case 'WL'
                    imshow(obj.RGBWTPhoto)
            end
        end

        %% Converts the RGB colour index to the L*a*b colour space
        function obj = RGB2LAB(obj, photoType)
            cform = makecform('srgb2lab');
            if nargin == 1
                photoType = 'UV';
            end
            switch photoType
                case 'UV'
                    obj.LabUVPhoto = applycform(obj.RGBUVPhoto,cform);
                case 'WT'
                    obj.LabWTPhoto = applycform(obj.RGBWTPhoto,cform);
            end
        end

        %% Filters the segmented (BW) image
        function BWFilter(obj)
            obj.BWErosion;
            obj.BWDilation;
            obj.BWDilation;
            obj.BWErosion;
        end

        %% Erodes the grayscale returning the eroded image based on
        % the structuring element object returned by
        % the STREL function
        function BWErosion(obj)
            if isempty(obj.BWImage)
                obj.imageSegmentation;
            end
            obj.BWImage = imerode...
```

```
            (obj.BWImage,obj.erosionDilationStructuringElement);
    end

    %% Delates the grayscale returning the eroded image based on
    % the structuring element object returned by
    % the STREL function
    function BWDilation(obj)
        if isempty(obj.BWImage)
            obj.imageSegmentation;
        end
        obj.BWImage = imdilate...
            (obj.BWImage,obj.erosionDilationStructuringElement);
    end

    %% Segments the UV image
    % using the parallelepipedic cutoff method
    function imageSegmentation(obj)
        if isempty(obj.LabUVPhoto)
            obj.RGB2LAB('UV');
        end
        obj.BWImage = obj.L('UV') > obj.LTUV & obj.a('UV') > ...
            obj.aTUV & obj.b('UV') > obj.bTUV;
        obj.BWFilter;
    end

    %% Displays BW image in Handle Graphics figure
    function BWShow(obj)
        if isempty(obj.BWImage)
            obj.imageSegmentation;
        end
        imshow(obj.BWImage)
    end

    %% Computes tracer dilution in the image
    function tc = tracerConcentration(obj, method)
        if isempty(obj.BWImage)
            obj.imageSegmentation(method);
        end
        tc = sum(obj.particles.area(:))/length(obj.BWImage(:));
    end

    %% Computes the number and area of tracer particles
    function countParticles(obj)
        if isempty(obj.BWImage)
            obj.imageSegmentation;
        end
        [B,L] = bwboundaries(obj.BWImage,'noholes');
        if isempty(obj.RGBWTPhoto)
            nParticles = length(B);
            obj.particles.area = zeros(nParticles, 1);
            obj.particles.nParticles = nParticles;
            obj.particles.boundaries = B;
            for k = 1:nParticles;
                boundary = B{k};
                obj.particles.area(k) = ...
                    polyarea(boundary(:,2),boundary(:,1));
            end
        else
            obj.RGB2LAB('WT');
            BWImageWT = obj.a('WT') > obj.aTWT & obj.b('WT')...
```

```
                    > obj.bTWT;
                marker = obj.BWImage .* BWImageWT;
                area = zeros(length(B), 1);
                for k = 1:length(B)
                    boundary = B{k};
                    mask = poly2mask(boundary(:,2),...
                        boundary(:,1),length(obj.BWImage(:,1)),...
                        length(obj.BWImage(1,:)));

                    if length(find(marker(mask)==1))/...
                            length(obj.BWImage(mask)) > 0.70
                        area(k) = polyarea(boundary(:,2),...
                            boundary(:,1));
                    else
                        area(k) = NaN;
                    end
                end
                obj.particles.area = area(~isnan(area));
                obj.particles.nParticles = length(obj.particles.area);
                obj.particles.boundaries = B(~isnan(area));
            end
        end

        %% Plots the tracer particles
        function plotParticles(obj)
            if isempty(obj.particles)
                obj.countParticles;
            end
            for k = 1:obj.particles.nParticles;
                boundary = obj.particles.boundaries{k};
                plot(boundary(:,2), boundary(:,1),'b','LineWidth', 1);
            end
        end

        %% Function to extract the spectral signature of the tracer
        % particles in the L*a*b colour space,
        % based on which thresholds can be defined
        function [LTrainingSamples, aTrainingSamples,...
                bTrainingSamples] = tracerLABsignature(obj, imageType)
            if nargin == 1
                msgbox('Specify the image type (UV or WT)',
'Error','error');
            end
            obj.RGB2LAB(imageType);
            obj.plotImageColorModel(imageType,'LAB')
            msgbox('(1) Make a zoom in of the intended area; (2) Press
enter to identify points for spectral signature; (3) Press enter to
see the result');
            pause
            t = ginput;
            L = obj.L(imageType);
            a = obj.a(imageType);
            b = obj.b(imageType);
            LTrainingSamples = L(round(sub2ind(size(L),t(:,2),...
                t(:,1))));
            aTrainingSamples = a(round(sub2ind(size(a),t(:,2),...
                t(:,1))));
            bTrainingSamples = b(round(sub2ind(size(b),t(:,2),...
                t(:,1))));
            figure
            plot3(aTrainingSamples,bTrainingSamples,...
```

```
                LTrainingSamples,'*')
            grid
            title('Spectral signature')
            xlabel('a')
            ylabel('b')
            zlabel('L')
        end

        %% Plots UV images in RGB or L*a*b colour space
        function plotImageColorModel(obj, imageType, colorSpace)
            if nargin == 1
                msgbox('Specify the image type (UV ot WT) and the
color model (RGB or LAB)', 'Error','error');
            end
            switch imageType
                case 'UV'
                    if  colorSpace == 'RGB' %#ok<STCMP>
                        imshow(obj.RGBUVPhoto)
                    else
                        if isempty(obj.LabUVPhoto)
                            obj.RGB2LAB('UV');
                        end
                        imshow(obj.LabUVPhoto)
                    end
                case 'WL'
                    if colorSpace == 'RGB' %#ok<STCMP>
                        imshow(obj.RGBWTPhoto)
                    else
                        if isempty(obj.LabWTPhoto)
                            obj.RGB2LAB('WT');
                        end
                        imshow(obj.LabWTPhoto)
                    end
            end
        end


        %% Lightness
        function L = L(obj, imageType)
            switch imageType
                case 'UV'
                    L = double(obj.LabUVPhoto(:,:,1));
                case 'WT'
                    L = double(obj.LabWTPhoto(:,:,1));
            end
        end

        %% a colour dimension
        function a = a(obj, imageType)
            switch imageType
                case 'UV'
                    a = double(obj.LabUVPhoto(:,:,2));
                case 'WT'
                    a = double(obj.LabWTPhoto(:,:,2));
            end
        end

        %% b colour dimension
        function b = b(obj, imageType)
            switch imageType
```

```
                case 'UV'
                    b = double(obj.LabUVPhoto(:,:,3));
                case 'WT'
                    b = double(obj.LabWTPhoto(:,:,3));
            end
        end

    end

end
```

Examples of scripts using *SedPhoto2*

```
%% Script 1
% Create a spectral signature of tracer particles to define thresholds
% for UV or WT images
f = SedPhoto2('ImageUV.jpg','ImageWT.jpg');
[L,a,b] = f.tracerLABsignature('UV');

%% Script 2
% Detection and counting of tracer particles
% using UV and WL images
f = SedPhoto2('ImageUV.jpg','ImageWT.jpg');
f.countParticles;

figure, f.imageShow('UV')
title('Tracer particles under UV ligth')
hold on
f.plotParticles

figure, f.imageShow('WL')
title('Tracer particles under WT ligth')
hold on
f.plotParticles
```

Tracer particles detected and projected on UV and WL images

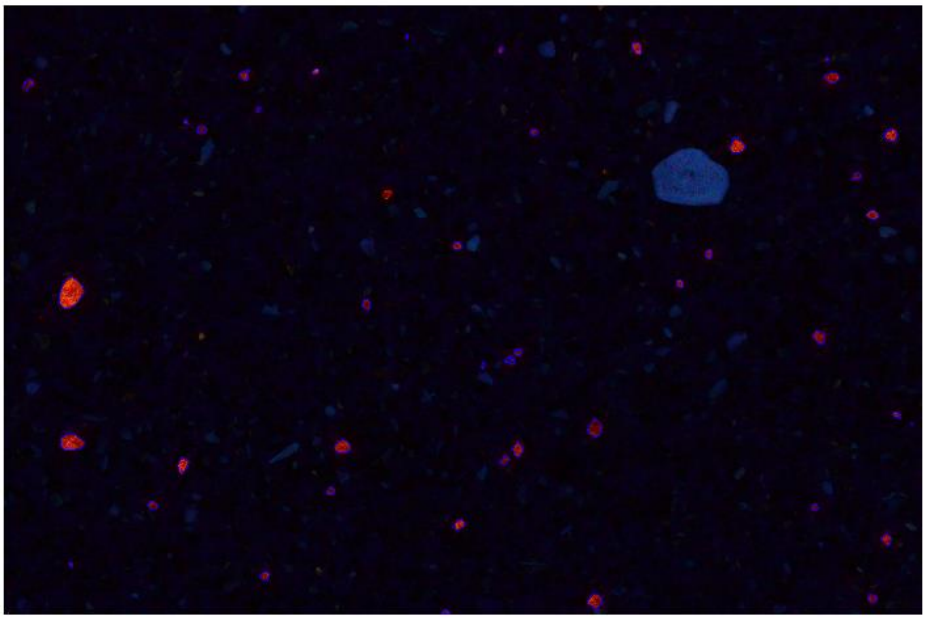

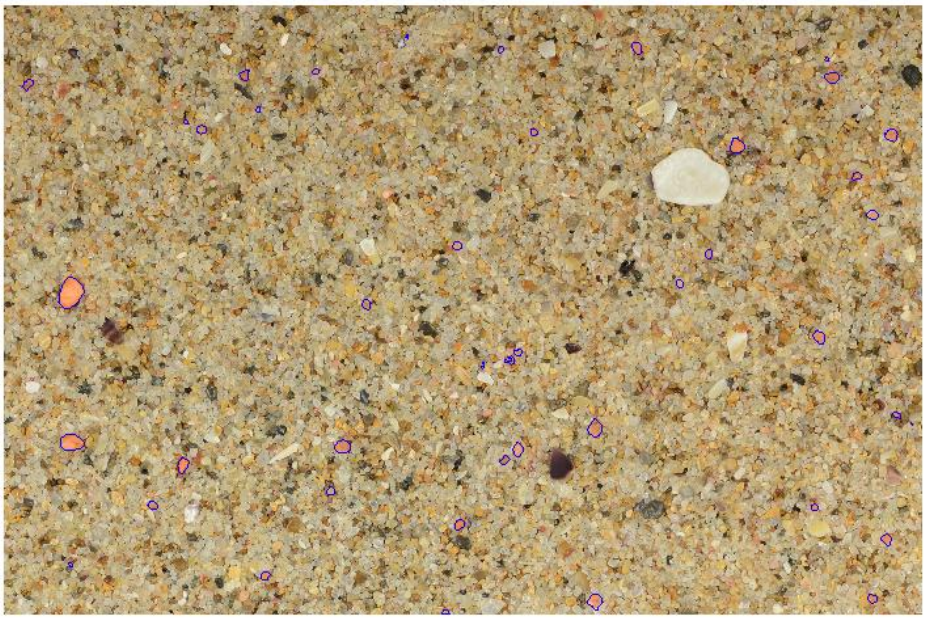

Appendix C – Tracer dilution modelling

This appendix includes the results of the advection-diffusion model that were not presented in chapter 5. The equilibrium concentration ($\bar{c}_{eq}$) assumed, advection velocity (v_a m.s^{-1}) and diffusion coefficient (D m^2.s^{-1}) used to fit the model are also presented.

Overall: $\bar{c}_{eq} = 2.30 \times 10^{-3}$ $v_a = 1.72 \times 10^{-2}$ $D = 4.18 \times 10^{-2}$

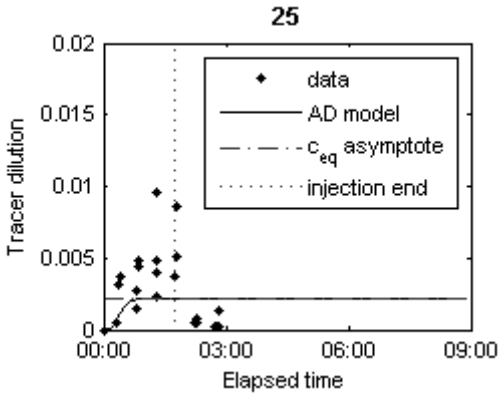

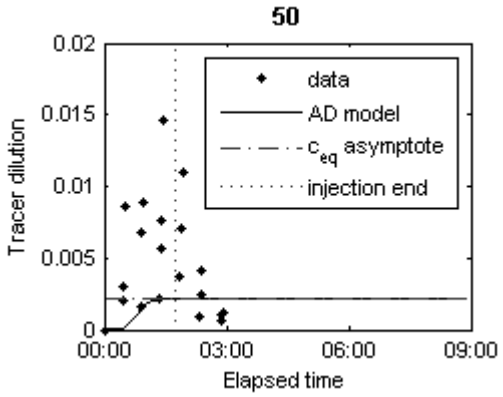

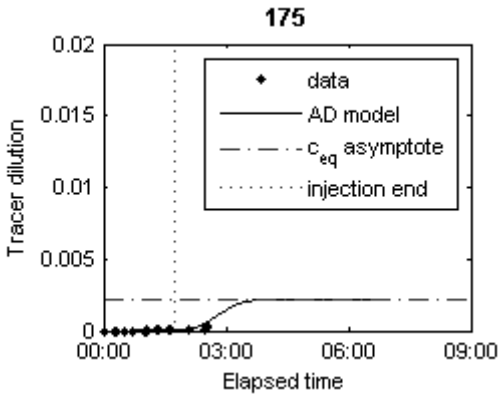

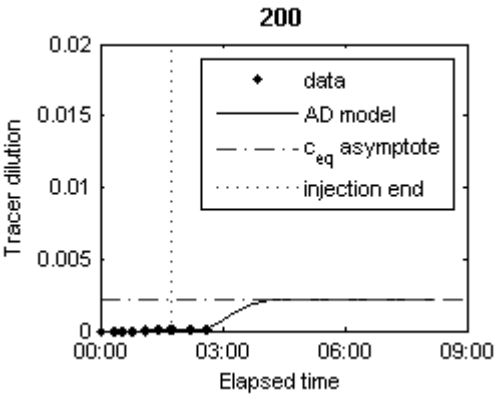

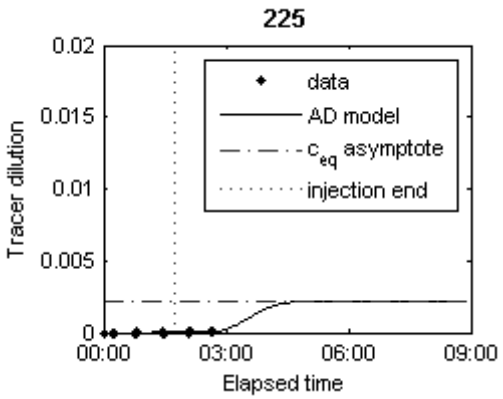

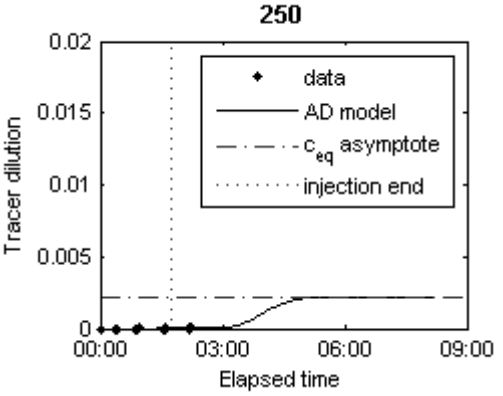

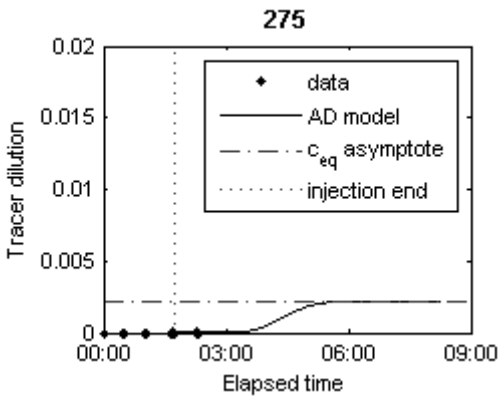
275
0.02
0.015
0.01
0.005
0
Tracer dilution
data
AD model
c_{eq} asymptote
injection end
00:00
03:00
06:00
09:00
Elapsed time

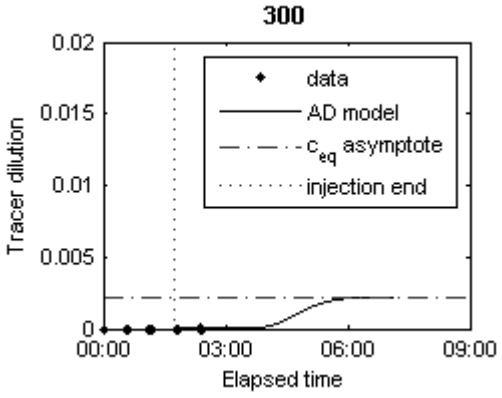
300
0.02
0.015
0.01
0.005
0
Tracer dilution
data
AD model
c_{eq} asymptote
injection end
00:00
03:00
06:00
09:00
Elapsed time

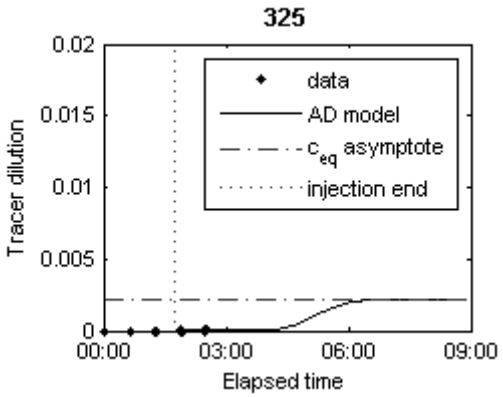
325
0.02
0.015
0.01
0.005
0
Tracer dilution
data
AD model
c_{eq} asymptote
injection end
00:00
03:00
06:00
09:00
Elapsed time

<u>Very coarse sand</u>: $\bar{c}_{eq} = 1.0 \times 10^{-3}$ $v_a = 1.61 \times 10^{-2}$ $D = 1.33 \times 10^{-2}$

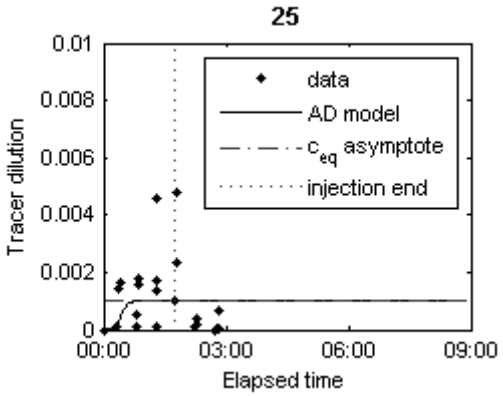

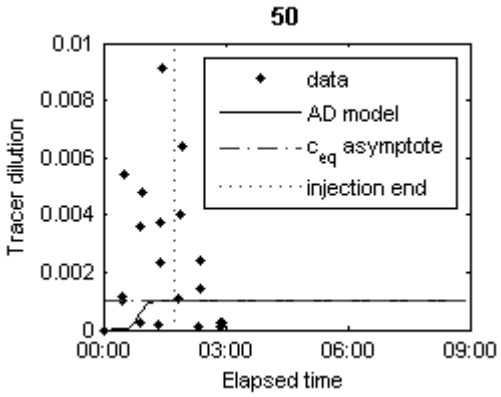

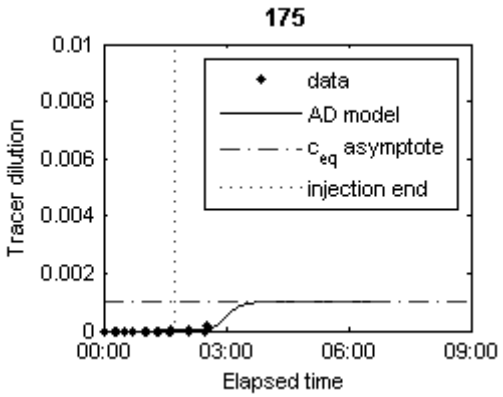

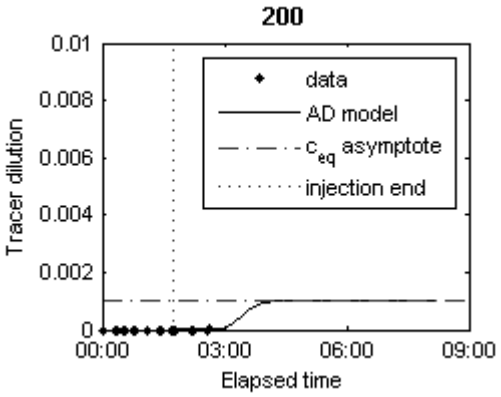

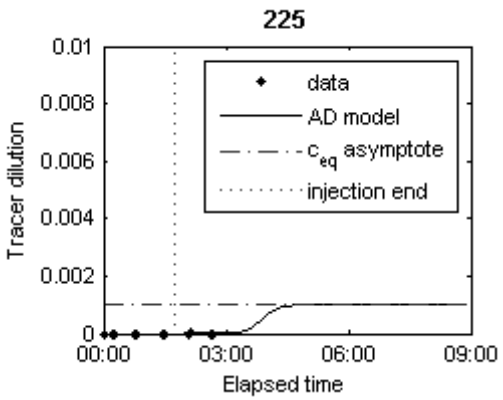

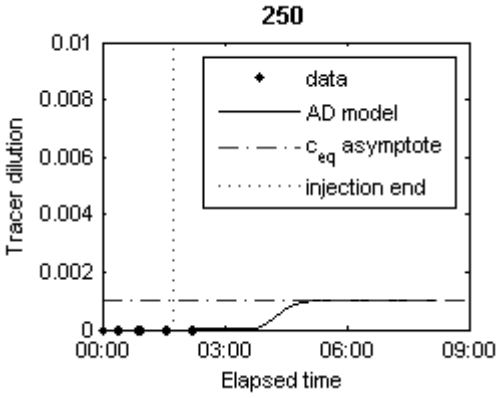

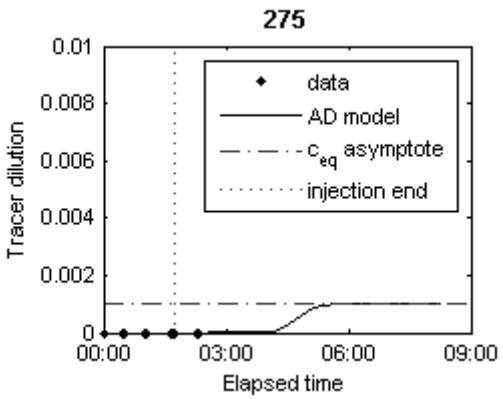
275
0.01
0.008
0.006
0.004
0.002
0
Tracer dilution
00:00
03:00
06:00
09:00
Elapsed time
data
AD model
c_{eq} asymptote
injection end

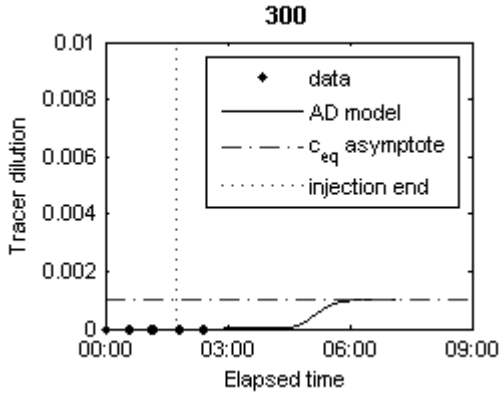
300
0.01
0.008
0.006
0.004
0.002
0
Tracer dilution
00:00
03:00
06:00
09:00
Elapsed time
data
AD model
c_{eq} asymptote
injection end

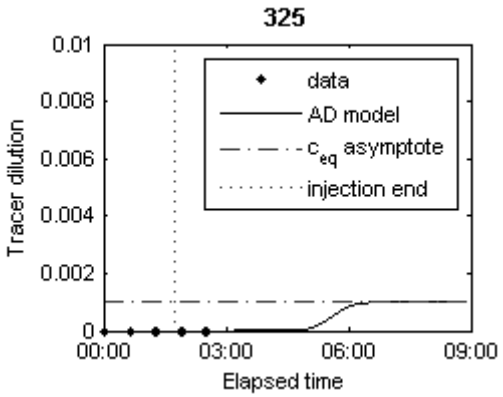
325
0.01
0.008
0.006
0.004
0.002
0
Tracer dilution
00:00
03:00
06:00
09:00
Elapsed time
data
AD model
c_{eq} asymptote
injection end

<u>Coarse sand</u>: $\bar{c}_{eq} = 1.0 \times 10^{-3}$ $v_a = 1.76 \times 10^{-2}$ $D = 4.63 \times 10^{-2}$

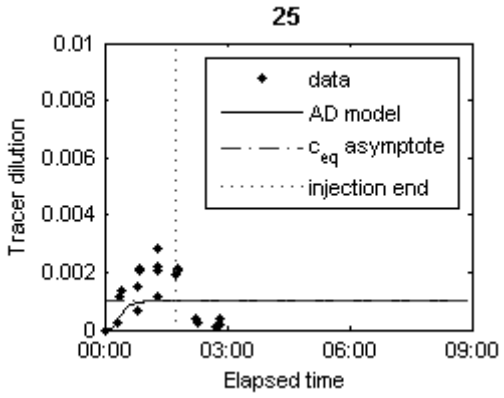

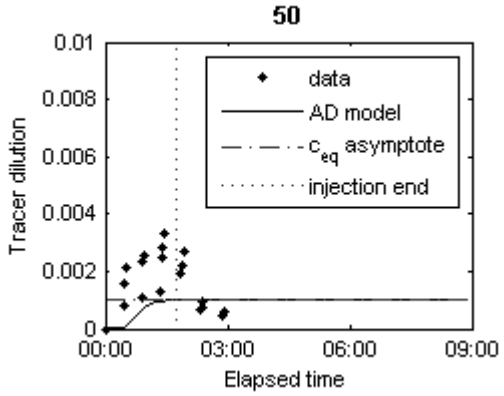

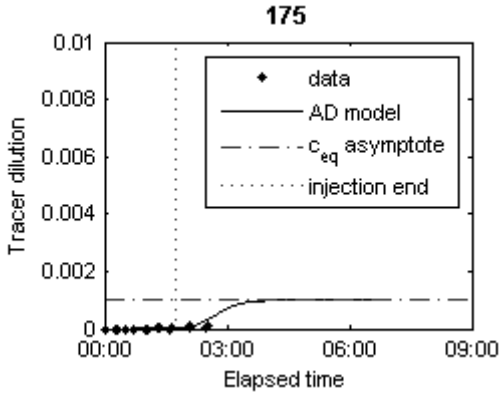

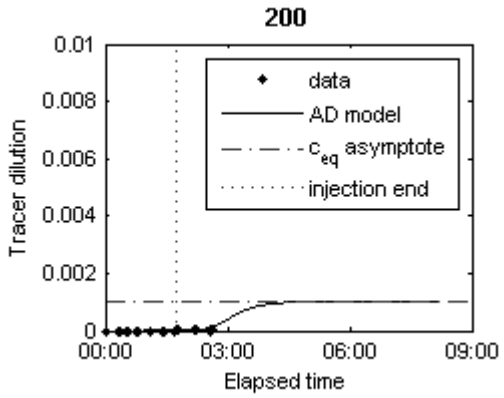

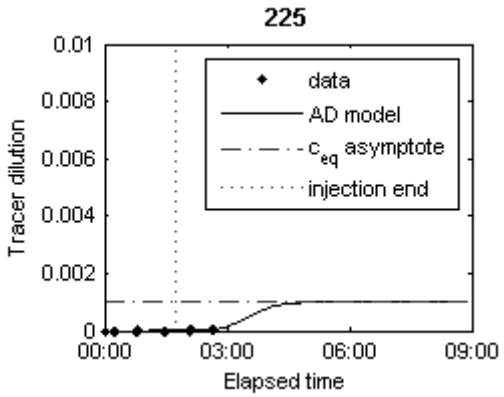

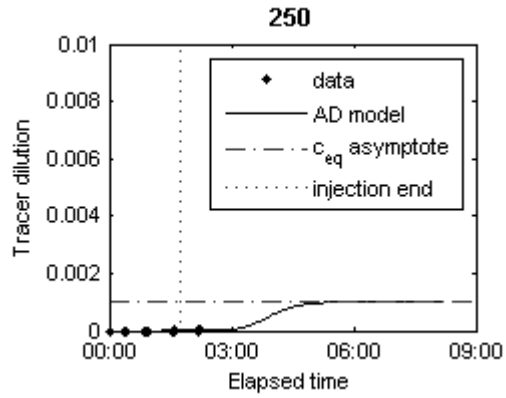

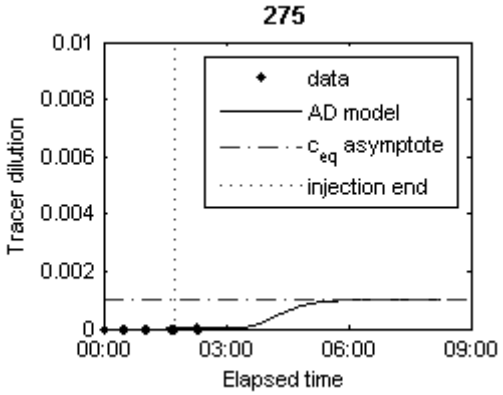
275
0.01
0.008
0.006
0.004
0.002
0
Tracer dilution
data
AD model
c_{eq} asymptote
injection end
00:00
03:00
06:00
09:00
Elapsed time

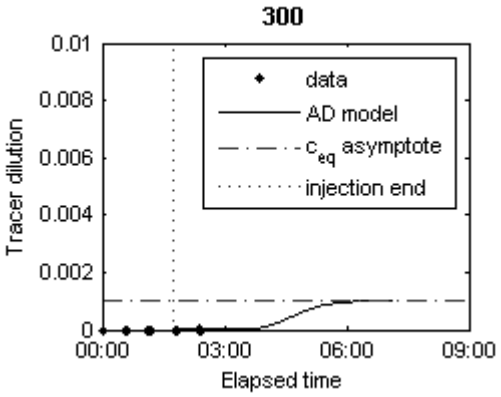
300
0.01
0.008
0.006
0.004
0.002
0
Tracer dilution
data
AD model
c_{eq} asymptote
injection end
00:00
03:00
06:00
09:00
Elapsed time

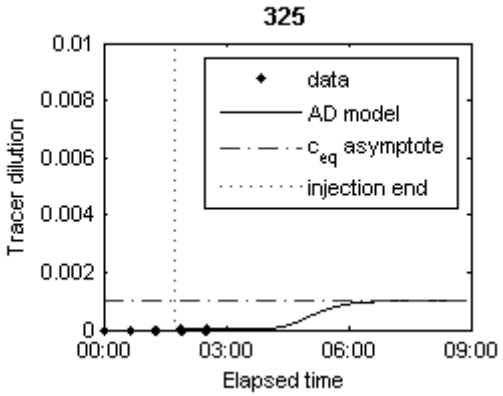
325
0.01
0.008
0.006
0.004
0.002
0
Tracer dilution
data
AD model
c_{eq} asymptote
injection end
00:00
03:00
06:00
09:00
Elapsed time

Medium sand: $\bar{c}_{eq} = 2.25 \times 10^{-4}$ $v_a = 1.92 \times 10^{-2}$ $D = 5.04 \times 10^{-2}$

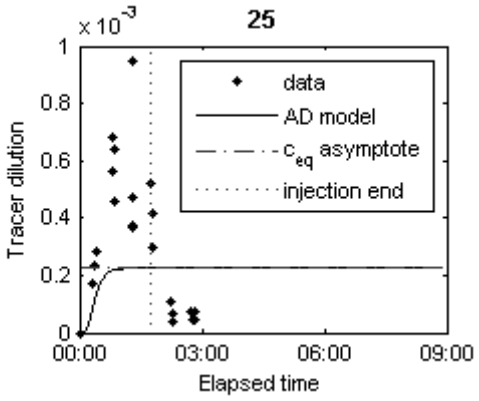

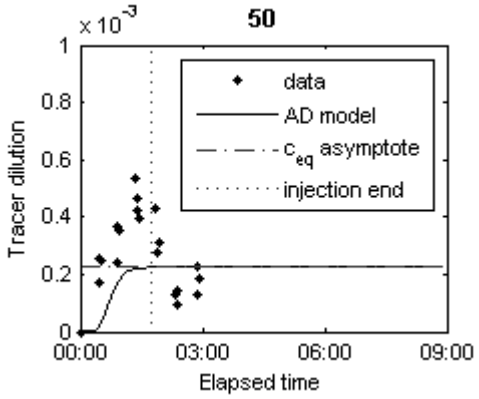

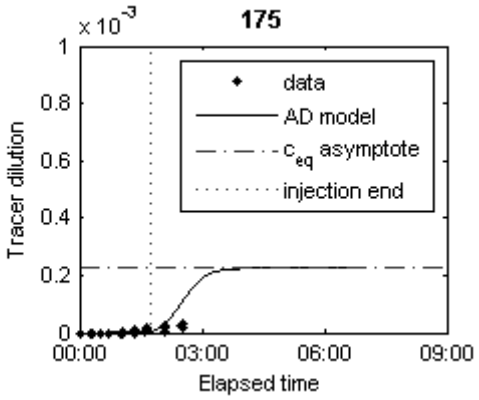

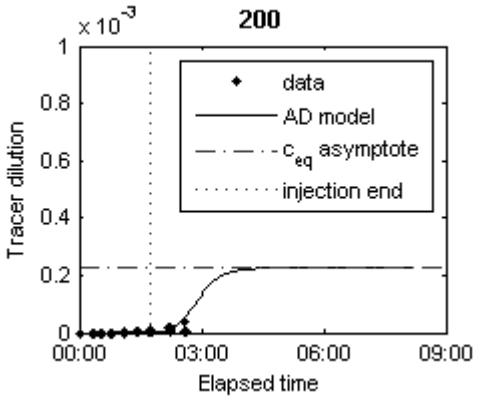

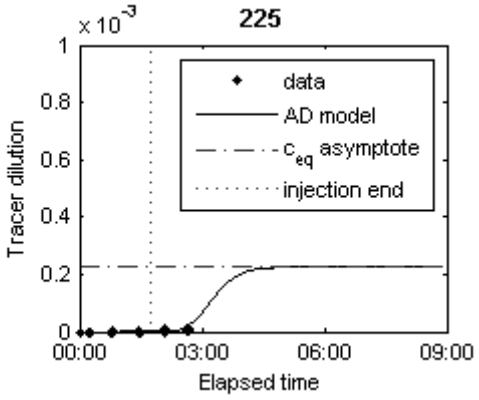

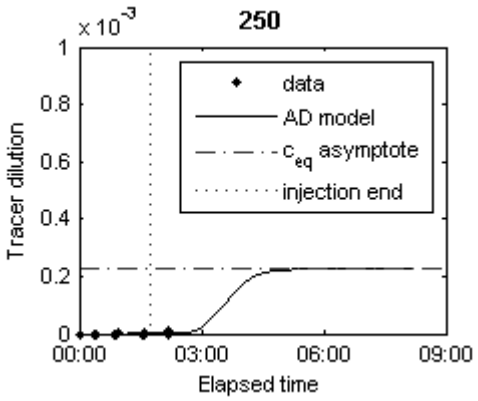

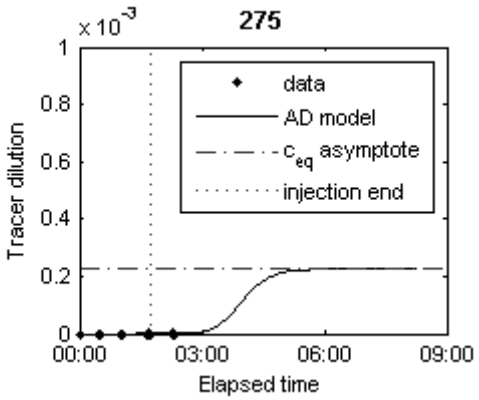
275
x 10^-3
1
0.8
0.6
0.4
0.2
0
Tracer dilution
00:00
03:00
06:00
09:00
Elapsed time
data
AD model
c_eq asymptote
injection end

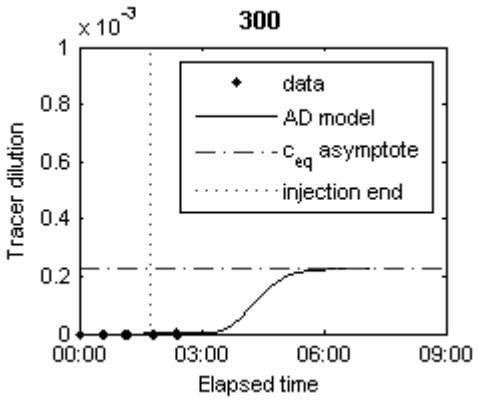
300
x 10^-3
1
0.8
0.6
0.4
0.2
0
Tracer dilution
00:00
03:00
06:00
09:00
Elapsed time
data
AD model
c_eq asymptote
injection end

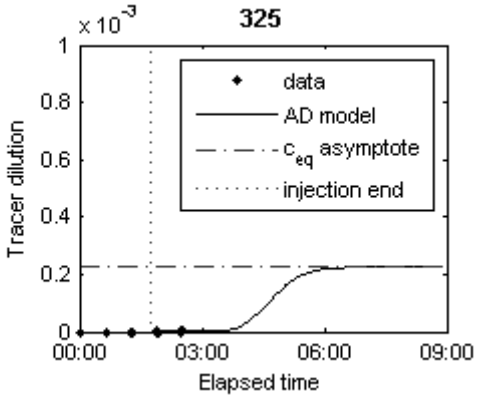
325
x 10^-3
1
0.8
0.6
0.4
0.2
0
Tracer dilution
00:00
03:00
06:00
09:00
Elapsed time
data
AD model
c_eq asymptote
injection end

Fine sand: $\bar{c}_{eq} = 1.75 \times 10^{-5}$ $v_a = 1.97 \times 10^{-2}$ $D = 6.62 \times 10^{-2}$

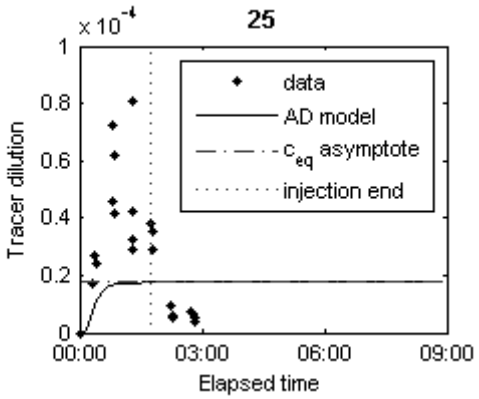

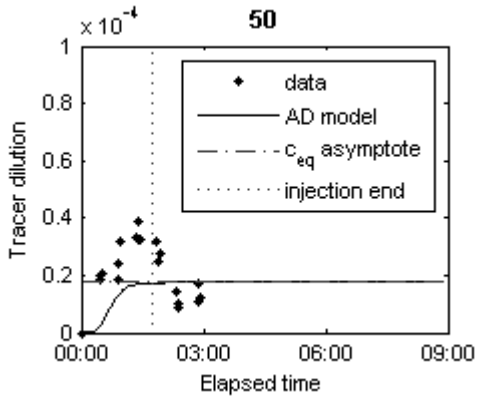

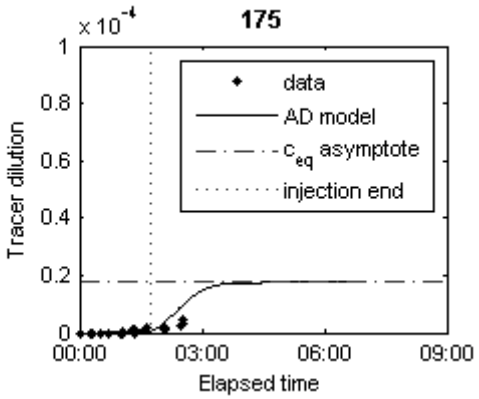

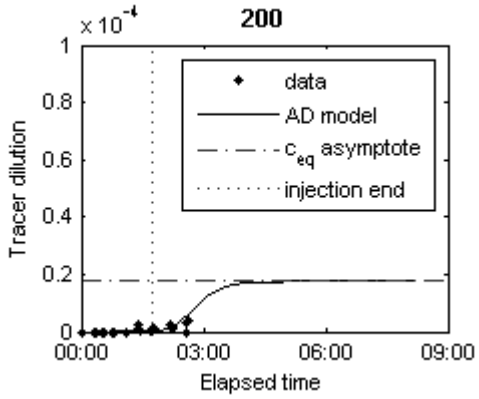

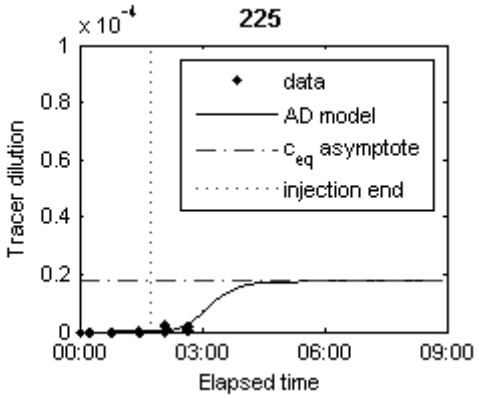

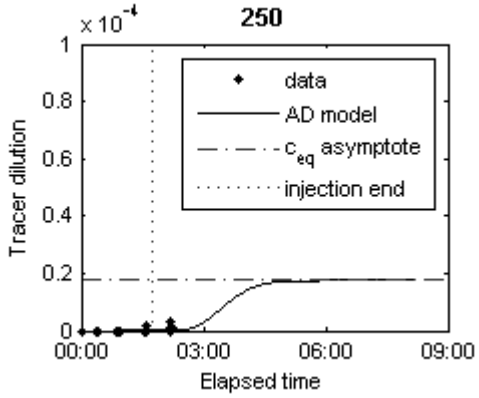

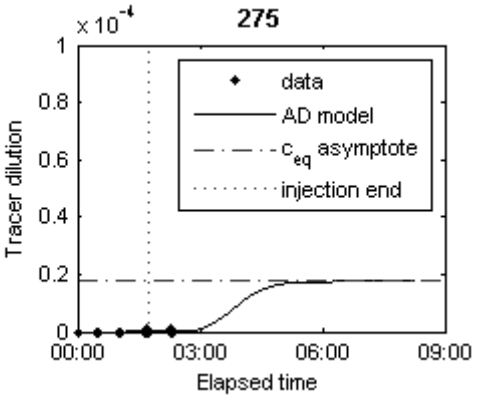
275
x 10^-4
1
0.8
0.6
0.4
0.2
0
Tracer dilution
00:00
03:00
06:00
09:00
Elapsed time
data
AD model
c_eq asymptote
injection end

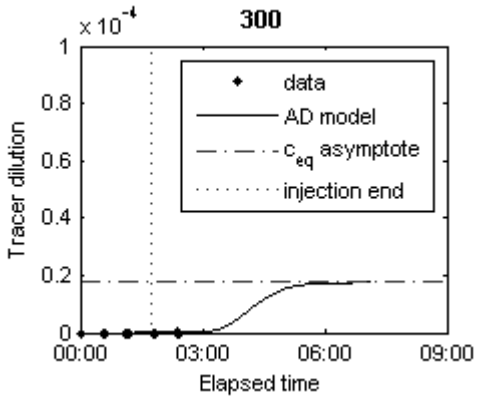
300
x 10^-4
1
0.8
0.6
0.4
0.2
0
Tracer dilution
00:00
03:00
06:00
09:00
Elapsed time
data
AD model
c_eq asymptote
injection end

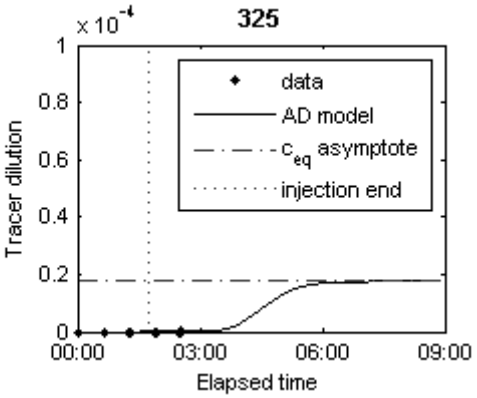
325
x 10^-4
1
0.8
0.6
0.4
0.2
0
Tracer dilution
00:00
03:00
06:00
09:00
Elapsed time
data
AD model
c_eq asymptote
injection end